

NICHTLINEARER ZUGANG FÜR DAS INVERSE
PROBLEM DER PHASENRÜCKGEWINNUNG AUS
EINZELMESSUNGEN DER RÖNTGENINTENSITÄTEN
BEI NUR EINEM PROPAGATIONSABSTAND

Zur Erlangung des akademischen Grades eines
DOKTORS DER NATURWISSENSCHAFTEN
von der Fakultät für Physik des
Karlsruher Instituts für Technologie (KIT)

genehmigte

DISSERTATION

von

Dipl.-Phys. Julian Philipp Moosmann
aus Bretten

Tag der mündlichen Prüfung: 09.01.2015

Referent: Prof. Dr. Tilo Baumbach

Korreferent: Dr. habil. Ralf Hofmann (Privatdozent)

Julian Philipp Moosmann: *Nichtlinearer Zugang für das inverse Problem der Phasenrückgewinnung aus Einzelmessungen der Röntgenintensitäten bei nur einem Propagationsabstand*. Nonlinear approaches to the inverse problem of phase retrieval from single-measurement X-ray intensity data. © 09.01.2015

JULIAN PHILIPP MOOSMANN

NONLINEAR APPROACHES TO THE INVERSE
PROBLEM OF PHASE RETRIEVAL FROM
SINGLE-MEASUREMENT X-RAY INTENSITY DATA

ABSTRACT

This thesis aims at the development of nonlinear approaches to the inverse problem of phase retrieval from single-measurement X-ray intensity data. Furthermore, intricacies of X-ray phase-contrast micro-tomography and its application for *in vivo* imaging in developmental biology are considered.

In the framework of Fresnel theory, approaches to single-distance phase retrieval that work beyond linearity are developed. Starting points are linear approximations to Fresnel theory. On the one hand, the transport-of-intensity equation (TIE) which is the imaginary part of the paraxial wave equation and valid in the limit of small propagation distances. On the other hand, the contrast transfer function (CTF) which is limited to weakly varying phases but not restricted to small propagation distances.

At large propagation distances, phase retrieval based on TIE exhibits limited resolution since the corresponding filter in transverse Fourier space acts as a low pass suppressing large frequencies. However, large propagation distances are required to enhance the signal-to-noise ratio, in particular with respect to a reduction of dose due to residual absorption. Here a systematic expansion of phase and intensity of the propagated wave front in powers of propagation distance is proposed. The expansion coefficients are determined by appeal to full Fresnel theory, i. e. using both the imaginary and the real part of the paraxial wave equation. This yields a partial differential equation in the phase at object exit. Nonlinear corrections to the phase are evaluated perturbatively in terms of the leading-order estimate which is given by the TIE-phase. While this approach improves phase retrieval quantitatively, it cannot enhance spatial resolution owing to the poor resolution of the TIE phase.

In order retrieve a highly resolved phase, we analyse the behaviour of CTF at strong phase variations as they occur in imaging of early developmental stages of model organisms in development biology. Under upscaling of phase variations, intensity contrast exhibits a critical phenomenon which is associated to a scaling symmetry, exact in the limit of vanishing phase variations. At finite phase variations, this symmetry is explicitly broken by non-linear (and non-local) propagation effects, causing a shift of zeros crossings of the Fourier transformed intensity. However, below a critical value of phase variations scaling symmetry is dynamically unbroken and the positions of lifted zeros remain fixed. Above phase variations of order one, positions of lifted zeros exhibit critical behaviour and start to move like order parameters in second-order phase transitions. Moreover, below crit-

ical upscaling, the distribution of information in Fourier space, which is concentrated between lifted zeros, remains unchanged. These two observations are exploited as after a renormalisation of the propagated intensity a quasi-linear relation between renormalised intensity and exit phase is restored, which can be used input for CTF phase retrieval. This is reminiscent to the ubiquitous concept of quasiparticles in condensed matter and quantum field theory. A significantly improved spatial resolution of the quasiparticle approach compared to linear methods is demonstrated on tomographic data of *Xenopus* frog embryos.

Furthermore, intricacies of tomographic reconstruction and related artifacts are considered. In particular, in the context of phase-contrast data and local tomography large-scale modulations arise which considerably impair subsequent data processing and analysis. A means to mitigate such artifacts is demonstrated upon reversing the order of phase retrieval and tomographic reconstruction.

The last part aims at the application of in vivo propagation-based phase contrast to image the early development of model organisms in developmental biology. Besides the effects of dose and the thus required fine tuning of the experimental setup, developmental aspects of the '*Xenopus laevis*' model system are discussed.

KURZFASSUNG

Ziel dieser Arbeit ist die Entwicklung nichtlinearer Zugänge für das inverse Problem der Phasenrückgewinnung aus Einzelmessungen der Röntgenintensitäten bei nur einem Propagationsabstand. Des weiteren werden Fragestellungen im Bezug auf Röntgenphasenkontrast-Mikrotomographie und deren Anwendungen für die *in vivo* Bildgebung in der Entwicklungsbiologie besprochen.

Im Rahmen der Fresneltheorie werden Erweiterungen gängiger Methoden der Phasenrückgewinnung aus einzelnen Intensitätsmessungen entwickelt. Ausgangspunkt sind lineare Näherungen der Fresneltheorie. Dies ist zum einen die Intensitätstransportgleichung, welche den Imaginärteil der paraxialen Wellengleichung darstellt und im Limes kleiner Propagationsabstände gültig ist. Zum anderen die Kontrasttransferfunktion, welche im Grenzfall schwach variierender Phasen angewandt wird, jedoch nicht auf kleine Propagationsabstände beschränkt ist.

Bei großen Propagationsabständen ist die Phasenrückgewinnung unter Verwendung der Intensitätstransportgleichung auflösungslimitiert, da der entsprechende Filter im transversalen Fourierraum als Tiefpass wirkt und hohe Frequenzen unterdrückt. Große Propagationsabstände sind aber erforderlich um ein gutes Signal-Rausch-Verhältnis zu erhalten. Insbesondere im Hinblick auf eine Begrenzung der Strahlendosis aufgrund residualer Absorption. Hier wird ein Ansatz gewählt welcher Phase und Intensität der propagierten Wellenfront in Potenzen des Propagationsabstands entwickelt. Die Entwicklungskoeffizienten werden dann mithilfe der vollen Fresneltheorie bestimmt, d.h. unter Zuhilfenahme von Imaginär- und Realteil der paraxialen Wellengleichung. Damit erhält man eine nichtlineare partielle Differentialgleichung in der Phase bei Objekt-Austritt. Korrekturen nichtlinear Ordnung zur Phase werden im Sinne einer Störungstheorie durch das Ergebnis zur ersten Ordnung ermittelt, welches mit dem der Intensitätstransportgleichung identisch ist. Dieses Zugang führt zu einer quantitativen Verbesserung der zurückgewonnenen Phasenkarte, erhöht jedoch nicht deren räumliches Auflösungsvermögen gegenüber der linearen Ordnung.

Um dennoch eine hochaufgelöste Phasenkarte bei großen Abständen zu gewinnen wird das Verhalten der Kontrasttransferfunktion bei starken Phasenvariationen betrachtet wie sie z.B. bei der Untersuchung früher Embryonalstadien von Modellorganismen in der Entwicklungsbiologie auftreten. Unter einer Hochskalierung der Phasenvariationen wird im propagierten Intensitätskontrast ein kritisches Phänomen beobachtet. Dieses steht im Zusammenhang mit einer im

Limes verschwindender Phasenvariationen exakten Skalierungssymmetrie. Aufgrund nichtlinear (und nichtlokaler) Propagationseffekte wird diese Symmetrie explizit gebrochen, was ein Anheben der Nullstellen der Fouriertransformierten Intensität bei endlichen Phasenvariationen zur Folge hat. Unterhalb eines kritischen Wertes der Phasenvariationen ist die Skalierungssymmetrie jedoch dynamisch nicht gebrochen und die Position der angehobenen Nullstellen bleibt unverändert. Oberhalb von Phasenvariationen der Ordnung eins wird ein kritisches Verhalten der Nullstellenpositionen beobachtet, welche beginnen fort zu laufen wie Ordnungsparameter in Phasenübergängen zweiter Ordnung. Des weiteren bleibt unterhalb kritischer Werte der Phasenvariationen die zwischen den Nullstellen im Fourierraum konzentrierte Verteilung der Information erhalten. Unter Ausnutzung dieser beiden Phänomene erhält man nach einer geeigneten Renormierung der propagierten Intensität eine quasilineare Beziehung zwischen Phasenkarte in der Objektebene und renormierter Intensität, welche die Phasenrückgewinnung mittels der linearen Kontrasttransferfunktion gestattet. Dies ähnelt dem Konzept von Quasiteilchen in der Theorie der kondensierten Materie oder Quantenfeldtheorie. An tomografische Daten von Froschembryonen wird eine deutlich erhöhte räumliche Auflösung des Quasiteilchen-Zugangs gegenüber linearen Methoden demonstriert.

Im weiteren wird auf Probleme bei der tomografischen Rekonstruktion und diesbezüglicher Artefakte eingegangen. Insbesondere im Zusammenhang mit Phasenkontrastdaten und lokaler Tomografie treten großskalige Variationsartefakte auf welche die nachfolgende Datenverarbeitung und -analyse erheblich erschweren. Zur Reduktion solche Artefakte wird hier unter anderem eine Umkehrung der Reihenfolge von Phasenrückgewinnung und tomografischer Rekonstruktion betrachtet.

Im letzten Abschnitt wird die Röntgenphasenkontrast-Mikrotomographie für die vierdimensionale Bildgebung der frühen Entwicklung in lebenden Modellorganismen angewandt. Neben den Auswirkungen der Strahlendosis und der damit einhergehenden notwendigen Optimierung des experimentellen Setups, wird auf entwicklungsbiologische Fragestellungen im Froschsystem '*Xenopus laevis*' eingegangen.

PUBLICATIONS

Some ideas and figures have appeared previously in the following publications:

- J. Moosmann, A. Ershov, V. Weinhardt, T. Baumbach, M. S. Prasad, C. LaBonne, X. Xiao, J. Kashef & R. Hofmann. Time-lapse X-ray phase-contrast microtomography for *in vivo* imaging and analysis of morphogenesis. *Nature Protocols* **9**, 294 (2014).
- J. Moosmann, A. Ershov, V. Altapova, T. Baumbach, M. S. Prasad, C. LaBonne, X. Xiao, J. Kashef & R. Hofmann. X-ray phase-contrast *in vivo* microtomography probes new aspects of *Xenopus* gastrulation. *Nature* **497**, 374 (2013).
- J. Moosmann, V. Altapova, L. Helfen, D. Hänschke, R. Hofmann & T. Baumbach. High-resolution X-ray phase-contrast tomography from single-distance radiographs applied to developmental stages of *Xenopus laevis*. *J. Phys.: Conf. Ser.* **425**, 192003 (2013).
- J. Moosmann, V. Altapova, D. Hänschke, R. Hofmann & T. Baumbach. Non-Linear, noniterative, single-distance phase retrieval and developmental biology. *AIP Conf. Proc.* **1437**, 57 (2012).
- R. Hofmann, J. Moosmann & T. Baumbach. Criticality in single-distance phase retrieval. *Opt. Express* **19**, 25881 (2011).
- J. Moosmann, R. Hofmann & T. Baumbach. Non-Linear, single-distance phase retrieval and Schwinger regularization. *Phys. Status Solidi A* **208**, 2511 (2011).
- J. Moosmann, R. Hofmann & T. Baumbach. Single-distance phase retrieval at large phase shifts. *Opt. Express* **19**, 12066 (2011).
- J. Moosmann, R. Hofmann, A. V. Bronnikov & T. Baumbach. Non-linear phase retrieval from single-distance radiograph. *Opt. Express* **18**, 25771 (2010).

CONTENTS

1	INTRODUCTION	1
2	THEORY OF IMAGING	11
2.1	Maxwell's theory	12
2.1.1	Macroscopic Maxwell's equations	12
2.1.2	The wave equation	16
2.1.3	Helmholtz equation	19
2.1.4	Scattering from inhomogeneous media	21
2.1.5	Fresnel diffraction theory	27
2.1.6	Projection approximation	35
2.1.7	Filtered backprojection	38
2.1.8	Coherence	44
2.2	Microscopic interactions of X-rays and matter	55
2.2.1	Scattering	55
2.2.2	Absorption	61
2.3	Phase retrieval	63
2.3.1	Transport of intensity equation	65
2.3.2	Contrast transfer function	69
2.3.3	Phase-attenuation duality	73
2.3.4	Regularisation in phase retrieval	77
3	EXPERIMENTAL IMPLEMENTATION	81
3.1	X-ray sources	81
3.1.1	X-ray tubes	83
3.1.2	Synchrotron radiation facilities	84
3.1.3	Free-electron laser	89
3.2	Monochromator	90
3.3	Detector system	93
4	PHASE RETRIEVAL BEYOND LINEARITY	99
4.1	Perturbation theory	99
4.1.1	Next-to-leading-order correction	99
4.1.2	Next-to-next-to-leading-order correction	104
4.1.3	Non-Linear phase retrieval	105
4.2	Quasiparticle approach	109
4.2.1	Linear models	110
4.2.2	Influence of noise	113
4.2.3	Quasiparticle transfer of contrast	115
4.2.4	Quasiparticle transfer under global phase-attenuation duality	120
4.2.5	Ex vivo X-ray phase-contrast microtomography	122
4.2.6	In vivo X-ray phase-contrast microtomography	125

5	TOMOGRAPHY AND PHASE RETRIEVAL	127
5.1	Large-scale modulations	129
5.2	Direct retrieval of the refractive index decrement	133
5.3	Noise-induced ring artifacts	137
5.4	Continuous versus discrete rotation	138
6	X-RAY PHASE-CONTRAST IN VIVO MICROTOMOGRAPHY OF EMBRYONIC DEVELOPMENT	143
6.1	Motivation	143
6.1.1	The Xenopus model organism	143
6.2	X-ray dose	145
6.2.1	Heat load	145
6.2.2	Direct impact	149
6.2.3	Radiolysis of water	150
6.3	Method	151
6.3.1	Comparison with other methods	153
6.3.2	Experimental setup	153
6.3.3	Optimisation of phase-contrast tomography setup	155
6.4	Gastrulation in <i>Xenopus laevis</i> live cell imaging	156

7	SUMMARY AND OUTLOOK	163
----------	----------------------------	------------

A	FOURIER ANALYSIS	167
A.1	Definitions using angular frequencies	167
A.1.1	Fourier transformation	167
A.1.2	Convolution theorem	168
A.1.3	Fourier derivative theorem	168
A.2	Definitions using ordinary frequencies	168
A.2.1	Fourier transformation	169
A.2.2	Convolution theorem	169
A.2.3	Fourier derivative theorem	169

LIST OF FIGURES	171
------------------------	------------

LIST OF TABLES	174
-----------------------	------------

ACRONYMS	175
-----------------	------------

BIBLIOGRAPHY	177
---------------------	------------

INTRODUCTION

The discovery of X-rays represents a milestone in the history of imaging. It opened up the possibility to visualise internal structures of objects that had hitherto been eluded human perception. Already in 1893 Helmholtz forecasted a high penetration ability and small refrangibility (refractivity) for propagating electromagnetic fields with wave lengths of atomic order. Prior to Röntgen's discovery of X-rays in 1895, Hertz and Lenard have noted the existence of metal penetrating rays producing photographic impressions [Gla34]. However, it was Röntgen who systematically studied the penetrating power of X-rays [Rön96] that led to immediate applications. The first clinical X-ray experiment was performed shortly after Röntgen's announcement [Spi95]. Since then X-rays have been beneficially applied across disciplines.

The characteristic spectrum of secondary X-rays emitted from materials irradiated with hard X- or gamma rays was discovered by Barkla [Baro4]. Peculiar to a particular substance, this fluorescent radiation is used for elemental and chemical analysis in X-ray spectroscopy. Furthermore, Barkla discovered the polarisation of X-rays [Baro5]. This and diffraction experiments on a single slit supported a wave-like interpretation of the X-radiation and suggested its wave length to be in the order of 10^{-10} m [Som12].

Another remarkable feat was the discovery of X-ray diffraction through crystals by Laue in 1912 [FKL13]. Attributing the observed diffraction pattern to the interference of waves which were diffracted by the crystal's atomic lattice, Bragg connected the macroscopic and the atomic (world) [Bra13]. Allowing to deduce the local position of atoms in a crystal, this did not only elucidate the wave nature of X-rays, but marks the advent of modern X-ray crystallography, which aims to understand the structure of matter. X-ray crystallography made it possible to determine the atomic structure of simple minerals, sophisticated materials such as graphene, or highly complex molecules and proteins such as deoxyribonucleic acid (DNA), enzymes, transcription factors, the components of the cytoplasm and the cellular machines, and viruses. The need for appropriately sized crystals is mitigated by powder diffraction using polycrystalline samples [DS16; Hul17] or by fibre diffraction in the case of oriented fibres such as DNA [Pol21]. The X-ray image of DNA, that was recorded by Franklin in 1952 [FG53] and which inspired Crick and Watson to their DNA model of the double helix [WC53], was acquired by means of fibre diffraction. Another versatile method to investigate a variety of ma-

terials, including non-crystalline solids or even liquids, is small-angle X-ray scattering (SAXS). It exploits the elastic scattering of X-rays by colloidal structures which are due to electron density inhomogeneities within the sample [KG82].

In 1905, explaining the photoelectric effect, Einstein introduced the concept of a photon as a quantum of light [Ein05]. His findings suggest a corpuscular interpretation of X-rays, confirmed by the observation of (inelastic) scattering of X-rays from electrons by Compton in 1923 [Com23]. X-ray absorption spectroscopy (XAS) exploits the photoelectric effect to probe the transition of photoelectrons from core electronic states (usually K-, L-, and M-edges) to excited states just below or unbound states in the continuum. The former is known as X-ray absorption near-edge structure (XANES), and the latter as extended X-ray absorption fine structure (EXAFS). Measuring the X-ray absorption fine structure (XASF), which comprises XANES and EXAFS, allows to deduce information about the local atomic environment and the chemical state in terms of the numbers, types, and distances of neighbouring atoms, their coordination numbers, or electronic structures [KP87].

While in radiation therapy they are also employed to treat cancer, X-rays are mostly applied in medical imaging where their use can be considered revolutionary. Conventional projection radiography provides a two-dimensional, superimposed representation of internal structures of the human body. It visualises strongly absorbing tissues such as bones, gall or kidney stones, but also contrast variations between air and the soft pulmonary tissue of the lungs or those introduced by cavities in carious teeth. In Fluoroscopy intensity contrast is enhanced by means of contrast agents. This enables to investigate the gastrointestinal tract or to visualise veins and arteries of the cardiovascular system or the cerebral spinal fluid (angiography). As a three-dimensional extension of these imaging strategies, X-ray computed tomography has become indispensable for medical imaging.

Tomography was invented to acquire more than a mere projection of the human body. Here, cross-sectional images of the inside of the body are obtained, allowing for a three-dimensional representation of the body's internal parts. Practical implementations of computed tomography were independently developed by Hounsfield [Hou73] and Oldendorf [Old61]. Mathematically, the problem of reconstructing an object from a set of its projections (line integrals) was already solved by Radon in 1917 [Rad86]; and 45 years later, simultaneous to the work of Hounsfield, by Cormack [Cor63; Cor64] being unaware of Radon's work. Rapidly X-ray computed tomography (CT) turned into an invaluable tool for medical diagnostics as well as industrial imaging, where CT scanners have found a broad scope of commercial applications as e.g. in metrology, non-intrusive inspection, non-destructive testing, or transport security.

Nowadays, modern synchrotron radiation facilities range among the most technologically complex scientific machines in the world [Wil96]. Devoted to the production of X-rays of extreme brilliance and coherence only, these facilities serve the scientific and applied community as sophisticated tools to explore the structure and dynamics of matter. Such X-ray sources allow to acquire data of unprecedented quality in terms of spatiotemporal resolution and intensity contrast. This, combined with recent developments in detector technologies [MKo6] and a growing computational infrastructure, has advanced the field of X-ray imaging tremendously.

In a typical imaging experiment, a quasi-parallel photon beam impinges on a sample whose electron density distribution is described by the refractive index. An imprint is left on the photon beam by the sample in terms of local amplitude and phase modulations of the transmitted wave front. The induced modulations are given by line integrals of the refractive index along the photon path and thus represent projections of the electron density. The exiting wave front then propagates towards the detector. This situation is well described by Fresnel diffraction theory [HYFoo].

For materials with high atomic number exhibiting strong absorption, the object information is encoded in local amplitude modulations of the exit wave. In the absence of propagation effects the amplitude is determined by the square root of the intensity. Materials of low atomic number and number density, such as polymers or soft biological tissue, exhibit a weak attenuation of hard X-rays only, and absorption contrast is poor. However, phase shifts of the exit wave front imparted by such samples are still sizable. Therefore we are obliged to appeal to the information contained in the phase variations of the exit wave. Already visible light oscillates at frequencies in the order of 10^{14} Hz, which is far beyond the read-out rates of current detectors. Only the temporal average of the squared modulus of the electromagnetic wave is accessible, rendering a direct measurement of the phase of a wave field impossible.

In optical microscopy, this problem was solved by Zernike who invented phase contrast microscopy [Zer42a; Zer42b; Zer55]. Upon conversion of specimen-induced phase shifts into brightness variations, Zernike could reveal structures invisible to traditional bright field microscopes. Nowadays, this technique is also employed in X-ray microscopes at synchrotron facilities [Sch+94]. Besides Zernike phase contrast, a diversity of interferometric phase-contrast techniques were developed to deduce the local phase variations of an X-ray wave front in the transverse plane, e. g. crystal interferometry [BH65], analyser-based or diffraction-enhanced imaging [Cha+97], grating interferometry [Mom+03], coded apertures [OSo8] or edge illumination [PP13]. An instrumentally simpler approach to sense the phase appeals to the self-interference of propagating (coherent) X-rays, an effect that

already Röntgen sought after [Rön96]. Yet, it was not before the advent of modern synchrotrons, producing highly coherent beams of X-rays, that advantage could be taken of such self-interference effects, making propagation-based phase-contrast possible [Sni+95; Wil+96; PN98]. Distortions in the exit wave front result in locally diffracted light rays which, by free-space propagation over a distance in the range of decimetres, start to interfere; and intensity contrast emerges.

Apart from an enhanced sample-to-detector distance and demands on beam coherence, the setup of a propagation-based phase-contrast experiment is practically identical to that of conventional absorption contrast radiography. It is free from additional optics such as crystals or gratings. Neither does it require a scanning or stepping procedure as in diffraction-enhanced imaging or grating interferometry, respectively, nor the meticulous alignment and stability of a crystal interferometer. Thus, the technique is dose efficient and instrumentally simple, and requires a single intensity measurement at a single distance only. Optionally, measurements at several distances can be acquired to improve image quality or to overcome restrictions posed by reconstruction algorithms. Therefore, propagation-based phase-contrast imaging has evolved into a standard technique at modern synchrotron.

Resorting to propagation-based phase contrast, the retrieval of the phase of the exiting wave front from the measured intensity is a precursor for two- or three-dimensional image analysis. In Fresnel theory, the exact inversion of the non-local and non-linear relation between phase and intensity represents an insurmountable obstacle. The problem of phase retrieval appears in various other fields such as electron and optical microscopy, wave front sensing, crystallography, or astronomy. Numerous approaches were devised to address this issue. Adaptive optics e.g. measure and correct for distortions in the wave front. Originally developed in astronomy to remove phase aberrations introduced by turbulences in the Earth's atmosphere [Bec93], adaptive optics have since been used in optical microscopy, too [Boo+07]. Iterative methods, such as the Gerchberg-Saxton algorithm, incorporate boundary conditions on the object in an iterative process of back-and-forward propagation of the wave field in the far-field regime [GS72; Sax78]. Here, the issue of convergence arises. Moreover, the iteration loop has to be provided with a termination condition and is computationally demanding. Hence, we adhere to direct, non-iterative methods for addressing the inverse problem of phase retrieval.

In the framework of Fresnel theory, there are two prevalent approaches. One is based on the TIE, which is the imaginary part of the paraxial wave equation [Tea82; RKT89], the other relies on a two-fold exploitation of the Fresnel diffraction integral, relating the two-point autocorrelation of the exit wave field to the measured intensity [Gui77].

For pure-phase objects and in the very near field, TIE is approximated by a linear relation between the intensity and the Laplacian of the phase [Pago6]. Increasing the sample-to-detector distance from zero, fringes emerges out of a homogeneous background at the edges of structures in the projected object. In this region, which is known as the edge-enhancement regime and typically ranges in the order of a few centimetres for X-ray energies of about 30 keV, the signal rises linearly with propagation distance. However, owing to the small sample-detector distances, the signal-to-noise ratio is poor. Moreover, being restricted to measure in the edge-enhancement regime impairs experiments where the sample is suspended in a large environment which is inaccessible to the detector. By inversion of linearised TIE in Fourier space, an efficient and robust algorithm is obtained. It is also applicable at large propagation distances, but then suffers from a poor spatial resolution because it acts as a low-pass filter in Fourier space suppressing the high frequencies. The thus retrieved phase deviates from the exact one when phase variations in the exit wave become large (>1) and/or propagation distances appreciable.

In this thesis we expand intensity contrast and phase shift in the detector plane in powers of the object-detector distance to perform phase retrieval beyond the solution to linearised TIE [Moo+10]. The expansion coefficients are determined by the full paraxial wave equation. Compared to TIE, which only involves the imaginary of the paraxial wave equation, expanding beyond leading order thus increasingly accounts for the constraints of full Fresnel theory. The Laplacian of the phase shift of the exit wave is then written as a local expression linear in the intensity contrast and non-linear in the phase shift of the exit wave. To leading order the linearised version of TIE is restored, which is linear in distance and phase variations. The non-linear expression is then evaluated perturbatively to obtain a correction to the leading-order estimate; this correction being approximated in terms of the leading-order estimate. While this perturbative approach cannot improve spatial resolution, due the limited resolution of the leading-order estimate (TIE acting as low-pass filter), the values of the retrieved phase, when including higher-order corrections, are more accurate than those of the leading order result. This is even more pronounced for exit phase maps which exhibit a hierarchy between small and large scales.

The other common approach is based on approximating the Fourier transform of the two-point autocorrelation of the exit wave in the limit of weak phase variations (and vanishing absorption). Thus, a linear relation between intensity and all powers of the Laplacian acting on the phase is obtained. In Fourier space this translates into a sinusoidal contrast transfer function multiplied by the Fourier transformed phase [Gui77; Gui78; Pap74]. The concept of transfer functions stems from transmission electron microscopes [Kir98] and is akin to optical

transfer functions in light microscopy [Str85]. Even beyond edge enhancement, inversion of the contrast transfer function (CTF) is not limited in resolution owing to a resummation of all powers of the distance. However, many specimen induce considerable phase variations violating the condition under which the CTF approach is valid. Exploring the formation of intensity contrast in Fresnel theory under a departure from the condition of weakly varying phases, we have observed a critical phenomenon [MHB11b]. Due to non-linear (and non-local) propagation effects zeros in the Fourier transformed intensity, intrinsic to CTF, become finite under an upscaling of phase variations. The positions of these lifted zeros, however, remain constant up to a critical upscaling, beyond which these positions start to move rapidly.

Interpreting the Fourier transformed intensity as complex energy and the Fourier transformed phase as complex momentum, the CTF relation can be regarded as a dispersion law. Away from the trivial limit of vanishing phase variations, an, in principle, non-linear and non-local relation emerges. Due to the afore mentioned critical behaviour, this relation can be cast into a linear and local relation after an appropriate renormalisation of the Fourier transformed intensity contrast [HMB11]. This situation is reminiscent of the concept of quasiparticles in condensed matter theory, e.g. the Fermi liquid [Lan57], or in quantum field theory [Hof11]. It allows to exploit the enhanced signal-to-noise ratio at large propagation distances and to retrieve strongly varying phases at a high spatial resolution.

The quasiparticle approach was successfully applied to image embryogenesis in the African clawed frog '*Xenopus laevis*'. Opaque to visible light, the *Xenopus* frog cannot be examined by optical light microscopy, apart from its surface. The *Xenopus* frog is an important vertebrate model organism in developmental biology due to the remarkable structural similarity of its genome with the human genome [Hel+10]. Imaging the development of living *Xenopus* embryos is thus in great demand, but extremely challenging. Here, the instrumental simplicity and efficiency make propagation-based phase-contrast favourable in terms of dose and speed. This and the fact that the quasiparticle phase retrieval depends on intensity measurements at a single distance only, facilitate the imaging of dynamic and *in vivo* processes.

In this thesis, we have applied and established single-distance X-ray phase-contrast microtomography to image *in vivo* the early development of model organisms in three spatial dimensions and throughout time [Moo+13b]. Imaging of living samples represents an optimisation problem in a high dimensional parameter space which requires a significant amount of fine tuning to arrive at an optimal setup within the constraints imposed by *in vivo* imaging (avoidance of motion blur due to development, constraints on dose, window of propaga-

tion distances, blur introduced by source function versus photon statistics, etc.). In addition, logistics and timing to provide living embryos at a certain developmental stage at a certain point in time to fully exploit the limited beam time at synchrotron facilities is challenging [Moo+14]. In this thesis we could observe and examine cell behaviours with micrometre-scale resolution throughout the optically opaque, living embryo over the course of gastrulation and neurulation. The insights into developmental dynamics thus acquired cannot be attained by imaging explants or fixed embryos nor using other methods such as fluorescence microscopy or microscopic resonance imaging. In particular, employing X-ray phase-contrast *in vivo* microtomography afforded to pin down key aspects of gastrulation in the *Xenopus* model system. With forthcoming upgrades of modern synchrotrons, essentially decreasing source size and thus boosting spatial coherence [Rei13], we expect a substantial improvement in resolution and dose efficiency. This will enable even longer time-lapse sequences than the previously recorded two-hour series.

In Chapter 2 we give an introduction to the theory of X-ray imaging with particular attention on propagation-based phase contrast. Section 2.1 reviews Maxwell's equations in free-space and within matter and discusses Fresnel theory in detail. Furthermore, we give a treatment of coherence and explain principles of filtered backprojection (FBP) for the reconstruction of tomographic data. In Section 2.2 we shortly review the interactions of X-rays with matter. Section 2.3 discusses prevalent methods of phase retrieval and their limitations in the context of Fresnel theory.

Chapter 3 is concerned with the implementation of an imaging experiment at a synchrotron beamline. In Section 3.1 different sources of X-rays are described, including X-ray tubes, synchrotron radiation facilities, and free-electron laser. Section 3.2 discusses monochromatisation by a multilayer or crystal, and Section 3.3 the typically employed indirect detector system, involving scintillation, magnifying optics, and semiconductor camera.

In Chapter 4 we discuss a departure from linear models of single-distance phase retrieval and present two new techniques. In Section 4.1, we propose an expansion of propagated intensity contrast and phase shift in the detector plane in powers of the object-detector distance. Thus, phase retrieval is performed beyond the solution to the linearised transport-of-intensity equation (TIE). These expansion coefficients are determined by appeal to the full paraxial wave equation, and not only its imaginary part. The Laplacian of the phase shift at the object exit is thus written as a local expression linear in the intensity contrast and non-linear in the phase shift in the object exit plane. A perturbative approach to this expression provides corrections to the linear-order estimate given by the linearised-TIE solution.

In Section 4.2 we consider the quasiparticle approach to single-distance phase retrieval. For small phase variations, ideal coherence assures that the ratio of Poisson distributed shot noise to signal in the intensity contrast decreases with the inverse square root of the propagation distance as image detection moves towards the far-field regime. Noise induced in the retrieved phase drops off as the inverse of the propagation distance. This implies a high dose efficiency at large distances. Including all orders in the propagation distance, phase retrieval from a single-distance measurement based on contrast transfer functions is linear and algebraic in Fourier space. However, considerable phase variations in the order of unity entail non-local and non-linear transfer to the propagated intensity. Here, a phase-scaling symmetry is identified in order to approximate a solution to the inverse problem. Exact in the limit of vanishing phase variations, this symmetry, though explicitly broken by non-linearities at finite phase variations, remains dynamically unbroken up to phase variations in the order of unity. There, contrast transfer experiences a series of second-order transitions. Using a mildly and a priori renormalised intensity, algebraic phase retrieval persists within this regime. This is reminiscent of the description of moderately interacting point-particle systems via free quasiparticles. Likewise, decay of phase noise with inverse propagation distance and a treatment of small absorptive effects by phase-attenuation duality abide. Based on coherent synchrotron radiation and quasiparticle phase retrieval, ex and in vivo microtomography is performed on optically opaque *Xenopus* embryos, demonstrating improved spatial resolution compared to linear-in-propagation-distance phase retrieval and beyond the limitation of weakly varying phases.

Chapter 5 is concerned with intricacies of tomographic reconstruction and related artifacts arising particularly in the context of phase-contrast data and local tomography. The latter is due to the sample environment not being fully immersed into the field of view. Section 5.1 examines the artifact of large-scale modulations superimposed on the reconstructed volume thereby obstructing small-scale details and hampering subsequent data processing and analysis. Such modulations originate from an enhancement of low-frequency components in the propagated intensity upon phase retrieval. A means to mitigate large-scale modulations is by reversing the order of phase retrieval and tomographic reconstruction as demonstrated in Section 5.2. The real refractive index decrement is then directly retrieved on the volume reconstructed from propagated intensity maps. In addition, this allows to use alternative (algebraic) reconstruction techniques which would otherwise be impaired by large-scale modulations immanent to the phase retrieved in the presence of absorptive contributions to the low-frequency part of the propagated-intensity spectrum. Section 5.3 is concerned with noise-induced ring artifacts

in the tomographic volume, induced by camera dark currents inherent to image sensors such as charge-coupled devices (CCDs) and complementary metal-oxide-semiconductors (CMOSs). In Section 5.4 we compare tomographic data acquisition under continuous or stepwise rotation and possible reconstruction modalities. Accounting for the continuous rotation in an appropriately adopted reconstruction scheme, results in a considerable reduction of streak artifacts and noise compared to stepwise scanning, though at the expense of angular resolution.

In Chapter 6 we demonstrate the application of X-ray phase-contrast microtomography (XPC μ T) to acquire *in vivo* time-lapse sequences of developing vertebrate embryos. Section 6.1 gives a short introduction to developmental biology and the *Xenopus laevis* model system (Section 6.1.1). In Section 6.2 the effects of radiation dose including heat load, direct impact, and the radiolysis of water are considered. In Section 6.3 propagation-based XPC μ T is conceived as a technique to capture cell and tissue motion during embryonic development of optically opaque model organisms such as *Xenopus* or lamprey. Section 6.3.1 compares XPC μ T with other imaging techniques. Experimental setup and optimisation of which are described in Section 6.3.2 and Section 6.3.3. Results on gastrulation in *Xenopus laevis* are present in Section 6.4.

The thesis concludes with a summary and outlook in Chapter 7.

2

THEORY OF IMAGING

In this chapter we review the theoretical background underlying the process of intensity-contrast formation in an X-ray imaging experiment and subsequent reconstruction of the three-dimensional distribution of the sample's refractive index. Here, one typically considers a beam of quasi-parallel X-rays impinging on a sample. The X-ray beam is modulated upon traversing the sample and then further propagates towards the detector. The distortions in the transmitted wave front, as induced by the interaction of the electromagnetic field with the sample, can be expressed in terms of phase and amplitude modulations of the exiting field. These modulations are usually described by projections, that is line integrals of the refractive index along the path of X-rays. Distortions in the exit wave front entail diffraction of the forward propagating wave front, i. e. local changes of propagation direction as encoded by the wave-front curvature. Thereby, intensity contrast emerges due to the interference of the diffracted light. For hard X-rays, this situation is well described by Fresnel diffraction theory.

In Section 2.1 we discuss the propagation of light and its interaction with matter at the macroscopic level on the basis of Maxwell's equations supplemented by material equations. Following from Maxwell's equations, the wave equation for the electromagnetic field and the time-independent Helmholtz equation for a scalar field describe the propagation of light; the latter neglecting the dynamics of polarisation states. In the limit of quasi-parallel light propagation the Helmholtz equation is approximated by the paraxial wave equation which is the differential manifestation of Fresnel diffraction. Both, the paraxial wave equation and the Fresnel diffraction integral build the basis of common approaches to the problem of phase retrieval from propagated intensities. Thus, in this thesis, emphasis is put on the wave nature of propagating light and the wave optical description as derived from Maxwell's equations.

In Section 2.2 the interaction of X-rays with matter is discussed on the atomic level; and the macroscopic quantities of Section 2.1 such as the refractive index are connected to microscopic properties such as the electron density distribution of the sample.

In Section 2.3 we review two widely used approaches to the problem of phase retrieval and point out their strengths and limitations. Both approaches present linear relations between the exit phase and propagated intensity. On one hand, Paganin phase retrieval derives from an approximation of the transport-of-intensity equation (TIE)

in the limit of small propagation distances. The latter represents the imaginary part of the paraxial wave equation. On the other hand, the contrast transfer function (CTF) approximates the Fourier transformed intensity being expressed through the Fresnel diffraction integral in terms of a two-point autocorrelation of the exit wave field. The CTF approximation is obtained from expanding the autocorrelation of the exit wave field in powers of small relative phase variations.

Moreover, we discuss a duality between phase and attenuation which allows the simultaneous reconstruction of phase and attenuation from one and the same intensity map.

2.1 MAXWELL'S THEORY

The results of most practical interest in this section are:

- The paraxial wave equation which is derived from the Helmholtz equation in the limit of forward propagating quasi-parallel light. It is the differential analogue of the Fresnel diffraction integral and provides a starting point to approach solutions to the inverse problem of phase retrieval of Section 2.3.
- The Fresnel diffraction integral which describes the forward propagation of a given wave front within the realm of the paraxial approximation. Implemented in Fourier space, it serves as a numerically efficient way to simulate intensity maps at a finite propagation distance from a given wave field. Likewise the paraxial wave equation, it prescribes ways on how to reconstruct phase and attenuation maps from the forward propagated intensity under certain approximations.
- The projection approximation which relates the exit wave front behind the sample to line integrals of its refractive index. It enables the tomographic reconstruction of the refractive index of the sample from a 180° data set of projections.
- The filtered backprojection (FBP), enabled by virtue of the projection approximation, serves as a stable and numerically efficient method to reconstruct the refractive index from a set of attenuation or phase maps. Thus three-dimensional information about the electron density distribution of the sample may be obtained.

2.1.1 *Macroscopic Maxwell's equations*

Fundamentally, Maxwell's equations together with the Lorentz force (and Newton's second law) represent the foundations for the description of classically interacting charged particles and electromagnetic fields. The electromagnetic field is the state of excitation established

in the presence of electric charges. It is constituted by the electric field \mathbf{E} and the magnetic induction \mathbf{B} . The sources of these fields are expressed by the electric charge density ρ and the electric current density \mathbf{j} . The interconnection of the electric field and the magnetic induction and their generation by electric charges and currents on the atomic level is described by Maxwell's equation [Max64]. In SI units (Système international d'unités)¹, which will be used throughout this thesis, they are given by the following set of partial differential equations

$$\begin{aligned}\nabla \cdot \mathbf{E} &= \frac{\rho}{\epsilon_0}, \\ \nabla \cdot \mathbf{B} &= 0, \\ \nabla \times \mathbf{E} + \partial_t \mathbf{B} &= 0, \\ \nabla \times \mathbf{B} - \mu_0 \epsilon_0 \partial_t \mathbf{E} &= \mu_0 \mathbf{j}.\end{aligned}\tag{1}$$

The partial derivatives with respect to time t and space coordinates \mathbf{r} are indicated by $\partial_t \equiv \frac{\partial}{\partial t}$ and $\partial_i \equiv \frac{\partial}{\partial x_i} \equiv \nabla_i$, $i = \{1, 2, 3\}$, respectively, when ∇ is the gradient operator. Then $(\nabla \phi)_i \equiv \frac{\partial \phi}{\partial x_i} \equiv \partial_i \phi$ is the gradient of a scalar field ϕ , $\nabla \cdot \mathbf{A} = \partial_i A_i$ the divergence of a vector field $\mathbf{A} = (A_i)$, and $(\nabla \times \mathbf{A})_i = \epsilon_{ijk} \partial_j A_k$ the curl of \mathbf{A} , where ϵ_{ijk} is the Levi-Civita symbol in three dimensions. We have used Einstein's summation convention with a summation over all values of an index appearing twice in a formula. The universal constants μ_0 and ϵ_0 are called the vacuum permittivity and vacuum permeability, respectively. While the value of the vacuum permeability is fixed by the definition of the Ampere¹ to

$$\mu_0 = 4\pi \cdot 10^{-7} \text{ N A}^{-2},\tag{2}$$

¹ For microscopic problems involving charged particles the Gaussian unit system is more suitable. In the Gaussian system, which is based on CGS (centimetre gram second) units, the electromagnetic fields, \mathbf{E} and \mathbf{B} , the auxiliary fields, \mathbf{H} and \mathbf{D} , and the material polarisation and magnetisation, \mathbf{P} and \mathbf{M} , own the same dimension and can be expressed entirely in mechanical units ($\text{cm}^{-1/2} \text{ g}^{1/2} \text{ s}^{-1}$). This applies also to the unit of the electric charge e ($\text{cm}^{-1/2} \text{ g}^{3/2} \text{ s}^{-1}$). Whereas in SI units, \mathbf{E} and \mathbf{B} have different dimensions and the electric charge bears its own unit, the Coulomb, which is a derived unit and defined via the basic SI unit Ampere (A) as $1 \text{ C} = 1 \text{ As} = 6.241 \times 10^{-18} \text{ e}$. The Ampere is defined as that constant current which, if maintained in two straight parallel conductors of infinite length and negligible circular cross-section and placed 1 m apart in vacuum, would produce between these conductors a force equal to $2 \times 10^{-7} \text{ N}$ newton per metre of length. The measured value of the unit electric charge in SI-units is $e = 1.602 \times 10^{-19} \text{ C}$. In Gaussian units, the unit of the electric charge, statC, is defined via Coulomb's law: two stationary objects, each carrying a charge of 1 statC and 1 cm apart, electrically repel each other with a force of 1 dyne = $10 \times 10^{-5} \text{ N} = 1 \text{ g cm s}^{-2}$. The value of the unit electric charge in CGS-units is $e = 4.803 \times 10^{-10} \text{ statC}$. Moreover, in Gaussian units the speed of light in vacuum, c , enters Maxwell equations directly, where in SI units it enters only via $c^2 = \frac{1}{\mu_0 \epsilon_0}$ with the vacuum permittivity ϵ_0 and vacuum permeability μ_0 . In Gaussian units ϵ_0 and μ_0 are not defined and thus set to unity [Jac99].

the value of the vacuum permittivity is defined via the speed of light in vacuum, c , by the relation

$$\epsilon_0 = \frac{1}{\mu_0 c^2} = 8.854 \times 10^{-12} \text{ F m}^{-1} = 8.854 \times 10^{-12} \text{ s}^4 \text{ A}^2 \text{ m}^{-2} \text{ kg}^{-1}. \quad (3)$$

Equation (1) is commonly referred to as microscopic Maxwell's equations since it takes into account all electric charges and currents down to the atomic and subatomic level, i. e. including bound charges and currents. The latter involves bound states and raises the question of atomic stability which cannot be explained by the classical laws of physics, thus requiring a quantum mechanical description to explain the structure and behaviour of atoms, molecules and condensed matter. In order to avoid considering the complicated behaviour of microscopic charges and currents at atomic scales, macroscopic fields are introduced representing the spatial averages of the microscopic fields. The average of the electric charge and current density is separated into a contribution which stems from movable charges and currents and one arising from their bound counterparts. The contribution from bound charges and currents is accounted for by the introduction of auxiliary fields, namely the electric displacement \mathbf{D} and the magnetic field \mathbf{H} . Let us now and in the following interpret \mathbf{E} and \mathbf{B} as macroscopic fields and ρ and \mathbf{j} as macroscopic free charge and current densities.

In order to describe the behaviour of matter under the influence of the electromagnetic field, the macroscopic Maxwell's equations have to be supplemented by a set of material equations, also called constitutive relations. They summarise the dynamical response of an aggregate of atoms in a macroscopic medium and connect the quantities \mathbf{D} and \mathbf{j} with \mathbf{E} , and \mathbf{H} with \mathbf{B} . For non-relativistically moving bodies, time-harmonic fields, and linear and isotropic materials, a set of material equation is given by [BW09]

$$\mathbf{j} = \sigma \mathbf{E}, \quad (4)$$

$$\mathbf{D} = \epsilon \mathbf{E}, \quad (5)$$

$$\mathbf{H} = \mu^{-1} \mathbf{B}, \quad (6)$$

where σ is the specific conductivity, ϵ the dielectric permittivity, and μ the magnetic constant or permeability. Equation (4) represents Ohm's law in differential form. While within a conductor $\sigma \neq 0$, in dielectric and insulating substances $\sigma \approx 0$ and the electric and magnetic properties of which are completely determined by ϵ and μ . In vacuum, μ reduces to the magnetic constant μ_0 and ϵ to the vacuum permittivity ϵ_0 . The ratios $\epsilon_r = \epsilon/\epsilon_0$ and $\mu_r = \mu/\mu_0$ are called relative permittivity and relative permeability, respectively. While within diamagnetic substances $\mu_r < 1$ and within paramagnetic substances

$\mu_r > 1$, for the majority of materials $\mu_r = 1$ and magnetic effects can be neglected. In ferromagnetic substances the value of \mathbf{B} is determined by the history of \mathbf{H} , which is called hysteresis. Fortunately, the effects of hysteresis are barely significant for high-frequency fields such as X-rays or visible light. In the case of very strong fields, e.g. generated by lasers, the material relations of Eqs. (5) and (6) are insufficient to describe physics. Instead, non-linear material relations have to be supplemented involving terms non-linear in \mathbf{E} and \mathbf{B} . In anisotropic media the dielectric permittivity ϵ and the inverse magnetic permeability μ^{-1} are promoted to tensors of second rank. Thus the direction of the auxiliary fields no longer coincides with that of the inducing electromagnetic field.

In matter and using the auxiliary and macroscopic fields, and the macroscopic charges and currents, Maxwell's equations are given by the macroscopic variant of Eq. (1) which reads [BW09; Jac99]

$$\begin{aligned} \nabla \cdot \mathbf{D} &= \rho, \\ \nabla \cdot \mathbf{B} &= 0, \\ \nabla \times \mathbf{E} + \partial_t \mathbf{B} &= 0, \\ \nabla \times \mathbf{H} - \partial_t \mathbf{D} &= \mathbf{j}. \end{aligned} \tag{7}$$

The inhomogeneous Maxwell equations implicitly contain an equation of continuity which expresses the conservation of charge as

$$\partial_t \rho + \nabla \cdot \mathbf{j} = 0. \tag{8}$$

Let us assume the material Eqs. (4) to (6) to be satisfied and ϵ and μ to be isotropic. Then the amount of energy which crosses per second a unit area normal to the direction of \mathbf{E} and \mathbf{H} is represented by the Poynting vector defined as

$$\mathbf{S} = \mathbf{E} \times \mathbf{H}. \tag{9}$$

The cross product of \mathbf{E} and \mathbf{H} is defined as $(\mathbf{E} \times \mathbf{H})_i = \epsilon_{ijk} E_j H_k$. The magnitude of the Poynting vector is a measure of the intensity of light. Due to the very high frequencies of optical light and hard X-rays, ranging from 10^{14} Hz to 10^{19} Hz, the instantaneous values of the magnitude and polarisation of the electromagnetic field cannot be observed directly. Only the time averaged intensity I is accessible, which we thus are primarily interested in. It is defined as the time average of the energy which crosses a unit area containing the electric and magnetic field in unit time,

$$I = \langle |\mathbf{S}| \rangle_t = \langle |\mathbf{E} \times \mathbf{H}| \rangle_t, \tag{10}$$

where $\langle f \rangle_t = \frac{1}{T} \int_0^T dt f$ denotes the temporal average of the quantity f over the interval T .

Instead of the multiplicative material relations of Eqs. (5) and (6), a more intuitive set of material equations can be supplemented if the

propagation of an electromagnetic field in matter is considered as follows. Excited by an incident field, electrons within a substance start to oscillate. Thus they behave like electric and magnetic dipoles and become a source of secondary electromagnetic fields called the electric polarisation \mathbf{P} and the magnetic polarisation (or magnetisation) \mathbf{M} . The auxiliary fields, \mathbf{D} and \mathbf{B} , can then be written as composed of the incident (vacuum) fields and the polarisation fields arising from the response of the medium to the incident fields. Thus Maxwell's equations are supplemented by the following set of additive material relations

$$\begin{aligned}\mathbf{D} &= \epsilon_0 \mathbf{E} + \mathbf{P}, \\ \mathbf{H} &= 1/\mu_0 \mathbf{B} - \mathbf{M}.\end{aligned}\tag{11}$$

The polarisation fields \mathbf{P} and \mathbf{M} represent the influence of matter and thus vanish in vacuum. Hysteretic materials such as ferromagnets or superconductors exhibit a more complex relationship between \mathbf{M} and \mathbf{B} .

Now, consider the electromagnetic field incident on an electron to be sufficiently weak such that the response of the medium, \mathbf{P} and \mathbf{M} , to the incident field is linear. Then the following relation can be assumed

$$\begin{aligned}\mathbf{P} &= \epsilon_0 \chi_e \mathbf{E}, \\ \mathbf{M} &= \mu_0 \chi_m \mathbf{H}.\end{aligned}\tag{12}$$

The factors χ_e and χ_m are called dielectric and magnetic susceptibility, respectively. In Section 2.2 we will relate χ_e to the electron density distribution. Comparing the multiplicative material relations (11) and (12) with the additive Eqs. (5) and (6), the dielectric permittivity and the magnetic permeability can be related to the dielectric and magnetic susceptibilities as

$$\begin{aligned}\epsilon &= \epsilon_0(1 + \chi_e), \\ \mu &= \mu_0(1 + \chi_m).\end{aligned}\tag{13}$$

2.1.2 The wave equation

Let us now consider the propagation of an electromagnetic disturbance in a homogeneous and isotropic medium. We confine our consideration to a region which is void of free charges and free currents. Hence $\epsilon \neq \epsilon(\mathbf{r})$, $\mu \neq \mu(\mathbf{r})$ and $\rho = 0$, $\mathbf{j} = 0$. Upon substitution of $\mathbf{D} = \epsilon \mathbf{E}$ and $\mathbf{H} = \mu^{-1} \mathbf{B}$ into Eq. (7), we obtain [Max64; Jac99]

$$\begin{aligned}\nabla \cdot \mathbf{E} &= 0, \\ \nabla \cdot \mathbf{B} &= 0, \\ \nabla \times \mathbf{E} + \partial_t \mathbf{B} &= 0, \\ \nabla \times \mathbf{B} - \epsilon \mu \partial_t \mathbf{E} &= 0.\end{aligned}\tag{14}$$

From Eq. (14) wave equations for the electric field and the magnetic induction are derived as [Max64; Jac99]

$$\begin{aligned} (\nabla^2 - \mu\epsilon\partial_t^2) \mathbf{E} &= 0, \\ (\nabla^2 - \mu\epsilon\partial_t^2) \mathbf{B} &= 0 \end{aligned} \quad (15)$$

where $\nabla^2 = \partial_i \partial_i$, $i = \{1, 2, 3\}$, denotes the three-dimensional Laplace operator. Assuming constancy of μ and ϵ , the Cartesian components of \mathbf{E} and \mathbf{B} independently obey the wave equation. Thus it is sufficient to consider a single component, Ψ , of the electromagnetic field and the corresponding scalar wave equation only,

$$(\nabla^2 - \mu\epsilon\partial_t^2) \Psi = 0. \quad (16)$$

Equation (16) is also called d'Alembert equation.

2.1.2.1 Scalar waves

A general solution to the d'Alembert equation is given in form of scalar plane waves as

$$\Psi = \Psi_1(\hat{\mathbf{k}}\mathbf{r} - vt) + \Psi_2(\hat{\mathbf{k}}\mathbf{r} + vt), \quad (17)$$

where $\hat{\mathbf{k}}$ is a unit vector pointing in a fixed direction and v denotes the phase velocity. Ψ_1 and Ψ_2 represent plane waves propagating with velocity v in the direction of the unit vector $\pm\hat{\mathbf{k}}$. Upon insertion of Eq. (17) into the d'Alembert equation (16) the phase velocity is connected to the electric permittivity and the magnetic permeability as

$$v = \frac{1}{\sqrt{\mu\epsilon}}. \quad (18)$$

Thus, Eq. (15) predicts the existence of electromagnetic waves propagating with a velocity which can be determined by purely electromagnetic measurements, see Section 2.1.2.2.

Another solution to the wave equation is given in the form of spherical waves as

$$\Psi(r, t) = \frac{\Psi_1(r - vt)}{r} + \frac{\Psi_1(r + vt)}{r}, \quad (19)$$

where $r = |\mathbf{r}|$. The first term on the right-hand side of Eq. (19) represents an outgoing spherical wave emanating from the origin and the second term an ingoing spherical wave converging towards the origin, both with a phase velocity given by Eq. (18).

A more general wave being harmonic in time but not periodic in space is given in the form

$$\Psi(\mathbf{r}, t) = a(\mathbf{r}) \exp[-i(\omega t - \phi(\mathbf{r}))], \quad (20)$$

where a and ϕ are real, scalar, and positive functions of r . Wave fronts advancing with a constant phase $\omega t - \phi(\mathbf{r})$ are determined by

$$d(\omega t - \phi(\mathbf{r})) = \omega dt - d\mathbf{r} \cdot \nabla \phi = 0. \quad (21)$$

From condition Eq. (21) we have

$$\nabla \phi \cdot \frac{d\mathbf{r}}{dt} \equiv \nabla \phi \cdot \mathbf{v} = \omega. \quad (22)$$

The phase velocity v_p of waves of the form of Eq. (20) is defined as the velocity for which the direction $\frac{\mathbf{v}}{|v|}$ is normal to the surface $\phi(\mathbf{r}) = \text{constant}$ and thus parallel to $\nabla \phi$ [BW09]. It then follows from Eq. (22) as

$$v_p = \frac{\omega}{|\nabla \phi|}. \quad (23)$$

2.1.2.2 Speed of light in vacuum

In the absence of matter the electric permittivity and the magnetic permeability reduce to their vacuum values ϵ_0 and μ_0 , respectively. The phase velocity in vacuum, denoted by the constant c , is

$$c = \frac{1}{\sqrt{\epsilon_0 \mu_0}}, \quad (24)$$

which was found to correspond to the speed of light in vacuum. Using Eq. (24), the value of c can be determined by the measurement of the electric permittivity and the magnetic permeability in vacuum. Indeed, in 1856 Kohlrausch and Weber determined a constant from the ratio of the value of the capacity of a conductor measured in electrostatic units and measured in electromagnetic units, which turned out to be the speed of light in vacuum [KW57; Sti57]. In 1864, this inspired Maxwell to the conjecture that light is an electromagnetic wave which propagates with a velocity c [Max64]. In a series of experiments conducted between 1886 and 1889 Hertz confirmed Maxwell's prediction [Her88]. The numerical value of the speed of light in vacuum is fixed by the definition of the metre to

$$c = 299\,792\,458 \text{ m/s}. \quad (25)$$

The metre is the length of the path travelled by light in vacuum during a time interval of $1/299\,792\,458$ of a second [TTo8].

2.1.2.3 Refractive index

Given the speed of light in vacuum, it is convenient to introduce the refractive index of a substance as the ratio of the speed of light in the medium and in vacuum,

$$n \equiv \frac{c}{v} = \sqrt{\frac{\mu \epsilon}{\mu_0 \epsilon_0}} = \sqrt{\mu_r \epsilon_r} = \sqrt{1 + \chi_e} \sqrt{1 + \chi_m}, \quad (26)$$

where we have used the definition of the susceptibilities of Eq. (13). Equation (26) is also referred to as Maxwell relation ². While for visible light and most transparent materials the refractive index ranges between 1.2 and 2, for X-rays it is usually below but very close to unity. At room temperature, e.g. the real-part decrement of the refractive index of water ranges from 2.31×10^{-6} to 2.56×10^{-7} for energies from 10 keV to 30 keV [HGD93]. As was already shown by Newton's experiments on prismatic colours, the refractive index is in general a function of the frequency ω of the probing light,

$$n = n(\omega) . \quad (27)$$

Accordingly, the dielectric permittivity and the magnetic permeability are not constants of the material, but functions of the frequency of the field. In Section 2.2 we will discuss this frequency dependence by taking into account the atomic structure of matter.

According to Einstein, introducing the photon as a quantum of light [Eino5], the energy E , conveyed by the electromagnetic field in a fundamental scattering process, is not related to its intensity but to its frequency as

$$E = \hbar\omega , \quad (28)$$

where \hbar is Planck's constant divided by 2π with a value of

$$\hbar = \frac{h}{2\pi} = 6.582 \times 10^{-16} \text{ eV s} . \quad (29)$$

Thus, as first postulated by Planck in 1899 in order to explain the spectral power of black-body radiation [Plao1], the energy of the electromagnetic field is quantised with the photon being its carrier [Eino5].

2.1.3 Helmholtz equation

Let us consider a non-dispersive medium where the refractive index n is independent of the frequency ω . An ansatz decomposing the scalar electromagnetic disturbance Ψ into a superposition of monochromatic components Ψ_ω is given by

$$\Psi(\mathbf{r}, t) = \frac{1}{\sqrt{2\pi}} \int_0^\infty d\omega \Psi_\omega(\mathbf{r}) \exp(-i\omega t) . \quad (30)$$

Upon inserting Eq. (30) into the d'Alembert equation (16), we arrive at the time-independent Helmholtz equation for a monochromatic spatial component

$$(\nabla^2 + k^2) \Psi_\omega(\mathbf{r}) = 0 . \quad (31)$$

² Not to be confused with the set of thermodynamic equations by the same name.

Here we have introduced the wave number k via the dispersion relation as

$$k = \frac{2\pi}{\lambda} = \sqrt{\mu\epsilon} \omega = n \frac{\omega}{c}, \quad (32)$$

where λ is the wave length in the medium. Furthermore, we define the wave number in vacuum as

$$k_0 = \frac{2\pi}{\lambda_0} = \frac{k}{n}, \quad (33)$$

where λ_0 is the wave length in free space. For a harmonic plane wave of angular frequency ω which propagates in the direction of the wave vector $\mathbf{k} = k \hat{\mathbf{k}}$ the phase velocity reads

$$v = \frac{\omega}{k} = \frac{1}{\sqrt{\mu\epsilon}}. \quad (34)$$

2.1.3.1 Wave packet and group velocity

The notion of a strictly monochromatic plane wave is an idealisation practically never met in reality. Hence we consider a one-dimensional wave packet, formed by a superposition of monochromatic plane waves $a_\omega \exp(-i\omega t + ikz)$, propagating along the z -axis as

$$\Psi(z, t) = \int_0^\infty d\omega a_\omega \exp[-i(\omega t - kz)]. \quad (35)$$

The amplitude of the plane wave components a_ω shall differ appreciably from zero only in a small interval $\Delta\omega$ about a mean frequency ω_0 with

$$\frac{\Delta\omega}{\omega_0} \ll 1. \quad (36)$$

Light satisfying property Eq. (36) is said to be quasi-monochromatic. Since Ψ is governed by the d'Alembert equation, frequency and wave number are related according to Eq. (32) as $k = k(\omega) = n \frac{\omega}{c}$. In a dispersive medium we have $n = n(\omega)$ and different plane wave components travel at different phase velocities. Assuming the wave number to be a smooth function of ω and mildly varying around ω_0 , we may expand $k(\omega)$ into a Taylor series as

$$\begin{aligned} k(\omega) &= k(\omega_0) + \left. \frac{\partial k}{\partial \omega} \right|_{\omega=\omega_0} (\omega - \omega_0) + \mathcal{O}(\omega^2) \\ &= k^{(0)} + k^{(1)}(\omega - \omega_0) + \mathcal{O}(\omega^2), \end{aligned} \quad (37)$$

with $k^{(0)} \equiv k(\omega_0) = n(\omega_0) \frac{\omega_0}{c}$ and $k^{(1)} \equiv \left. \frac{\partial k}{\partial \omega} \right|_{\omega=\omega_0}$. Inserting Eq. (37) truncated to second order in ω into Eq. (35), the wave packet is expressed in the form

$$\Psi(z, t) = A(z, t) \exp \left[-i(\omega_0 t - k^{(0)} z) \right], \quad (38)$$

with the complex amplitude

$$A(z, t) = \int_0^\infty d\omega a_\omega \exp \left[-i(\omega - \omega_0)(t - k^{(1)}z) \right]. \quad (39)$$

Thus, Ψ may be interpreted as a plane wave of frequency ω_0 and wave number $k^{(0)}$ modulated by the amplitude $A(z, t)$. Since we have assumed a_ω to be concentrated about the mean frequency ω_0 , the amplitude A varies with a frequency of about $(\omega - \omega_0)$ which is small in comparison to that of the plane wave $\exp[-i(\omega_0 t - k^{(0)}z)]$. At $t = k^{(1)}z$ the amplitude A is constant and represents surfaces advancing with a velocity

$$v_g = \frac{1}{k^{(1)}} = \frac{\partial \omega}{\partial k} \Big|_{\omega=\omega_0}. \quad (40)$$

The velocity v_g in Eq. (40) is thus called group velocity. With the definition of the refractive index, $n = \frac{c}{v_p}$, and the dispersion relation, $k = n \frac{\omega}{c}$, the frequency reads $\omega = kv_p$. Substituting this into Eq. (40) (for arbitrary ω_0) and considering the phase velocity to be a function of k or λ , the group velocity reads

$$v_g = \frac{\partial \omega(k)}{\partial k} = \frac{\partial}{\partial k} k v_p(k) = v_p + k \frac{\partial v_p}{\partial k} = v_p - \lambda \frac{\partial v_p}{\partial \lambda}. \quad (41)$$

If the refractive index is used instead of the phase velocity with $v_p = \frac{c}{n}$ and $n = n(\omega) = n(\omega(k))$, the group velocity follows from

$$\frac{\partial \omega}{\partial k} = \frac{\partial}{\partial k} \frac{ck}{n(\omega(k))} = \frac{c}{n} - \frac{ck}{n^2} \frac{\partial n}{\partial \omega} \frac{\partial \omega}{\partial k} \quad (42)$$

as

$$v_g = \frac{\partial \omega}{\partial k} = \frac{c}{n + \omega \frac{\partial n}{\partial \omega}} \quad (43)$$

In a non-dispersive medium n is independent of ω and thus $v_g = v_p$.

2.1.4 Scattering from inhomogeneous media

Let us now consider the interaction of X-rays with a medium in terms of a spatially inhomogeneous refractive index $n = n(\mathbf{r})$. We restrict our considerations to a region void of free electric charges and currents ($\rho(\mathbf{r}, t) = 0$, $\mathbf{j}(\mathbf{r}, t) = 0$) and assume the material to be linear ($\mathbf{D} = \epsilon \mathbf{E}$, $\mathbf{B} = \mu \mathbf{H}$), isotropic (ϵ, μ are scalar), static ($\epsilon \neq \epsilon(t)$, $\mu \neq \mu(t)$), and non-magnetic ($\mu = \mu_0$). Then, the following equation for the electric field is obtained from Maxwell's equations (7)

$$\nabla^2 \mathbf{E} - \mu_0 \epsilon \partial_t^2 \mathbf{E} = \nabla[\mathbf{E} \cdot \nabla \ln \epsilon]. \quad (44)$$

Note that the right-hand side of Eq. (44) couples the components of the electric field with each other. If we consider the electric field to

be harmonic in time with frequency ω , and after substituting the refractive index

$$n = n(\mathbf{r}, \omega) = \sqrt{\frac{\epsilon(\mathbf{r}, \omega)}{\epsilon_0}} = \sqrt{1 + \chi_e(\mathbf{r}, \omega)}, \quad (45)$$

Eq. (44) reads

$$\nabla^2 \mathbf{E} + k^2 \mathbf{E} = \nabla[\mathbf{E} \cdot \nabla \ln \epsilon], \quad (46)$$

where we have used

$$k = k(\mathbf{r}, \omega) \equiv n(\mathbf{r}, \omega)k_0 = n(\mathbf{r}, \omega)\frac{\omega}{c}. \quad (47)$$

Let $\mathbf{q} = \mathbf{k} - \mathbf{k}_0$ denote the momentum transfer (modulo \hbar) between the incident (\mathbf{k}_0) and the scattered (\mathbf{k}) photon. To proceed we assume that the dielectric permittivity varies slowly on the scale of typical inverse photon-momentum transfers $|\mathbf{q}|^{-1}$. Then the right-hand side of Eq. (46) may be neglected. Since the Cartesian components of \mathbf{E} are now decoupled, we may consider a single component of the electric field only, which we denote by Ψ_ω . Thus we obtain the Helmholtz equation for a scalar electromagnetic disturbance in an inhomogeneous medium [Jac99; Pago06]

$$[\nabla^2 + k_0^2 n^2(\mathbf{r}, \omega)] \Psi_\omega(\mathbf{r}) = 0, \quad (48)$$

which is a central equation for diffraction theory.

2.1.4.1 Green's function for the inhomogeneous Helmholtz equation

An integral solution to Eq. (48) may be obtained by means of the Green's function formalism. To see this, we define

$$V_\omega(\mathbf{r}) = k_0^2[n^2(\mathbf{r}, \omega) - 1] \quad (49)$$

and rewrite Eq. (48) as

$$(\nabla^2 + k_0^2) \Psi_\omega(\mathbf{r}) = -V_\omega(\mathbf{r}) \Psi_\omega. \quad (50)$$

The term V_ω is called scattering potential in analogy to quantum mechanical scattering theory which rests upon the time-dependent Schrödinger equation. The Green's function G_ω is defined to be a solution of the inhomogeneous Helmholtz equation in the case of a static point-source inhomogeneity via

$$(\nabla^2 + k_0^2) G_\omega(\mathbf{r}, \mathbf{r}') = -4\pi\delta^3(\mathbf{r} - \mathbf{r}'), \quad (51)$$

where $\delta^3(\mathbf{r})$ denotes the Dirac delta distribution in three-dimensional space. The differential operator $(\nabla^2 + k_0^2)$ is isotropic and invariant under spatial translations. As a consequence, the Green's function is also shift and rotationally invariant

$$G_\omega(\mathbf{r}, \mathbf{r}') = G_\omega(|\mathbf{r} - \mathbf{r}'|). \quad (52)$$

An expression for the Green's functions can be found upon considering Eq. (51) in Fourier space. Thereby, an expression for the Fourier transform of G_ω is obtained. To evaluate the real-space form of G_ω the (inverse) Fourier integration is performed by means of a closed contour integral in the complex \mathbf{k} -plane and employing the residue theorem [Pago06]. Here, \mathbf{k} denotes the Fourier coordinate conjugate to \mathbf{r} . The resulting expression for the Green's function represents an outgoing or ingoing spherical wave as

$$G_\omega^\pm(\mathbf{r}) = \frac{\exp(\pm i\mathbf{k}_0|\mathbf{r}|)}{|\mathbf{r}|}, \quad (53)$$

with G_ω^+ and G_ω^- denoting the outgoing and ingoing Green's function, respectively.

Let us express the disturbance Ψ_ω as the sum of the incident field $\Psi^{(0)}$ and the scattered field $\Psi^{(s)}$ as

$$\Psi_\omega(\mathbf{r}) = \Psi_\omega^{(0)}(\mathbf{r}) + \Psi_\omega^{(s)}(\mathbf{r}). \quad (54)$$

The incident field $\Psi_\omega^{(0)}$ satisfies the homogeneous Helmholtz equation, i. e. Eq. (50) with $V_\omega = 0$. Using the outgoing Green's function, an integral solution to Eq. (50) is formally given by

$$\Psi_\omega(\mathbf{r}) = \Psi_\omega^{(0)}(\mathbf{r}) + \frac{1}{4\pi} \int d^3\mathbf{r}' G_\omega^+(\mathbf{r} - \mathbf{r}') V_\omega(\mathbf{r}') \Psi_\omega(\mathbf{r}'). \quad (55)$$

Indeed, applying the operator $(\nabla^2 + k_0^2)$ to Eq. (55), the inhomogeneous Helmholtz equation (50) is seen to be restored.

2.1.4.2 First-order Born approximation and far-field limit

In analogy to quantum mechanics, an iterative solution to Eq. (55) may be formulated in terms of a Dyson series where the higher-order terms can be understood to describe multiple scattering processes within the interaction volume [Sak93]. If the distortions of the incident field induced by the scattering potential are small, then such an iterative expansion may be truncated at first order. Thus $\Psi_\omega(\mathbf{r}')$ in the integrand on the right-hand side of Eq. (55) may be replaced by $\Psi_\omega^{(0)}(\mathbf{r}')$. This corresponds to a single-scattering scenario, and the resulting formula is known as the first-order Born approximation [Bor26a; Bor26b]. The resulting expression reads

$$\Psi_\omega(\mathbf{r}) = \Psi_\omega^{(0)}(\mathbf{r}) + \frac{1}{4\pi} \int d^3\mathbf{r}' G_\omega^+(\mathbf{r} - \mathbf{r}') V_\omega(\mathbf{r}') \Psi_\omega^{(0)}(\mathbf{r}'). \quad (56)$$

Now let the incident field be a plane wave propagating along \mathbf{k}_0 with $|\mathbf{k}_0| = k_0 = \omega/c$,

$$\Psi_\omega^{(0)}(\mathbf{r}) = \exp(i\mathbf{k}_0 \cdot \mathbf{r}), \quad (57)$$

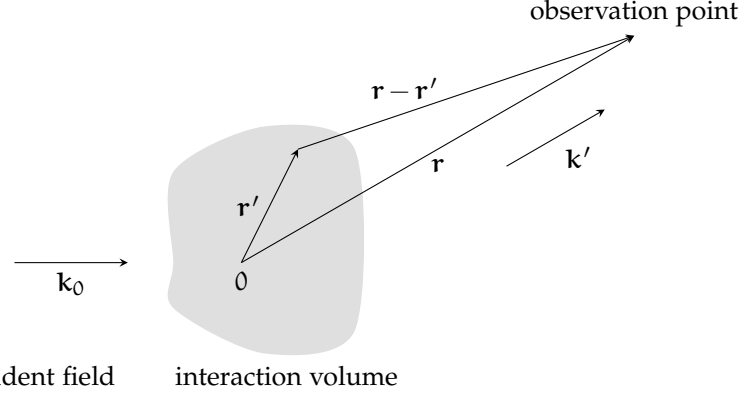


Figure 1: Finite-range scattering potential. A plane wave with wave vector \mathbf{k}_0 is incident on the scattering potential which is confined to a small region around the origin at 0. The observation point at \mathbf{r} is assumed to be far away from the interaction volume. Points within the interaction volume are denoted by \mathbf{r}' . The wave vector \mathbf{k}' denotes the propagation direction towards the observer.

and the scattering potential be confined to a small region around the origin as depicted in Fig. 1. If we consider a point far way from the scattering volume such that $|\mathbf{r} - \mathbf{r}'| \approx |\mathbf{r}| - \hat{\mathbf{r}} \cdot \mathbf{r}'$ for $|\mathbf{r}| \gg |\mathbf{r}'|$ with the unit vector $\hat{\mathbf{r}} = \frac{\mathbf{r}}{|\mathbf{r}|}$. Then the scattered wave field can be written as

$$\Psi_{\omega}^{(s)}(\mathbf{r}) = f(\mathbf{k}', \mathbf{k}_0) \frac{\exp(i\mathbf{k}_0 |\mathbf{r}|)}{|\mathbf{r}|}. \quad (58)$$

The factor f in front of the outgoing spherical wave is called scattering amplitude. Using first-order Born approximation it is given by

$$f(\mathbf{k}', \mathbf{k}_0) = \frac{1}{4\pi} \int d^3\mathbf{r}' \exp(-i\mathbf{k}' \cdot \mathbf{r}') V_{\omega}(\mathbf{r}') \Psi_{\omega}^{(0)}(\mathbf{r}'), \quad (59)$$

where $\mathbf{k}' = \mathbf{k}_0 \hat{\mathbf{r}}$ denotes the propagation vector for waves reaching the observation point \mathbf{r} . Thus we have

$$\Psi_{\omega}(\mathbf{r}) = \exp(i\mathbf{k}_0 \cdot \mathbf{r}) + f(\mathbf{k}', \mathbf{k}_0) \frac{\exp(i\mathbf{k}_0 |\mathbf{r}|)}{|\mathbf{r}|}. \quad (60)$$

For the incident plane wave of Eq. (57) and a point in the far field of the scattering volume, the scattering amplitude of Eq. (59) evaluated in first-order Born approximation is given by

$$f(\mathbf{k}', \mathbf{k}_0) = \frac{1}{4\pi} \int d^3\mathbf{r}' \exp(-i(\mathbf{k}' - \mathbf{k}_0) \cdot \mathbf{r}') V_{\omega}(\mathbf{r}'). \quad (61)$$

Using the definition of the three-dimensional Fourier transform as in Eq. (A.7), the scattering amplitude of Eq. (61) is identified with the Fourier transform of the scattering potential as

$$f(\mathbf{k}', \mathbf{k}_0) = \sqrt{\frac{\pi}{2}} \widehat{V}_{\omega}(\mathbf{k}_0 - \mathbf{k}'). \quad (62)$$

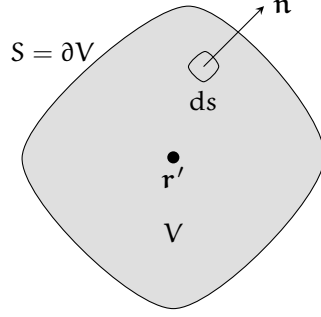


Figure 2: Situation related to the Helmholtz-Kirchhoff diffraction integral. A volume V is enclosed by a smooth surface $S = \partial V$. A point r' within the V is considered to be the (point) source of an outgoing spherical wave. The vector \mathbf{n} is normal to the surface S , and ds denotes an infinitesimal surface element. At an arbitrary point \mathbf{r} within V , the value of a wave field governed by the Helmholtz equation is determined via the Helmholtz-Kirchhoff diffraction integral, given both the field and its first normal derivative over an arbitrary surface S .

To obtain the differential scattering cross-section $\frac{d\sigma}{d\Omega}$, let $\mathbf{j}^{(in)}$ denote the number of incident photons per unit time and unit area and $\mathbf{j}^{(s)}$ the number of photon scattered into solid angle $d\Omega$ per unit time traversing an area subtended by $d\Omega$. Then the number of photons detected within an area $|\mathbf{r}|^2 d\Omega$ at a distance $|\mathbf{r}|$ scattered from an area element $d\sigma$ within the scattering volume is given by

$$|\mathbf{j}^{(s)}| |\mathbf{r}|^2 d\Omega = |\mathbf{j}^{(in)}| d\sigma. \quad (63)$$

Apart from normalisation factors the current densities are obtained from $\mathbf{j}^{(in)} \propto |\Psi_{\omega}^{(0)}|^2$ and $\mathbf{j}^{(s)} \propto |\Psi_{\omega}^{(s)}|^2$. Using Eq. (60) the differential scattering cross-section in terms of the scattering amplitude (Eq. (59)) reads as

$$\frac{d\sigma}{d\Omega} = \frac{|\mathbf{r}|^2 |\mathbf{j}^{(s)}|}{|\mathbf{j}^{(in)}|} = |f(\mathbf{k}', \mathbf{k})|^2. \quad (64)$$

2.1.4.3 Helmholtz-Kirchhoff integral theorem

Let us now consider the situation depicted in Fig. 2. The point r' within the volume V enclosed by the smooth surface $S = \partial V$ is considered to be the source of an outgoing spherical wave. The normal to the surface is denoted by \mathbf{n} and the corresponding surface vector of the infinitesimal surface element ds as $ds = \mathbf{n} ds$. Having an expression of the Green's function at one's disposal, the Helmholtz-Kirchhoff integral theorem is derived by means of Green's theorem. The resulting diffraction integral expresses the solution of the homogeneous Helmholtz equation at an arbitrary point \mathbf{r} in terms of both

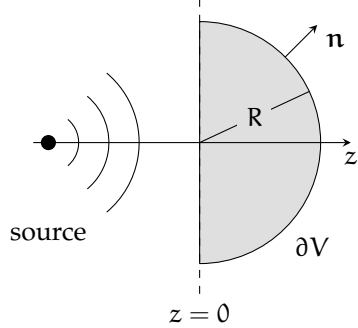


Figure 3: Situation related to the Helmholtz-Kirchhoff diffraction integral in the case where all sources are located within the half-space $z < 0$ and emit disturbances which propagate along z into the half-space $z > 0$. \mathbf{n} denotes the outward pointing normal to the surface $S = \partial V$. Supplementing Sommerfeld radiation conditions and letting $R \rightarrow \infty$, the electromagnetic disturbance at a point \mathbf{r} within S is determined by the value of both the unpropagated wave field and its normal derivative over the plane $z = 0$.

the field and its first normal derivative over an arbitrary smooth and closed surface enclosing \mathbf{r} [Pago6; BWo9] as

$$\Psi_\omega(\mathbf{r}) = \frac{1}{4\pi} \oint_S d^2 s' [G_\omega^+(\mathbf{r} - \mathbf{r}') \partial_n \Psi_\omega(\mathbf{r}') - \Psi_\omega(\mathbf{r}') \partial_n G_\omega^+(\mathbf{r} - \mathbf{r}')] , \quad (65)$$

where ∂_n denotes the derivative normal to the surface S given by $\partial_n \equiv \mathbf{n} \cdot \nabla$.

Let us now consider the case where all sources are located in the half-space $z < 0$ and a wave field propagating along the positive z direction as depicted in Fig. 3. Consider the surface integration in Eq. (65) to be performed over a hemisphere of radius R situated in the half-space $z > 0$ as in Fig. 3. To evaluate the Helmholtz-Kirchhoff diffraction integral for a point \mathbf{r} in the half-space $z > 0$ we have to supplement the Sommerfeld radiation condition, i. e. we demand that the field and its derivative vanish as $R \rightarrow \infty$. Then Eq. (65) transforms into

$$\Psi_\omega(\mathbf{x}_\perp, z > 0) = \frac{1}{4\pi} \int_{-\infty}^{\infty} d^2 \mathbf{x}'_\perp (G_\omega^+(\mathbf{r} - \mathbf{r}') \partial_z \Psi_\omega(\mathbf{r}') - \Psi_\omega(\mathbf{r}') \partial_z G_\omega^+(\mathbf{r} - \mathbf{r}')) , \quad (66)$$

where the \mathbf{r}' is confined to the plane $z = 0$, thus $\mathbf{r}' = (\mathbf{x}'_\perp, z' = 0)$.

2.1.4.4 Rayleigh-Sommerfeld diffraction integral

The requirement to know both the field and its derivative over a closed surface in order to obtain the field at a point within the surface can be relaxed by an appropriate choice of the Green's function. Employing the method of images, a Green's function can be reconstructed such that either the first or the second term in the parentheses of

Eq. (66) vanish. Thus the remaining integral depends on Neumann or Dirichlet boundary conditions only. The Dirichlet Green's function is defined such as to vanish at the plane $z = 0$

$$G^{(D)}(\mathbf{r} - \mathbf{r}') = G^+(\mathbf{r} - \mathbf{r}') - G^+(\mathbf{r} + \mathbf{r}'). \quad (67)$$

The Neumann Green's function is defined such that its derivative vanishes at $z = 0$

$$G^{(N)}(\mathbf{r} - \mathbf{r}') = G^+(\mathbf{r} - \mathbf{r}') + G^+(\mathbf{r} + \mathbf{r}'). \quad (68)$$

If we consider the same situation as for Eq. (66) and use the Dirichlet Green's function, the Rayleigh-Sommerfeld diffraction integral of the first kind is obtained as

$$\begin{aligned} \Psi_\omega(\mathbf{r}) &= \frac{1}{4\pi} \int_{-\infty}^{\infty} d^2\mathbf{x}'_\perp \Psi_\omega(\mathbf{x}'_\perp, z=0) \partial_z G^{(D)}(\mathbf{r} - \mathbf{r}') . \\ &= \frac{1}{2\pi} \int_{-\infty}^{\infty} d^2\mathbf{x}'_\perp \Psi_\omega(\mathbf{x}'_\perp, z=0) \partial_z \frac{\exp(i k_0 |\mathbf{r} - \mathbf{r}'|)}{|\mathbf{r} - \mathbf{r}'|} . \end{aligned} \quad (69)$$

Again, \mathbf{r}' is confined to the plane $z = 0$ and the propagated field at a point in the half-space $z > 0$ is determined by its boundary value at $z = 0$. In the last line of Eq. (69) we have used the fact that, due to the symmetry of the situation, the derivative of the spherical wave emanating from $-\mathbf{r}'$ is the negative of the derivative of the spherical wave emanating from \mathbf{r}' .

Employing Neumann boundary conditions, the Rayleigh-Sommerfeld diffraction integral of the second kind is obtained as

$$\Psi_\omega(\mathbf{r}) = -\frac{1}{2\pi} \int_{-\infty}^{\infty} d^2\mathbf{x}'_\perp \frac{\exp(i k_0 |\mathbf{r} - \mathbf{r}'|)}{|\mathbf{r} - \mathbf{r}'|} \left. \frac{\partial \Psi_\omega(\mathbf{r}')}{\partial z} \right|_{z=0} . \quad (70)$$

where, as in Eq. (69), \mathbf{r}' is confined to the plane $z = 0$ and we have invoked the mirror symmetry of the situation.

2.1.5 Fresnel diffraction theory

Fresnel's formulation of the wave theory of light is a synthesis of the principle of Huygens and Young [BW09]. According to Huygens' principle each point on a wave front may be regarded as the source of secondary waves which combine such that their envelope determines the wave front at any later point in time [HYF00]. Invoking to this principle Huygens was able to derive the laws of refraction and reflection. Conducting his famous double-slit experiment, Young demonstrated the phenomenon of interference and enunciated the principle of the interference of light [You02]. By a combination of Huygens' envelope construction and Young's principle of interference, Fresnel could explain the rectilinear propagation and diffraction of light. Poisson concluded that, according to Fresnel's theory, a bright spot

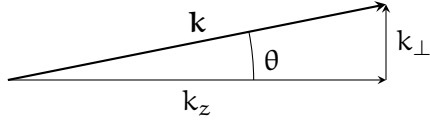


Figure 4: Illustration of the small-angle approximation in Fourier space. The wave vector \mathbf{k} of the incoming light subtends a small angle θ with respect to the optical axis pointing in z direction.

should appear in the centre of shadow of a small circular disc blocking a point source of light. According to Newton's particle theory of light, which was prevalent at that time, there should be complete darkness. Poisson's prediction was experimentally confirmed by Arago and is since known as Arago spot.

The Fresnel diffraction integral can be derived from the Rayleigh-Sommerfeld diffraction integral of the first kind (Eq. (69)) in the paraxial approximation. First, we will discuss this approximation. Therefore, we consider the case of a forward propagating wave front such that its wave vector \mathbf{k} subtends a small angle with respect to the optical axis as in Fig. 4. Let k_{\perp} and k_z denote the transverse and the longitudinal component of the wave vector. Then the modulus of k_{\perp} and k_z can be approximated as

$$\begin{aligned} k_{\perp} &\equiv |k_{\perp}| = k \sin \theta \approx k \theta , \\ k_z &= k \cos \theta \approx k \left(1 - \frac{\theta^2}{2}\right) . \end{aligned} \quad (71)$$

The paraxial approximation refers to the truncation

$$k_z \approx k \left(1 - \frac{k_{\perp}^2}{2k^2}\right) , \quad (72)$$

with $k_{\perp} \ll k_z$. Equation (72) is also known as slowly varying envelope approximation, which will become evident in the following.

In the context of the Huygens-Fresnel principle, where wave propagation is understood as a superposition of forward propagating spherical waves emanating from point sources, the paraxial approximation corresponds to the replacement of spherical waves by parabolic wave fronts in the propagator (\mathcal{P}) as

$$\exp(i\mathbf{k}|\mathbf{r}|) = \exp\left(i\mathbf{k}\sqrt{x^2 + y^2 + z^2}\right) \rightarrow \exp\left(i\mathbf{k}z\left(1 + \frac{x^2 + y^2}{2z^2}\right)\right) . \quad (73)$$

Let a denote the size of the smallest length scale that is resolvable in the wave field and λ the wave length of the probing light, the maximum transverse spatial frequency corresponding to a is $k_{\perp,\max} = \frac{2\pi}{a}$. Then the paraxial approximation amounts to the statement, that the

characteristic length scale a is much larger than the wave length of the probing light:

$$k_{\perp} \leq k_{\perp,\max} = \frac{2\pi}{a} \ll k = \frac{2\pi}{\lambda} \Rightarrow a \gg \lambda. \quad (74)$$

Thus the paraxial approximation is guaranteed to work well above the diffraction limit which is set by $k = \frac{2\pi}{\lambda}$, see Section 2.1.5.2.

In the following we derive the Fresnel diffraction integral from Eq. (69). Therefore, we evaluate the derivative of the Green's function with respect to z as

$$\partial_z \frac{\exp(ik_0 r)}{r} = ik_0 \left(1 + \frac{i}{k_0 r}\right) \frac{z}{r^2} \exp(ik_0 r), \quad (75)$$

with $r = |\mathbf{r}|$. In the paraxial limit, r appearing the denominator of Eq. (75) can be approximated as $r \approx z$. Moreover, in a typical X-ray imaging situation we have $z = \mathcal{O}(1 \text{ m})$, $k_0 = \frac{2\pi}{\lambda} = \mathcal{O}(10^{10} \text{ m}^{-1})$, and thus $\frac{1}{k_0 r} \approx 0$. Oscillations due the exponential in Eq. (75) are small but non-vanishing, and thus are included to quadratic order in x_{\perp} as

$$r = |\mathbf{r}| = z \sqrt{1 + \frac{x_{\perp}^2}{z}} \approx z \left(1 + \frac{x_{\perp}^2}{2z}\right). \quad (76)$$

Hence Eq. (75) becomes

$$\partial_z \frac{\exp(ik_0 r)}{r} \rightarrow \frac{ik_0}{z} \exp(ik_0 z) \exp\left(\frac{ik_0}{2z} x_{\perp}^2\right), \quad (77)$$

and the formula of the Fresnel diffraction integral is obtained as

$$\begin{aligned} \Psi_{\omega}(\mathbf{x}_{\perp}, z > 0) = \\ \frac{ik_0 \exp(ik_0 z)}{2\pi z} \int_{-\infty}^{\infty} d^2 x'_{\perp} \Psi_{\omega}(\mathbf{x}'_{\perp}, z=0) \exp\left(\frac{ik_0}{2z} (\mathbf{x}_{\perp} - \mathbf{x}'_{\perp})^2\right). \end{aligned} \quad (78)$$

Equation (78) corresponds to the integral form of the paraxial wave equation supplemented by boundary conditions, which will be derived in the following.

Recall the homogeneous Helmholtz equation for the monochromatic component of a complex scalar field

$$(\nabla^2 + k^2) \Psi_{\omega}(\mathbf{r}) = 0, \quad (79)$$

with wave number $k = n \frac{\omega}{c}$ and $n = \text{constant}$. In the paraxial limit the Helmholtz equation reduces to the paraxial wave equation as follows. Consider an ansatz for the wave field in the form of a plane wave propagating along the optical axis with wave vector k_z and modulated by the envelope $\Psi_{\omega}^{(\text{env})}$ as

$$\Psi_{\omega}(\mathbf{r}) = \Psi_{\omega}^{(\text{env})}(\mathbf{r}) \exp(ikz). \quad (80)$$

Inserting ansatz (80) into Eq. (79), we obtain a partial differential equation for the envelope function as

$$\begin{aligned} 0 &= (\nabla^2 + 2ik\partial_z) \Psi_\omega^{(\text{env})}(\mathbf{r}) \\ &= (\nabla_\perp^2 + 2ik\partial_z + \partial_z^2) \Psi_\omega^{(\text{env})}(\mathbf{r}), \end{aligned} \quad (81)$$

where we have decomposed the Laplace operator into a transverse (∇_\perp^2) and a longitudinal part (∂_z^2). If the transverse variations of $\Psi_\omega^{(\text{env})}$ exceed the longitudinal ones, the second derivative $\partial_z^2 \Psi_\omega^{(\text{env})}$ may be omitted in Eq. (81). Such a wave front is called beam-like. The resulting parabolic partial differential equation is referred to as homogeneous paraxial wave equation:

$$(\nabla_\perp^2 + 2ik\partial_z) \Psi_\omega^{(\text{env})}(\mathbf{r}) = 0. \quad (82)$$

This is a Schrödinger equation for the z-evolution of the wave field $\Psi_\omega^{(\text{env})}$, i. e. quantum mechanics in two spatial (x_\perp) and one temporal (z) dimensions [Sch26]. Along the lines of the conservation of probability of a wave function governed by Schrödinger's equation, the conservation of intensity can be derived from Eq. (82). For the intensity of the wave field Ψ_ω we have

$$I_\omega = |\Psi_\omega|^2 = |\Psi_\omega^{(\text{env})}|^2. \quad (83)$$

In analogy to the probability current in non-relativistic quantum mechanics, we define the flux of intensity which is transverse to the direction of propagation as

$$\begin{aligned} j_\omega &= \frac{1}{2ik} \left[\left(\Psi_\omega^{(\text{env})} \right)^* \nabla_\perp \Psi_\omega^{(\text{env})} - \Psi_\omega^{(\text{env})} \nabla_\perp \left(\Psi_\omega^{(\text{env})} \right)^* \right] \\ &= \frac{1}{2ik} \left[(\Psi_\omega)^* \nabla_\perp \Psi_\omega - \Psi_\omega \nabla_\perp (\Psi_\omega)^* \right] \\ &= \frac{1}{k} I_\omega \nabla_\perp \phi_\omega. \end{aligned} \quad (84)$$

In the last line of Eq. (84) we have expressed the wave field in terms of phase and amplitude as

$$\Psi_\omega(\mathbf{r}) = \sqrt{I_\omega(\mathbf{r})} \exp(i\phi_\omega(\mathbf{r})). \quad (85)$$

Using the above definitions a continuity equation for Fresnel theory follows as

$$\partial_z I_\omega + \nabla_\perp \cdot j_\omega = 0. \quad (86)$$

Thus, the conservation of probability for the time evolution of a wave function governed by Schrödinger's equation in quantum mechanics translates into the conservation of intensity for a forward propagating paraxial wave field in Fresnel theory. This is just the conservation of energy under forward propagation. Defining the 'power' P that is

irradiated along the optical axis from a source located upstream into the field of view (FOV) as

$$P = \int_{\text{FOV}} d^2x_\perp I_\omega , \quad (87)$$

the integral version of Eq. (86) reads

$$\frac{dP}{dz} + \oint_{\partial\text{FOV}} d^2s j_\omega = 0 , \quad (88)$$

where ds denotes the vector ‘surface’ element normal to the boundary ∂FOV .

We now show that the Fresnel diffraction integral is the integral form of the paraxial wave equation, supported by Dirichlet boundary conditions at $z = 0$. Using the Fourier transform as defined in Eq. (A.6), the Fourier representation of $\Psi_\omega^{(\text{env})}$ reads

$$\Psi_\omega^{(\text{env})}(x_\perp) = \mathcal{F}^{-1} x_\perp \hat{\Psi}_\omega^{(\text{env})} = \frac{1}{2\pi} \int_{-\infty}^{\infty} d^2k_\perp \hat{\Psi}_\omega^{(\text{env})}(k_\perp) \exp(-ik_\perp x_\perp) . \quad (89)$$

Inserting Eq. (89) into the paraxial wave equations, we obtain the following equation for the Fourier components $\hat{\Psi}_\omega^{(\text{env})}$

$$(-k_\perp^2 + 2ik\partial_z) \hat{\Psi}_\omega^{(\text{env})}(k_\perp, z) = 0 . \quad (90)$$

Assuming k_\perp to be fixed, Eq. (90) converts into an ordinary differential equation for $\hat{\Psi}_\omega^{(\text{env})}$ in z which can be solved upon a separation of variables as

$$\frac{d\hat{\Psi}_\omega^{(\text{env})}}{\hat{\Psi}_\omega^{(\text{env})}} = \frac{-ik_\perp^2}{2k} dz . \quad (91)$$

Integration of Eq. (91) yields the Fourier transform of the envelope wave field as

$$\hat{\Psi}_\omega^{(\text{env})}(k_\perp, z > 0) = \hat{\Psi}_\omega^{(\text{env})}(k_\perp, 0) \exp\left(-\frac{iz}{2k} k_\perp^2\right) . \quad (92)$$

Substitution of Eq. (92) into the Fourier representation of $\hat{\Psi}_\omega^{(\text{env})}$ yields an integral solution for $\Psi_\omega^{(\text{env})}$. Resubstituting $\Psi_\omega^{(\text{env})} = \Psi_\omega \exp(-ikz)$, we obtain the Fresnel diffraction integral for the forward propagating wave field Ψ_ω as [Pago06; BW09]

$$\Psi_\omega(x_\perp, z > 0) = e^{ikz} \mathcal{F}^{-1} \left[\exp\left(-\frac{iz}{2k} k_\perp^2\right) \mathcal{F}[\Psi_\omega(x_\perp, z = 0)] \right] , \quad (93)$$

given its boundary values at $z = 0$

A real-space version of Eq. (93) is found by appeal to the convolution theorem of Eq. (A.9). Let $\ast\ast$ denote the two-dimensional convolution with respect to the transverse coordinates x_\perp as in Eq. (A.8),

the convolution theorem in two dimension for the Fourier transform as defined in Eq. (A.6) reads

$$\mathcal{F}[f * g] = 2\pi(\mathcal{F}f) \times (\mathcal{F}g). \quad (94)$$

By means of Eq. (94) the Fourier transform formulation of the Eq. (93) is recast into a convolution integral as

$$\begin{aligned} \Psi_\omega(\mathbf{x}_\perp, z > 0) &= \int d^2\mathbf{x}'_\perp \mathcal{P}_F(\mathbf{x}_\perp - \mathbf{x}'_\perp, z) \Psi_\omega(\mathbf{x}'_\perp, z = 0) \\ &= \mathcal{P}_F(\mathbf{x}_\perp, z) \ast \Psi_\omega(\mathbf{x}_\perp, z = 0). \end{aligned} \quad (95)$$

The function \mathcal{P}_F is called Fresnel propagator. Comparing Eqs. (93) and (95) the Fresnel propagator in Fourier space reads

$$(\mathcal{F}\mathcal{P}_F)(\mathbf{k}_\perp, z) = \frac{\exp(ikz)}{2\pi} \exp\left(-\frac{iz}{2k} \mathbf{k}_\perp^2\right). \quad (96)$$

The real-space version of \mathcal{P}_F is obtained from the inverse Fourier transformation of Eq. (96). The Fourier integral is evaluated upon quadratic completion and use of the Gaussian integral formula. It is given by

$$\mathcal{P}_F(\mathbf{x}_\perp, z) = \frac{-ik}{2\pi z} \exp(ikz) \exp\left(\frac{ik}{2z} \mathbf{x}_\perp^2\right). \quad (97)$$

Given a monochromatic wave front at $z = 0$, the intensity at distance z computes as

$$I_\omega(\mathbf{x}_\perp, z > 0) = |\Psi_\omega(\mathbf{x}_\perp, z > 0)|^2. \quad (98)$$

Equation (93) is well apt for a numerical implementation by means of fast Fourier transform (FFT) algorithms in order to simulate the intensity map for a given wave field $\Psi_\omega(\mathbf{x}_\perp, z = 0)$.

Let us express the wave field at the boundary $z = 0$ in terms of a (frequency-dependent) amplitude and phase as

$$\Psi_\omega(\mathbf{x}_\perp, z = 0) = \exp[-B_\omega(\mathbf{x}_\perp)] \exp[i\phi_\omega(\mathbf{x}_\perp)]. \quad (99)$$

The intensity obtained from the Fresnel diffraction integral is invariant under a global shift of the phase

$$\phi_\omega(\mathbf{x}_\perp) \rightarrow \phi'_\omega(\mathbf{x}_\perp) = \phi_\omega(\mathbf{x}_\perp) + \bar{\phi}_\omega, \quad (100)$$

with $\bar{\phi}_\omega = \text{constant}$. However, a global shift \bar{B}_ω of the attenuation

$$B_\omega(\mathbf{x}_\perp) \rightarrow B'_\omega(\mathbf{x}_\perp) = B_\omega(\mathbf{x}_\perp) + \bar{B}_\omega \quad (101)$$

entails a rescaling of the intensity. Namely, under global shifts of phase and attenuation, the Fresnel diffraction integral implies that

$$I_\omega(\phi_\omega, B_\omega) \rightarrow I'_\omega(\phi'_\omega, B'_\omega) = \exp(-2\bar{B}_\omega) I_\omega(\phi_\omega, B_\omega). \quad (102)$$

Thus a phase retrieved in Fresnel theory is only defined modulo a constant offset.

2.1.5.1 Fraunhofer diffraction

Fraunhofer diffraction refers to Fresnel diffraction in the case of propagation distances that are large compared to the characteristic scale of the unpropagated wave field. The expression for Fraunhofer diffraction is found upon expanding the exponential in the integrand of Eq. (78). The disturbance to be propagated from the plane $z = 0$ is considered to be non-negligible only over a region of diameter a . If the Fresnel number N_F is much less than unity,

$$N_F \equiv \frac{a^2}{\lambda z} \ll 1, \quad (103)$$

we may ignore the term quadratic in $x'_\perp^2 \leq a^2$ in the exponent of Eq. (78). The Fraunhofer diffraction integral then follows from the Fresnel diffraction integral as

$$\begin{aligned} \Psi_\omega(x_\perp, z > 0) &= \frac{i}{\lambda_0 z} \exp(ik_0 z) \exp\left(\frac{ik_0}{2z} x_\perp^2\right) \\ &\times \int_{-\infty}^{\infty} d^2x'_\perp \Psi_\omega(x'_\perp, z = 0) \exp\left(-\frac{ik_0}{z} x_\perp \cdot x'_\perp\right). \end{aligned} \quad (104)$$

The intensity pattern arising from Fraunhofer diffraction is thus given by the (rescaled) Fourier transform of the boundary wave field evaluated at frequencies $k_\perp = \frac{k_0}{z} x_\perp$.

Next we consider the Fraunhofer diffraction pattern emerging from a circular aperture of radius a . Introducing polar coordinates

$$x_\perp = \begin{pmatrix} x \\ y \end{pmatrix} = \begin{pmatrix} r \cos \theta \\ r \sin \theta \end{pmatrix}, \quad (105)$$

the diffraction integral Eq. (104) for a circular aperture reads

$$\begin{aligned} \Psi_\omega(x_\perp, z > 0) &= \frac{i}{\lambda_0 z} \exp(ik_0 z) \exp\left(\frac{ik_0}{2z} x_\perp^2\right) \\ &\times \int_0^a dr' \int_0^{2\pi} d\theta' r \exp\left(-\frac{ik_0}{z} r r' \cos(\theta - \theta')\right). \end{aligned} \quad (106)$$

The angular integration in Eq. (106) is identified with an integral representation of the Bessel function of first kind and zeroth order J_0 [BW09]. We thus have

$$\begin{aligned} \Psi_\omega(x_\perp, z > 0) &= \frac{i2\pi}{\lambda_0 z} \exp(ik_0 z) \exp\left(\frac{ik_0}{2z} x_\perp^2\right) \\ &\times \int_0^a dr' r' J_0\left(\frac{k_0 r r'}{z}\right). \end{aligned} \quad (107)$$

Using a recurrence relation between J_0 and the Bessel function of first kind and first order J_1 [BW09], Eq. (107) becomes

$$\Psi_\omega(x_\perp, z > 0) = \frac{i\pi a^2}{\lambda_0 z} \exp(ik_0 z) \exp\left(\frac{ik_0}{2z} x_\perp^2\right) \frac{2J_1\left(\frac{k_0 r a}{z}\right)}{\frac{k_0 r a}{z}}. \quad (108)$$

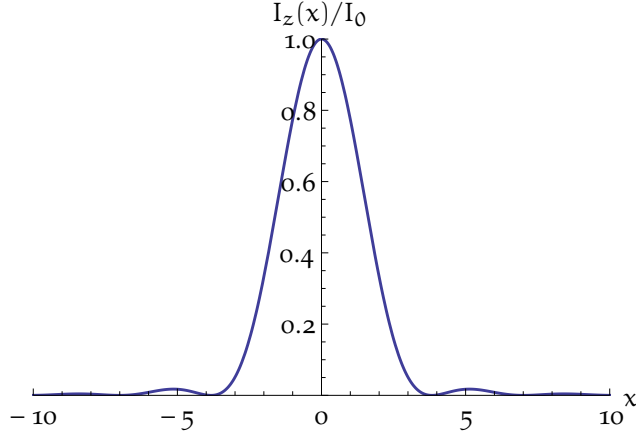


Figure 5: Airy pattern emerging from Fraunhofer diffraction at a circular aperture of radius a . The normalised intensity is given by $\frac{I_z(x)}{I_0} = \left[2 \frac{J_1(x)}{x} \right]^2$ where J_1 denotes the Bessel function of the first kind and first order. The abscissa is $x = \frac{k_0 r a}{z}$ with wave vector $k_0 \equiv \frac{2\pi}{\lambda_0}$ and r being the distance to the optical axis in the observation plane. First and second minima occur at $x = 3.833$ and 7.016 , respectively.

This is a well-known formula first derived by Airy. The diffraction pattern resulting from Eq. (108) is thus called Airy pattern [Air35], see Fig. 5.

2.1.5.2 Angular spectrum representation

In the following we consider the angular spectrum approach to construct a solution to the Helmholtz equation for a forward propagating field in terms of plane waves. It will become evident from the angular spectrum approach that plane waves with the transverse wave vector components exceeding the modulus of the wave vector k correspond to evanescent waves; the amplitude of which decay exponentially with propagation distance. Thus transverse length scales related to transverse components of the wave vector cannot be resolved in the far field, which is a statement of the diffraction limit.

Consider a plane wave denoted as

$$\Psi_{\omega}^{(\text{pw})}(\mathbf{r}) = \exp(i\mathbf{k}\mathbf{r}), \quad (109)$$

with $\mathbf{r} = (x_{\perp}, z)$ and wave vector $\mathbf{k} = (k_{\perp}, k_z)$. Inserting ansatz Eq. (109) into the Helmholtz equation (79) fixes the modulus of the wave vector to $|\mathbf{k}| = k = \frac{\omega}{c}$, which we solve for k_z . Taking the positive solution of k_z , which corresponds to propagation along the positive z -direction, the plane wave solution reads

$$\begin{aligned} \Psi_{\omega}^{(\text{pw})}(x_{\perp}, z) &= \exp(i\mathbf{k}_{\perp}x_{\perp}) \exp\left(i\sqrt{k^2 - x_{\perp}^2}z\right) \\ &= \Psi_{\omega}^{(\text{pw})}(x_{\perp}, z=0) \exp\left(i\sqrt{k^2 - x_{\perp}^2}z\right). \end{aligned} \quad (110)$$

We assume an arbitrary wave field to be given at the plane $z = 0$. Its (transverse) Fourier representation reads

$$\Psi_\omega(\mathbf{x}_\perp, z = 0) = \frac{1}{2\pi} \int d^2 k_\perp \hat{\Psi}_\omega(k_\perp, z = 0) \exp(i k_\perp \mathbf{x}_\perp). \quad (111)$$

Since Eq. (110) represents a plane wave propagated from $z = 0$ to distances $z > 0$ and Eq. (111) the boundary wave field decomposed it into plane waves, the wave field of Eq. (111) propagated to distances $z > 0$ can be composed as

$$\begin{aligned} \Psi_\omega(\mathbf{x}_\perp, z > 0) \\ = \frac{1}{2\pi} \int d^2 k_\perp \hat{\Psi}_\omega(k_\perp, z = 0) \exp(i k_\perp \mathbf{x}_\perp) \exp(i k_z z), \end{aligned} \quad (112)$$

with $k_z = \sqrt{k^2 - k_\perp^2}$.

For plane waves with $k_\perp > k$, the longitudinal component k_z becomes imaginary and the according exponent in Eq. (112) real. Thus, plane waves with $|k_\perp| > k$ decay exponentially. After Ψ_ω has propagated from $z = 0$ to the far field, only plane waves with $k_\perp < k$ will remain to contribute to the diffraction pattern. The maximum of the transverse wave vector $k_{\perp,\max}$ relates to the smallest resolvable transverse length scale Δx within the unpropagated wave field as

$$k_{\perp,\max} \equiv \frac{2\pi}{\Delta x} \leq \frac{2\pi}{\lambda}. \quad (113)$$

This is a statement of the diffraction limit.

2.1.6 Projection approximation

Consider the situation of an imaging experiment as depicted in Fig. 6. Here a monochromatic plane wave propagates along the optical axis z and is incident upon a sample which is described in terms of an inhomogeneous refractive index $n(\mathbf{r})$. This situation is governed by the inhomogeneous Helmholtz equation (48). Assuming paraxiality of the traversing wave field as discussed in Section 2.1.5, Eq. (48) transforms into the inhomogeneous paraxial wave equation for the envelope wave field $\Psi_\omega^{(\text{env})}$,

$$(\nabla_\perp^2 + 2ik\partial_z + k^2[n_\omega^2(\mathbf{r}) - 1]) \Psi_\omega^{(\text{env})}(\mathbf{r}) = 0. \quad (114)$$

In the X-ray regime the refractive index is typically close to unity and its real part smaller than one. Thus a dense region in the sample would cause the phase of the incident wave field to advance relative to its surroundings. It is convenient to express the refractive index in terms of a real part decrement δ_ω and an imaginary part β_ω as

$$n(\omega) = 1 - \delta_\omega + i\beta_\omega, \quad (115)$$

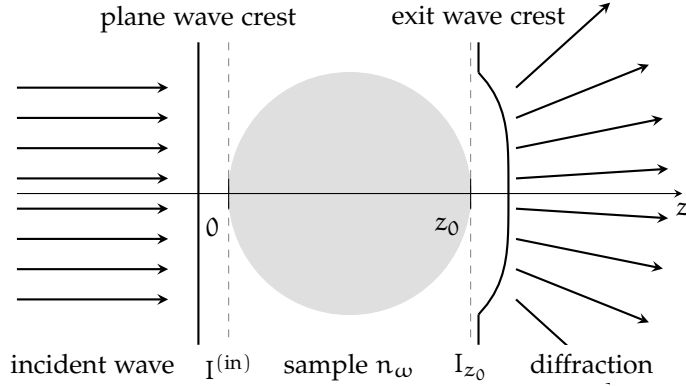


Figure 6: Projection approximation and forward propagating in Fresnel theory. An incident monochromatic plane wave of constant intensity $I^{(\text{in})}$ impinges on the sample at $z = 0$ and exits at $z = z_0$ with intensity $I_{z_0} \equiv I_\omega(\mathbf{x}_\perp, z_0)$. The interaction of light with matter is described in terms of the refractive index n_ω . While traversing the sample the incident wave accumulates phase shift and attenuation according to Eqs. (118) and (119), causing local diffraction at the object exit. Subsequent self-interference upon forward propagation of the diffracted exit wave front is described by the Fresnel diffraction integral, see Section 2.1.5.

where δ_ω and β_ω are small real numbers and depend on the frequency ω . While the real-part decrement δ_ω is attributed to elastic scattering, the imaginary part β_ω is related to the attenuation of the electromagnetic wave in an absorptive medium, see Sections 2.2.1 and 2.2.2, respectively. Below the threshold for the creation of an electron-positron pair, the refractive index approaches unity with increasing energy and δ_ω and β_ω tend to zero, see Fig. 7 and Section 2.2. In the X-ray regime and away from absorption edges, see Section 2.2.2, the refractive index decrement is typically several orders of magnitude larger than the imaginary part.

The projection approximation amounts to a neglect of the transverse Laplacian in Eq. (114) which couples neighbouring ray trajectories. Thus, using the small-angle approximation, Eq. (115), and disregarding scattering away from the ray path, the inhomogeneous paraxial wave equation (114) reduces to

$$\partial_z \Psi_\omega^{(\text{env})}(\mathbf{r}) = -k_0 [i\delta_\omega(\mathbf{r}) + \beta_\omega(\mathbf{r})] \Psi_\omega^{(\text{env})}(\mathbf{r}), \quad (116)$$

A solution to this boundary value problem is given by

$$\Psi_\omega^{(\text{env})}(\mathbf{x}_\perp, z) = \exp(i\phi_\omega(\mathbf{x}_\perp, z_0) - B(\mathbf{x}_\perp, z_0)) \Psi_\omega^{(\text{env})}(\mathbf{x}_\perp, z = 0), \quad (117)$$

where we have introduced phase shift and attenuation of the exit wave front as

$$\phi_\omega(\mathbf{x}_\perp, z_0) = -k_0 \int_{z=0}^{z=z_0} dz \delta_\omega(\mathbf{x}_\perp, z), \quad (118)$$

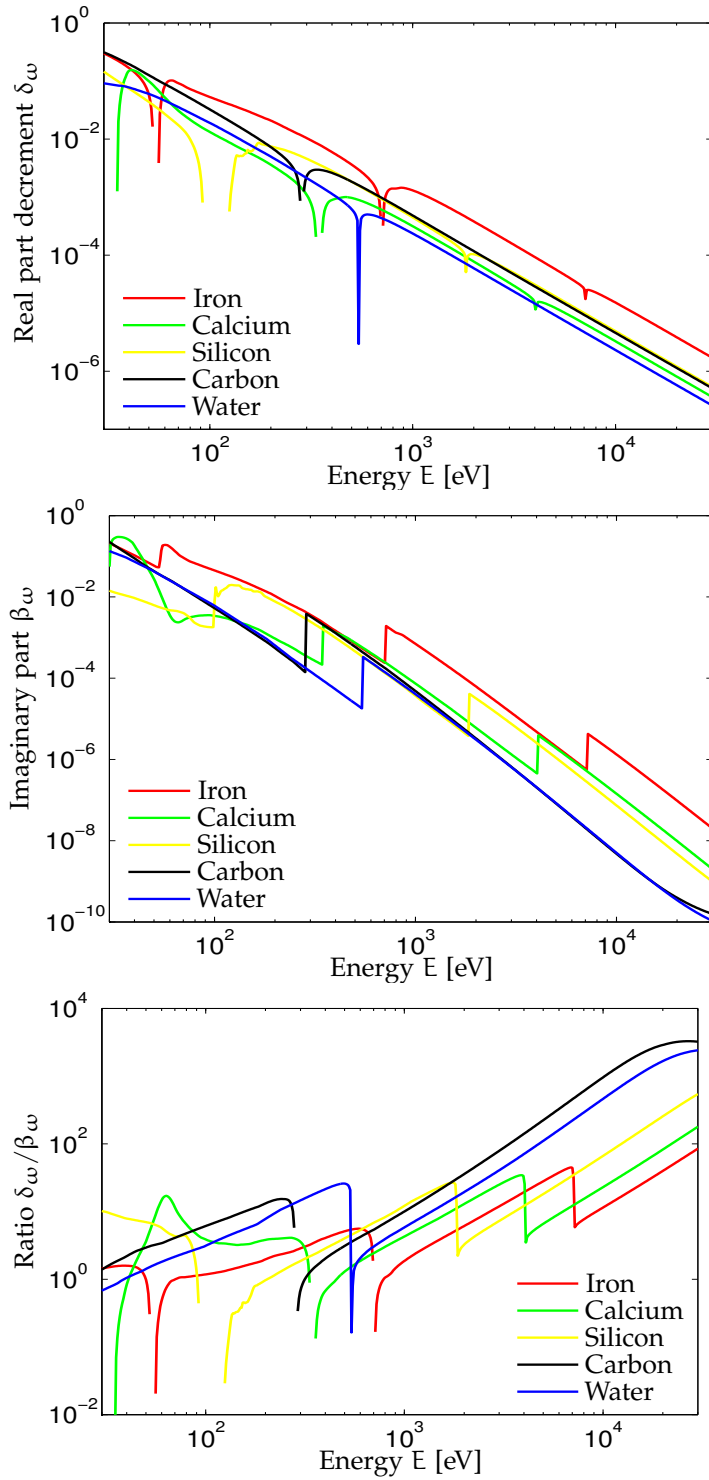


Figure 7: The refractive index $n(\omega) = 1 - \delta_\omega + i\beta_\omega$ and the ratio $\frac{\delta_\omega}{\beta_\omega}$ as a function of photon energy $E = \hbar\omega$ for various substances at room temperature. Apart from the regions close to absorption edges, both δ_ω and β_ω decrease with increasing energy and the refractive index approaches unity. The ratio $\frac{\delta_\omega}{\beta_\omega}$, however, increases with energy.

and

$$B_\omega(\mathbf{x}_\perp, z_0) = k_0 \int_{z=0}^{z=z_0} dz \beta_\omega(\mathbf{x}_\perp, z), \quad (119)$$

respectively. Introducing the transmission function as

$$T_\omega(\mathbf{x}_\perp) \equiv \exp(i\phi_\omega(\mathbf{x}_\perp, z_0) - B_\omega(\mathbf{x}_\perp, z_0)), \quad (120)$$

we may write the wave field immediately downstream the object as

$$\Psi_\omega^{(\text{env})}(\mathbf{x}_\perp, z_0) \equiv T_\omega(\mathbf{x}_\perp) \Psi_\omega^{(\text{in})}(\mathbf{x}_\perp), \quad (121)$$

where $\Psi_\omega^{(\text{in})}(\mathbf{x}_\perp) \equiv \Psi_\omega^{(\text{env})}(\mathbf{x}_\perp, z = 0)$ denotes the incident wave field. The functions ϕ_ω and B_ω essentially are Radon transforms of the refractive index along the ray path [Rad86], see Eq. (131), and can be interpreted as the projection of the electron density as will be shown in Sections 2.2.1 and 2.2.2. If β_ω is assumed to be constant, we may define the linear attenuation coefficient μ_ω as

$$\mu_\omega = \frac{2}{z_0} B_\omega = 2k_0 \beta_\omega. \quad (122)$$

From Eq. (117) and using $I_\omega = |\Psi_\omega|^2$ we obtain Beer's law of absorption

$$I_\omega(\mathbf{x}_\perp, z) = I_\omega(\mathbf{x}_\perp, z = 0) \exp(-\mu_\omega z) \quad (123)$$

for $z < z_0$.

2.1.7 Filtered backprojection

In the previous section we have found expressions for the phase and attenuation of an exit wave front in terms of integrals of the refractive index along straight lines assuming strict paraxiality of the transmitted light. As a consequence of the projection approximation, a two-dimensional object function f can be reconstructed by means of the inverse Radon transform from the set of its one-dimensional projections, i. e. line integrals of f along the ray path. A numerically efficient and stable implementation of the inverse Radon transform is provided by the filtered backprojection (FBP). While Radon derived and stated his inversion formula in real space [Rad86], FBP employs Fourier transformations in its derivation and for its final formula. Upon extraction of phase shift and attenuation of a tomographic set of intensity measurements, the electron density distribution (see Section 2.2) of the imaged object is reconstructed from the extracted maps using FBP. The majority of imaging experiments conducted during this thesis were of the tomographic kind. Therefore and in view of Chapter 5, which is concerned with the intricacies of tomographic reconstruction and

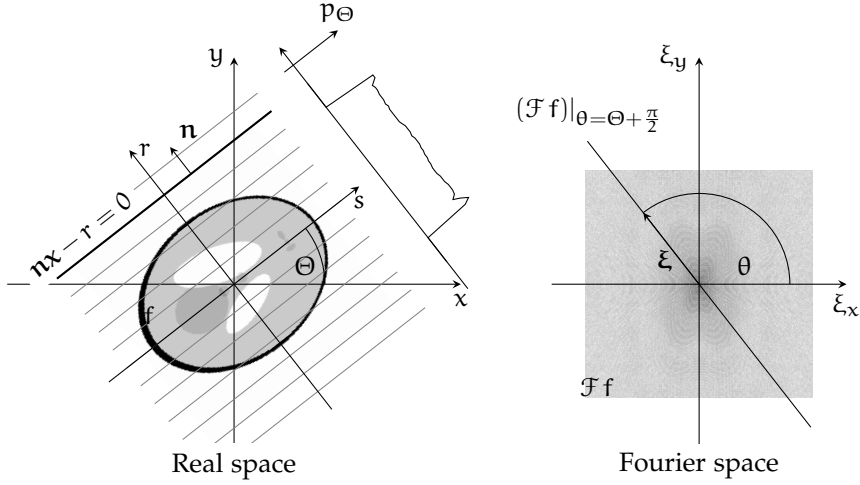


Figure 8: Situation related to the Fourier slice theorem and the filtered back-projection (FBP). Slice through a three-dimensional object described by the object function $f(x, y)$, where (x, y) refer to coordinate system that is fixed to the object. A straight ray path through the object is defined by $\mathbf{n} \cdot \mathbf{x} - r = 0$, where r is the distance of the ray to the origin (impact parameter) and \mathbf{n} normal to the ray. The ray path is parametrised by the variable s . The coordinate system (s, r) is rotated by an angle Θ with respect to the (x, y) coordinate system. The angular coordinate θ in Fourier space is related to the rotation angle Θ in real space by $\theta = \Theta + \pi/2$. The Fourier slice theorem relates the Fourier transform of a projection p_Θ of the object function f to a slice (line) of the Fourier transform of f as $(\mathcal{F}_r p_\Theta)(\xi_r) = (\mathcal{F}_{x,y} f)(\xi_r \cos \theta, \xi_r \sin \theta)$. The object on the left is the (modified) Shepp-Logan phantom. The image on the right displays the modulus of the Fourier transform of the Shepp-Logan phantom.

the combination of tomography and phase retrieval (Section 5.2), we will review FBP in more detail.

Consider a slice, taken perpendicular to the z -axis, through a three-dimensional object as depicted in Fig. 8. The cross-sectional slice of the object is described by the scalar the function $f(\mathbf{x})$, $\mathbf{x} = (x, y)^\top$ being the two-dimensional vector in the plane. The projection of f obtained at an angle of rotation Θ is denoted p_Θ .

To derive the parallel-beam formula for FBP the object function f is written in terms of its Fourier transform \hat{f} , the Cartesian coordinates are transformed into to polar coordinates, and the Fourier slice theorem is applied.

The Fourier (or projection) slice theorem relates the two-dimensional Fourier transform of the object function to the one-dimensional Fourier transform of the projections of the object function.

In the following we will derive the Fourier slice theorem from which the FBP formula follows immediately. Using ordinary frequen-

cies (see Appendix A.2), the Fourier representation of the object function reads as

$$f(x) \equiv \mathcal{F}^{-1}_\xi \hat{f} \equiv \int_{-\infty}^{\infty} d^2\xi \exp(-i2\pi\xi \cdot x) \hat{f}(\xi). \quad (124)$$

Now let us convert the integral measure in Eq. (124) from Cartesian to polar coordinates with

$$\xi = \begin{pmatrix} \xi_x \\ \xi_y \end{pmatrix} = \begin{pmatrix} \xi_r \cos \theta \\ \xi_r \sin \theta \end{pmatrix}, \quad (125)$$

where ξ_r and θ denote modulus and angle of Fourier space coordinate ξ as depicted Fig. 8. Then the Fourier representation of f reads

$$\begin{aligned} f(x, y) &= \int_0^{2\pi} d\theta \int_0^{\infty} d\xi_r \xi_r e^{-i2\pi\xi_r(x \cos \theta + y \sin \theta)} \hat{f}(\xi_r \cos \theta, \xi_r \sin \theta) \\ &= \int_0^{\pi} d\theta \int_{-\infty}^{\infty} d\xi_r |\xi_r| e^{-i2\pi\xi_r(x \cos \theta + y \sin \theta)} \hat{f}(\xi_r \cos \theta, \xi_r \sin \theta). \end{aligned} \quad (126)$$

To change the integration from $\theta \in [0, 2\pi]$ and $\xi_r \in [0, \infty]$ to $\theta \in [0, \pi]$ and $\xi_r \in [-\infty, \infty]$ in the second line of Eq. (126), we have substituted $\theta = \theta' + \pi$ and $\xi_r = -\xi_r'$ in the lower half-space $\xi_y < 0$ and used $\cos(\theta + \pi) = -\cos \theta$ and $\sin(\theta + \pi) = -\sin \theta$. Now ξ_r also assumes negative values. This will become favourable later on, since the integral over ξ_r can then implemented using standard FFT algorithms.

To define the projection we consider a straight line with a normal n and a distance r to the origin as depicted on the left in Fig. 8. The ray path is then defined by the linear equation

$$r - n \cdot x = 0. \quad (127)$$

A point on the ray is parametrised by the coordinate s . The normal in terms of the angle of rotation Θ reads

$$n = \begin{pmatrix} -\sin \Theta \\ \cos \Theta \end{pmatrix}. \quad (128)$$

The coordinates (s, r) refer to a system that is rotated by an angle Θ with respect to the system (x, y) which is fixed to the object. The transformation relating the two coordinate system reads

$$x = \begin{pmatrix} x \\ y \end{pmatrix} = \begin{pmatrix} \cos \Theta & -\sin \Theta \\ \sin \Theta & \cos \Theta \end{pmatrix} \begin{pmatrix} s \\ r \end{pmatrix}. \quad (129)$$

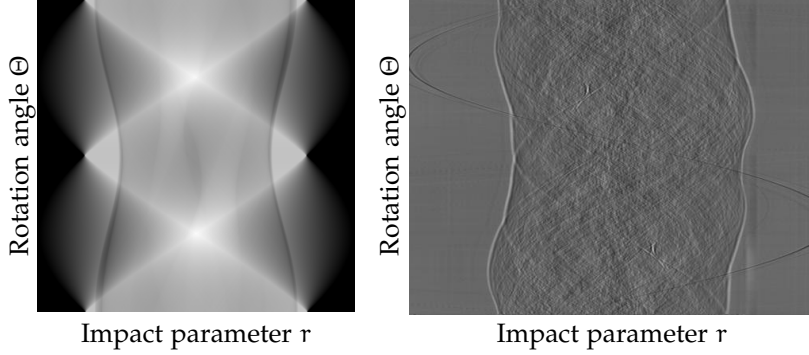


Figure 9: Sinograms. Left: Sinogram of the Shepp-Logan phantom which depicted on the left in Fig. 8. The projected axis of rotation is located at the vertical centre. The greyscale is inverted compared to Fig. 8 for better visibility. Right: Sinogram of propagated intensity maps of a Xenopus frog embryo recorded with beamline ID19 at ESRF. Cropped sine curves originate from features (small inclusions, gas bubbles, dirt, etc.) which are located at a distance from the rotation axis larger than half the diameter of the field of view.

The projection p_Θ of the object function f along a ray path is given by the line integral of f over s as

$$\begin{aligned} p_\Theta(r) &= \int_{-\infty}^{\infty} ds f(x(r, s), y(r, s)) \\ &= \int_{-\infty}^{\infty} ds f(s \cos \Theta - r \sin \Theta, s \sin \Theta + r \cos \Theta). \end{aligned} \quad (130)$$

This is a Radon transform and can be written in terms of a two-dimensional integral of f over x as

$$p_\Theta(r) = \int_{-\infty}^{\infty} d^2x \delta(r - \mathbf{n} \cdot \mathbf{x}) f(\mathbf{x}), \quad (131)$$

where δ is the one-dimensional Dirac delta distribution, see Eq. (A.13). Note the identity

$$p_\Theta(r) = p_{\Theta+\pi}(-r). \quad (132)$$

The stack of projections as a function of the rotation angle Θ and the impact parameter (detector pixel) r is called sinogram, see e. g. Fig. 9. To derive the Fourier slice theorem, we take the Fourier transform of p_Θ with respect to r , express the projection in terms of a Radon transform using Eq. (131), and perform the integration over r :

$$\begin{aligned} \hat{p}_\Theta(\xi_r) &= \mathcal{F}_r p_\Theta = \int_{-\infty}^{\infty} dr \exp(i2\pi\xi_r r) p_\Theta(r) \\ &= \int_{-\infty}^{\infty} d^2x \int_{-\infty}^{\infty} dr \exp(i2\pi\xi_r r) \delta(r - \mathbf{n} \cdot \mathbf{x}) f(\mathbf{x}) \\ &= \int_{-\infty}^{\infty} d^2x \exp(i2\pi\xi_r \mathbf{n} \cdot \mathbf{x}) f(\mathbf{x}) \\ &= (\mathcal{F}_{x,y} f)(-\xi_r \sin \Theta, \xi_r \cos \Theta). \end{aligned}$$

(133)

The projection angle Θ in real space is shifted by $-\pi/2$ with respect to the angle θ in Fourier space, see Fig. 8. By substituting $\Theta = \theta - \frac{\pi}{2}$ into Eq. (133) the standard form of the Fourier slice theorem is obtained as

$$(\mathcal{F}_r p_\theta)(\xi_r) = (\mathcal{F}_{x,y} f)(\xi_r \cos \theta, \xi_r \sin \theta). \quad (134)$$

Equation (134) states that the Fourier transform of the projection p_θ of an object function f corresponds to a one-dimensional slice of the two-dimensional Fourier transform of f taken at the angle which the projection subtends to the x -axis. Upon insertion of Eq. (134) into Eq. (126), we arrive at the formula for the filtered backprojection (FBP)

$$\begin{aligned} f(x, y) &= \int_0^\pi d\theta \int_{-\infty}^\infty d\xi_r |\xi_r| e^{-i2\pi\xi_r(x \cos \theta + y \sin \theta)} (\mathcal{F}_r p_\theta)(\xi_r) \\ &\equiv \text{FBP}\{p_\theta\}. \end{aligned} \quad (135)$$

The integral over θ amounts to a smearing of each pixel of the projection over the ray path and is thus referred to as backprojection (BP). The factor $|\xi_r|$ is called Ram-Lak or ramp filter and suppresses low frequencies. It originates from the coordinate transformation from Cartesian to polar coordinates. More precisely, it is the determinant of the Jacobian matrix for this coordinate transformation. Thereby it takes into account the increasing sampling density towards the origin when p_θ is backprojected as illustrated in Fig. 10. Thus, tomographic reconstruction based on Eq. (135) can be considered as a two-step process composed of filtering (F) and backprojection (BP).

From Eq. (135) we can derive the inversion formula in real space as it was given by Radon [Rad86]. Rewriting Eq. (135) as a one-dimensional convolution integral in the variable $r = x \cdot n = x \cos \theta + y \sin \theta$ by means of the Fourier convolution theorem (Eq. (A.15)), we have

$$\begin{aligned} f(x, y) &= \int_0^\pi d\theta \int_{-\infty}^\infty d\xi_r e^{-i2\pi\xi_r r} |\xi_r| (\mathcal{F}_r p_\theta)(\xi_r) \\ &= \int_0^\pi d\theta \mathcal{F}^{-1}_{\xi_r} [\mathcal{F}_r [\mathcal{F}^{-1}_{\xi_r} |\xi_r|] \mathcal{F}_r p_\theta] \\ &= \int_0^\pi d\theta h(r) * p_\theta(r)|_{r=xn}. \end{aligned} \quad (136)$$

Here h denotes the inverse Fourier transform of the ramp filter given by [EB54]

$$h(r) = \mathcal{F}^{-1}_{\xi_r} |\xi_r| = \int_{-\infty}^\infty d\xi_r |\xi_r| e^{-i2\pi\xi_r r} = \frac{-1}{2\pi^2 |r|}. \quad (137)$$

To proceed, we substitute h by virtue of Eq. (137) in Eq. (136), write out the convolution integral, change the integration from $\theta \in [0, \pi]$

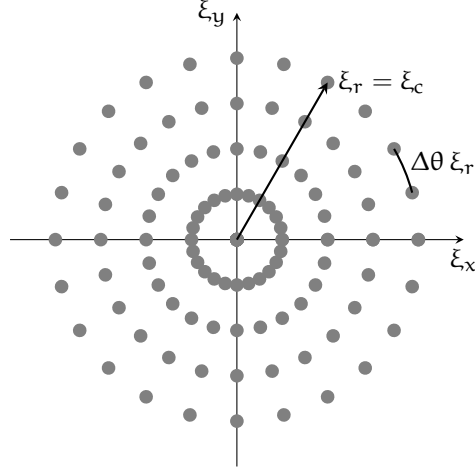


Figure 10: Fourier space sampling upon backprojection of tomographic data according to the Fourier slice theorem. The number N of projections required to maintain detector resolution after backprojection, is determined by the angular sampling density at maximum spatial frequency $\xi_r = \xi_c$ matching the radial sampling density $\frac{2\xi_c}{N_x}$, N_x being the number of horizontal detector pixels.

and $r \in [-\infty, \infty]$ to $\theta \in [0, 2\pi]$ and $r \in [0, \infty]$ with aid of Eq. (132), and integrate by parts with respect to variable r' . Thus we obtain

$$\begin{aligned} f(x, y) &= \frac{-1}{2\pi^2} \int_0^\pi d\theta \int_{-\infty}^\infty dr' \frac{1}{|r'|^2} p_\theta(r - r')|_{r=x \cdot n} \\ &= \frac{-1}{2\pi^2} \int_0^{2\pi} d\theta \int_0^\infty dr' \frac{1}{r'^2} p_\theta(r + r')|_{r=x \cdot n} \\ &= \frac{-1}{2\pi^2} \int_0^{2\pi} d\theta \int_0^\infty dr' \frac{1}{r'} \frac{\partial}{\partial r'} p_\theta(x \cos \theta + y \sin \theta + r') . \end{aligned} \quad (138)$$

This is Radon's inversion formula.

Having derived expressions Eqs. (135) and (138) for the reconstruction of a function from its projections, the question arises of the minimum number of projections required to maintain detector resolution after tomographic reconstruction. Therefore, we appeal to the Fourier slice theorem again. Each projection acquired under an angle Θ corresponds to a slice in Fourier space at an angle $\theta = \Theta + \frac{\pi}{2}$ as depicted in Fig. 8. Thus having obtained N projections over an angular range of 180° at a constant angle increment $\Delta\Theta = \Delta\theta$, Fourier space is filled up accordingly with slices as illustrated in Fig. 10. Consider a horizontal detector line of length L , effective pixel size Δx , and number of pixels $N_x = \frac{L}{\Delta x}$. Along such a slice, the maximum spatial (cut-off) frequency reads $\xi_c = \frac{1}{2\Delta x}$, the sampling density is $\frac{1}{L}$, and the number of (equidistant) sampling points is that of the detector line N_x . To maintain detector resolution after backprojection the angular sampling density at cut-off frequency ξ_c should not fall below

the radial sampling density. Thus $\frac{\pi \xi_c}{N} \leq \frac{2\xi_c}{N_x}$ and the minimum number of projections is given as

$$N \geq \frac{\pi}{2} N_x . \quad (139)$$

2.1.8 Coherence

In this section we consider the generation of (transverse) spatial coherence from an incoherent source induced by the process of propagation, with the essential result given by the van Cittert-Zernike theorem [Wolo7; BWo9]. As in Section 2.1.3.1, we consider quasi-monochromatic light with the amplitude of its plane wave components differing appreciably from zero only within a bandwidth $\Delta\omega$ about the mean frequency ω_0 ,

$$\frac{\Delta\omega}{\omega_0} \ll 1 . \quad (140)$$

From optical experiments on Michelson interferometers [Wolo7] it is known that the appearance of fringes in the detection plane, which is a manifestation of temporal coherence, is observed only as long as the time delay Δt , introduced between the beams which are brought to interfere, is less than

$$\Delta t \leq \frac{2\pi}{\Delta\omega} . \quad (141)$$

For $\Delta t > \frac{2\pi}{\Delta\omega}$ spectral components within the quasi-monochromatic wave packet run out of phase and cancel each other on average. Thus, Δt is called coherence time and the corresponding path delay is referred to as longitudinal coherence length

$$l_l = v\Delta t \approx v \frac{2\pi}{\Delta\omega} , \quad (142)$$

where $v = \frac{c}{n}$ is the velocity of light in the medium of propagation with $n = \text{constant}$ and c being the speed of light in vacuum, see Eqs. (18) and (26). E.g. at an X-ray energy of $E = 30 \text{ keV}$ and a monochromatisation of 10^{-4} resulting in a bandwidth of $\Delta\omega = 4.56 \times 10^{16} \text{ s}^{-1}$, the coherence length in vacuum ($v = c$) has a value of $l_l = 0.413 \mu\text{m}$, which is e.g. considerably less than that of optical lasers ranging from centimetres to kilometres.

Considering a point source which emits a quasi-monochromatic spherical wave packet, a longitudinal coherence length translates into a transverse coherence length upon propagation, see Fig. 11. In a given plane at a distance z afar from the source, coherent interference can only arise from points within this plane which exhibit a relative path delay of the incident wave of less than

$$l_l \geq \sqrt{z^2 + l_z^2} - z = z \sqrt{1 + \left(\frac{l_z}{z}\right)^2} - z \approx \frac{l_z^2}{2z} \quad (143)$$

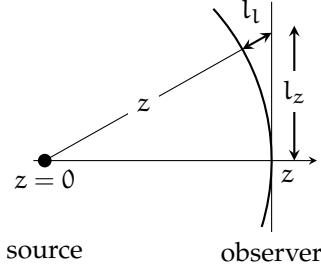


Figure 11: Emergence of a transverse coherence limit l_z upon propagation of a spherical wave packet emitted from a quasi-monochromatic point source with longitudinal coherence length l_l and a distance z afar from the plane at z . On the other hand, for a given transverse coherence length l_z , the bandwidth of the source imposes a lower bound on z .

and thus are separated less than $l_z \leq \sqrt{2Rl_l}$. For the above value of $l_l = 0.413 \mu\text{m}$ and at a distance $z = R = 100 \text{ m}$, the emergent transverse coherence length is $l_z = 9.1 \text{ mm}$. In turn, for interference to occur at a given transverse coherence length l_z , the finite bandwidth of radiation emitted by a quasimonochromatic source imposes a lower bound on z as

$$z \geq \frac{l_z^2}{2l_l}. \quad (144)$$

Because of the great rapidity of light oscillations in the visible or X-ray regime, the instantaneous intensity $\Psi^*\Psi$ of a wave field Ψ is technically inaccessible. Only the intensity averaged over time intervals T can be measured

$$\langle \Psi(\mathbf{r}, t)^* \Psi(\mathbf{r}, t) \rangle_t \equiv \frac{1}{2T} \int_{-T}^T dt \Psi(\mathbf{r}, t)^* \Psi(\mathbf{r}, t). \quad (145)$$

For time intervals much larger than the reciprocal bandwidth, $T \gg \frac{1}{\Delta\omega}$, we may formally let $T \rightarrow \infty$ as

$$I(\mathbf{r}) \equiv \lim_{T \rightarrow \infty} \frac{1}{2T} \int_{-T}^T dt \Psi(\mathbf{r}, t)^* \Psi(\mathbf{r}, t). \quad (146)$$

Using the ergodicity theorem [Bol98], the time average of a quantity Q , such as in Eq. (145), can be replaced by the ensemble average [Wol07]

$$\langle Q(t) \rangle_t = \langle Q(t) \rangle_e \equiv \lim_{N \rightarrow \infty} \frac{1}{N} \sum_{k=1}^N Q^{(k)}(t), \quad (147)$$

where $Q^{(k)}$ denotes a particular realisation within an ensemble $\{Q^{(k)}\}$. In the remainder of this section we thus denote the expectation value of a quantity Q simply as $\langle Q \rangle$.

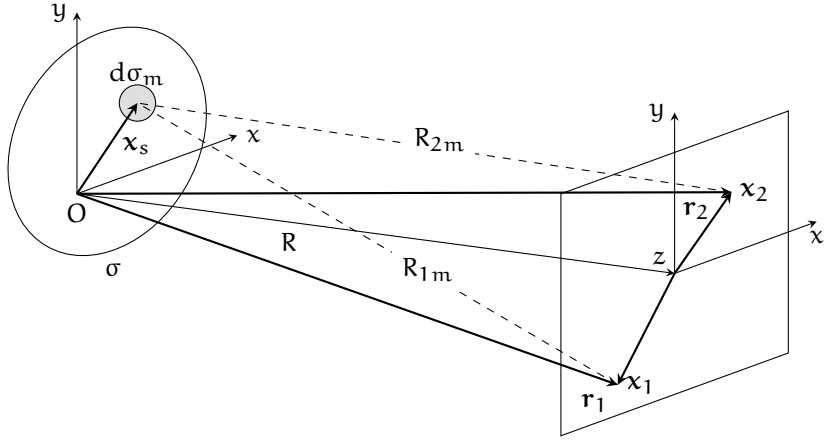


Figure 12: Notation relating to the far-zone version of the van Cittert-Zernike theorem. An extended planar source, situated at the origin $O(z = 0)$ and described by the source function σ , incoherently emits quasi-monochromatic radiation of frequency ω_0 and bandwidth $\Delta\omega$. The source is divided into elements $d\sigma_m$ which, statistically independent from each other, emit an electromagnetic disturbance Ψ_m . Vectors in the source plane are denoted $\mathbf{r}_m = (\mathbf{x}_s, 0)$. The plane of observation at $z = R$ is taken to be parallel to the source plane. Vectors in the observation plane are denoted $\mathbf{r}_i = (\mathbf{x}_i, R)$. The distance between a source element at \mathbf{r}_m and a point in the observation plane at \mathbf{r}_i is denoted R_{im} . In the limit of a continuous source we let $R_{1m} \rightarrow R_1$ and $R_{2m} \rightarrow R_2$.

A generalisation of the definition of intensity is given by the mutual coherence function Γ . It is defined as the cross correlation of the field Ψ at distinct space-time points (\mathbf{r}_1, t) and $(\mathbf{r}_2, t + \tau)$ as

$$\Gamma(\mathbf{r}_1, \mathbf{r}_2, \tau) \equiv \langle \Psi^*(\mathbf{r}_1, t) \Psi(\mathbf{r}_2, t + \tau) \rangle . \quad (148)$$

The mutual coherence function at equal times is called mutual intensity

$$J(\mathbf{r}_1, \mathbf{r}_2) \equiv \Gamma(\mathbf{r}_1, \mathbf{r}_2, 0) \equiv \langle \Psi^*(\mathbf{r}_1, t) \Psi(\mathbf{r}_2, t) \rangle . \quad (149)$$

The mutual intensity normalised by the intensities at \mathbf{r}_1 and \mathbf{r}_2 is usually referred to as the complex degree of coherence

$$j(\mathbf{r}_1, \mathbf{r}_2) \equiv \frac{J(\mathbf{r}_1, \mathbf{r}_2)}{\sqrt{I(\mathbf{r}_1)I(\mathbf{r}_2)}} . \quad (150)$$

Obviously, the degree of coherence exhibits a global maximum at $\mathbf{r}_1 = \mathbf{r}_2$. From Eqs. (148) and (149) the intensity reads as

$$I(\mathbf{r}) \equiv J(\mathbf{r}, \mathbf{r}) . \quad (151)$$

2.1.8.1 Van Cittert-Zernike theorem

In the following we will determine the mutual intensity and the complex degree of coherence for light emitted from an extended, incoherent and quasi-monochromatic source. Consider an extended planar

source situated at the origin O and described by the source function σ as in Fig. 12. The linear extent of the source and the detector shall be small compared to the distance R between source and observer. The source is divided into elements $d\sigma_m$ located at \mathbf{r}_m . Each source element is assumed to emit quasi-monochromatic light of frequency ω_0 and bandwidth $\Delta\omega$ such that there is no correlation between wave trains emanating from distinct elements $d\sigma_m$. The medium between source and observer is considered to be homogeneous ($n = \text{constant}$). Let Ψ_m be the electromagnetic disturbance produced by a source element $d\sigma_m$ as shown in Fig. 12. The total field Ψ at a position \mathbf{r}_i is given by the sum of Ψ_m as

$$\Psi(\mathbf{r}_i, t) = \sum_m \Psi_m(\mathbf{r}_i, t). \quad (152)$$

The mutual intensity of Eq. (149) then reads

$$\begin{aligned} J(\mathbf{r}_1, \mathbf{r}_2) &= \langle \Psi^*(\mathbf{r}_1) \Psi(\mathbf{r}_2) \rangle \\ &= \sum_m \langle \Psi_m^*(\mathbf{r}_1, t) \Psi_m(\mathbf{r}_2, t) \rangle + \sum_{m \neq n} \langle \Psi_m^*(\mathbf{r}_1, t) \Psi_n(\mathbf{r}_2, t) \rangle. \end{aligned} \quad (153)$$

If we assume the light emitted from different source elements to be statistically independent (mutually incoherent) and of zero mean value, the second term in the last of Eq. (153) vanishes as

$$\langle \Psi_m^*(\mathbf{r}_1, t) \Psi_n(\mathbf{r}_2, t) \rangle = \langle \Psi_m^*(\mathbf{r}_1, t) \rangle \langle \Psi_n(\mathbf{r}_2, t) \rangle = 0. \quad (154)$$

The distance between the observation point at \mathbf{r}_i and a source element $d\sigma_m$ at \mathbf{r}_m is denoted $R_{im} = |\mathbf{r}_i - \mathbf{r}_m|$, see Fig. 12. Furthermore, we assume the disturbance emitted from an source element $d\sigma_m$ to be a spherical harmonic wave of (complex) amplitude $a_m(t)$. The field Ψ_m , emitted from an element $d\sigma_m$ at a time $t - \frac{R_{im}}{v}$, is observed at \mathbf{r}_i at a later time t . Thus we have

$$\Psi_m(\mathbf{r}_i, t) = a_m \left(t - \frac{R_{im}}{v} \right) \frac{\exp \left[-i\omega_0 \left(t - \frac{R_{im}}{v} \right) \right]}{R_{im}}. \quad (155)$$

Substituting Eq. (155) into Eq. (153) and using Eq. (154), the mutual intensity reads

$$\begin{aligned} J(\mathbf{r}_1, \mathbf{r}_2) &= \sum_m \left\langle a_m^* \left(t - \frac{R_{1m}}{v} \right) a_m \left(t - \frac{R_{2m}}{v} \right) \right\rangle \frac{\exp \left[-i\omega_0 \left(\frac{R_{2m} - R_{1m}}{v} \right) \right]}{R_{1m} R_{2m}} \\ &= \sum_m \left\langle a_m^*(t) a_m \left(t - \frac{R_{2m} - R_{1m}}{v} \right) \right\rangle \frac{\exp \left[-i\omega_0 \left(\frac{R_{2m} - R_{1m}}{v} \right) \right]}{R_{1m} R_{2m}}, \end{aligned} \quad (156)$$

where we have exploited the time-shift invariance of Eq. (146). Amplitude variations within path differences $|R_{2m} - R_{1m}|$ smaller than

the longitudinal coherence length of Eq. (142) will average out in Eq. (156). Thus, for $|R_{2m} - R_{1m}| < l_l$, we may neglect the retardation term $\frac{R_{2m} - R_{1m}}{v}$ in the argument of a_m . The quantity $\langle a_m^*(t)a_m(t) \rangle$ represents the intensity of the radiation emitted from the source element $d\sigma_m$. Let $I(r_m)$ denote the intensity emitted per unit area $d\sigma_m$ of the source. Then we have

$$\langle a_m^*(t)a_m(t) \rangle = I(r_m)d\sigma_m . \quad (157)$$

In the limit of a continuous source, Eq. (156) becomes

$$\begin{aligned} J(r_1, r_2) &= \sum_m \langle a_m^*(t)a_m(t) \rangle \frac{\exp[-ik(R_{2m} - R_{1m})]}{R_{1m}R_{2m}} \\ &= \int_\sigma d\sigma I(\sigma) \frac{\exp[-ik(R_2 - R_1)]}{R_1R_2} , \end{aligned} \quad (158)$$

where $R_{im} \rightarrow R_i$ denotes the distance between a point on the source at r_m and the observation point at r_i , and $k = \frac{\omega_0}{v} = n \frac{\omega_0}{c}$ is the (mean) wave number in the medium, see Eq. (32). Normalising the right-hand side of Eq. (158) by the intensities at r_1 and r_2 , we obtain the complex degree of coherence (Eq. (150)) as

$$j(r_1, r_2) = \frac{1}{\sqrt{I(r_1)I(r_2)}} \int_\sigma d\sigma I(\sigma) \frac{\exp[-ik(R_2 - R_1)]}{R_2R_2} , \quad (159)$$

with

$$I(r_i) = J(r_i, r_i) = \int_\sigma d\sigma \frac{I(\sigma)}{R_i^2} \quad (160)$$

being the averaged intensity at r_i . Equation (159) is called van Cittert-Zernike theorem.

2.1.8.2 Van Cittert-Zernike theorem in the far field

In the far zone of the source and for observation points in a plane parallel to the source plane, the van-Cittert-Zernike theorem takes on a simpler form. The position vectors in the observation plane at $z = R$ and the source plane at $z = 0$ are written as $r_i = (\mathbf{x}_i, R)$ and $r_m = (\mathbf{x}_s, 0)$, respectively, where R is the distance between these planes, see Fig. 12. For values of R being large in comparison to the local extend of the source and the transverse area of observation, the distance R_i between a point on the source and a point in the observation plane can be approximated by its Taylor series to leading order as

$$R_i = \sqrt{(\mathbf{x}_i - \mathbf{x}_s)^2 + R^2} \approx R + \frac{(\mathbf{x}_i - \mathbf{x}_s)^2}{2R} . \quad (161)$$

The path difference then follows as

$$R_2 - R_1 \approx \frac{\mathbf{x}_2^2 - \mathbf{x}_1^2}{2R} - \frac{(\mathbf{x}_2 - \mathbf{x}_1) \cdot \mathbf{x}_s}{R} . \quad (162)$$

Furthermore, we define a phase

$$\psi \equiv k \frac{x_2^2 - x_1^2}{2R} . \quad (163)$$

Approximating the denominator under the integral in Eq. (159) by R^2 and substituting Eq. (162) into Eq. (159), the far-field version of the van Cittert-Zernike theorem follows as

$$j(r_1, r_2) = \frac{\exp(i\psi)}{\int_{\sigma} d^2x_s I_s(x_s)} \int_{\sigma} d^2x_s \exp\left(\frac{ik}{R}(x_2 - x_1) \cdot x_s\right) I_s(x_s) , \quad (164)$$

where $I_s(x_s) \equiv I(r_m)$ denotes the intensity at the source plane, and $d^2x_s = d\sigma$ the corresponding surface element. Thus, if the linear dimension of the source and the distance $|x_2 - x_1|$ are small compared to R , the complex degree of coherence is, apart from a phase and normalisation factor, equal to the Fourier transform of the intensity distribution across the source

$$j(r_1, r_2) \propto \hat{I}_s \left(\frac{x_2 - x_1}{\lambda R} \right) , \quad (165)$$

where $\hat{I}_s \equiv \mathcal{F} I_s$ demands the Fourier transform of I_s as in Eq. (A.18).

2.1.8.3 Incoherently illuminated object

In Section 2.3.2, the following expression for the forward propagated spectral intensity is derived in Fresnel theory and under the assumption of perfect spatial coherence

$$\hat{I}_z^{(coh)}(\xi_{\perp}) = \int d^2x_{\perp} \exp(-i2\pi x_{\perp} \xi_{\perp}) \Psi_0(x^-) \Psi_0^*(x^+) . \quad (166)$$

Here, x_{\perp} denotes a transverse position vector, ξ_{\perp} the conjugate Fourier coordinate, and $x^{\pm} = x_{\perp} \pm \frac{\lambda z}{2} \xi_{\perp}$. To account for partial coherence, we have to replace $I_z^{(coh)}$ in Eq. (166) with its expectation value $I_z \equiv I_z(x_{\perp}) = \langle I_z^{(coh)} \rangle$. Fourier transformation and expectation value (Eq. (146)) commute and thus can be interchanged. If the longitudinal extent of the object is small compared to distances R and z , we may assume the projection approximation to hold. The wave field Ψ_0 upon object exit can then be expressed in terms of the incident wave field $\Psi^{(in)} \equiv \Psi_{\omega}^{(in)}$ and the transmission function $T \equiv T_{\omega}$ as in Eq. (121). Thus, we may rewrite Eq. (166) as

$$\begin{aligned} \hat{I}_z(\xi_{\perp}) &= \int d^2x_{\perp} e^{-i2\pi x_{\perp} \xi_{\perp}} \langle \Psi_0(x^-) \Psi_0^*(x^+) \rangle \\ &= \int d^2x_{\perp} e^{-i2\pi x_{\perp} \xi_{\perp}} \langle T(x^-) T^*(x^+) \Psi^{(in)}(x^-) \Psi^{(in)*}(x^+) \rangle \\ &= \int d^2x_{\perp} e^{-i2\pi x_{\perp} \xi_{\perp}} T(x^-) T^*(x^+) \langle \Psi^{(in)}(x^-) \Psi^{(in)*}(x^+) \rangle . \end{aligned} \quad (167)$$

In the last line of Eq. (167) we have used that the transmission function is independent of the source statistics and can be moved out of the expectation value. The expectation value in the last line of Eq. (167) is identified with the mutual intensity (Eq. (149)) of the incident wave field as

$$J^{(in)} = \langle \Psi^{(in)}(\mathbf{x}^-) \Psi^{(in)*}(\mathbf{x}^+) \rangle . \quad (168)$$

In the far field of the source we can use Eq. (164) for the normalised mutual intensity $j^{(in)}$. If we assume the source intensity I_s to be normalised, we may omit the normalisation factor in $j^{(in)}$ and thus use $j^{(in)}$ instead of $J^{(in)}$ in Eq. (168). The only position dependent quantity appearing in Eq. (164) is the phase factor ψ entailing a rescaling of Fourier coordinates in Eq. (167). The rescaled Fourier transform \hat{I}_s in Eq. (164) depends on relative coordinates only and thus can be moved out of the Fourier integral in Eq. (167). Hence, we have

$$\begin{aligned} \hat{I}_z(\xi_{\perp}) &= \int d^2x_{\perp} e^{-i2\pi x_{\perp}\xi_{\perp}} T(x^-) T^*(x^+) j^{(inc)}(x^-, x^+) \\ &= \hat{I}_s\left(\frac{x^+ - x^-}{\lambda R}\right) \int d^2x_{\perp} e^{-i2\pi x_{\perp}(\frac{R+z}{R}\xi_{\perp})} T(x^-) T^*(x^+) \quad (169) \\ &= \hat{I}_s\left(\frac{z}{R}\xi_{\perp}\right) \int d^2x_{\perp} e^{-i2\pi x_{\perp}M\xi_{\perp}} T(x^-) T^*(x^+) , \end{aligned}$$

where have introduced the magnification factor M as

$$M \equiv \frac{z+R}{R} , \quad (170)$$

see also Fig. 28. Furthermore, we define the defocusing distance D as

$$D \equiv \frac{z}{M} = \frac{zR}{z+R} . \quad (171)$$

The argument x^{\pm} then reads $x^{\pm} \equiv x_{\perp} + \frac{\lambda DM}{2}\xi_{\perp}$. Using Eq. (166) and the definitions of M and D , Eq. (169) simplifies as

$$\hat{I}_z(\xi_{\perp}) = \hat{I}_s\left(\frac{z}{z+R}M\xi_{\perp}\right) \hat{I}_D^{(coh)}(M\xi_{\perp}) . \quad (172)$$

In the far field of the source and for moderate propagation distances, we may approximate $M \approx 1$, $D \approx z$, and $z+R \approx R$. E.g. for in vivo scans performed at beamline station 32-ID-B at Advanced Photon Source (APS) as described in Section 4.2.6, we have $R = 70$ m and $z = 0.7$ m, and thus a negligible magnification of $M = 1\%$. Then Eq. (172) becomes

$$\hat{I}_z(\xi_{\perp}) = \hat{I}_s\left(\frac{z}{R}\xi_{\perp}\right) \hat{I}_z^{(coh)}(\xi_{\perp}) . \quad (173)$$

Using the convolution theorem (Eq. (A.15)) we can express the intensity arising from an incoherent source as

$$I_z(x_{\perp}) = \left(\frac{R}{z}\right)^2 \int d^2x'_{\perp} I_s\left(\frac{R}{z}x'_{\perp}\right) I_z^{(coh)}(x_{\perp} - x'_{\perp}) . \quad (174)$$

2.1.8.4 Circular source

Let us consider Eq. (164) for a circular source of radius s and constant intensity. In this case the integration in Eq. (164) can be carried out [BWoo] and one finds the complex degree of coherence to be given by

$$j(\mathbf{r}_1, \mathbf{r}_2) = \exp(i\psi) \frac{2J_1(\nu)}{\nu}, \quad (175)$$

where J_1 denotes the Bessel function of the first kind and first order. The argument of J_1 in Eq. (175) is

$$\nu \equiv ks \frac{|\mathbf{x}_2 - \mathbf{x}_1|}{R}. \quad (176)$$

Apart from the phase factor, Eq. (175) is identical to the Airy formula of the Fraunhofer diffraction pattern originating from a circular aperture uniformly illuminated by coherent light, see Section 2.1.5.1. The function $\frac{J_1(\nu)}{\nu}$ steadily decreases from unity at $\nu = 0$ to zero at $\nu = 3.83$. Thus there is complete incoherence for points separated by a distance

$$|\mathbf{x}_2 - \mathbf{x}_1| = \frac{3.83R}{ks} \approx \frac{0.61R\lambda}{s}. \quad (177)$$

At $\nu = 1$ the value of $\frac{J_1(\nu)}{\nu}$ has decreased to 0.88 which is typically regarded as a permissible departure from ideal coherence. The corresponding transversal coherence length for a circular shaped source of constant intensity reads

$$l_{\perp}^{(\text{circ})} = \frac{R}{ks} = \frac{\lambda R}{2\pi s} \approx \frac{0.16\lambda R}{s}. \quad (178)$$

2.1.8.5 Gaussian shaped source

Let us now consider a symmetric, Gaussian shaped source of standard deviation σ_s and peak intensity I_0

$$I_s(\mathbf{x}_s) = \frac{I_0}{2\pi\sigma_s^2} \exp\left(-\frac{\mathbf{x}_s^2}{2\sigma_s^2}\right). \quad (179)$$

The Fourier transform of the source function appearing in the far-field version of the van Cittert-Zernike theorem (Eq. (164)) yields again a Gaussian function

$$\hat{I}_s\left(\frac{\mathbf{x}_2 - \mathbf{x}_1}{\lambda R}\right) = I_0 \exp\left(-2 \left[\frac{\pi\sigma_s |\mathbf{x}_2 - \mathbf{x}_1|}{\lambda R}\right]^2\right). \quad (180)$$

Thus, the complex degree of coherence reads

$$j(\mathbf{r}_1, \mathbf{r}_2) = \exp(i\psi) \exp\left(-2 \left[\frac{\pi\sigma_s |\mathbf{x}_2 - \mathbf{x}_1|}{\lambda R}\right]^2\right). \quad (181)$$

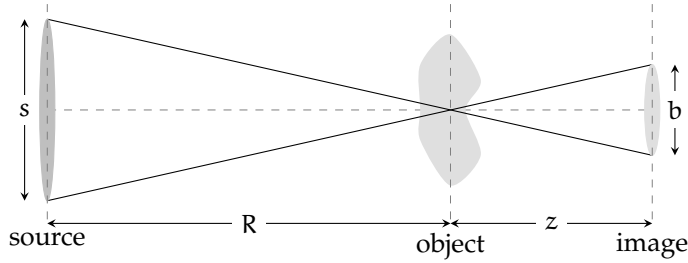


Figure 13: Geometrical blurring induced by an extended source of diameter s situated at distance R from the object. Object points imaged in the detector plane at a distance z from the object are blurred by a factor $b = \frac{sz}{R}$ according to the intercept theorem.

Identifying the source size s with the full width at half maximum (FWHM) of the Gaussian profile in Eq. (179) as

$$s = \text{FWHM}(I_s) = 2\sqrt{2 \ln 2} \sigma_s \approx 2.355 \sigma_s , \quad (182)$$

we may define the transverse coherence length as the value where of the degree of coherence $|j(\mathbf{r}_1, \mathbf{r}_2)|$ has dropped to $\frac{1}{2}$. The transverse coherence length of a Gaussian shaped source then reads

$$l_{\perp}^{(\text{Gauss})} = \sqrt{\frac{\ln 2}{2}} \frac{\lambda R}{\pi \sigma_s} = 2 \ln 2 \frac{\lambda R}{\pi s} = 0.441 \frac{\lambda R}{s} . \quad (183)$$

Note the factor of $4 \ln 2 = 2.773$ compared to the coherence length of a circular source (Eq. (178)). E.g. at an X-ray energy of 30 keV ($\lambda = 4.13 \times 10^{-11}$ m), a source-to-detector distance of $R = 100$ m, and a source diameter of $s = 100$ μm , the transverse coherence length takes on a value of $l_{\perp}^{(\text{Gauss})} = 4 \ln 2 \times l_{\perp}^{(\text{circ})} = 4 \ln 2 \times 6.58 \mu\text{m} = 20.66 \mu\text{m}$. For convenience, we define the transverse coherence length as

$$l_{\perp} \equiv \frac{\lambda R}{2s} . \quad (184)$$

2.1.8.6 Source blurring

The finite extent of the source introduces a blur of object points at the detector as illustrated in Fig. 13. It follows from the intercept theorem that the blur b of image points is given by

$$b = \frac{sz}{R} , \quad (185)$$

where z denotes the distance between sample and detector. This effect is experimentally demonstrated in Fig. 14, depicting a sequence of (flat-field corrected) intensity maps recorded with beamline Topo-Tomo at Angströmquelle Karlsruhe (ANKA). There, intensity contrast

diminishes as propagation distance is increased above $z \gtrsim 0.5$ m. Substituting the source diameter by virtue of Eq. (184) into Eq. (185), the blur relates to the coherence length as

$$b = \frac{\lambda z}{2l_{\perp}}. \quad (186)$$

The (Gaussian) blurring of object points imaged at the detector plane can be described by means of a convolution of the coherent image, arising from a point source, with a Gaussian function. Let I_b denote the blurred version of the coherent intensity I given as

$$\begin{aligned} I_b(x_{\perp}) &= I \ast G \equiv \int d^2x'_{\perp} G(x'_{\perp}) I(x_{\perp} - x'_{\perp}) \\ &= \mathcal{F}^{-1}[(\mathcal{F}G)(\mathcal{F}I)], \end{aligned} \quad (187)$$

where the convolution theorem of Eq. (A.15) was used, and \mathcal{F} demands Fourier transformation as in Eq. (A.18). The blurring filter G is given by a normalised Gaussian function in two dimensions as

$$G(x_{\perp}) = \frac{1}{2\pi\sigma_b^2} \exp\left(-\frac{x_{\perp}^2}{2\sigma_b^2}\right), \quad (188)$$

where σ_b is the standard deviation. The blurring length is identified with the full width at half maximum (FWHM) of G as

$$b = \text{FWHM}(G) = 2\sqrt{2\ln 2}\sigma_b \approx 2.355\sigma_b. \quad (189)$$

Comparing Eqs. (174) and (187), the blurring filter connects to the source function as

$$G(x_{\perp}) = \left(\frac{R}{z}\right)^2 I_s\left(\frac{R}{z}x_{\perp}\right). \quad (190)$$

For a Gaussian shaped source as in Eq. (179), we have

$$G(x_{\perp}) = \left(\frac{R}{z}\right)^2 \frac{1}{2\pi\sigma_s^2} \exp\left(-\frac{1}{2\sigma_s^2}\left(\frac{R}{z}x_{\perp}\right)^2\right), \quad (191)$$

where we have set $I_0 = 1$ because in Eq. (174) we assumed I_s to be normalised. Comparing Eqs. (188) and (191) the blur is identified with the source size as

$$\sigma_b = \frac{z}{R}\sigma_s, \quad (192)$$

in compliance with Eq. (185).

Let us now consider the effect of blurring on the spectrum of the propagated intensity using Eq. (187). Since the Fourier transform of a Gaussian function yields a Gaussian function, \hat{G} acts as low-pass

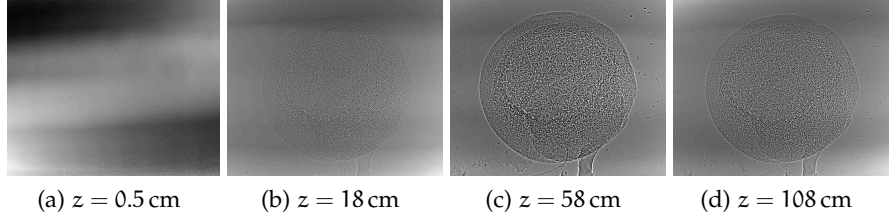


Figure 14: Sequence of (flat-field-corrected) intensity maps with increasing propagation distance z . (a-c) Increasing phase-contrast-induced enhancement of intensity contrast (see Section 2.3). (d) Intensity contrast diminishes upon a further increase of z due to source blurring. Data was acquired with bending-magnet beamline TopoTomo at ANKA under parallel-beam incidence at an energy of $E = 12\text{ keV}$, a bandwidth of $\Delta E = 10^{-2}E$ using a multilayer monochromator, an effective pixel size of $\Delta x = 1\text{ }\mu\text{m}$, and an exposure time of $\Delta t = 180\text{ s}$. The sample, an early-stage Xenopus frog embryo, was embedded in agarose within an Eppendorf tube of diameter 0.6 cm to avoid large phase jumps at the object boundary and reduce large-scale absorptive effects.

filter on \hat{I} attenuating high frequencies. The Fourier transform of G evaluates as

$$\hat{G}(\xi_{\perp}) \equiv \int d^2x_1 \exp(i2\pi\xi_{\perp} \cdot x_1) G(x_1) = \exp(-2(\sigma_b\pi\xi_{\perp})^2). \quad (193)$$

We may use Eq. (193) to define the blurring-induced transverse cut-off frequency ξ_b as the frequency where \hat{G} has dropped to the value e^{-1} ,

$$\xi_b = \frac{1}{\sqrt{2}\sigma_b\pi} = \frac{2\sqrt{\ln 2}}{\pi b} \approx 0.53 \frac{1}{b}, \quad (194)$$

where we have substituted σ_b from Eq. (189). Demanding a drop of $\frac{1}{2}$ instead results in a slightly stronger cut-off $\xi_b \approx 0.44 \frac{1}{b}$. Using Eq. (186), ξ_b relates to the coherence length as

$$\xi_b = 4\sqrt{\ln 2} \frac{l_{\perp}}{\pi\lambda z} \approx 1.06 \frac{l_{\perp}}{\lambda z}. \quad (195)$$

For convenience, we define the blurring-induced cut-off frequency as

$$\xi_b \equiv \frac{1}{2b}, \quad (196)$$

or in terms of the transverse coherence length

$$\xi_b = \frac{l_{\perp}}{\lambda z}. \quad (197)$$

Equation (197) is in compliance with the relation for the cut-off frequency directly obtained from the expression for $\hat{I}_z^{(coh)}$ in Eq. (166). Regarding the autocorrelation on the right-hand side of Eq. (166),

only those points in the transverse plane contribute to $\hat{I}_z^{(coh)}$ that are separated less than $|x^+ - x^-| \leq \lambda z |\xi_{\perp}|_{\max}$. The maximum frequency $|\xi_{\perp}|_{\max}$ is either set by the detector resolution to $\xi_c = \frac{1}{2\Delta x}$ or by Eq. (196).

2.2 MICROSCOPIC INTERACTIONS OF X-RAYS AND MATTER

Hitherto the interaction of light with matter were only taken into account macroscopically in terms of the refractive index. In this section we will consider the interaction of X-rays and matter on the atomic level. This will allow us to relate the electron density distribution to the refractive index. The basic processes of the interaction of light with matter are scattering and absorption of a photon by an electron, obeying indeterministic rules that conspire towards determinism at macroscopic scales, which is either considered to be free or bound in an atom or molecule. Thus an understanding of the structure of atoms and matter is required. Presently, the best tested and efficient framework to address this is quantum mechanics. To precisely describe the interaction of light and matter, quantum mechanics has to be extended to quantum field theories involving the second quantisation of gauge and particle fields [Tom46; Sch48a; Sch48b; Fey49a; Fey49b; Fey50; Dys49]. The processes of scattering and absorption will be discussed in the Sections 2.2.1 and 2.2.2, respectively.

2.2.1 Scattering

The fundamental scattering unit of a photon in an atom or molecule is the electron. In the classical description the electron is accelerated by an incident electromagnetic wave and commences to oscillate, thereby emitting secondary electromagnetic waves of the same far-field wave length as that of the incident field. We thus are dealing with an elastic scattering process which, in the limit of free electrons, is called Thomson scattering. This is the dominant scattering process for X-rays. In the case of inelastic scattering, when energy is transferred from the photon to the electron, there is no classical electrodynamic description and a quantum mechanical treatment is mandatory. This is known as Compton effect.

First, we will consider a semi-classical treatment of the scattering process where a time-harmonic electromagnetic wave is incident on an electron which is bound in an atom. Let the electric field of the incident wave at the position of the electron be

$$E_i = E_0 \exp(-i\omega t), \quad (198)$$

where E_0 is a constant amplitude. To a good approximation the electron can be considered to behave under the influence of a restoring force $-k_h r$, where k_h denotes the force constant according to Hooke's

law and \mathbf{r} the displacement vector with respect to the equilibrium position of the electron. A dissipative force resisting the motion accounts for damping effects, e. g. due to the emission of radiation or collisions between atoms. This force reads $-g\mathbf{v}$, where g is the damping coefficient and $\mathbf{v} = \frac{d\mathbf{r}}{dt}$ denotes the electron's velocity vector. The Lorentz force acting on a particle which carries a charge q and moves with a velocity \mathbf{v} in an electric and magnetic field, \mathbf{E} and \mathbf{B} , is given by

$$\mathbf{F} = q(\mathbf{E} + \mathbf{v} \times \mathbf{B}) . \quad (199)$$

Disregarding magnetic interactions, the driving Lorentz force reduces to $q\mathbf{E}$. The forces exerted on the electron of charge $q = -e$ imply the well-known equation of motion of a damped harmonic oscillator, driven by a periodic force:

$$m\ddot{\mathbf{r}} + g\dot{\mathbf{r}} + k_h\mathbf{r} = -e\mathbf{E}_i . \quad (200)$$

A particular solution to Eq. (200) is

$$\mathbf{r} = \frac{-e\mathbf{E}_i}{m(\omega_0^2 - \omega^2) - i\omega g} , \quad (201)$$

where the angular frequency $\omega_0 = \sqrt{\frac{k_h}{m}}$ denotes the resonance or absorption frequency of the undamped system which is related to electronic transitions in atoms and molecules. The occurrence of such frequencies at discrete values is a consequence of quantum mechanics. We now assume a given distribution of electrons described by the electron density ρ_e . Let each electron contribute a dipole moment $-e\mathbf{r}$ to the total polarisation \mathbf{P} . Neglecting the contributions from the nuclei, the total polarisation reads

$$\mathbf{P} = -e\rho_e\mathbf{r} = \frac{e^2\rho_e\mathbf{E}_i}{m(\omega_0^2 - \omega^2) - i\omega g} . \quad (202)$$

From Eq. (12) we have $\mathbf{P} = \epsilon_0\chi_e\mathbf{E}_i$. The dielectric susceptibility and, via Eq. (26), the refractive index n follow as

$$\chi_e = n^2 - 1 = \frac{1}{\epsilon_0 m_e} \frac{e^2 \rho_e}{(\omega_0^2 - \omega^2) - i\omega g} . \quad (203)$$

Thus, we have related the microscopic electron density distribution to the macroscopic refractive index. For vanishing frequencies of the driving electromagnetic field the refractive index approaches

$$n^2(\omega = 0) = 1 + \frac{e^2 \rho_e}{\epsilon_0 m_e \omega_0} . \quad (204)$$

Note that for photon energies above the absorption edge, $\omega > \omega_0$, and neglecting dissipative effects, Eq. (203) assumes negative values. Introducing the classical electron radius defined as

$$r_e = \frac{e^2}{4\pi\epsilon_0 m_e c^2} = 2.828 \times 10^{-15} \text{ m} = 2.828 \times 10^{-5} \text{ \AA} , \quad (205)$$

we have

$$n^2 - 1 = -\frac{e^2 \rho_e}{\epsilon_0 m (\omega^2 - \omega_0^2)} \approx -\frac{e^2 \rho_e}{\epsilon_0 m \omega^2} = -\frac{4\pi r_e \rho_e}{k_0^2}, \quad (206)$$

with the wave number in vacuum $k_0 = \frac{\omega}{c}$ (see Eq. (33)). For X-rays, the right-hand of Eq. (206) is close to zero and the refractive index approximates

$$n = 1 - \delta_\omega = \sqrt{1 - \frac{4\pi r_e \rho_e}{k^2}} \approx 1 - \frac{1}{2} \frac{4\pi r_e \rho_e}{k^2} = 1 - \frac{\lambda^2 r_e \rho_e}{2\pi}. \quad (207)$$

Consequently, the refractive index is smaller than unity and the phase velocity of light is larger than the speed of light in vacuum, $v = \frac{c}{n} > c$. This is yet in accordance with special relativity because in regions of normal dispersion, where $\frac{\partial n}{\partial \omega} > 0$, the propagation of energy takes place with the group velocity

$$v_g = \frac{d\omega}{dk} = \frac{c}{n(\omega) + \omega \frac{\partial n}{\partial \omega}}, \quad (208)$$

which is smaller than c . In regions of anomalous dispersion, i. e. close above the absorption edge, the group velocity cannot be interpreted as the velocity at which energy propagates [Bri60]. As shown in Fig. 7, the refractive index approaches unity from below with increasing energy. This is related to the fact that X-ray frequencies are usually higher than the transition frequencies, except for those involving the inner K- or L-shell electrons. In the visible spectrum, where $\omega \ll \omega_0$, the boundedness of electrons cannot be neglected. Thus the refractive index is greater than unity and normal dispersion is observed.

Let us sketch the derivation of the differential cross-section for the elastic Thomson scattering of a linearly polarised electromagnetic wave by a single free electron. To evaluate the electric field which is emitted by the electron, the retarded vector potential \mathbf{A} , produced by the current density \mathbf{j} , is employed. Working in Lorenz gauge

$$\partial_\mu A^\mu = \frac{1}{c} \partial_t + \nabla \cdot \mathbf{A} = 0, \quad (209)$$

the retarded potential reads as [Jac99]

$$\mathbf{A}(\mathbf{r}, t) = \frac{1}{4\pi\epsilon_0 c^2} \int d^3 r' \frac{\mathbf{j}(\mathbf{r}', t - |\mathbf{r} - \mathbf{r}'|/c)}{|\mathbf{r} - \mathbf{r}'|}. \quad (210)$$

The magnetic field is computed as $\mathbf{B} = \nabla \times \mathbf{A}$ and is related to the electric field by $|\mathbf{E}| = c |\mathbf{B}|$. The current is identified with the induced dipole moments of the electrons as $\mathbf{j} = \rho \mathbf{v}_p$, where ρ is the electron charge density and $\mathbf{v}_p \equiv \frac{d\mathbf{r}_p}{dt}$ with \mathbf{r}_p given by Eq. (201). Let the dipole be situated at the origin and oscillate along a fixed axis. The dipole approximation is assumed, hence the electromagnetic field is considered in the far field only. In this region the only significant

contribution of the electric field is the polar component E_ψ which is perpendicular to the direction of observation and the magnetic field. It is given as

$$E_\psi = -\frac{1}{4\pi\epsilon_0 c^2} \frac{-e}{r} \frac{d^2 r_p}{dt^2} \cos \psi , \quad (211)$$

where $r = |\mathbf{r}|$ is the distance to the observer, $\cos \psi$ the polarisation factor, and ψ the angle subtended by the unit vector $\hat{\mathbf{r}} = \mathbf{r}/r$ and the plane perpendicular to the direction $\hat{\mathbf{r}}_p = \mathbf{r}_p/|\mathbf{r}_p|$ of the electric dipole oscillation. Thus the polarisation factor is calculated from $\cos \psi = |\hat{\mathbf{r}}_p \times \hat{\mathbf{r}}|$. Since the electron is considered free, the resonance frequency ω_0 is set to zero; or for photon energies far above the absorption edge we have $\omega_0/\omega \approx 0$. Moreover, damping is neglected and the damping coefficient g set to zero. Thus, $\frac{d^2 r_p}{dt^2} = \frac{-e}{m} E_i$ and the ratio of the radiated to incident electric field is found to be [Jac99]

$$\frac{E_\psi}{|E_i|} = -r_e \frac{\exp(ik_0 r)}{r} \cos \psi . \quad (212)$$

Here $k_0 = \frac{\omega}{c}$ is the incident wave number. The minus sign in Eq. (212) means that the phase of the scattered wave emitted by the electron is shifted by π with respect to the incident wave.

From Eqs. (64) and (212) the differential cross-section for the incident radiation to be scattered into a solid angle $d\Omega$ follows as

$$\frac{d\sigma_T}{d\Omega} = r_e^2 \cos^2 \psi . \quad (213)$$

Therefore, the classical electron radius r_e is also known as Thomson scattering length. Assuming a distribution of charges given by the charge density ρ , Eq. (213) becomes

$$\frac{d\sigma_T}{d\Omega} = r_e^2 \cos^2 \psi |f_0(\mathbf{q})|^2 . \quad (214)$$

Here, the atomic form factor f_0 computes as the phase-weighted integral of ρ and thus involves the Fourier transform of ρ as

$$f_0(\mathbf{q}) = \int d^3 \mathbf{r} \rho(\mathbf{r}) \exp(i\mathbf{q}\cdot\mathbf{r}) , \quad (215)$$

where $\mathbf{q} = \mathbf{k}_i - \mathbf{k}_f$ denotes the momentum transfer between incoming (\mathbf{k}_i) and scattered wave (\mathbf{k}_f). When the photon scatters off an atom in a molecule (or a unit cell), an additional summation over the atomic form factors of individual atoms, located at \mathbf{r}_j , is required. The atomic form factor in Eq. (214) is then replaced with

$$f_0(\mathbf{q}) \rightarrow F(\mathbf{q}) = \sum_j f_j(\mathbf{q}) \exp(i\mathbf{q}\cdot\mathbf{r}_j) . \quad (216)$$

For a crystal lattice constituting an array of unit cells, a significant scattering signal is obtained only when the momentum transfer coincides with a lattice vector \mathbf{G} of the reciprocal space. Thus $\mathbf{q} = \mathbf{G}$,

which is called Laue condition. Summing over all unit cells of the crystal, Eq. (216) becomes the structure factor.

The total cross section for Thomson scattering owns a constant value of

$$\sigma_T = \frac{8\pi}{3} r_e^2 = 0.665 \times 10^{-24} \text{ cm}^2 = 0.665 \text{ barn}. \quad (217)$$

In terms of the Compton wave length $\lambda_C = \frac{h}{m_e c}$ and the fine-structure constant $\alpha = \frac{1}{4\pi\epsilon_0}\frac{e^2}{\hbar c}$, the Thomson cross-section reads $\sigma_T = \frac{8\pi}{3} \frac{\alpha \lambda_C^2}{2\pi}$.

For photon energies considerably greater than the electron binding energy the electron can be considered free and the atomic form factor is to a good approximation given by f_0 . For energies less than the electron binding energy resonant scattering behaviour is observed, which can be accounted for by supplementing dispersion corrections to f_0 . Then the atomic form factor is written as the sum of the energy-independent part f_0 and the dispersion corrections f' and f'' which are due to bound-state effects of the electron in an atom

$$f(\mathbf{q}, \omega) = f_0(\mathbf{q}) + f'(\omega) + i f''(\omega). \quad (218)$$

The imaginary part f'' of Eq. (218) represents the dissipation in the system. The extrema of the dispersion corrections are encountered at energies corresponding to the absorption edges of an atom.

In a quantum mechanical description the differential cross section for elastic scattering can be calculated via Fermi's Golden rule which states that the transition rate $w_{i \rightarrow f}$, i. e. the transition probability per unit time for the system to evolve from an initial state $|i\rangle$ to a final state $|f\rangle$, provided by first-order time-dependent perturbation theory, is given by [Sak93]

$$w_{i \rightarrow f} = \frac{2\pi}{\hbar} M_{if}^2 \delta(E_f - E_i). \quad (219)$$

The factor M_{if} denotes the transition matrix element to be computed from the interaction Hamiltonian \mathcal{H}_I by

$$M_{if} = \langle f | \mathcal{H}_I | i \rangle. \quad (220)$$

If there is a group of final states $\{f\}$ with nearly the same energy as the energy of the initial state $|i\rangle$ and with a density of states $\rho(E)$ within an energy interval $(E, E + dE)$, the left-hand side of Eq. (219) must be integrated with $\int dE_f \rho(E_f)$ to yield $w_{i \rightarrow \{f\}}$. Given a beam of flux density Φ_0 incident on a sample, the differential cross section for elastic scattering follows as

$$\frac{d\sigma}{d\Omega} = \frac{w_{i \rightarrow \{f\}}}{\Phi_0 \Delta\Omega} = \left(\frac{V}{2\pi} \right)^2 \frac{\hbar^4}{c^4} \int dE_f |M_{if}|^2 E_f^2 \delta(E_f - E_i). \quad (221)$$

Here, V is the interaction volume introduced for normalisation purposes, and E_i and E_f denote the initial and final energy of the incident

and the scattered photon, respectively. The energy of the vector potential \mathbf{A} is normalised to E_i within the interaction volume V via

$$\int_V d^3r \frac{1}{2} \left(\epsilon_0 E^2 + \frac{1}{\mu_0} B^2 \right) = E_i = \hbar\omega \quad (222)$$

such that V drops out in Eq. (221) because a cancellation between $|M_{if}|^2$ and the factor V takes place. The same holds for Eq. (231). The interaction Hamiltonian of the photon-electron system is given by

$$\mathcal{H}_I = \frac{e\mathbf{p} \cdot \mathbf{A}}{m_e} + \frac{e^2 \mathbf{A}^2}{2m_e}, \quad (223)$$

where $\mathbf{p} = \mathbf{p}_{\text{kin}} - e\mathbf{A}$ is the electron's canonical momentum and \mathbf{A} the vector potential of the electromagnetic field in physical Coulomb gauge. $\mathbf{p}_{\text{kin}} = m_e \mathbf{v}$ is the kinematic momentum with $\mathbf{v} = \frac{d\mathbf{r}}{dt}$ denoting the electron velocity. Thomson scattering is related to the part of the interaction Hamiltonian which is quadratic in the vector potential. This is because scattering involves the annihilation of the incident photon state and the creation of the scattered photon state when the vector potential is expressed in terms of annihilation and creation operators acting on the state kets according the second quantisation [Ryd96]. The polarisation factor in Eq. (214) corresponds to the squared product of the polarisation vectors of the incident and scattered photon, and the form factor is given by $f(\mathbf{q}) = \langle \mathbf{p} | \exp(i\mathbf{q}\mathbf{r}) | \mathbf{p} \rangle$.

The vector potential \mathbf{A} is defined only modulo gauge transformations. The full Hamiltonian is thus a gauge-invariant transforming term given by

$$\frac{\mathbf{p}_{\text{kin}}^2}{2m_e} = \frac{(\mathbf{p} - q\mathbf{A})^2}{2m_e} = \frac{(\frac{1}{i\hbar} \nabla + e\mathbf{A})^2}{2m_e}. \quad (224)$$

Equation (224) is artificially decomposed into a time-independent Hamilton H_0 of the undisturbed system and a potentially time-dependent interacting part H_I . If H_0 and H_I are treated separately, each individual term is no longer gauge invariant. Nevertheless we may employ the vector potential as long as we work in a physical gauge such as the Coulomb gauge. The Coulomb gauge, also called radiation gauge or transversal gauge, renders the vector potential divergence free

$$\nabla \cdot \mathbf{A}(\mathbf{r}, t) = 0. \quad (225)$$

Then, in the absence of sources, the vector potential itself is governed by the wave equation and the scalar potential by the Poisson equation $\nabla^2 \phi = -\rho(\mathbf{r}, t)/\epsilon_0$. Thus ϕ represents the instantaneous Coulomb potential.

Inelastic scattering is described by the Compton effect which involves a transfer of energy from the photon to the electron. The corresponding change in wave length of the scattered photon is given by

$$\lambda_f - \lambda_i = \lambda_C(1 - \cos \theta) , \quad (226)$$

where θ is the scattering angle and λ_C the Compton scattering length defined as

$$\lambda_C = \frac{h}{m_e c} = 3.86 \times 10^{-13} \text{ m} . \quad (227)$$

Note that Compton scattering is incoherent, while Thomson scattering is coherent (Bragg's law, Laue condition). The contribution of Compton scattering to the total scattering cross section increases with increasing energy. The differential cross-section for photons scattered from a single free electron in lowest order of quantum electrodynamics is calculated by the Klein-Nishina formula [KN29]. The corresponding total cross section is given as

$$\sigma_{KN} = 2\pi r_e^2 \left(\frac{1+\eta}{\eta^2} \left[\frac{2(1+\eta)}{1+2\eta} - \frac{1}{\eta} \ln(1+2\eta) \right] + \frac{1}{2\eta} \ln(1+2\eta) - \frac{1+3\eta}{(1+2\eta)^2} \right) , \quad (228)$$

where η denotes the ratio of the incident photon energy to the electron rest energy as $\eta = \frac{E_\gamma}{m_e c^2}$. At low-frequencies, $\eta \ll 1$, the Klein-Nishina formula reduces to the classical Thomson scattering formula of Eq. (217).

2.2.2 Absorption

The absorption of a photon by an atom is called photoelectric effect. It is the extreme inelastic limit of Compton scattering. During this process photon energy is transferred to an electron which subsequently is expelled from the atom being left ionised. The photoelectric effect is a manifestation of the quantisation of the electromagnetic field energy. The energy of the emitted photoelectron is proportional to the frequency of the incident light, but not to its intensity [Eino5]. Quantitatively, the average photoelectric absorption is described in terms of the linear absorption coefficient μ . According to Beer's law (Eq. (123)), the attenuation of an incident beam of intensity I_0 is given by

$$I(z) = I_0 \exp(-\mu_\omega z) . \quad (229)$$

The linear absorption coefficient is related to the absorption cross-section σ_a by

$$\mu_\omega = 2k_0 \beta_\omega = \rho_a \sigma_a = \frac{\rho_m N_A}{A} \sigma_a , \quad (230)$$

where ρ_a is the atomic number density, ρ_m the mass density, N_A Avogadro's number, and A the atomic mass number.

Likewise Compton scattering the photoelectric absorption evades a classical explanation and a quantum mechanical treatment is mandatory. By means of Fermi's Golden Rule (Eq. (219)) the absorption cross-section can be expressed in terms of the transition matrix element M_{if} of the interaction Hamiltonian as

$$\sigma_a = \frac{w_{i \rightarrow \{f\}}}{\Phi_0} = \frac{2\pi V}{\hbar c} \int dE_{pe} |M_{if}|^2 \rho(E_{pe}) \delta(E_{pe} - (E_i - E_b)), \quad (231)$$

where E_i is the energy of the incident photon, E_b the electron binding energy, and E_{pe} the kinetic energy of the photoelectron. As for Eq. (221), the interaction volume V is introduced for normalisation purposes and cancels with $|M_{if}|^2$. Here, $\{f\}$ indicates that the integration is performed over the entire solid of 4π to account for that the photoelectron can be expelled in all possible directions. The matrix element for photoelectric absorption is related to the part of the interaction Hamiltonian which is linear in the vector potential

$$M_{if} = \frac{e}{m} \langle f | \mathbf{p} \cdot \mathbf{A} | i \rangle, \quad (232)$$

thus allowing for the annihilation of a photon.

Following photoelectric absorption and an expel of an electron from the inner atomic shell, the created hole can be filled by either of two distinct processes: (i) Fluorescent X-ray emission [Baro4]: the hole is filled by an electron from the outer shell. The transition entails the emission of a photon with an energy equal to the difference in binding energies of the involved electronic states. The monochromatic radiation can be used as a fingerprint to identify the atom which has emitted the fluorescent X-ray photon. (ii) Auger electron emission [Mei22]: alternatively to the emission of fluorescent X-rays, the energy, released during the transition of an outer shell electron to the inner shell, can be transferred to another electron from the outer shell which subsequently will be expelled from the atom. This process is called Auger effect. The hole in the inner atomic shell can also be created by γ -rays or charged particles such as electrons or positrons.

Away from absorption edges, the photoelectric absorption cross-section is approximately proportional to E^{-3} . For condensed matter and close to an absorption edge the absorption spectrum exhibits a fine structure which depends on the chemistry of the material. This phenomenon is exploited in experiments measuring the spectrum of the X-ray absorption fine structure (XASF), comprising X-ray absorption near-edge structure (XANES) and extended X-ray absorption fine structure (EXAFS). These two methods give complementary structural information, the XANES spectra being sensitive to electronic structures and the symmetry of a metal site, and EXAFS spectra telling about numbers, types, and distances to ligands and neighbouring atoms

with respect to the absorbing element [KP87]. A detailed treatment of X-ray absorption and XASF is given in [KP87].

Conventional X-ray imaging employing absorption contrast relies on the strong dependence of the photoelectric absorption cross-section on the atomic number Z varying with Z^4 . The photoelectric effect is the dominant contribution to the absorption cross-section for photon energies much less than the electron rest mass of $m_e = 511 \text{ keV}/c^2$.

2.3 PHASE RETRIEVAL

In the following we consider phase variations induced in the exit wave field by the interaction of hard, monochromatic, electromagnetic radiation with the sample. Furthermore, we confine our consideration to the idealised situation of perfect spatial coherence and in the absence of noise. A treatment of the case subject to shot-noise (Poisson) in the context of non-linear phase retrieval is given in Section 4.2.

Numerous methods have been devised to retrieve the phase of an exit wave (transmission function) from measurements of the associated intensity. Interferometric techniques rely on the interference of the phase-distorted wave front with an undistorted or biasing reference beam [Zer42a; Zer42b; BH65; Mom95; BW99]. Crystal interferometry e.g. is based on Bragg reflection (in Bragg or Laue geometry). It requires an extremely high stability of the experimental setup in order to prevent spatial displacements down to atomic scales within the interferometer. Unless the interferometer is build from a monolithic block, this involves a meticulous alignment of the reflecting crystals. An alternative interferometric technique employs diffraction gratings, which is much less prone to problems relating to the positioning and stability of the setup [PS01; Dav+02; Koh+03; Momo3; Pfe+06]. Diffraction enhanced imaging, also known as Schlieren technique or analyser-based imaging, appeals to the linear relation $\Delta\alpha = \frac{1}{k} |\nabla_{\perp} \phi_0|$ between the angle $\Delta\alpha$, subtended by the diffracted beam to the optical axis z , and the transverse derivative of the phase $\nabla_{\perp} \phi_0$.³ A quantitative analysis of the acquired rocking curves (intensity as a

³ In Sections 2.1.5 and 2.1.6 we found that, assuming forward propagation and constant absorption, the monochromatic exit wave field can be written in terms of the exit phase, ϕ_0 , as

$$\Psi_{\omega}(\mathbf{r}) = \Psi_0 \exp(i\phi_0(\mathbf{x}_{\perp}) + ikz), \quad (233)$$

with $\mathbf{r} = (\mathbf{x}_{\perp}, z)$, see Eqs. (80) and (121). From Eq. (233) and using the three-dimensional Fourier representation of Ψ_{ω} and the Fourier derivative theorem, the gradient ∇ of the wave field relates to the wave vector \mathbf{k} as

$$\begin{aligned} \nabla \Psi_{\omega}(\mathbf{r}) &= i(\nabla_{\perp} \phi_0(\mathbf{x}_{\perp}), k) \Psi_{\omega}(\mathbf{r}) \\ &= \mathcal{F}_{\mathbf{k}}^{-1} i(\nabla_{\perp} \phi_0(\mathbf{x}_{\perp}), k) \widehat{\Psi}_{\omega}(\mathbf{k}) \\ &= \mathcal{F}_{\mathbf{k}}^{-1} (-ik) \widehat{\Psi}_{\omega}(\mathbf{k}), \end{aligned} \quad (234)$$

function of $\Delta\alpha$) involves input from dynamical diffraction theory (finite Darwin width) [FGZ80; Dav+95; BIB96; Lüb+oo; NWo8].

The majority of phase-sensitive imaging methods mentioned above involves a scanning or stepping procedure. This renders the instrumental setup more demanding and less robust, and the data acquisition slower and less dose efficient in comparison to single-measurement techniques. On the other hand, free-space (or in-line) propagation-based phase-contrast imaging is free of additional optics and relies on the measurement of a single intensity map at a single distance only [Sni+95; Wil+96]. The acquired intensity pattern emerges due to the self-interference of light diffracted at exiting the object and propagating towards the detector (Fresnel theory). To retrieve the phase of the exit wave from measurements of the propagated intensity poses an inverse problem, typically addressed in linear approximations by appeal to the transport-of-intensity equation (TIE) [Tea82; Tea83; GRN95; GN96; PN98; Gur+04; Keio5] or the contrast transfer function (CTF) [Tur+04; Gur+06a; Gur+06b].

In the following sections we discuss the most widely used approaches to single-distance and single-measurement phase retrieval. In Sections 2.3.1 and 2.3.2 we discuss linear models based on TIE and CTF, respectively. Section 2.3.3 reviews the linear algorithms of Sections 2.3.1 and 2.3.2 in the context of the phase-attenuation duality which assumes proportionality between attenuation and phase. Section 2.3.4 is concerned with regularisation procedures for phase retrieval.

In the remaining part of this thesis we will omit the subscript ω , indicating the dependence on energy, and introduce the following notation for the sake of better readability:

$$\begin{aligned} I_z(\mathbf{x}_\perp) &\equiv I_\omega(\mathbf{x}_\perp, z), \\ \Psi_z(\mathbf{x}_\perp) &\equiv \Psi_\omega(\mathbf{x}_\perp, z), \\ \phi_z(\mathbf{x}_\perp) &\equiv \phi_\omega(\mathbf{x}_\perp, z), \\ B_z(\mathbf{x}_\perp) &\equiv B_\omega(\mathbf{x}_\perp, z). \end{aligned} \tag{237}$$

where ∇_\perp denotes the transverse two-dimensional gradient operator with $\nabla = (\nabla_\perp, \partial_z)$. From Eq. (234) the wave vector reads as

$$\mathbf{k} = -(\nabla_\perp \phi_0(\mathbf{x}_\perp), k). \tag{235}$$

Assuming the angular deviations $\Delta\alpha$ of the diffracted beam with respect to the incident wave propagating along z to be small (see Fig. 4), it follows from Eqs. (71) and (235) that

$$\Delta\alpha \approx \sin \Delta\alpha = \frac{|\mathbf{k}_\perp|}{k} = \frac{1}{k} |\nabla_\perp \phi_0(\mathbf{x}_\perp)|. \tag{236}$$

2.3.1 Transport of intensity equation

In Section 2.1.5, we derived the paraxial wave equation for a wave field propagating within a static, homogeneous, and non-magnetic medium by virtue of the paraxial approximation. The z -evolution of the envelope of the wave field was found to be governed by

$$(\nabla_{\perp}^2 + 2ik\partial_z) \Psi_z^{(\text{env})}(\mathbf{x}_{\perp}) = 0, \quad (238)$$

where ∇_{\perp} denotes the two-dimensional derivative transverse to the optical axis and $k = \frac{2\pi}{\lambda} = n\frac{\omega}{c}$ with $n = \text{constant}$ and c the speed of light in vacuum. In the following we will omit the superscript (env) for the envelope of the wave field. Rewrite the envelope field in terms of intensity and phase shift as

$$\Psi_z(\mathbf{x}_{\perp}) = \sqrt{I_z(\mathbf{x}_{\perp})} \exp[i\phi_z(\mathbf{x}_{\perp})], \quad (239)$$

and substitute Eq. (239) into Eq. (238). The imaginary part of the resulting equation is called transport-of-intensity equation (TIE). It reads [Tea83; RKT89]

$$k \partial_z I_z(\mathbf{x}_{\perp}) = -\nabla_{\perp} \cdot [I_z(\mathbf{x}_{\perp}) \nabla_{\perp} \phi_z(\mathbf{x}_{\perp})]. \quad (240)$$

Note that Eq. (240) corresponds to a continuity equation of Fresnel theory, see Eq. (86). The corresponding real part is given as

$$2k\partial_z \phi_z(\mathbf{x}_{\perp}) = \frac{\nabla_{\perp}^2 \sqrt{I_z(\mathbf{x}_{\perp})}}{\sqrt{I_z(\mathbf{x}_{\perp})}} - (\nabla_{\perp} \phi_z(\mathbf{x}_{\perp}))^2. \quad (241)$$

Employing TIE for phase retrieval takes into account only an incomplete version of Fresnel theory.

The edge-enhancement regime is defined as the region of small propagation distances where the intensity varies in an approximately linear way in z . For sufficiently small z the derivative on the left-hand side of Eq. (240) can be expressed by a Taylor expansion of $I_z(\mathbf{x}_{\perp})$ in z truncated at linear order. The z -derivative then reduces to the forward difference quotient at first order in z as

$$\partial_z I_z(\mathbf{x}_{\perp}) \approx \frac{I_{z+\Delta z}(\mathbf{x}_{\perp}) - I_z(\mathbf{x}_{\perp})}{\Delta z}. \quad (242)$$

Evaluating Eq. (240) for small values of z and using Eq. (242), we obtain the following relation between the intensity at $z > 0$ and the phase of the exit wave at $z = 0$

$$I_z(\mathbf{x}_{\perp}) = I_0(\mathbf{x}_{\perp}) - \frac{z}{k} \nabla_{\perp} \cdot (I_0(\mathbf{x}_{\perp}) \nabla_{\perp} \phi_0(\mathbf{x}_{\perp})). \quad (243)$$

The actual signal is given by the intensity contrast g_z defined as

$$g_z(\mathbf{x}_{\perp}) \equiv g_{\omega}(\mathbf{x}_{\perp}, z) = \frac{I_z(\mathbf{x}_{\perp})}{I^{(\text{in})}(\mathbf{x}_{\perp})} - 1. \quad (244)$$

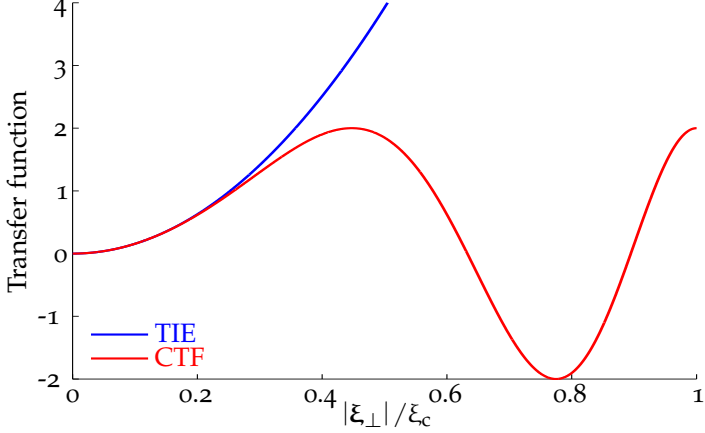


Figure 15: Radial dependence of transfer functions related to Eqs. (249) and (265): $\text{TIE}(x) = 2x$ and $\text{CTF}(x) = 2 \sin x$ with $x = \pi \lambda z \xi_{\perp}^2$. Energy was set to $E = 12.4 \text{ keV}$ ($\lambda = 10^{-10} \text{ m}$), propagation distance to $z = 0.1 \text{ m}$, and pixel size to $\Delta x = 1 \mu\text{m}$. The maximal (cut-off) frequency is given by $\xi_c = (2\Delta x)^{-1}$. Thus $x = \frac{\pi \lambda z}{(2\Delta x)^2} \frac{|\xi_{\perp}|^2}{\xi_c^2} = 2.5\pi \frac{|\xi_{\perp}|^2}{\xi_c^2}$, and CTF encounters two additional zero crossings compared to TIE . See Fig. 16 for the inverted transfer functions.

2.3.1.1 Pure-phase objects

Here we consider a pure-phase object exhibiting a constant attenuation B_0 at the exit plane. The incident field $\Psi^{(\text{in})}$ impinging on the sample is taken to be a plane wave of intensity $I^{(\text{in})} = |\Psi^{(\text{in})}|^2$. For the intensity at the exit plane we have

$$I_0(x_{\perp}) = I^{(\text{in})} \exp(-2B_0) = \text{constant}. \quad (245)$$

In this case, intensity contrast reads

$$g_z(x_{\perp}) = \frac{I_z(x_{\perp})}{I_0(x_{\perp})} - 1, \quad (246)$$

and linearised TIE (243) becomes [Bre52]

$$g_z(x_{\perp}) = -\frac{z}{k} \nabla_{\perp}^2 \phi_0(x_{\perp}). \quad (247)$$

Equation (247) states that out of given phase map at the object exit, intensity contrast emerges at edges of the projected object and strengthens with increasing propagation distance, see Figs. 14 and 17. An algebraic inversion of Eq. (247) is obtained by means of the Fourier derivative theorem (Eq. (A.10)) reading

$$\nabla_{\perp} f(x_{\perp}) = \mathcal{F}^{-1} [-ik_{\perp} \mathcal{F} f(x_{\perp})], \quad (248)$$

which holds for the Fourier transformation as defined in Eq. (A.6). Thus, a solution of the phase-retrieval problem from a single-distance measurement at small z is given by

$$\phi_0(x_{\perp}) = \frac{k}{z} \mathcal{F}^{-1} \left[\frac{\widehat{g}_z(k_{\perp})}{k_{\perp}^2} \right], \quad (249)$$

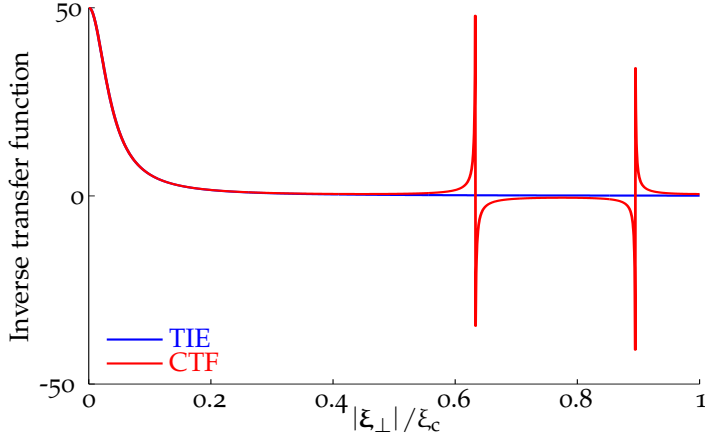


Figure 16: Radial dependence of regularised inverse transfer functions related to Eqs. (249) and (265). See Fig. 15 for the transfer functions itself. Using the regularisation of Eqs. (287) and (294), the regularised inverse transfer functions read $\text{TIE}(x) = \frac{1}{2}(x + \alpha)^{-1}$ and $\text{CTF}(x) = \frac{\text{sgn}(\sin x)}{2|\sin x| + \alpha}$ with $x = \pi\lambda z \xi_{\perp}^2$. Energy was set to $E = 12.4 \text{ keV}$ ($\lambda = 1 \times 10^{-10} \text{ m}$), propagation distance to $z = 0.1 \text{ m}$, pixel size to $\Delta x = 1 \mu\text{m}$, and the regularisation parameter to $\alpha = 10^{-2}$. The maximal (cut-off) frequency is given by $\xi_c = (2\Delta x)^{-1}$. Thus $x = \frac{\pi\lambda z}{(2\Delta x)^2} \frac{|\xi_{\perp}|^2}{\xi_c^2} = 2.5\pi \frac{|\xi_{\perp}|^2}{\xi_c^2}$, and CTF encounters two additional singularities compared to TIE. At $x = 0$, $\text{CTF}(0) = \text{TIE}(0) = \frac{1}{2\alpha}$, implying that regularisation rescales the mean value of the retrieved phase (see also Section 2.3.3.1).

provided that the singularity arising from the denominator at zero frequency is properly regularised, see Section 2.3.4. In the following we will refer to phase retrieval based on Eq. (249) as linearised TIE. Considering the right-hand side of Eq. (249), it becomes evident that the inversion of the Laplacian acts as a low-pass filter on the intensity data suppressing high frequencies with a factor k_{\perp}^{-2} , see Figs. 15 and 16 where transfer functions and their regularised inverse functions are plotted. This is why linearised TIE phase retrieval performs robust and is applicable even beyond the edge-enhancement regime though at the expense of spatial resolution. This will be analysed in more detail in Section 4.2.1. A numerically fast and efficient implementation is provided by Eq. (249) using fast FFT algorithms.

Equation (247) was derived in several contexts [Nug+96; Pago06] and can also be obtained from the Fresnel diffraction integral as in [Broo2]. Therefore we consider the Taylor expansion of the exponential in the Fourier-space version of the Fresnel propagator truncated at quadratic order in k_{\perp} as

$$\begin{aligned} (\mathcal{F}\mathcal{P}_F)(k_{\perp}, z) &= \frac{\exp(ikz)}{2\pi} \exp\left(-\frac{iz}{2k} k_{\perp}^2\right) \\ &\approx \frac{\exp(ikz)}{2\pi} \left(1 - \frac{iz}{2k} k_{\perp}^2\right). \end{aligned} \quad (250)$$

By insertion of Eq. (250) into the Fourier representation of the Fresnel diffraction integral (Eq. (93)) and using the Fourier derivative theorem (Eq. (248)), the intensity follows as

$$\begin{aligned} I_z(\mathbf{x}_\perp) &= |2\pi \mathcal{F}^{-1} [\mathcal{P}_F \cdot \mathcal{F} \Psi_0]|^2 \\ &= \left| \left(1 + \frac{iz}{2k} \mathcal{F}^{-1}(ik_\perp)^2 \mathcal{F} \right) \Psi_0 \right|^2 \\ &= \left| \left(1 + \frac{iz}{2k} \nabla_\perp^2 \right) \Psi_0 \right|^2. \end{aligned} \quad (251)$$

To continue we evaluate the Laplacian as

$$\nabla_\perp^2 \Psi_0 = [i(\nabla_\perp^2 \phi_0) - (\nabla_\perp \phi_0)^2] \Psi_0, \quad (252)$$

and the modulus in Eq. (251) as

$$\begin{aligned} I_z(\mathbf{x}_\perp) &= \left| \left(1 + \frac{iz}{2k} \nabla_\perp^2 \right) \Psi_0 \right|^2 \\ &= I_0 \left[1 - 2 \frac{z}{2k} \nabla_\perp^2 \phi_0 + \left(\frac{z}{2k} \nabla_\perp^2 \phi_0 \right)^2 + \left(\frac{z}{2k} \right)^2 (\nabla_\perp \phi_0)^4 \right] \\ &= I_0 \left[1 - \frac{z}{k} \nabla_\perp^2 \phi_0 + \mathcal{O}(\phi_0^2) \right]. \end{aligned} \quad (253)$$

Thus, to linear order in ϕ_0 , linearised TIE (247) is recovered.

Let us consider the validity regime of Eq. (247). For the truncation in Eq. (250) to be valid, higher orders in the power-series expansion of the exponential in Eq. (250) must be negligible. The following condition must then be satisfied for all accessible values of k_\perp :

$$1 \gg \left| \frac{1}{2} \frac{z}{2k} k_\perp^2 \right|. \quad (254)$$

An upper limit of the transverse spatial frequency is set by the linear size Δx of the detector pixels to $|k_\perp| \leq \left| \frac{2\pi}{2\Delta x} \right|$. Thus condition (254) reads

$$1 \gg \frac{\lambda z \pi}{8(\Delta x)^2}. \quad (255)$$

In a typical imaging experiment using propagation-based phase contrast at an energy of $E = 20$ keV with a pixel size of $\Delta x = 1 \times 10^{-6}$ m and a moderate sample-to-detector distance of $z = 0.1$ m, the right-hand side of (255) already assumes a value of 2.4. Strictly speaking, the validity of linearised TIE is limited to the very near field regime of Fresnel theory. At the expense of an ever decreasing spatial resolution, phase retrieval based on Eq. (247) is applicable beyond the validity of Eq. (255) owing to its low-pass filter characteristic. Even though linearised TIE is applicable at large phase shifts, the retrieved phase over- or underestimates the exact phase, see Figs. 31 and 32. How to overcome this mismatch using a perturbative approach is subject of Section 4.1.

Within the edge-enhancement regime, where the validity of linearised TIE (247) is assured and appropriately models the recorded data, the signal strength is typically low since intensity contrast rises linearly with z , see Figs. 17 and 33(a). Thus, if we cannot afford long exposure times to acquire data of an acceptable signal-to-noise ratio (SNR), we opt for larger propagation distances to enhance the signal and thus SNR. Then, however, the low-pass filtering behaviour, inherent to the inversion of linearised TIE, impedes phase retrieval at a high spatial resolution. To do so we appeal to approaches based on the CTF relation, which will be discussed in the following section.

2.3.2 Contrast transfer function

An alternative approach to TIE related phase retrieval is based on contrast transfer functions (CTFs) which are closely related to transfers functions encountered in optical and electron microscopy [Str85; Kir98]. In Fourier space, CTF represents a local and linear relation between phase shift and attenuation at the object-exit plane and the propagated intensity contrast. An important relation, valid in Fresnel theory, states that the Fourier transformed intensity can be written as the Fourier transform of a two-point autocorrelation of the exit wave field (transmission function) [Gui77; Gui78; Pap74]. The CTF expression is derived from this relation by an expansion of the transmission functions truncated at linear order in the attenuation and in relative phase variations. To derive the autocorrelation relation, the convolution form of the Fresnel diffraction integral is used twice to evaluate the intensity as follows

$$\begin{aligned} \hat{I}(\mathbf{k}_\perp) &\equiv (\mathcal{F} I)(\mathbf{k}_\perp) \\ &= \mathcal{F}[\Psi_z(\mathbf{x}_\perp)\Psi_z^*(\mathbf{x}_\perp)] \\ &= \mathcal{F}[(\mathcal{P}_F \ast \ast \Psi_0)(\mathcal{P}_F^* \ast \ast \Psi_0^*)] \\ &= \mathcal{F}\left[\int d^2\mathbf{x}'_\perp \int d^2\mathbf{x}''_\perp \Psi_0(\mathbf{x}'_\perp)\Psi_0^*(\mathbf{x}''_\perp)\mathcal{P}_F(\mathbf{x}_\perp - \mathbf{x}'_\perp)\mathcal{P}_F^*(\mathbf{x}_\perp - \mathbf{x}''_\perp)\right]. \end{aligned} \quad (256)$$

As the Fourier transformation only affects the propagators in the last line of Eq. (256), it can be evaluated yielding a (two-dimensional) Dirac delta distribution (Eq. (A.13)) as

$$\begin{aligned} &\mathcal{F}[\mathcal{P}_F(\mathbf{x}_\perp - \mathbf{x}'_\perp)\mathcal{P}_F^*(\mathbf{x}_\perp - \mathbf{x}''_\perp)] \\ &= \frac{2\pi}{(\lambda z)^2} \exp\left[\frac{i\pi}{\lambda z}(\mathbf{x}'_\perp'^2 - \mathbf{x}''_\perp'^2)\right] \delta^2\left(\mathbf{k}_\perp + \frac{2\pi}{\lambda z}(\mathbf{x}'_\perp - \mathbf{x}''_\perp)\right) \\ &= \frac{1}{2\pi} \exp\left[\frac{i\pi}{\lambda z}(\mathbf{x}'_\perp'^2 - \mathbf{x}''_\perp'^2)\right] \delta^2\left(\mathbf{x}'_\perp - \mathbf{x}''_\perp + \frac{\lambda z}{2\pi}\mathbf{k}_\perp\right), \end{aligned} \quad (257)$$

where we have used the scaling property of the Dirac delta distribution, see Eq. (A.4). To proceed, Eq. (257) is substituted into Eq. (256)

and the integration over \mathbf{x}'_\perp is performed. The remaining integration variable is shifted by $\mathbf{x}''_\perp = \mathbf{x}_\perp + \frac{\lambda z}{4\pi} \mathbf{k}_\perp$ yielding the Fourier transform of the two-point autocorrelation of Ψ_0 . Thus we arrive at the final result

$$\hat{I}_z(\mathbf{k}_\perp) = \frac{1}{2\pi} \int d^2\mathbf{x}_\perp e^{-i\mathbf{x}_\perp \cdot \mathbf{k}_\perp} \Psi_0 \left(\mathbf{x}_\perp - \frac{z}{2k} \mathbf{k}_\perp \right) \Psi_0^* \left(\mathbf{x}_\perp + \frac{z}{2k} \mathbf{k}_\perp \right). \quad (258)$$

In statistical mechanics, the right-hand side of Eq. (258) is known as Wigner distribution function introduced to account for quantum mechanical corrections to the thermodynamic equilibrium [Wig32]. Equation (258) is also closely related to the ambiguity function in Fourier optics [Pap74; Gui78]. Note that Eq. (258) is valid in the case of perfect spatial coherence only. In the situation of partial coherence the product $\Psi_0 \Psi_0^*$ has to be substituted by the ensemble average quantity $\langle \Psi_0 \Psi_0^* \rangle_e$, see Eq. (147) and Section 2.1.8. Employing the Fourier transform defined in ordinary instead of angular frequencies $\xi_\perp = \frac{\mathbf{k}_\perp}{2\pi}$, Eq. (258) reads

$$\hat{I}_z(\xi_\perp) = \int d^2\mathbf{x}_\perp e^{-i2\pi\mathbf{x}_\perp \cdot \xi_\perp} \Psi_0 \left(\mathbf{x}_\perp - \frac{\lambda z}{2} \xi_\perp \right) \Psi_0^* \left(\mathbf{x}_\perp + \frac{\lambda z}{2} \xi_\perp \right), \quad (259)$$

where we have used $k = \frac{2\pi}{\lambda}$. Considering the right-hand side of Eq. (259) it becomes clear that intensity contrast emerges due to the interference of points in the exit wave field which are separated by a distance $\lambda z |\xi_\perp|$ growing linearly in z . With increasing z small object scales such as fine-structure edges increasingly contribute to the propagated intensity pattern in terms of a multiplicity of fringes, see Fig. 17 for the z -evolution of such a fringe pattern. Note that Eq. (259) is tied to the full Fresnel theory. The Fraunhofer limit of the paraxial approximation would yield a different relation between Ψ_0 and \hat{I}_z , see Section 2.1.5.1.

2.3.2.1 Weakly varying phase and weak absorption

In the limit of small relative phase variations and a small attenuation, Eq. (258) simplifies to yield the linear CTF relation. The validity of this approximation is guaranteed when the following conditions for relative phase variations and attenuation of the exit wave are satisfied for all admissible values of \mathbf{x}_\perp and ξ_\perp :

$$|\delta\phi_0| \equiv \left| \phi_0 \left(\mathbf{x}_\perp - \frac{\lambda z}{2} \xi_\perp \right) - \phi_0 \left(\mathbf{x}_\perp + \frac{\lambda z}{2} \xi_\perp \right) \right| \ll 1 \quad (260)$$

and

$$B_0(\mathbf{x}_\perp) \ll 1. \quad (261)$$

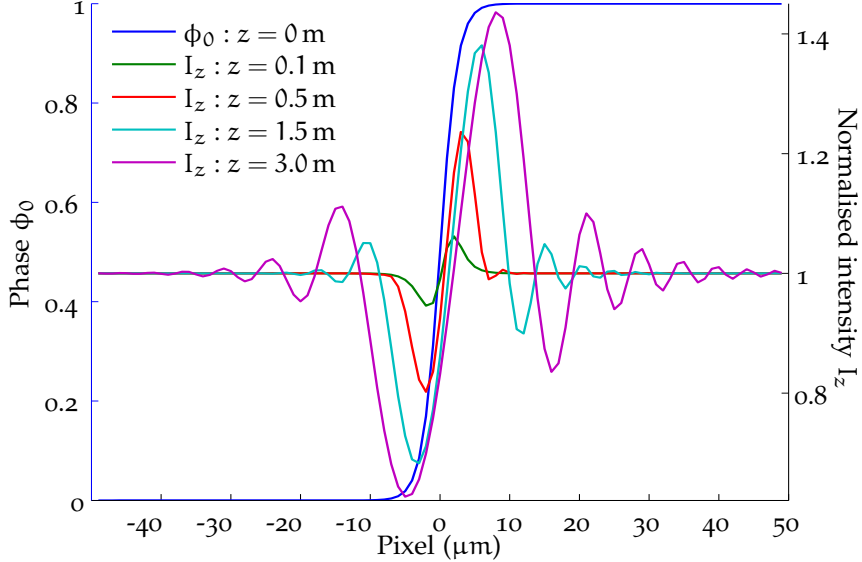


Figure 17: Evolution of fringes in the intensity contrast from an edge-like phase object in simulated forward propagation. Energy was set to $E = 20 \text{ keV}$ ($\lambda = 6.12 \times 10^{-11} \text{ m}$) and the pixel size to $\Delta x = 1 \mu\text{m}$. The edge profile of the exit phase was modelled using a Fermi-Dirac distribution $\phi_0(x) = (1 + \exp(-kx))^{-1}$ with $k = 0.975 \times \Delta x$. In the edge-enhancement regime, a first intensity fringe emerges out of a homogeneous background, the profile of which is given by the Laplacian of the phase. In the far near field, the distance between the fringe minima and maxima nearest to the phase edge increases with $\sqrt{\lambda z}$. Analogue to the irradiation of an electromagnetic disturbance in the far field, fringe modulations decouple from the emitter (edge profile) and the distance between fringes is given by $\sqrt{\lambda z}$, involving the only scales available. In the edge-enhancement regime at small z , average signal modulus $\bar{g}_z \equiv \langle |g_z| \rangle$ (see Eq. (355)) rises linearly with z . This is due to the linear gain of the local signal at edges of the projected object as $g_z \propto z \nabla_\perp^2 \phi_0$. For large z the signal rise slows down to \sqrt{z} and the increase of average signal modulus \bar{g}_z is predominantly due to the multiplicity of fringes at edges of the projected object.

While x_\perp takes on all values within the field of view, the transverse frequency vector is limited by the effective detector pixel size to $|\xi_\perp| \leq \xi_c = \frac{1}{2\Delta x}$ in the case of perfect transverse spatial coherence. In the case of insufficient transverse coherence ensuing a blurring of image points by the linear scale b (intercept theorem), the transverse frequency is limited approximately by $\xi_\perp \leq \xi_b \approx \frac{1}{b}$, see Section 2.1.8.6.

Equations (260) and (261) are referred to as CTF criteria. Upon substituting $\Psi_0 = \sqrt{I_0} \exp(i\phi) = \exp(-B_0 + i\phi_0)$ into Eq. (259) and truncating the power-series expansion of the exponential at linear order in $\delta\phi_0$ and $B_0(x_\perp - \frac{\pi z}{k} \xi_\perp) + B_0(x_\perp + \frac{\pi z}{k} \xi_\perp)$, we arrive at the CTF formula in Fourier space

$$\hat{g}_z(\xi_\perp) = 2\hat{\phi}_0(\xi_\perp) \sin(\pi\lambda z \xi_\perp^2) - 2\hat{B}_0(\xi_\perp) \cos(\pi\lambda z \xi_\perp^2). \quad (262)$$

Using g_z , the Dirac delta distribution arising from the zeroth order in the expansion of the exponential in Eq. (259) is absorbed into \hat{g}_z .

2.3.2.2 Pure-phase objects

Considering the case of pure-phase objects Eq. (262) reduces to

$$\hat{g}_z(\xi_{\perp}) = 2\hat{\phi}_0(\xi_{\perp}) \sin(\pi\lambda z \xi_{\perp}^2). \quad (263)$$

Truncating the power-series expansion of the sine function in Eq. (263) at linear order, one recovers linearised TIE (247) in Fourier space

$$\hat{g}_z(\xi_{\perp}) = 2\pi\lambda z \xi_{\perp}^2 \hat{\phi}_0(\xi_{\perp}). \quad (264)$$

Equation (263) provides an algebraic solution of the phase-retrieval problem as

$$\phi_0(x_{\perp}) = \mathcal{F}^{-1} [\hat{\phi}_0(\xi_{\perp})] = \frac{1}{2} \mathcal{F}^{-1} \left[\frac{\hat{g}_z(\xi_{\perp})}{\sin(\pi\lambda z \xi_{\perp}^2)} \right], \quad (265)$$

provided that singularities in Eq. (265), originating from zero crossings of the sine function, are regularised, see Section 2.3.4. When higher powers of $\delta\phi_0$ in the expansion of the exponential in Eq. (259) are taken into account, an algebraic inversion in the sense of Eq. (265) no longer is possible. This is because in Fourier space quadratic and higher orders enter in a highly non-local way, see Eq. (350) for an expansion of \hat{g}_z up to quadratic order in Ψ_0 and neglecting absorption.

Employing the Fourier derivative theorem (Eq. (248)) in the power expansion of the sine function in Eq. (263), the position-space version of CTF is obtained as

$$g_z(x_{\perp}) = -2 \left[\sum_{m=1}^{\infty} \frac{1}{(2m-1)!} \left(\frac{z}{2k} \right)^{2m-1} (\nabla_{\perp}^2)^{2m-1} \right] \phi_0(x_{\perp}). \quad (266)$$

Linearised TIE (247) in position space is recovered from Eq. (266) by a truncation at linear order in z .

Common to both linearised TIE and CTF approaches is that low frequencies of pure-phase objects are poorly retrieved. This is because the coefficients (transfer functions) of the Fourier transform $\hat{\phi}_0$ in Eqs. (263) and (264) vanish at zero frequencies, see Fig. 15 where transfer functions for linearised TIE and CTF are plotted.

The existence of zero crossings in the transfer function can be understood as a loss of information at the corresponding frequencies in the Fourier domain. This loss, however, is localised to small regions about the zero crossings of the transfer function, see Figs. 15 and 16. Thus, for objects void of long-range order and exhibiting a democratic distribution of frequencies in Fourier space, the loss of information is in general negligible. Such an object (Lena test pattern) and its Fourier transform are depicted in Fig. 18.

Single-distance phase retrieval based on CTF is considered and successfully applied in [Tur+04; Gur+06a; Gur+06b]. In [Tur+04] an extended regime of validity for the linear CTF and TIE expression is explored. There, the projected thickness for a homogeneous object with weak absorption and large, but slowly varying phase shift is correctly retrieved from a single-distance radiograph using CTF. TIE retrieval is found to be valid only at lower frequencies. In [Gur+06a; Gur+06b] the combination of a TIE- and CTF-based approaches, both linear in the exit phase and the propagated intensity, is discussed. The combined approach appeals to a multiplicative separation of a slowly varying factor from a small factor in the transmission function. Another mixed approach between TIE and CTF is presented and applied in [WLo4; Gur+04; Lan+08].

Algebraic approaches to the phase retrieval problem, stemming from electron microscopy, are presented in [Kir98; BDC96; Clo99]. Here, CTF or linearised TIE is used to overdetermine B_0 and ϕ_0 by performing intensity measurements at several distances z_i . The zeros of the sine functions at non-vanishing frequencies in the pure-phase CTF relation are regularised by a summation over appropriately chosen values of z_i such that the sum $\sum_i \sin(\pi\lambda z_i \xi_\perp^2)$ remains well above zero for frequencies below the maximum frequency $\xi_c = \frac{1}{2\Delta x}$. This approach yields remarkably accurate results with non-linear effects taken into account iteratively. An iterative, single-distance approach, void of additional constraints on phase or attenuation, is presented in [Ruh+14]. Here, by a coupling of phase retrieval and tomographic reconstruction correlations in different tomographic projections are exploited (data redundancy), thus facilitating the three-dimensional reconstruction of the refractive index.

2.3.3 Phase-attenuation duality

In single-distance phase retrieval, an absorptive contribution to the intensity contrast can be accounted for assuming a global duality between attenuation and phase. While phase shifts in the exit wave arise from coherent scattering (Thomson scattering, see Section 2.2.1), attenuation is due to photoelectric absorption, coherent scattering (photons scattered away from the field of view), or incoherent scattering (Compton scattering, see Section 2.2.1). In [WLY05] it was found upon investigation of the corresponding cross sections, that the attenuation cross section is dominated by the contribution from incoherent (Compton) scattering for soft tissues composed of light elements with atomic numbers $Z < 10$ and X-ray energies ranging from 60 keV to 500 keV. Light-matter interactions are thus dominated by quasi-free



(a) Lena test image.

(b) Modulus of the Fourier transformed Lena image.

Figure 18: The Lena standard test pattern exhibiting a democratic distribution of spatial frequencies. (a) The Lena image contains fine details, flat regions, shading, and texture. Therefore it is well apt as a standard test pattern. (b) The modulus of the Fourier transform of the Lena image exhibits a democratic distribution of spatial frequencies. The Lena image was padded symmetrically in both dimensions in order to provide symmetric boundary conditions for the discrete Fourier transform. As a consequence, truncation rods are not present in (b) which would otherwise appear in the Fourier transformed image along the ξ_x - and ξ_y -axis due to discontinuities at the border of the input image.

valence electrons. As a consequence the intensity of the exit wave field is approximately given by

$$\begin{aligned} I_0(\mathbf{x}_\perp) &= |\Psi_0|^2(\mathbf{x}_\perp) \\ &= I^{(in)} \exp(-2B_0(\mathbf{x}_\perp)) \\ &= I^{(in)} \exp \left[-\sigma_{KN} \int dz \rho_e(\mathbf{r}) \right], \end{aligned} \quad (267)$$

where ρ_e denotes the electron density and σ_{KN} the total Compton cross section according to the Klein-Nishina Equation (228). Away from absorption edges the phase shift of the exit wave is related to the electron density via Eq. (118) and Eq. (207) as

$$\phi_0(\mathbf{x}_\perp) = -\lambda r_e \int dz \rho_e(\mathbf{r}), \quad (268)$$

where r_e is the classical electron radius (Thomson scattering length), see Eqs. (205) and (213). Since both Eqs. (267) and (268) involve the projected electron density, phase and attenuation can be calculated from a single intensity measurement. Utilising the phase-attenuation duality, the following expression was obtained in [WLY05] from the Fresnel diffraction integral for small Fresnel propagator phases

$$\phi(\mathbf{x}_\perp) = -\frac{\lambda r_e}{\sigma_{KN}} B(\mathbf{x}_\perp) = \frac{\lambda r_e}{\sigma_{KN}} \ln \left[\mathcal{F}^{-1} \frac{\mathcal{F} I(\mathbf{x}_\perp, z)/I^{(in)}}{1 + \frac{\lambda^2 r_e z}{2\pi\sigma_{KN}} \mathbf{k}_\perp} \right]. \quad (269)$$

Here the definition of Fourier transform as in Eq. (A.6) applies. Note that due to the truncation of the power-series expansion of exponential in the Fresnel propagator (Eq. (250)), Eq. (269) is only valid for small object-detector distances or low spatial resolution (small pixel sizes).

The high phase sensitivity of hard X-rays for soft tissues manifests as a large ratio of $\frac{\lambda r_e}{\sigma_{KN}}$. E.g. for soft tissues and X-ray energies below 150 keV and above 60 keV, this ratio is $\frac{\lambda r_e}{\sigma_{KN}} \approx 10^3$ to 10^4 [WLY05; WYo9]. In [WYo9] a more general formula between exit phase and intensity, valid also for large propagation distances and high spatial resolution, was found, provided that $\frac{\sigma_{KN}}{\lambda r_e} \approx 10^{-3}$.

In [Pag+02] an expression identical to Eq. (269) was obtained from TIE for a homogeneous object consisting of a single material only. In this case the projected electron density of Eqs. (267) and (268) translates into a function of the projected thickness for the sample. Then, the same expression as in Eq. (269) applies, when the following substitution is performed

$$\frac{\lambda r_e}{\sigma_{KN}} \rightarrow \frac{2\pi \delta_\omega}{\lambda \mu_\omega}. \quad (270)$$

At a given X-ray energy, this requires the knowledge of the constant of proportionality $\frac{\delta_\omega}{\mu_\omega}$. In principle, ϵ can be extracted from a two-distance measurement of the propagated intensity [Che+11].

For a more local approach to phase-attenuation duality in the case of multi-material and heterogeneous objects see [Lan+12; Lan+14].

Let us now consider the implications for single-distance CTF phase retrieval under the assumption of phase-attenuation duality. Recall CTF relation (262), valid for weakly varying phase shifts and small absorption. In Fourier space it reads as

$$\hat{g}_z(\xi_\perp) = 2\hat{\phi}_0(\xi_\perp) \sin(\pi\lambda z \xi_\perp^2) - 2\hat{B}_0(\xi_\perp) \cos(\pi\lambda z \xi_\perp^2). \quad (271)$$

For very hard X-ray energies or chemically homogeneous samples, we may assume the attenuation to be linearly proportional to the phase shift

$$B_0 = -\epsilon \phi_0. \quad (272)$$

The minus sign appears in Eq. (272) because we have defined the phase shift as the line integral of the negative real decrement of the refractive index, see Eq. (118). By virtue of Eq. (272), Eq. (271) simplifies as

$$\begin{aligned} \hat{g}_z(\xi_\perp) &= 2(\sin(\pi\lambda z \xi_\perp^2) + \epsilon \cos(\pi\lambda z \xi_\perp^2)) \hat{\phi}_0(\xi_\perp) \\ &= 2\sqrt{1+\epsilon^2} \sin(\pi\lambda z \xi_\perp^2 + \arctan \epsilon) \hat{\phi}_0(\xi_\perp). \end{aligned} \quad (273)$$

As ϵ increases the sine function in the last line of Eq. (273) is shifted to the left. For $\epsilon \ll 1$ and $m \geq 1$, the zeros of the shifted sine are

$$|\xi_\perp|_m = \sqrt{\frac{m}{\lambda z}} \sqrt{1 - \frac{\epsilon}{m\pi}} \approx \sqrt{\frac{m}{\lambda z}} \left(1 - \frac{\epsilon}{2m\pi}\right). \quad (274)$$

The double zero of $\hat{g}_z(\xi_{\perp})$ at $|\xi_{\perp}|_0 = 0$ in the case of $B_0 = 0$ splits into two single zeros at $|\xi_{\perp}|_0 = \pm \frac{i\epsilon}{\pi\lambda z}$ for finite values of B_0 and the presence of an associated pole in the retrieved phase is prevented by absorptive effects. Thus, for vanishing spatial frequencies, the shift inducing term $\arctan \epsilon$ can be considered as a regularisation parameter since it renders the sine function finite at $\xi_{\perp} = 0$. If the constant of proportionality ϵ assumes appropriate values, the phase-attenuation duality renders a regularisation at vanishing frequencies obsolete.

For small arguments of the trigonometric functions in Eq. (271) and assuming duality, the TIE equivalent to Eq. (273) is obtained as

$$\hat{g}_z(\xi_{\perp}) = 2(\pi\lambda z\xi_{\perp}^2 + \epsilon) \hat{\phi}_0(\xi_{\perp}). \quad (275)$$

Contrast transfer is thus rendered finite at $\xi_{\perp} = 0$ due to the presence of the terms involving $\arctan \epsilon$ and ϵ in Eqs. (273) and (275), respectively, and large scales may occur in the intensity in contrast to the pure-phase case.

2.3.3.1 Mean phase

As was seen on the basis of Eq. (102), a phase retrieved in Fresnel theory is defined only modulo a global phase offset. Here, we analyse this behaviour in the context of a global phase-attenuation duality. Therefore, we split physical phase and attenuation of the exit wave into a mean value and a fluctuating part of zero transverse mean as

$$\begin{aligned} \phi_0 &= \langle \phi_0 \rangle + \delta\phi_0, \\ B_0 &= \langle B_0 \rangle + \delta B_0, \end{aligned} \quad (276)$$

with $\langle \delta\phi \rangle = 0$, $\langle \delta B \rangle = 0$, and $\langle f \rangle$ demanding the transverse average of function f over the field of view (FOV) as

$$\langle f(\mathbf{x}_{\perp}) \rangle \equiv \frac{\int_{\text{FOV}} d^2\mathbf{x}_{\perp} f(\mathbf{x}_{\perp})}{\int_{\text{FOV}} d^2\mathbf{x}_{\perp}}. \quad (277)$$

A constant phase offset $\langle \phi_0 \rangle$ renders the forward propagated intensity unchanged according to Eq. (102), unless the phase-attenuation duality of Eq. (272) is assumed. In this case $\langle \phi_0 \rangle$ rescales the intensity as

$$\begin{aligned} I_z(\phi_0, B_0) &= \exp(-2\langle B_0 \rangle) I_z(\delta\phi_0, \delta B_0) \\ &= \exp(2\epsilon \langle \phi_0 \rangle) I_z(\delta\phi_0, \delta B_0) \\ &\equiv \exp(2\epsilon \langle \phi_0 \rangle) I_z^{(\text{fluct})}. \end{aligned} \quad (278)$$

Here, $I_z^{(\text{fluct})}$ represents intensity that would emerge from $\delta\phi_0$ alone. Thus we have

$$\begin{aligned} g_z &= \exp(2\epsilon \langle \phi_0 \rangle) \frac{I_z^{(\text{fluct})}}{I^{(\text{in})}} - 1 \\ &= \exp(2\epsilon \langle \phi_0 \rangle) g_z^{(\text{fluct})} - 1 + \exp(2\epsilon \langle \phi_0 \rangle), \end{aligned} \quad (279)$$

where $g_z^{(\text{fluct})}$ denotes the intensity contrast emerging from $\delta\phi_0$ alone,

$$g_z^{(\text{fluct})} \equiv \frac{I_z^{(\text{fluct})}}{I^{(\text{in})}} - 1 . \quad (280)$$

For small variations of the absorptive factor in the exit wave, $\delta B_0 \ll 1$ or $\epsilon \ll 1$, we have

$$\begin{aligned} \langle \exp(-2\delta B_0) \rangle &= \langle \exp(2\epsilon\delta B_0) \rangle = \langle 1 - 2\delta B_0 + \mathcal{O}((\delta B_0)^2) \rangle \\ &\approx (1 - 2\langle \delta B_0 \rangle) \\ &= 1 . \end{aligned} \quad (281)$$

Thus, $\delta\phi_0$ does not reduce the mean intensity. The conservation of mean intensity in free-space propagation (see discussion to Eq. (86) in Section 2.1.5) implies that $\langle I_z \rangle = \langle I_0 \rangle$ or $\langle g_z \rangle = \langle g_0 \rangle$. From this, Eqs. (278) and (281), and assuming plane wave incidence, it follows that the mean intensity of the propagated wave field is determined by the offset $\langle B_0 \rangle = -\epsilon \langle \phi_0 \rangle$ as

$$\begin{aligned} \langle I_z(\phi_0, B_0) \rangle &= \langle I_{z=0}(\phi_0, B_0) \rangle \\ &= \langle \exp(-2\langle B_0 \rangle) I_0(\delta\phi_0, \delta B_0) \rangle \\ &= \exp(-2\langle B_0 \rangle) \langle I_0(\delta\phi_0, \delta B_0) \rangle \\ &= \exp(-2\langle B_0 \rangle) \langle I^{(\text{in})} \exp(-2\delta B_0) \rangle \\ &= \exp(-2\langle B_0 \rangle) I^{(\text{in})} \langle \exp(-2\delta B_0) \rangle \\ &\approx \exp(-2\langle B_0 \rangle) I^{(\text{in})} \\ &= \exp(2\epsilon \langle \phi_0 \rangle) I^{(\text{in})} . \end{aligned} \quad (282)$$

Assuming duality and small variations of B_0 , the phase offset is then recovered from the mean value of the intensity if the duality factor of proportionality is known a priori as

$$\begin{aligned} \langle \phi_0 \rangle &= \frac{1}{2\epsilon} \ln \left\langle \frac{I_z}{I^{(\text{in})}} \right\rangle \\ &= \frac{1}{2\epsilon} \ln(1 + \langle g_z \rangle) . \end{aligned} \quad (283)$$

In practice, the average phase is obtained from Eq. (283) and $\delta\phi_0$ can be retrieved according to Eq. (273) upon substitutions $g_z \rightarrow g_z^{(\text{fluct})}$ and $\phi_0 \rightarrow \delta\phi_0^{(\text{fluct})}$.

2.3.4 Regularisation in phase retrieval

In Sections 2.3.1.1 and 2.3.2.2 we have seen that upon an algebraic inversion of CTF and linearised TIE for pure-phase objects, singularities are encountered due to zeros in the denominator in Eqs. (249) and (265). While the double pole at zero frequency is common to

both, pure-phase CTF retrieval encounters additional singularities at non-vanishing frequencies. Thus a numerical implementation of Eqs. (249) and (265) requires a regularisation of these singularities.

Let Δx be the linear pixel size and L the linear extend of the field of view of a square detector. Then the number of pixels in a row (or column) reads $N = \frac{L}{\Delta x}$. Regarding a discrete implementation, we write the transverse position-space vector as $\mathbf{x}_\perp = \Delta x \mathbf{x}'_\perp$ and the corresponding conjugate frequency vector related to the Fourier transform as defined in Eq. (A.18) as $\xi_\perp = \frac{\xi'_\perp}{\Delta x}$. The admissible transverse frequency range is limited by half of the effective size of a detector pixel. We define the cut-off frequency as

$$\xi_c \equiv \frac{\xi'_{\perp,c}}{\Delta x} = \frac{1}{2\Delta x} \quad (284)$$

Then, the components of the dimensionless spatial frequency vector ξ'_\perp take on following numerical values

$$\xi'_i \equiv (\xi'_\perp)_i = \left\{ -\frac{1}{2} + \frac{1}{N}, -\frac{1}{2} + \frac{2}{N}, \dots, \frac{1}{2} - \frac{1}{N}, \frac{1}{2} \right\}, \quad (285)$$

with $i = x, y$. For pure-phase objects the sine function in the CTF relation has a zero crossing at $\xi_\perp = 0$, independent of experimental parameters E , z , and Δx . Additional zero crossings occur at

$$|\xi_\perp| = |\xi_\perp|_m \equiv \sqrt{\frac{m}{\lambda z}}, \quad m \in \mathbb{N} \mid m \leq \frac{\lambda z}{4(\Delta x)^2}. \quad (286)$$

The double pole at vanishing frequency appearing in the algebraic Fourier inversion of CTF can be treated along the lines of the TIE case. Singularities arising at finite frequencies require a different regularisation due the change of sign at the zero crossings of the sine function.

Let us first consider the singularity at $\xi_\perp = 0$. A widely used pragmatic approach is to simply let

$$\frac{1}{\pi \lambda z \xi_\perp^2} \rightarrow \frac{1}{\pi \lambda z \xi_\perp^2 + \alpha}, \quad (287)$$

where α is a real constant. If the regularisation parameter is chosen too large, such that $\pi \lambda z \xi_\perp^2 + \alpha \approx \alpha$, phase retrieval using prescription (287) simply restores a rescaled version of the data as

$$\begin{aligned} \phi_0(\mathbf{x}_\perp) &= \frac{1}{2} \mathcal{F}^{-1} \left[\frac{\hat{g}_z(\xi_\perp)}{\pi \lambda z \xi_\perp^2 + \alpha} \right] \\ &\approx \frac{1}{2} \mathcal{F}^{-1} \left[\frac{\hat{g}_z(\xi_\perp)}{\alpha} \right] \\ &= \frac{1}{2\alpha} g_z. \end{aligned} \quad (288)$$

On the other hand, for decreasing values of α , low frequencies (large spatial scales) in g_z start to dominate the retrieved phase. As soon

as α drops below the numerical precision, the sole Fourier component that remains to contribute to the phase after the algebraic inversion is $\hat{g}_z(0) \propto \langle g_z \rangle$. The retrieved phase then essentially represents a rescaled version of the mean of g_z over the transverse plane. Thus, optimal phase retrieval requires an optimal choice of α , which is not known a priori. Demanding that the retrieved phase to be insensitive to a variation of α fixes the value of α . For simulated pure-phase-contrast data an independence of the retrieved phase with respect to the regularisation parameter is observed over several order of magnitude of α , which is thus chosen within this range. However, this prescription breaks down in the case of real data. There the intensity is contaminated by absorptive (and other) contributions originating from the sample itself, the sample container, or from features along the optical path (Beryllium window, monochromator). The latter distort the intensity image recorded with and without sample (flat field), see Figs. 25 and 26.

From the Fourier derivative theorem Eq. (A.10), we have

$$\nabla_{\perp}^2 f(\mathbf{x}_{\perp}) = \mathcal{F}^{-1} [(-i\mathbf{k}_{\perp})^2 \mathcal{F} f(\mathbf{x}_{\perp})] . \quad (289)$$

We define the regularised version of the inverse derivative operator ∇_{\perp}^{-2} as

$$\nabla_{\perp,\alpha}^{-2} f(\mathbf{x}_{\perp}) = \mathcal{F}^{-1} \left[\frac{-1}{\mathbf{k}_{\perp}^2 + \alpha} \mathcal{F} f(\mathbf{x}_{\perp}) \right] . \quad (290)$$

Using Eq. (290) we can show that the mean value of the regularised inverse Laplacian acting on a function f results in a rescaling of f as

$$\begin{aligned} \langle \nabla_{\perp,\alpha}^{-2} f(\mathbf{x}_{\perp}) \rangle &= \mathcal{F}^{-1} \left[\frac{-1}{\mathbf{k}_{\perp}^2 + \alpha} \mathcal{F} f(\mathbf{x}_{\perp}) \right] \\ &= \frac{1}{4\pi^2 A_{\text{FOV}}} \int_{\text{FOV}} d^2 \mathbf{x}_{\perp} \int d^2 \mathbf{k}_{\perp} e^{-i\mathbf{k}_{\perp} \cdot \mathbf{x}_{\perp}} \frac{-1}{\mathbf{k}_{\perp}^2 + \alpha} \int d^2 \mathbf{x}'_{\perp} e^{i\mathbf{k}_{\perp} \cdot \mathbf{x}'_{\perp}} f(\mathbf{x}'_{\perp}) \\ &= \frac{-1}{4\pi^2 A_{\text{FOV}}} \int d^2 \mathbf{x}'_{\perp} \int d^2 \mathbf{k}_{\perp} e^{i\mathbf{k}_{\perp} \cdot \mathbf{x}'_{\perp}} \frac{f(\mathbf{x}'_{\perp})}{\mathbf{k}_{\perp}^2 + \alpha} \int_{\text{FOV}} d^2 \mathbf{x}_{\perp} e^{-i\mathbf{k}_{\perp} \cdot \mathbf{x}_{\perp}} \\ &= \frac{-1}{A_{\text{FOV}}} \int d^2 \mathbf{x}'_{\perp} \int d^2 \mathbf{k}_{\perp} e^{i\mathbf{k}_{\perp} \cdot \mathbf{x}'_{\perp}} \frac{f(\mathbf{x}'_{\perp})}{\mathbf{k}_{\perp}^2 + \alpha} \delta(\mathbf{k}_{\perp}) \\ &= \frac{-1}{A_{\text{FOV}}} \int d^2 \mathbf{x}'_{\perp} \frac{f(\mathbf{x}'_{\perp})}{\alpha} \\ &= \frac{-1}{\alpha^{-1}} \langle f(\mathbf{x}_{\perp}) \rangle , \end{aligned} \quad (291)$$

with $A_{\text{FOV}} = \int_{\text{FOV}} d^2 \mathbf{x}_{\perp}$. We will make use of Eq. (291) in Section 4.2.

Instead of prescription (287), one may use a Schwinger parametrisation to circumvent the occurrence of the singularity at $\xi_{\perp} = 0$ in the expression $\frac{1}{\xi_{\perp}^2}$. Following Schwinger [Sch92], one may write

$$\frac{1}{\xi_{\perp}^2} = \int_0^{\infty} ds s \exp(-s |\xi_{\perp}|) . \quad (292)$$

By means of Eq. (292), the linearised TIE retrieval for pure-phase objects can be written as

$$\begin{aligned}\phi_0(x_\perp) &= \frac{(\Delta x)^2}{2\pi\lambda z} \mathcal{F}^{-1} \left[\frac{\hat{g}_z(\xi_\perp)}{\xi_\perp'^2} \right] \\ &= \frac{(\Delta x)^2}{2\pi\lambda z} \lim_{s_{\max} \rightarrow \infty} \int_0^{s_{\max}} ds s \mathcal{F}^{-1} [\exp(-s|\xi_\perp'|) \hat{g}_z(\xi_\perp)] .\end{aligned}\quad (293)$$

Thus, the Fourier transformation of a regular integrand is now performed in Eq. (293). Analytically, the Schwinger regularisation is parameter-free. However, a numerical implementation of Eq. (293) requires to prescribe values for the cut-off parameter s_{\max} and the sampling density ds .

Let us now turn to the singularities arising from the inverse sine function at non-vanishing frequencies. A simple and efficient regularisation is to rewrite the sine function in terms of the sign function and use Eq. (285) as

$$\frac{1}{\sin x} = \frac{\operatorname{sgn}(\sin x)}{|\sin x|} \rightarrow \frac{\operatorname{sgn}(\sin x)}{|\sin x| + \alpha} , \quad (294)$$

where sgn denotes the sign function with $\operatorname{sgn} x = \frac{x}{|x|}$ for $x \neq 0$ and $\operatorname{sgn} 0 = 0$. For small arguments $x = \pi\lambda z \xi_\perp^2$, approaching zero from above, Eq. (294) is approximated by Eq. (287). Instead of Eq. (294) a slightly different regularisation can be used by rewriting the sine function as

$$\frac{1}{\sin x} = \frac{\sin x}{\sin^2 x} \rightarrow \frac{\sin x}{\sin^2 x + \alpha} , \quad (295)$$

Notice that a regularisation using Eqs. (287) and (294) mimics the effect of an absorptive contribution to the intensity contrast. This becomes evident when comparing the denominators in Eqs. (287) and (294) with the transfer functions in Eqs. (273) and (275), respectively.

3

EXPERIMENTAL IMPLEMENTATION

In this chapter we discuss the implementation of an X-ray imaging experiment. A typical experimental setup at a synchrotron beamline for propagation-based phase-contrast is illustrated in Fig. 19. Section 3.1 describes different sources of X-rays, i. e. X-ray tubes in Section 3.1.1, synchrotron radiation facilities in Section 3.1.2, and free-electron laser Section 3.1.3. Section 3.2 discusses monochromatisation by a crystal or multilayer. Section 3.3 is concerned with the typically employed indirect detector system involving scintillator, magnifying optics, and semiconductor camera.

3.1 X-RAY SOURCES

Before the discussion of different sources of X-rays, it is appropriate to introduce parameters describing source properties such as emittance and brightness. Let σ_x and σ_y denote the horizontal and vertical root-mean-square width of the source, and σ_{θ_x} and σ_{θ_y} the horizontal and vertical beam divergence. The source emittance is defined as

$$\epsilon_x = \sigma_x \sigma_{\theta_x}, \quad \epsilon_y = \sigma_y \sigma_{\theta_y}. \quad (296)$$

A characteristic of a photon beam, the spectral brightness (or brilliance), is defined as

$$\mathcal{B} = \frac{\Phi(E)}{4\pi^2 \epsilon_x \epsilon_y} = \left[\frac{\text{photons/s}}{\text{mrad}^2 \text{ mm}^2 0.1 \% \text{ bandwidth}} \right], \quad (297)$$

where $\Phi(E)$ is the (spectral) flux of photons within a relative energy bandwidth chosen to be fixed at 0.1 % and centred at energy E .

In the framework of geometrical optics the effects of diffraction and interference are neglected and the propagation of light is described in terms of pencils of rays [BW09]. The laws of geometrical optics can be derived from the principle of least time. Also known as Fermat's principle it states that 'Nature always acts by the shortest course'¹ [BW09]. Using Fermat's principle, which is the basis of Hamiltonian (or Lagrangian) optics, Snell's law of refraction and the law of reflection can be derived.

As a consequence of Huygens' principle in the limit of small wave lengths, Fermat's principle asserts that the optical path length S , taken by a ray between two points P_1 and P_2 , is shorter than the optical path

¹ " . . . la nature agit toujours par les voies les plus courtes." Fermat, Oeuvres, Vol. II, pp. 354 and 458.

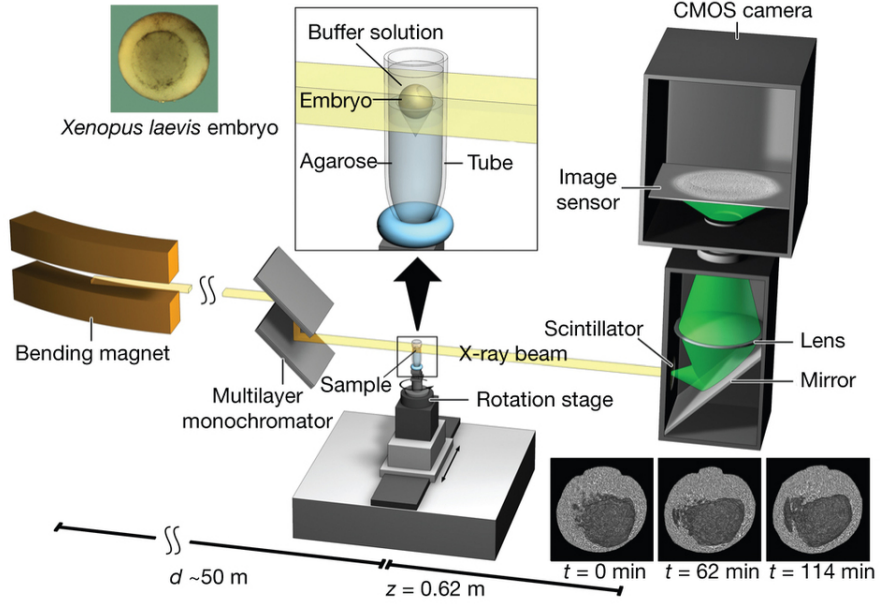


Figure 19: Experimental setup for propagation-based X-ray phase-contrast microtomography. X-rays generated in a bending magnet (BM) or insertion device (ID) are monochromatised by a multilayer or crystal before they impinge on the sample container. The sample container is mounted on top of a rotation stage and provides for a life sustaining environment. As X-rays traverse the sample container, an imprint is left on phase and amplitude of the exiting wave front. The dominant contribution to the attenuation stems from the sample container, while sample-induced local absorption contrast can be neglected for soft tissues and hard X-rays. To yield usable intensity contrast, the X-ray wave front is left to propagate in free space towards the detector system for distances in the order of 1 m. Thereby intensity contrast emerges due to self-interference effects of the forward propagated wave front. The detector system consists of a scintillator, an optical light microscope, and a camera. In the scintillator X-rays are converted to visible light which is subsequently magnified by microscope optics and detected via a CMOS or CCD image sensor. Image adopted from [Moo+13b].

length of any other curve joining these points. The optical path of a ray travelling in a medium of refractive index $n = n(x, y, z)$ is defined as the line integral of n along the ray trajectory which is parametrised by s . Assuming a ray of light to propagate along the optical axis z and between fixed points P_1 and P_2 , the optical path length reads

$$S = \int_{P_1}^{P_2} ds n(s) = \int_{P_1}^{P_2} dz \frac{ds(x, y, z)}{dz} n(x, y, z). \quad (298)$$

If z is interpreted as time, and x and y as generalised coordinates, Eq. (298) corresponds to an action functional. Then the trajectory of a ray is determined by the Euler-Lagrange equations which follow from the variation of S under the boundary condition $P_1 = (x_1(z_1), y_1(z_1), z_1)$ and $P_2 = (x_2(z_2), y_2(z_2), z_2)$, i.e. the functional

\mathcal{S} is stationary and its variation vanishes $\delta\mathcal{S} = 0$. From Eq. (298) the Lagrangian of the system reads as

$$\mathcal{L} = n \frac{ds}{dz} = n(x, y, z) \sqrt{1 + \dot{x}^2 + \dot{y}^2}, \quad (299)$$

where \dot{x} and \dot{y} denote the generalised velocities defined as $\dot{x} \equiv \frac{dx}{dz}$ and $\dot{y} \equiv \frac{dy}{dz}$. The conjugate momenta follow from the Lagrangian as

$$\begin{aligned} p_x &\equiv \frac{\partial \mathcal{L}}{\partial \dot{x}} = n \frac{\dot{x}}{\sqrt{1 + \dot{x}^2 + \dot{y}^2}} = n \frac{dx}{ds}, \\ p_y &\equiv \frac{\partial \mathcal{L}}{\partial \dot{y}} = n \frac{\dot{y}}{\sqrt{1 + \dot{x}^2 + \dot{y}^2}} = n \frac{dy}{ds}. \end{aligned} \quad (300)$$

The optical momentum is then given by

$$\mathbf{p} \equiv (p_x, p_y, p_z) = n \frac{d\mathbf{r}}{ds} = n(\cos \alpha_x, \cos \alpha_y, \cos \alpha_z), \quad (301)$$

where α_x , α_y , and α_z denote the angles that \mathbf{p} subtends to the x -, y -, and z -axis. The optical momentum is thus given by the vector norm $|\mathbf{p}| = n$ and points in the propagation direction of a light ray.

Now consider light emitted across a source of given width $\sigma_x \times \sigma_y$ into a small solid angle $\sigma_{\theta_x} \times \sigma_{\theta_y}$. The beam divergence is identified with the conjugate momenta of marginal rays as

$$\begin{aligned} \sigma_{\theta_x} &\approx \tan \sigma_{\theta_x} = \frac{p_x}{p_z}, \\ \sigma_{\theta_y} &\approx \tan \sigma_{\theta_y} = \frac{p_y}{p_z}. \end{aligned} \quad (302)$$

As a consequence of Liouville's theorem [Gib02], the volume in phase space occupied by the beam emittance given in Eq. (296) is a conserved quantity. The brightness of a photon beam is thus an invariant characteristic of the source strength under optical transformations invoked by free-space propagation, refraction, or reflection [Kim86].

3.1.1 X-ray tubes

The very first source of X-rays was an X-ray tube, e.g. the Coolidge tube [Coo17], still being the most common one. Apart from the introduction of systems employing a rotating anode, the design of X-ray tubes remained practically unchanged to this day. Owing to the improved dissipation of head load, a rotating anode enables higher electron and thus photon fluxes. Emitted by a hot cathode and accelerated by the voltage applied across the tube, electrons impinge on the anode material where they are decelerated and eventually stopped. Thereby, X-rays emanate in a continuous spectrum related to the effect of bremsstrahlung [Jac99]. The maximum energy in the X-ray spectrum corresponds to the voltage applied to the tube. On top of

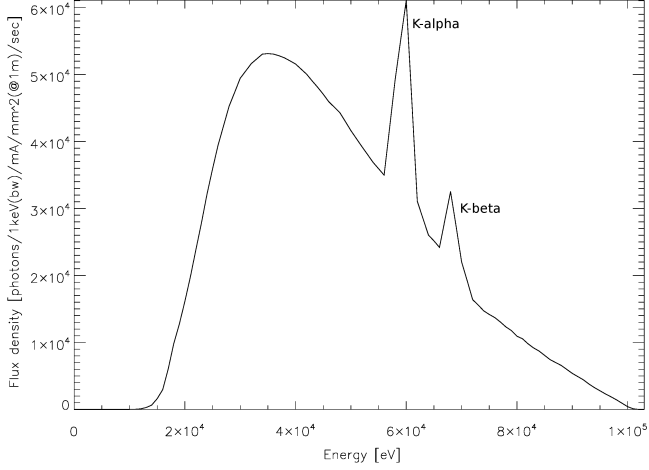


Figure 20: Spectrum of a Tungsten X-ray tube operated at $E = 100 \text{ keV}$ without filters. The two characteristic lines in the spectrum are the K_{α} - and K_{β} -line of of Tungsten. They correspond to X-rays emitted during the transition of electrons from the L-shell and M-shell to the K-shell, respectively. The fine-structure splitting of energy levels, which is indicated by a subindex, is not resolved in the plot. The energies belonging to the mentioned transitions are: $K_{\alpha_1} = 59.32 \text{ keV}$, $K_{\alpha_2} = 57.99 \text{ keV}$, $K_{\beta_2} = 69.10 \text{ keV}$, $K_{\beta_1} = 67.24 \text{ keV}$, and $K_{\beta_3} = 66.95 \text{ keV}$ [HGD93]. The spectrum was calculated using XOP (X-ray Oriented Programs) provided by ESRF [SD11].

a continuous background, the spectrum exhibits peaks at distinct energies. These peaks are called characteristic (X-ray) lines and depend on the material used in the target anode. First discovered by Barkla as secondary radiation [Baro4; Baro5], these lines are caused by X-ray fluorescence. Created by a photon (or electron), a vacancy in the orbital of the innermost K-shell (principal quantum number $n = 1$) is filled by an electron jumping in from a higher shell. During the transition a photon is emitted whose energy, typically in the order of 1 keV to 100 keV, corresponds to the difference between the two energy levels. The spectrum of an X-ray tube using a Tungsten target operated at 100 keV is depicted Fig. 20.

3.1.2 Synchrotron radiation facilities

Synchrotron light sources are categorised into three generations. This number increases to four when free-electron laser (FEL) are included. First generation sources refer to accelerators and storage rings which were primarily meant for experiments in high-energy physics. Designated to collide or store particles, synchrotron radiation is an unwanted by-product of storage rings. Initially, the radiation was used in parasitic operation only. For example, one of the first diffraction experiments (on an insect muscle) was conducted at the German electron synchrotron DESY providing parasitic radiation in the X-ray

regime down to sub-angström wave lengths [RHW71; TVo1]. From the beginning in 1974, the double ring storage DORIS (Doppel-Ring Speicher) at Deutsches Elektron-Synchrotron (DESY) was also used as a source of synchrotron radiation, and by 1993 this was its sole purpose [TVo1]. In X-ray crystallography synchrotron facilities have become the most important source of X-rays, for both minerals and organic crystals. As a consequence of the large unit cell volume of crystallised biological macromolecules the diffracting power is weak compared to minerals and metals. Moreover, the growth of large crystals of biological macromolecules is difficult. Therefore the use of intense and brilliant radiation provided by synchrotrons is essential for structural studies of biological macromolecules [Lin95]. By now, synchrotron facilities have contributed to the structure determination of tens of thousands of proteins and nucleic acids. For instance, the structural determination of the ribosome, which is the molecular machine that serves as the primary site for protein synthesis and consists of the large and small ribosomal sub-unit, was partly done at DORIS [Sch+oo; Har+o1]. Second- and third-generation synchrotrons refer to facilities devoted to the production of brilliant and intense light only. While in second-generation facilities X-rays are produced by bending magnets which force electrons onto a circular trajectory, third generation sources exploit periodic arrays of magnets, called insertion devices (IDs), which are situated in straight sections of the storage ring. The alternating magnetic field in an insertion device forces the electrons to move sinusoidally. Light emitted at each period adds up to boost the intensity by up to four orders of magnitude compared to that of a bending magnet (BM). The first light source of the third generation type to be built was the ESRF, completed in 1991.

The principal layout of the accelerator complex in a synchrotron radiation facility is composed of a pre-injector, the booster synchrotron, and the storage ring, see e.g. Fig. 21. The pre-injector is typically composed of an electron gun, where electrons are produced by local heating, a bunch compressor, where electrons are packed in bunches, and a linear accelerator such as a microtron, where electrons are accelerated to energies sufficient for injection into the booster synchrotron. In the booster synchrotron the electrons are pre-accelerated before being injected into the storage ring. Unless injected at full energy, the beam has to be ramped up in energy in the storage ring to reach final operating conditions. Thus a refill of electrons followed by a ramp-up is usually required once or twice per day. In a full energy injector a booster synchrotron is used whose circumference and energy match that of the storage ring. This enables top-up operation to compensate for beam losses by periodically injecting small amounts of current. The aim of the top-up operation mode is to maintain a steady current in the storage ring to overcome lifetime limitations and to keep a constant photon flux at the beamline. A constant flux is not only im-

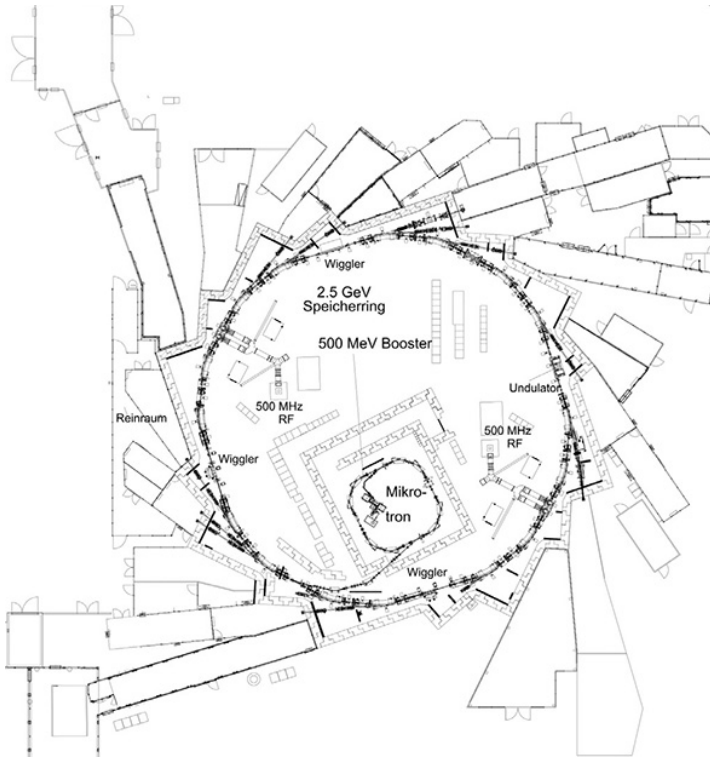


Figure 21: Layout of the ANKA synchrotron radiation facility including pre-injector (Mikrotron), booster synchrotron (500 MeV Booster), and storage ring (2.5 GeV Speicherring). Also shown is the outline of the optics and experimental hutsches, the radiation shield wall, radio cavities (500 MHz RF), and insertion devices (Undulator, Wiggler). Image taken from [ANK13].

portant to keep up photon statistics during the measurement, but also to attain thermal equilibrium of the heat load on the X-ray optics, see Fig. 26 for the distorting impact of heat load on a multilayer monochromator. Typical machine components of the accelerator complex involve radio frequency cavities for direct acceleration, dipole magnets (bending magnets) for deflection of particles, and quadrupole or sextupole magnets for beam focusing.

The basic physical properties of synchrotron radiation are determined by the fact that a charge moves at relativistic velocities towards the observer. A non-relativistic electron moving on a circular trajectory acts similar to a Hertz dipole, isotropically emitting radiation perpendicular to its axis of acceleration. In a synchrotron, however, electrons travel at relativistic speed v with their energy E_e being large compared to the rest energy of $m_e c^2 = 511 \text{ keV}$. This is expressed by the Lorentz factor as

$$\gamma = \frac{E_e}{m_e^2 c^2} = \frac{1}{1 - \frac{v^2}{c^2}} = \frac{1}{1 - \beta^2} \gg 1 , \quad (303)$$

where $\beta = v/c$ denotes the modulus of the velocity $v = |\mathbf{v}|$ normalised to the speed of light in vacuum c , and m_e is the electron rest

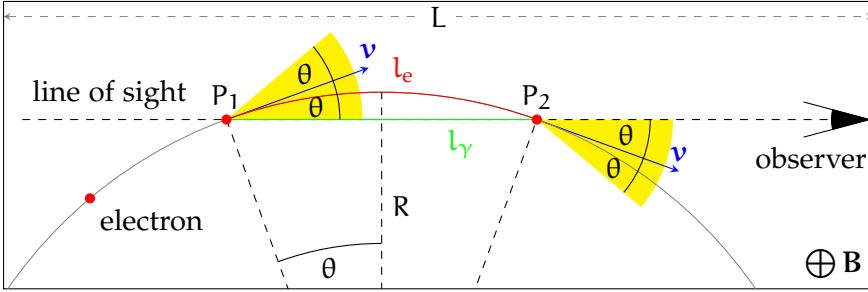


Figure 22: Electron moving at a velocity $v = |\mathbf{v}|$ in a long magnet of constant magnetic field $B = |\mathbf{B}|$ and length $L > \frac{2R}{\gamma} = \frac{2m_e}{eB}$. Thereby, radiation is emitted into a light cone (yellow) with an opening angle θ . The emitted radiation is received by the observer as long as the velocity subtends an angle to the line of sight less than the opening angle θ of the radiation cone. Therefore, the length of the radiation pulse as seen by the observer is given by the difference in time for the charge and the radiation to travel from P_1 to P_2 .

mass. As a consequence, the radiation received by the observer in the laboratory frame is confined in a light cone centred around the instantaneous velocity of the electron. The opening angle θ of the light cone is approximately given in terms of the Lorentz factor as [Hofo4]

$$\theta \approx \sin(\theta) = \frac{1}{\gamma}. \quad (304)$$

The time in the rest frame of the charge during which an observer receives radiation emitted by that charge is much longer than the time in the laboratory frame of the observer. This compression of time (Doppler effect) is what determines the spectrum of synchrotron radiation.

Consider a charge which is moving on a circular trajectory with radius R and velocity v in a constant magnetic field B as depicted in Fig. 22. The radiation emitted by the charge is received by the observer only as long as the velocity vector of the charge subtends an angle to the line of sight less than the opening angle of the radiation cone. The corresponding locations of the trajectory are indicated by P_1 and P_2 in Fig. 22. The length of the pulse received by the observer is thus determined by the difference in time for the charge and the radiation to travel from P_1 to P_2 . Hence the pulse length in a long magnet reads from Fig. 22 as

$$\Delta t_{lm} = t_e - t_\gamma = \frac{l_e}{v} - \frac{l_\gamma}{c} = \frac{2R}{\beta\gamma c} - \frac{2R \sin(1/\gamma)}{c} \approx \frac{4R}{3c\gamma^3}, \quad (305)$$

where an approximation for ultra-relativistic velocities, $\beta \approx 1$ and $\gamma \gg 1$, and an expansion of the trigonometric function was used. The radiation obtained from a long magnet is usually referred to as (ordinary) synchrotron radiation. It exhibits a broad spectrum characterised by the critical frequency ω_{crit} which is proportional to the

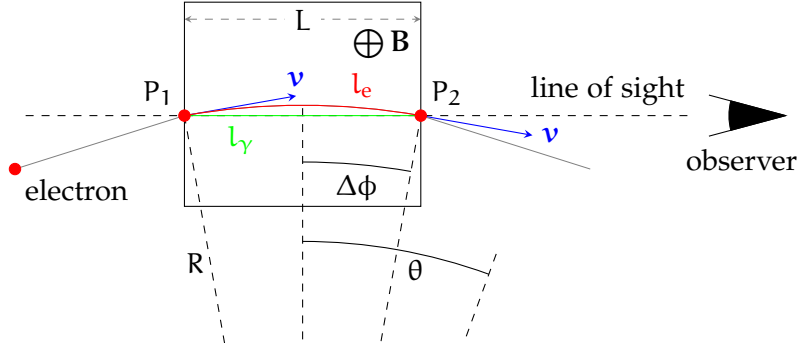


Figure 23: Electron moving at a velocity $v = |\mathbf{v}|$ in a short and weak magnet of constant magnetic field $B = |\mathbf{B}|$ and of length $L < \frac{2R}{\gamma} = \frac{2m_e}{eB}$. The deflection angle $\Delta\phi$ is less than the opening angle of the radiation cone θ . Thus, the length of the radiation pulse Δt_{sm} , given by the difference in time for the charge and the radiation to travel from point P_1 to P_2 , becomes a function of L .

frequency associated to Eq. (305). Defined such as to halve the emitted power, the critical frequency is found as [Hofo4]

$$\omega_{crit} = \frac{3c\gamma^3}{2R} = \frac{2}{\Delta t_{lm}} . \quad (306)$$

Consider a charged particle moving in a short and weak magnet of length L and constant magnetic field B as depicted in Fig. 23. For $L < \frac{2R}{\gamma} = \frac{2m_e}{eB}$ an electron is deflected by an angle

$$2\Delta\phi = 2 \arcsin\left(\frac{L}{2R}\right) \approx \frac{L}{R} < \frac{1}{\gamma} , \quad (307)$$

which is less than the opening angle of the radiation cone. Then, the length of the radiation pulse becomes proportional to the length of the magnet. In the ultra-relativistic case $\beta \approx 1$, we have

$$\Delta t_{sm} = t_e - t_\gamma = \frac{2R}{\beta c} \arcsin\left(\frac{L}{2R}\right) - \frac{L}{c} \approx \frac{L}{\beta c}(1 - \beta) \approx \frac{L}{2c\gamma^2} . \quad (308)$$

The radiation obtained from a series of short and weak magnets is thus distinguished from ordinary synchrotron radiation. Insertion devices are composed of an array of short magnets where electrons move on an oscillatory path within the radiation cone. Interference effects may become important depending on the strength of the magnetic field which influences amplitude and deflection angle of the electron trajectory in an insertion device. This is parametrised by the deflection or undulator parameter K . It is defined by the ratio of the maximum deflection angle $\Delta\phi$ of an electron moving in a periodic magnetic field to the opening angle $1/\gamma$ of the emitted radiation. If

the deflection angle is expressed by the magnetic field, the undulator parameter reads as

$$K = \frac{\Delta\phi}{1/\gamma} = \frac{eB_0\lambda_u}{2\pi m_e c}, \quad (309)$$

where B_0 is the peak magnetic field in the insertion device, e the electron charge, and λ_u the period length of the insertion device. For a particular insertion device called wiggler ($K \gg 1$) the radiation emitted from different parts along the electron trajectory adds up incoherently and thus interference effects are insignificant. In the case of a weak undulator ($K < 1$), the radiation from different periods adds up coherently producing quasimonochromatic peaks in the emission spectrum. These peaks correspond to the harmonics of the fundamental frequency ω_0 given as

$$\omega_0 = \frac{2\pi}{\lambda_u} \frac{c\gamma^2}{1 + \frac{K^2}{2} + \gamma^2\theta^2}, \quad (310)$$

where θ denotes the observation angle with respect to the undulator axis. Given typical parameters found at synchrotrons, Eq. (310) implies that centimetre periods (λ_u) of the undulator translate into nanometre wavelengths $\lambda_0 = \frac{2\pi c}{\omega}$. For $K \ll 1$ and on-axis observation ($\theta = 0$) the result of Eq. (305) is restored with $L = \lambda_u$. In a strong undulator ($K > 1$) the spectrum is more complicated containing many harmonics.

A detailed treatment of synchrotron radiation on the basis of retarded electromagnetic potentials, the Liénard-Wiechert potentials, is given in [Kim89] or [Hofo4] and references therein.

3.1.3 Free-electron laser

In a free-electron laser (FEL), or its much more powerful successor the X-ray free-electron laser (XFEL) in terms of energy radiated per unit time and area, a bunch of electrons is accelerated to relativistic energies (in the order of 10 GeV) by a linear array of normal or superconducting resonators. The electrons then undulate through a periodic arrangement of magnets, thereby generating laser light of extreme intensity. Compared to common synchrotron undulators, the light generated in the undulator of a free-electron laser interacts with the undulating electron significantly. In a process called microbunching, electrons are accelerated or decelerated and gradually organise themselves into a multitude of thin disks by ponderomotive forces [Kra79]. In contrast to conventional undulators, the radiation is now emitted synchronously by the microbunched electrons and adds up coherently. This mechanism is known as self-amplified spontaneous emission (SASE) [And+oo]: spontaneous emission from initial shot noise in the electron beam is further amplified by the interaction of

the emitted light with the electron bunch over the full length of the magnetic undulator. This results in extremely short pulses of 10^1 fs to 10^2 fs duration (10^1 flashes/s to 10^5 flashes/s), a high degree of coherence, and intense light with a peak and average brightness of

$$B_{\text{peak}} \approx \frac{10^{29} \text{ to } 10^{33} \text{ photons}}{\text{s mm}^2 \text{ mrad}^2 0.1 \% \text{ bandwidth}}, \quad (311)$$

$$B_{\text{average}} \approx \frac{10^{17} \text{ to } 10^{25} \text{ photons}}{\text{s mm}^2 \text{ mrad}^2 0.1 \% \text{ bandwidth}}.$$

Note that starting up from noise results in poor temporal coherence and a broad and noisy spectrum. To overcome these deficiencies an external signal can be used to initiate the process of amplification. This not only improves monochromaticity, but allows to increase the photon flux by a highly efficient undulator field taper. Since external seeding at angström-scale wavelengths is difficult, self seeding was first proposed for soft X-rays, and successfully applied for soft and hard X-rays [Ama+12]. The idea is to use X-rays from the first half of the undulator to seed the second half.

The extremely intense flashes of light emitted by an XFEL allow to study tiny structures down to the atomic scale, ultrafast processes such as the formation or dissociation of molecules, or extreme states or conditions of pressure and temperature as found deep inside a star. This comes at the expense of the destruction of the sample by the radiation delivered by FELs and XFELs. At femtosecond timescale, however, the unfolding of a molecular explosion is slow enough (roughly 10 fs), that X-ray photons, which are not absorbed within the sample, can scatter off the atoms of the crystalline structure before thermalisation of the unit cells occurs and thus give rise to an unadulterated diffraction pattern [Neu+00; Cha+11]. This is also called diffraction before destruction.

3.2 MONOCHROMATOR

The experimental setup for propagation-based phase contrast does not require additional optical components with the exception of a monochromator, unless single-line harmonics of appropriate bandwidth are available at undulator beamlines. When the full energy spectrum of the X-ray beam is used, the only appreciable phase contrast is due to the enhancement of edges of the projected object. Higher-order fringes in the propagated intensity are smeared out due to the superposition of different monochromatic components. Moreover, intensity contrast is dominated by low-energy components which produce broader fringes (see also Fig. 17) and are more pronounced due to larger phase shifts at low energies. The only phase retrieval to be performed on such data is the inversion of the Laplacian, which mainly acts as a low-pass filter suppressing high spatial frequencies

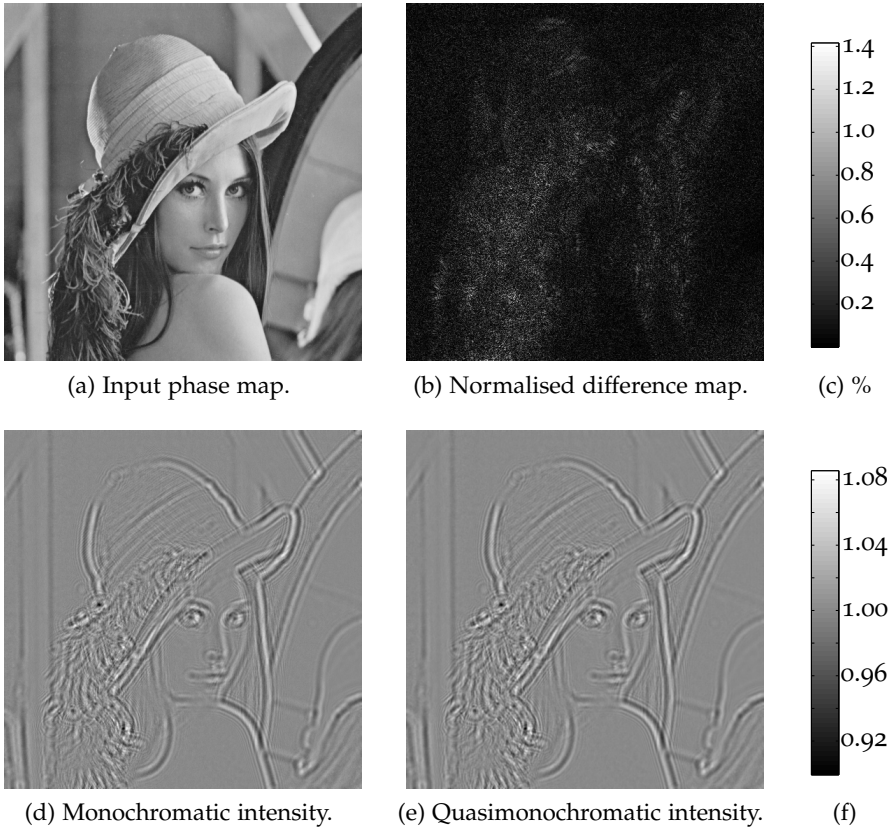


Figure 24: Comparison of monochromatic and quasimonochromatic intensities in simulated forward propagation of an exit wave in Fresnel theory. (a) Lena test pattern with 500×500 pixels is used as pure-phase object. The maximum phase variation $\Delta\phi$ over the entire field of view is $\Delta\phi = 0.1$ at an energy $E = 20$ keV, a pixel size $\Delta x = 1$ μm , and a propagation distance $z = 1$ m. (d) Intensity I_{mono} due to a monochromatic spectrum at $E = 20$ keV. (e) Intensity I_{quasi} due to a quasimonochromatic spectrum which is modelled using a Gaussian distribution with a mean energy $\langle E \rangle = 20$ keV and a bandwidth 10^{-1} . The corresponding full width at half maximum (FWHM) is $\Delta E = 2$ keV or a standard deviation of $\sigma = \Delta E / (2\sqrt{2\ln(2)}) \approx 0.85$ keV. The spectrum is sampled at 500 points within an energy range of $\langle E \rangle \pm 5\sigma$. The quasimonochromatic intensity pattern is obtained using the Gaussian weighted sum of monochromatic intensities computed from phase maps where $\Delta\phi$ varies with energy according to the real part of the refractive index [HGD93] δ and with $\Delta\phi = 0.1$ at $E = 20$ keV. Within $\langle E \rangle \mp 5\sigma$, $\Delta\phi$ decreases from 1.61 to 0.68. (b) Difference between the monochromatic and quasimonochromatic intensity normalised to the monochromatic intensity $|I_{\text{quasi}} - I_{\text{mono}}|/I_{\text{mono}}$. At a broad bandwidth of 10^{-1} the deviations due to a quasimonochromatic spectrum are in the order of 1% only, which is comparable to or less than the typical noise level in a measured intensity map. This simulation, however, does not account for the effects of finite transverse and longitudinal coherence lengths. With regard to high-resolution phase retrieval, the longitudinal coherence (Eq. (143))) imposes a more severe bound on monochromaticity than that could be inferred from this simulation. (c) Grayscale to (b). (f) Grayscale to (d) and (e) for normalized intensity maps

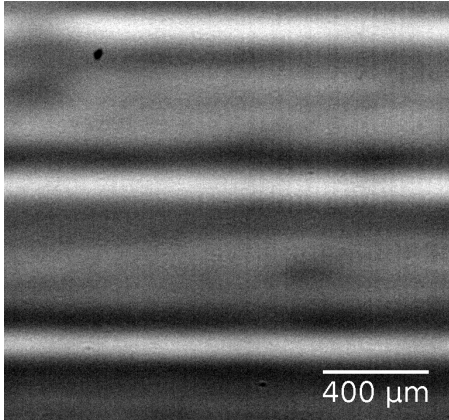


Figure 25: Flat field image showing a horizontal stripe pattern which typically occurs in synchrotron X-ray beams subject to a multilayer monochromator. Depending on the exposure time, a temporal variation of the position of the horizontal stripes can be observed. This is due to cooling-induced thermal instabilities of the multilayer monochromator. Image was recorded at bending magnet beamline station 2-BM-B of APS at Argonne National Laboratory. A quasimonochromatic X-ray beam of energy $E = 30\text{ keV}$ with a bandwidth of $\Delta E/E \approx 10^{-2}$ used.

and thus noise. Using a white spectrum, only a mean phase can be retrieved due to the superposition of monochromatic components. Thus, neither a quantitative result nor a high spatial resolution can be obtained. For quantitative and high-resolution phase retrieval methods to work requires a bandwidth of about 10^{-2} or less, depending strongly on experimental parameters. This result derives from empirical values, the simulation presented in Fig. 24, and Section 2.1.8. In this simulation a monochromatic intensity map is compared to a quasimonochromatic intensity map with a considerable bandwidth of 10^{-1} . The absolute difference between the two maps is found to be $\sim 1\%$, which is comparable or less than the typical noise in a measured intensity map. A more severe constraint, however, is imposed by the finite longitudinal coherence length, see Eq. (143). Hence, in propagation-based phase-contrast experiments we can work with a crystal or multilayer monochromator resulting in a bandwidth in the order of 10^{-2} or 10^{-4} , respectively. If radiation damage, induced by the absorbed dose, is insignificant multilayer are preferred due to the higher flux density while a sufficient degree of monochromaticity is retained. The gain in flux density, however, comes at the expense of an inhomogeneous background field (flat field). Typical artifacts in the reflected wave front introduced by a multilayer are background modulations in terms of an irregular, stripe pattern [Rac+10; Die+11; Moo+13b], see e. g. Fig. 25 and Fig. 26 or images in reference [Rac+10]. Variations in the surface texture of the substrate underlying the multilayer coating are reproduced by the multilayer coating. These variations result in a different path lengths introducing phase shifts in the

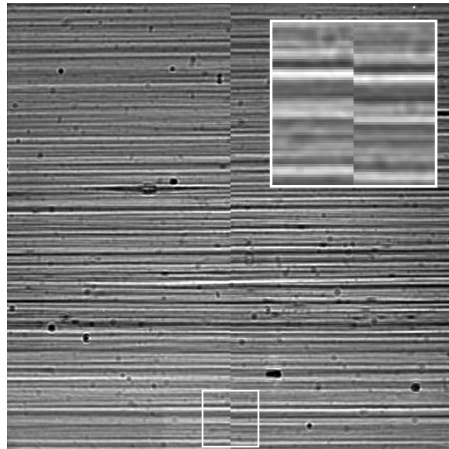


Figure 26: Heat load induced thermal expansion of the multilayer affecting stripe-like modulations in the flat field. The left and right half of the image depict flat fields which were taken with a delay of ~ 13 min. The inset at the upper right is an enlarged view of the encircled region in the lower half. Due to thermal expansion of the multilayer the stripe pattern becomes magnified and shifted. Data was recorded with beamline ID19 at ESRF using a single multilayer monochromator at 30 keV.

reflected wave front. By free-space propagation of the reflected beam, these phase shifts translate into intensity modulation downstream of the multilayer. The stripe pattern is thus influenced by the roughness and composition of the multilayer [Die+11; Rac+10]. This is aggravating the flat-field correction procedure and introduces artifacts in the reconstructed images or tomographic volumes. Moreover, heat load on the multilayer results in thermal expansion and instabilities which causes the stripe modulations to vary with time. While thermal expansion induces enlargement and shift of the stripe pattern as seen in Fig. 26, thermal instabilities, e. g. introduced by the cooling system of the monochromator, induce oscillations of the stripe pattern if the exposure time is smaller than the inverse frequency of the oscillations.

3.3 DETECTOR SYSTEM

To fully exploit the intense radiation available at synchrotron beamline requires not only fast detectors with a spatial resolution in the micrometre or submicrometre regime, but also an online data acquisition. This enables tomography and time-resolved experiments and facilitates selection, processing, and distribution of acquired images.

Using photographic films for X-ray detection achieves micron resolution for hard X-rays, but is slow, off-line, and has a low dynamic range [Koc+98]. Photoresists achieve submicrometre resolution, but only for soft X-rays, and only work off-line [Koc+98]. Therefore image acquisition with a digital sensor such as a CCD or a CMOS is preferred with the further benefit of excellent linearity, high stability,

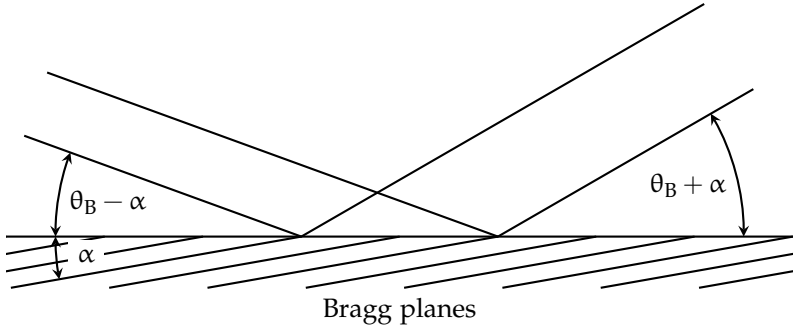


Figure 27: Asymmetric one-dimensional Bragg diffraction. The Bragg planes subtend an angle α to the surface of reflection. θ_B denotes the Bragg angle. The incident and reflected wave subtend an angle $\theta_B - \alpha$ and $\theta_B + \alpha$ with respect to the surface. The magnification factor is $M = \frac{\sin(\theta_B + \alpha)}{\sin(\theta_B - \alpha)}$.

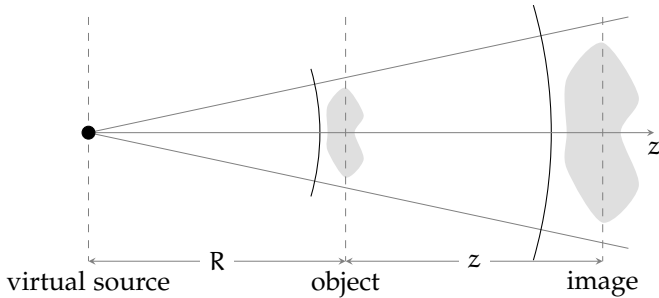


Figure 28: Magnification by cone-beam geometry which is due to a (virtual) point source emitting spherical waves. The object is situated at a distance R to the source. At a distance $R + z$ from the source, the image of the object is magnified by a factor of $M = \frac{z+R}{R}$.

a large dynamic range, and image readout a few milliseconds after exposure [TGE97]. Limiting factors of digital cameras in direct detection mode are pixel sizes (currently in the order of a few microns), radiation damage, and X-ray stopping power. Luminescent screens are employed to increase the stopping power. For instance, phosphor screens can be used which consist of a fine grain powder deposited on a substrate [GTEo2]. Multiple photon scattering at the granular structure of the phosphor screen degrades spatial resolution. This can be mitigated by the use of structured scintillators [MKo6].

Another means to improve spatial resolution is the Bragg magnifier system consisting of a pair of asymmetric cut crystals. The cross section of the X-ray beam is increased by asymmetric Bragg reflection yielding a magnification of up to two orders of magnitude [Sta+02; SKo3], see Fig. 27. Avoiding the conversion of X-rays into visible light, this setup facilitates the use of directly converting detectors to achieve submicron spatial resolution imaging while a high detection efficiency is maintained.

Spatial resolutions down to a few nanometres is enabled by hard X-ray microscopes. An incoming quasi-parallel beam of X-rays is focused by a Fresnel zone plate or a pair of Kirkpatrick-Baez mirrors [Hig+05] producing a virtual source with a focal spot size of below $1\text{ }\mu\text{m}$. The cone beam geometry of the transmitted X-rays results in a magnification which increases with increasing propagation distance, see Fig. 28. Compared to conventional imaging beamlines, access to hard X-ray microscopes is rather limited and the setup is much more restrictive with regard to data acquisition rates and dose requirements. Concerning time-resolved or in vivo experiments only local tomography is feasible.

A detailed comparison of different approaches for fast, dose efficient, high-resolution detectors is found in [MKo6] and references therein. In the following we restrict our discussion to indirect detector systems, which are regularly used in X-ray imaging experiments, see Fig. 29. Such a system is comprised of a luminescent screen (scintillator), a microscope optic, and a digital camera [Koc+98]. The scintillator converts absorbed X-ray photons into visible or ultraviolet light. The luminescent light is subsequently magnified by a microscope optic and relayed onto a digital camera. The image sensor in digital cameras is usually a CCD, CMOS, or thin-film transistor (TFT). Assuming 100 % transmission of the luminescent light through the microscope optics, the image formation can be summarised into the following relation for the number of counts per pixel and second

$$N = \Phi \cdot DQE \cdot ADU , \quad (312)$$

where, as in Eq. (297), Φ denotes the spectral flux of X-ray photons impinging on the detector system, DQE is the detective quantum efficiency, and ADU the conversion factor of photons detected within the image sensor to be converted into electrons in the analog to digital unit.

For a shot-noise limited system and low spatial frequencies, the detective quantum efficiency, defined as the ratio of the input and output signal-to-noise ratios (SNRs) of the detector system, is given as [Koc+98; MKo6]

$$DQE \equiv \frac{\text{SNR}_{\text{out}}^2}{\text{SNR}_{\text{in}}^2} \approx \eta_{\text{abs}} \left(1 + \frac{1 + \frac{1}{\eta_{v \rightarrow e}}}{\eta_{\text{coll}} \frac{E}{E_v} \eta_{X \rightarrow v}} \right) . \quad (313)$$

The absorption efficiency η_{abs} denotes the fraction of X-ray photons absorbed within the scintillator as a function of X-ray energy E . It is given by Beer's law (Eq. (229)) as $\eta_{\text{abs}} = 1 - \exp(-\mu(E)z)$, μ being the linear attenuation coefficient of Eq. (122) and z the thickness of the scintillator. $\eta_{X \rightarrow v}$ denotes the energy conversion efficiency of X-rays into visible light of energy E_v . η_{coll} is the collection efficiency of light emitted from the transparent luminescent screen to be collected by the optical system. $\eta_{v \rightarrow e}(E_v)$ is the quantum efficiency of the

image sensor for the conversion of visible photons into electrons as a function of the energy E_v of visible photons.

From Fig. 29 the collection efficiency of the objective follows as

$$\eta_{\text{coll}} = \frac{1}{4\pi} \int_0^{2\pi} d\varphi \int_0^{\theta_{\text{sc}}} \sin \theta = \frac{1}{2} \left(1 - \sqrt{\sin^2 \theta_{\text{sc}}} \right) \approx \frac{1}{4} \left(\frac{\text{NA}}{n_{\text{sc}}} \right)^2 , \quad (314)$$

where φ is the polar angle with respect to the optical axis, and θ_{sc} the opening angle of the light cone within the scintillator determined by Snell's law as

$$n_{\text{sc}} \sin \theta_{\text{sc}} = n_{\text{obj}} \sin \theta_{\text{obj}} = \text{NA} . \quad (315)$$

Let us now consider the characteristics of the scintillator required for high-resolution imaging. The X-ray stopping power (or absorption efficiency) η_{abs} is maximised by increasing number density and atomic number. Radiation hardness is a prerequisite, but often derogates producibility and image quality (reduced light yield, increased surface roughness, etc.). The conversion efficiency $\eta_{X \rightarrow v}$ of absorbed X-rays into visible light should be high. The spectrum $S_v(E_v)$ of emitted photons should match the quantum efficiency $\eta_{v \rightarrow e}$ of the image sensor of the camera which is described by the spectral matching factor

$$\text{SMF} \equiv \frac{\int dE_v \eta_{X \rightarrow v} S_v(E_v)}{\int dE_v S_v(E_v)} . \quad (316)$$

Afterglow affects the effective dynamic range at high frame rates of the detector and needs to be minimised. Linearity between the flux of absorbed X-rays and the flux of emitted light is demanded. The transmittance of the emitted optical light should be high and the scattering low. Technical aspects are also important such as machinability, non-toxicity, mechanical strength, and non-hygroscopicity. Commonly used scintillating films consist of layers of e. g. YAG ($\text{Y}_3\text{Al}_5\text{O}_{12}$), LAG ($\text{Lu}_3\text{Al}_5\text{O}_{12}$), GGG ($\text{Gd}_3\text{Ga}_5\text{O}_{12}$), or LSO (Lu_2SiO_5) doped with Ce, Eu, or Tb [Mar+09; Cec+11]. A detailed discussion of the characteristics of different scintillators is given in [MKo6; Mar+09; Cec+11].

To maximise the intensity signal while maintaining spatial resolution, it is crucial to understand the interplay of scintillator and microscope. Consider a parallel beam setup as depicted in Fig. 29, where X-rays impinge perpendicularly onto a scintillator. The intensity distribution in the scintillator in planes perpendicular to the optical axis is assumed to be identical apart from the attenuation by the absorption of X-rays. The intensities of these planes sum up to the total signal recorded by the camera. Thus, to acquire a sharp image the objective needs to be focused at a plane within the scintillator and its depth of focus has to match the thickness or the absorption length of the scintillator. The depth of focus (or depth of field) characterises the distance away from the focal plane where a point object, which

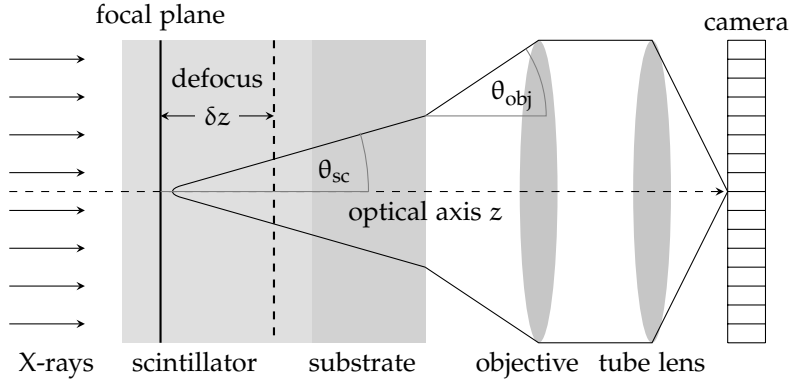


Figure 29: Sketch of a detector system involving a scintillating screen, microscope optics, and a digital camera. A parallel beam of X-rays impinges perpendicularly onto the surface of a luminescent screen (scintillator) grown on a substrate. X-rays that are absorbed within the scintillator are converted to visible light which is subsequently collected by a microscope objective with numerical aperture NA and acceptance angle θ_{obj} . Due to refraction, the opening angle θ_{sc} of the light cone within the scintillator is smaller than the acceptance angle. The objective is placed such that its front focal plane lies within the scintillator. The magnified light is then imaged on a digital camera. The tube lens, offering the flexibility of infinity focus, produces an intermediate image which is either directly recorded with a digital camera or further relayed to an eyepiece. An eyepiece produces a real image and offers an additional magnification of the intermediate image.

is blurred due to defocusing, still produces a point image. The resolution limit of a microscope due to diffraction can only be reached if the thickness or the absorption length of the scintillator is smaller than the depth of focus. Let R denote the resolving power of the microscope, i. e. the minimum size of a pattern that can be resolved. The depth of focus affects the spatial resolution according to [Hop55; Koc+98]

$$R \approx \delta z \text{NA} , \quad (317)$$

where δz is the distance between the plane in focus and a plane out of focus, and NA the numerical aperture. The numerical aperture is a dimensionless number which characterises the angular range that a lens can accept. It is defined as

$$\text{NA} = n \sin \theta_{\text{obj}} , \quad (318)$$

where θ_{obj} denotes the half-angle of the acceptance cone of the lens and n the refractive index of the medium the lens is immersed in, see Fig. 29. The resolving power of a microscope is further limited by diffraction. Given light of wave length λ propagating in a medium of refractive index n , the Abbe diffraction limit for incoherent illumination (or a self-luminous object) is given by [BW09]

$$R \approx \frac{1}{2} \frac{\lambda}{n \text{NA}} . \quad (319)$$

In geometrical optics, the Abbe diffraction limit can be understood as follows: the objective lens can be regarded as a device which produces at the back focal plane a Fourier transformed image of the object in the front focal plane. The maximum transverse wave vector that can be transmitted by the objective is limited by the aperture of the lens to

$$k_{\perp,\max} = |\mathbf{k}| \sin \theta_{\text{obj}} = k \sin \theta_{\text{obj}} = \frac{2\pi}{\lambda_0} n \sin \theta_{\text{obj}} = \frac{2\pi}{\lambda_0} NA . \quad (320)$$

Using the (two-dimensional) Fourier representation of the object situated at the front focal plane, the object is decomposed into plane waves perpendicular to the optical axis. Thus the image of the object transmitted by the lens only contains wave vectors up to $k_{\perp,\max}$. The maximum transverse wave vector associates to the finest detail R that can be resolved as $k_{\perp,\max} = \frac{2\pi}{2R}$, where the factor of two takes into account the Nyquist–Shannon sampling theorem [Nyq28; Sha49]. Thus, the diffraction limit follows as $R = \frac{\lambda}{2NA}$.

By matching the resolving powers related to Eqs. (317) and (319), the maximum thickness of the scintillator in the case of diffraction-limited resolution reads as

$$\delta z = \frac{\lambda}{2NA^2} . \quad (321)$$

The larger the numerical aperture the better the resolving power according to Eq. (319). Moreover, at fixed n , a larger numerical aperture results in a larger angle θ_{obj} , which increases the collection efficiency η_{coll} of the objective. However, at the same time the depth of focus decreases according to Eq. (317). A smaller depth of focus requires thinner scintillators decreasing the number of absorbed X-ray photons ($\propto \eta_{\text{abs}}$). Furthermore, a large numerical aperture means a short focal length which limits the working distance of the objective. The working distance directly influences the longitudinal extent of the detector system and is defined the distance between the front end of the objective and its focal plane where the sample is placed. It typically decreases with increasing magnification and numerical aperture. To protect the camera from radiation damage, a mirror is usually placed between scintillator and camera chip. Using a long working distance objective the mirror can be placed between scintillator and microscope objective. This setup is favourable for high-dose experiments since the objective is protected from radiation damage. Objectives with a short working distance have to be placed before the mirror and are exposed to X-rays.

4

PHASE RETRIEVAL BEYOND LINEARITY

4.1 PERTURBATION THEORY

In order to characterise object scales larger than can be achieved within the edge-enhancement regime, the object-to-detector distance is increased to values where the intensity pattern contains information from larger object scales. This is due to the interference of distant points in the exit wave field as discussed on the basis of Eq. (258) in Section 2.3.2. At large z , however, the linear model that is assumed in Section 2.3.1 breaks down and a more general ansatz is required. Here we propose and develop a systematic extension of phase retrieval based on transport-of-intensity equation (TIE) for pure-phase objects. This extension systematically works beyond the linear approximation of Eq. (247) while maintaining its single-distance and single-measurement attributes. In order to do so we appeal to a model where intensity contrast and phase shift are expanded in powers of the propagation distance z . Phase retrieval to leading order (LO) in z restores the result of linearised TIE (249). The expansion coefficients related to higher orders in z are determined from the paraxial wave equation (238). Explicit expressions are given up to next-to-leading order (NLO) and next-to-next-to-leading order (NNLO) in terms of transverse derivatives acting on ϕ_0 . Higher order contributions provide non-linear corrections to the Laplacian of the phase which are evaluated perturbatively in terms of the leading-order result. Such a perturbative approach is well known and successfully applied in the field of high-energy physics. We analyse the extended algorithm on simulated phantom data. The discussion presented in the following is adopted from the publications [Moo+10; MHB11a].

4.1.1 Next-to-leading-order correction

Recall the imaginary (TIE) and the real part of the paraxial wave equation given by

$$k \partial_z g_z(\mathbf{x}_\perp) = -\nabla_\perp [(g_z(\mathbf{x}_\perp) + 1)\nabla_\perp \phi_z(\mathbf{x}_\perp)] , \quad (322)$$

and

$$2k\partial_z \phi(\mathbf{x}_\perp, z) = \frac{\nabla_\perp^2 \sqrt{g_z(\mathbf{x}_\perp) + 1}}{\sqrt{g_z(\mathbf{x}_\perp) + 1}} - (\nabla_\perp \phi(\mathbf{x}_\perp, z))^2 , \quad (323)$$

respectively. A power-series ansatz for the propagated phase shift at $z > 0$ reads

$$\phi_z(\mathbf{x}_\perp) = \sum_{l=0}^{l_{\max,\phi}} \phi^{(l)}(\mathbf{x}_\perp) z^l. \quad (324)$$

Accordingly, we make a power-series ansatz for the intensity contrast

$$g_z(\mathbf{x}_\perp) = \sum_{l=1}^{l_{\max,g}} g^{(l)}(\mathbf{x}_\perp) z^l. \quad (325)$$

Here, $g^{(l)}$ and $\phi^{(l)}$ denote z -independent coefficients of the z -dependent functions g_z and ϕ_z . Since we assume a pure-phase object with $g_{z=0} = g^{(0)} = 0$, the summation index in the ansatz for g_z starts at $l = 1$. To determine the coefficients $g^{(l)}$ and $\phi^{(l)}$, we substitute ansatz Eqs. (324) and (325) into the imaginary part of the paraxial wave equation (322) and sort by powers in z . The resulting equation demands that the sum of coefficients of a given power in z has to vanish individually to each power in z . Comparing coefficients to lowest order in z yields

$$g^{(1)} = -\frac{1}{k} \nabla_\perp^2 \phi^{(0)}. \quad (326)$$

To linear order in z and using Eq. (326) we have

$$\begin{aligned} g^{(2)} &= -\frac{1}{2k} \left[\nabla_\perp g^{(1)} \cdot \nabla_\perp \phi^{(1)} + \nabla_\perp^2 \phi^{(1)} + g^{(1)} \nabla_\perp^2 \phi^{(0)} \right] \\ &= \frac{1}{2k} \left[\frac{1}{k} \left((\nabla_\perp \nabla_\perp^2 \phi^{(0)}) \cdot \nabla_\perp \phi^{(0)} + (\nabla_\perp^2 \phi^{(0)})^2 \right) - \nabla_\perp^2 \phi^{(1)} \right]. \end{aligned} \quad (327)$$

Coefficients $\phi^{(l)}$ can be computed from Eq. (324) as

$$\phi^{(l)} = \lim_{z \rightarrow 0} \frac{1}{l!} \partial_z^l \phi_z \equiv \lim_{z \rightarrow 0} \frac{1}{l!} \frac{\partial^l}{\partial z^l} \phi_z. \quad (328)$$

The coefficient $\phi^{(1)}$ in Eq. (327) then follows from Eqs. (323) and (328) in the limit $z \rightarrow 0$ as

$$\phi^{(1)} = \lim_{z \rightarrow 0} \partial_z \phi_z = -\frac{1}{2k} (\nabla_\perp \phi^{(0)})^2. \quad (329)$$

Setting $l_{\max,g} = 1$ and $l_{\max,\phi} = 0$ in Eqs. (324) and (325), respectively, and using Eq. (326), we obtain to linear order in z

$$\nabla_\perp^2 \phi_{z=0} \equiv \nabla_\perp^2 \phi^{(0)} = -\frac{k}{z} g_z, \quad (330)$$

which is the linearised TIE as in Section 2.3.1. Combining Eqs. (324) and (325) truncated at $l_{\max,g} = 2$ and $l_{\max,\phi} = 1$ and Eqs. (326), (327)

and (329), we obtain an expression for the Laplacian of the phase to next-to-leading order as

$$\begin{aligned} \nabla_{\perp}^2 \phi^{(0)} &= -\frac{k}{z} g_z \\ &+ \frac{z}{2k} \left[\left(\nabla_{\perp} \nabla_{\perp}^2 \phi^{(0)} \right) \cdot \nabla_{\perp} \phi^{(0)} + \left(\nabla_{\perp}^2 \phi^{(0)} \right)^2 + \frac{1}{2} \nabla_{\perp}^2 \left(\nabla_{\perp} \phi^{(0)} \right)^2 \right]. \end{aligned} \quad (331)$$

This result can also be obtained from the Fresnel diffraction integral assuming constant absorption as it was shown for the lowest-order result in Section 2.3.1, see Eqs. (250), (251) and (253). The counting in powers of z then is due to the Taylor expansion of the Fresnel propagator in Fourier space, see Eq. (250). However, in such a derivation it is hardly possible to keep track of how non-linear corrections arise. This becomes evident if we appeal directly to Eqs. (326) and (327): the first two terms in the square bracket arise from the unpropagated phase while the third term is due to the propagated phase. For later use we notice the fact, that the non-linear correction in Eq. (331) represents a sum of total derivatives in x_{\perp} . The expansion of $\nabla_{\perp}^2 \phi^{(0)}$ on the right-hand side of Eq. (331) can formally be expressed in powers of derivatives of $\phi^{(0)}$. This requires the variation of $\phi^{(0)}$ with respect to x_{\perp} to be weak. Otherwise the coefficients of the powers in z become unacceptably large when the order of the expansion in powers of z is increased.

The exit phase is linked to the data g_z via Eq. (331) representing a non-linear partial differential equation for $\phi^{(0)}$. In the following we discuss how to approach a solution to Eq. (331). In principle, Eq. (331) could be solved numerically, subjecting it to appropriate boundary conditions. Notice that linearised TIE (331) is invariant under global shifts of the gradient of the phase

$$\nabla_{\perp} \phi^{(0)} \rightarrow \nabla_{\perp} \phi'^{(0)} = \nabla_{\perp} \phi^{(0)} + \mathbf{a}, \quad (332)$$

with \mathbf{a} being a constant two-dimensional vector, and thus $\nabla_{\perp}^2 \phi'^{(0)} = \nabla_{\perp}^2 \phi^{(0)}$. The presence of additional powers of $\nabla_{\perp} \phi^{(0)}$ in Eq. (331) as compared to Eq. (330) clears this ambiguity.

Phase retrieval to leading order is only constrained by TIE, being the imaginary part of the paraxial wave equation, and represents Fresnel theory only incompletely. Expanding beyond leading order also involves the real part of the paraxial wave equation, and thus increasingly accounts for the constraints of the full Fresnel theory. This should also reduce the influence of optical vortices in $\phi^{(0)}$ [GRN95; PN98].

Instead of a brute-force numerical treatment of Eq. (331) to find a useful approximation, the right-hand side of Eq. (331) can be approached perturbatively in terms of the leading-order result obtained

from Eq. (330). This approximates the non-linear terms in the square bracket in Eq. (331) in terms of the solution $\phi^{(0)}$ of Eq. (330).

A general expression of the right-hand side of Eq. (331) is given in terms of the following power series

$$\nabla_{\perp}^2 \phi^{(0)} = \sum_{l=0}^{l_{\max,g}+1} c^{(l)}(\mathbf{x}_{\perp}) z^l. \quad (333)$$

In the ideal case, the only coefficient that remains in Eq. (333) is $c^{(0)}$. E.g. when setting $l_{\max,g} = 2$, as was assumed in the derivation of Eq. (331), the term $-\frac{k}{z} g_z$ generates a contribution $-k(g^{(1)} + g^{(2)}z)$. In the ideal case, the term in the square bracket in Eq. (331), which by definition is linear in z , cancels the linear term arising in $-\frac{k}{z} g_z$. Increasing $l_{\max,g} = 2 \rightarrow l_{\max,g} = 3$ the quadratic correction on the right-hand side of Eq. (346) cancels the quadratic term in $-\frac{k}{z} g_z$, and so forth.

Such a counting in powers of z is respected in perturbation theory, since by the inversion of the Laplacian in a truncation of the right-hand side of Eq. (331) at leading order, we yield an estimate for $\phi^{(0)}$ which is independent of z . However, this estimate does not completely cancel the respective powers in z in the term $-\frac{k}{z} g_z$ when substituted in the corrections to next-to-leading and next-to-next-to-leading order of Eq. (346). Nevertheless, the modulus of the coefficients of these powers is reduced.

Let us now discuss in more detail the next-to-leading-order (NLO) terms appearing in the square bracket in Eq. (331). Therefore, we introduce following abbreviations

$$\begin{aligned} \text{NLO}_1(\mathbf{x}_{\perp}) &= \left(\nabla_{\perp} \nabla_{\perp}^2 \phi^{(0)} \right) \cdot \nabla_{\perp} \phi^{(0)}, \\ \text{NLO}_2(\mathbf{x}_{\perp}) &= \left(\nabla_{\perp}^2 \phi^{(0)} \right)^2, \\ \text{NLO}_3(\mathbf{x}_{\perp}) &= \frac{1}{2} \nabla_{\perp}^2 \left(\nabla_{\perp} \phi^{(0)} \right)^2. \end{aligned} \quad (334)$$

To leading order we have $g^{(1)} = \frac{g_z}{z}$. Thus, in perturbation theory, the next-to-leading-order terms follow as

$$\text{NLO}_1(\mathbf{x}_{\perp}) = k^2 \left(\nabla_{\perp} g^{(1)} \right) \cdot \nabla_{\perp} \left(\nabla_{\perp}^{-2} g^{(1)} \right), \quad (335)$$

$$\text{NLO}_2(\mathbf{x}_{\perp}) = k^2 (g^{(1)})^2, \quad (336)$$

$$\text{NLO}_3(\mathbf{x}_{\perp}) = \frac{k^2}{2} \nabla_{\perp}^2 \left(\nabla_{\perp} \left(\nabla_{\perp}^{-2} g^{(1)} \right) \right)^2. \quad (337)$$

Here, ∇_{\perp}^{-2} denotes the inverse of the Laplace operator obtained via the Fourier derivative theorem (Eq. (248)), requiring an appropriate regularisation as in Eq. (290). Up to the factor $\nabla_{\perp} \phi^{(0)}$ in NLO_1 , linking the Laplacian of $\phi^{(0)}$ to the data $g^{(1)}$ in a non-local fashion, the right-hand side of Eq. (335) is local in $g^{(1)}$. Loosely speaking, $\nabla_{\perp} \phi^{(0)}$

is obtained by means of a single integration of the leading-order equation $\nabla_{\perp}^2 \phi_{z=0} = \nabla_{\perp}^2 \phi^{(0)} = -\frac{k}{z} g_z$. Furthermore, NLO₂ is completely local in $g^{(1)}$ while NLO₃ is non-local. Each of the terms NLO₁, NLO₂, and NLO₃ can be decomposed into a fluctuating and a mean part as

$$\text{NLO}_i(\mathbf{x}_{\perp}) = \langle \text{NLO}_i \rangle + \delta \text{NLO}_i(\mathbf{x}_{\perp}), \quad i = \{1, 2, 3\}, \quad (338)$$

where $\langle \text{NLO}_i \rangle$ denotes the average of NLO_i over the field of view (FOV) as

$$\langle \text{NLO}_i \rangle \equiv \frac{\int_{\text{FOV}} d^2 \mathbf{x}_{\perp} \text{NLO}_i(\mathbf{x}_{\perp})}{\int_{\text{FOV}} d^2 \mathbf{x}_{\perp}}. \quad (339)$$

Since $\text{NLO}_1 + \text{NLO}_2$ and NLO_3 separately are sums of partial derivatives, the sum of their means is zero

$$\sum_{i=1}^3 \langle \text{NLO}_i \rangle = 0. \quad (340)$$

Because NLO_3 is non-local in g_z , this term smears $g^{(1)}$ averaging out large amplitudes.

Equations (291) and (340), and the conservation of average intensity for pure-phase objects in forward propagation (see Eq. (86)) imply that

$$\langle g_z \rangle = 0. \quad (341)$$

From Eq. (341) it follows that the phase, retrieved by applying the regularised inverse Laplace operator $\nabla_{\perp,\alpha}^{-2}$ (Eq. (290)) to the right-hand side of Eq. (331), is of zero mean. Each of the terms $\langle \text{NLO}_1 \rangle$ and $\langle \text{NLO}_2 \rangle$ can individually be large but their sum vanishes. Deviations from this situation can occur by numerical artifacts, introduced through discrete Fourier transformations, and thus are subtracted (see also Section 2.3.3.1). In Section 2.1.6 we have expressed the exact phase by a line integral over the real decrement δ_{ω} of the sample's refractive index. Due to δ_{ω} being semi definite, the exact phase exhibits a non-vanishing mean. This ambiguity, already inherent to Fresnel theory (see Eq. (102)), persists in the perturbative approach: the addition of an arbitrary constant to the phase

$$\phi^{(0)}(\mathbf{x}_{\perp}) \equiv \langle \phi^{(0)} \rangle + \delta \phi^{(0)}(\mathbf{x}_{\perp}), \quad (342)$$

does not change Eq. (331) for $\phi^{(0)}$. Therefore, when comparing exact (simulated) with retrieved phase, we subtract the mean values of which.

Let us now compare the perturbative approach with phase retrieval based on CTF. In position space and for pure-phase objects CTF reads

$$g_z(\mathbf{x}_{\perp}) = -2 \left[\sum_{l=1}^{\infty} \frac{1}{(2l-1)!} \left(\frac{z}{2k} \right)^{2l-1} (\nabla_{\perp}^2)^{2l-1} \right] \phi_0(\mathbf{x}_{\perp}). \quad (343)$$

The inversion of Eq. (343) corresponds to an infinite summation of powers of ∇_{\perp}^2 acting on $\phi^{(0)}$. Note that the expansion Eq. (325) contains these powers of ∇_{\perp}^2 in a truncated way, see left-hand side of Eq. (331) multiplied by z at order z . In addition to these terms non-linear corrections in $\phi^{(0)}$ enter at these orders. Therefore, the assumption of weak phase variations (Eq. (260)) can be increasingly relaxed by taking increasing powers of z into account in Eq. (325). The series of Eq. (325) expands in powers of transverse derivatives including non-linearities in $\phi^{(0)}$. On the contrary, the expansion in Eq. (343) takes into account all powers of the Laplacian ∇_{\perp}^2 at linear order in $\phi^{(0)}$ only. For pragmatic reasons, the non-linear expansion of Eq. (325) requires to be truncated at a finite order in z . Thus, large frequencies are retrieved worse than they are by inverting Eq. (343) within the validity regime of this equation.

4.1.2 Next-to-next-to-leading-order correction

The formal expansion of $\nabla_{\perp}^2 \phi_z$ in powers of $\frac{z}{k}$ can be carried out to higher orders. Truncation of ansatz Eqs. (324) and (325) at $l_{\max,g} = 2$ and $l_{\max,\phi} = 1$, yields the coefficient of g_z to third order in z

$$g^{(3)} = -\frac{1}{3k} \left[\nabla_{\perp} g^{(1)} \cdot \nabla_{\perp} \phi^{(1)} + \nabla_{\perp} g^{(2)} \cdot \nabla_{\perp} \phi^{(0)} + \nabla_{\perp}^2 \phi^{(2)} + g^{(1)} \nabla_{\perp}^2 \phi^{(1)} + g^{(2)} \nabla_{\perp}^2 \phi^{(0)} \right]. \quad (344)$$

The coefficient of ϕ_z to second order in z is obtained from Eq. (323) and its z -derivative in the limit $z \rightarrow 0$ as

$$\begin{aligned} \phi^{(2)} &= \frac{1}{4k} \left[\frac{1}{2} \nabla_{\perp}^2 g^{(1)} - 2 \nabla_{\perp} \phi^{(0)} \cdot \nabla_{\perp} \phi^{(1)} \right] \\ &= \frac{1}{4k^2} \left[-\frac{1}{2} \nabla_{\perp}^4 \phi^{(0)} + \nabla_{\perp} \phi^{(0)} \cdot \nabla_{\perp} (\nabla_{\perp} \phi^{(0)})^2 \right]. \end{aligned} \quad (345)$$

The Laplacian of the exit phase including the corrections up to next-to-next-to leading order then reads

$$\begin{aligned}
\nabla_{\perp}^2 \phi^{(0)} = & - \left(\frac{z}{k} \right)^{-1} g_z \\
& + \frac{1}{2} \left(\frac{z}{k} \right) \left[\left(\nabla_{\perp} \nabla_{\perp}^2 \phi^{(0)} \right) \cdot \nabla_{\perp} \phi^{(0)} + \left(\nabla_{\perp}^2 \phi^{(0)} \right)^2 \right. \\
& \quad \left. + \frac{1}{2} \nabla_{\perp}^2 \left(\nabla_{\perp} \phi^{(0)} \right)^2 \right] \\
& + \frac{1}{12} \left(\frac{z}{k} \right)^2 \left[2 \nabla_{\perp} \left(\nabla_{\perp}^2 \phi^{(0)} \right) \cdot \nabla_{\perp} \left(\nabla_{\perp} \phi^{(0)} \right)^2 \right. \\
& \quad \left. + 2 \nabla_{\perp} \phi^{(0)} \cdot \nabla_{\perp} \left(\nabla_{\perp} \phi^{(0)} \cdot \nabla_{\perp} \left(\nabla_{\perp}^2 \phi^{(0)} \right) \right) \right. \\
& \quad \left. + 2 \nabla_{\perp} \phi^{(0)} \cdot \nabla_{\perp} \left(\nabla_{\perp}^2 \phi^{(0)} \right)^2 + \nabla_{\perp} \phi^{(0)} \cdot \nabla_{\perp} \left(\nabla_{\perp}^2 \left(\nabla_{\perp} \phi^{(0)} \right)^2 \right) \right. \\
& \quad \left. - \frac{1}{2} (\nabla_{\perp}^2)^3 \phi^{(0)} + \nabla_{\perp}^2 \left(\nabla_{\perp} \phi^{(0)} \cdot \nabla_{\perp} \left(\nabla_{\perp} \phi^{(0)} \right)^2 \right) \right. \\
& \quad \left. + 3 \nabla_{\perp}^2 \phi^{(0)} \nabla_{\perp}^2 \left(\nabla_{\perp} \phi^{(0)} \right)^2 \right. \\
& \quad \left. + 2 \nabla_{\perp}^2 \phi^{(0)} \nabla_{\perp} \phi^{(0)} \cdot \nabla_{\perp} \left(\nabla_{\perp}^2 \phi^{(0)} \right) + 2 \left(\nabla_{\perp}^2 \phi^{(0)} \right)^3 \right]. \tag{346}
\end{aligned}$$

4.1.3 Non-Linear phase retrieval

Let us now apply the algorithm for non-linear phase retrieval devised in Section 4.1.1 to simulated data. A Siemens star pattern is taken as pure-phase test object. The ad hoc regularisation of Eq. (290) is used to invert the Laplacian in Eq. (331), both in the perturbative estimate and the final expression for $\phi^{(0)}$.

To characterise the dependence of the retrieved phase on the regularisation parameter α we define a function Φ as follows

$$\Phi(\alpha) \equiv \sum_{\mathbf{x}_{\perp}} |\phi^{(0)}(\mathbf{x}_{\perp})|, \tag{347}$$

where $\phi^{(0)}$ is the retrieved phase with a regularisation parameter α . The value of α is then chosen such that $\Phi(\alpha)$ is least sensitive to a variation in α . For the Siemens-star phantoms considered we observe $\Phi(\alpha)$ to be insensitive over a region of several orders of magnitude with a central value of $\alpha_c \sim 10^{-6}$.

To measure the performance achieved when including the perturbatively evaluated correction terms in Eq. (331) compared to the leading-order linear term, we define the absolute difference map Ψ as

$$\Psi \equiv |\phi^{(0)} - \phi^{(0,\text{exact})}|, \tag{348}$$

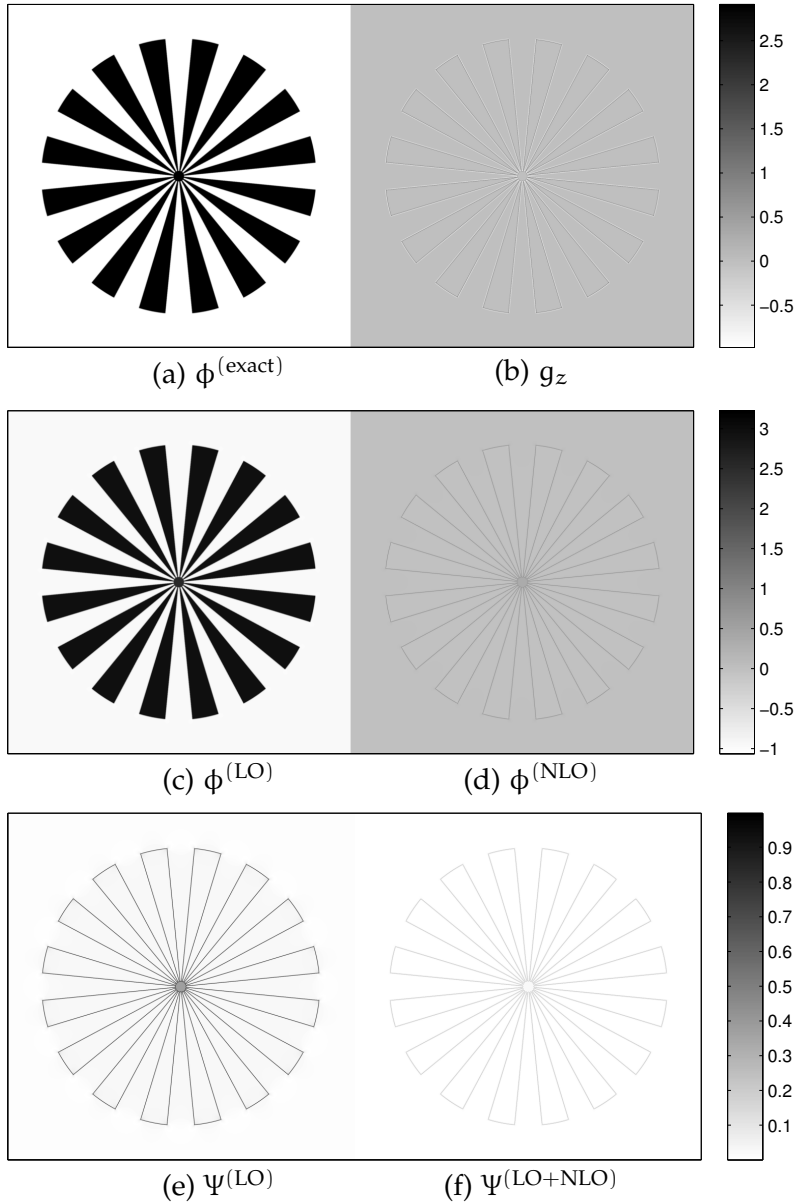


Figure 30: Phase and intensity maps for a Siemens star phase object in central projection at a resolution of 2048×2048 pixels. Mean values were subtracted in all cases. (a) Exact phase map at $z = 0$. (b) Map of the intensity contrast at $z = 0.3$ m generated from the input phase map (a) by Fresnel propagation. (c) Leading-order phase $\phi^{(LO)}$ retrieved from intensity map (b). (d) Next-to-leading-order correction $\phi^{(NLO)}$. (e,f) Difference maps $\Psi^{(NLO)}$ and $\Psi^{(LO+NLO)}$, see Eq. (348) for definition. Cuts of the phase maps presented in Fig. 31 are taken along the green line indicated in (a). Image adopted with modifications from [Moo+10].

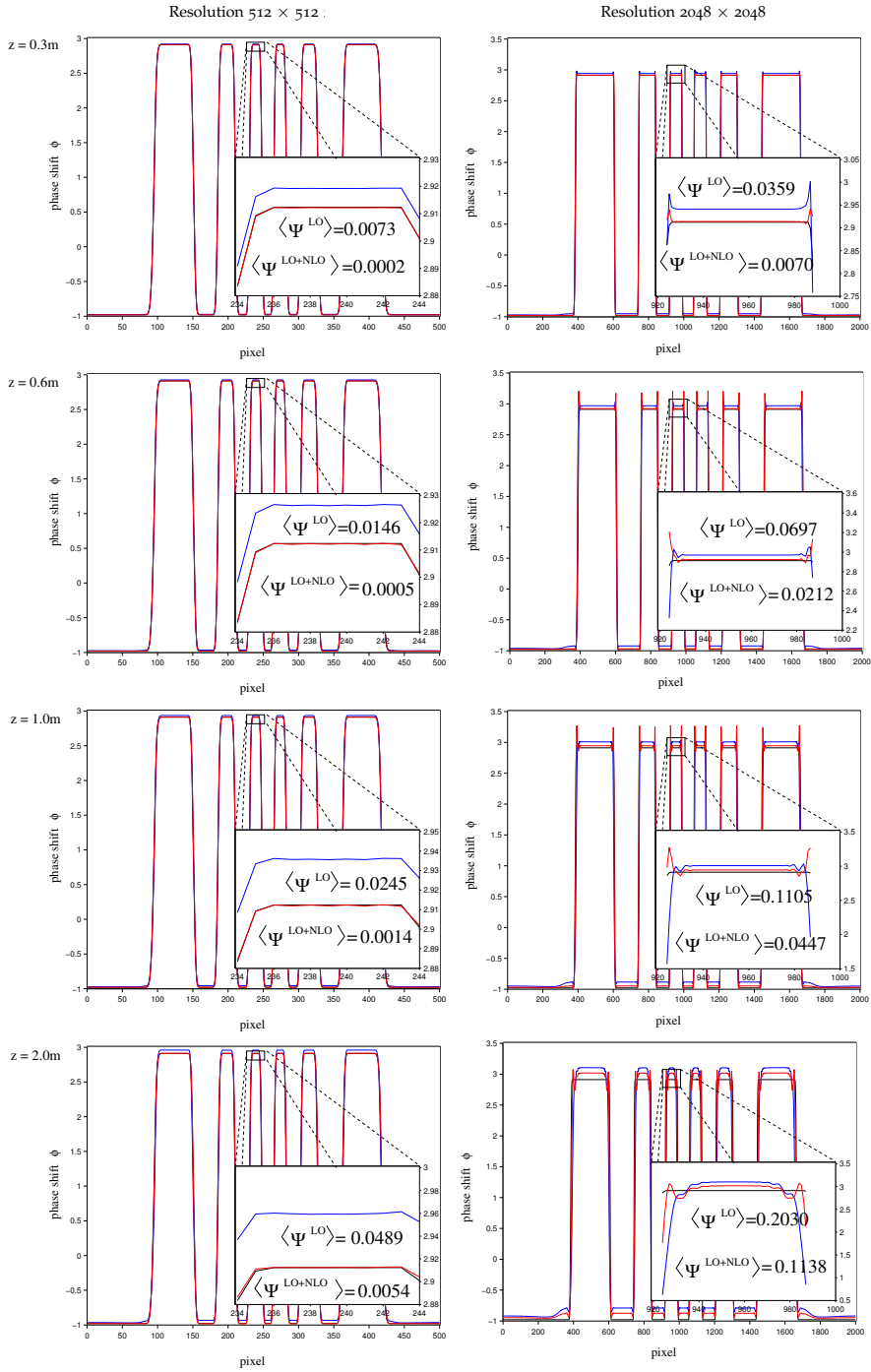


Figure 31: Line cuts through phase maps along the line indicated in Fig. 30(a) for a Siemens star with 32 spokes in dependence of propagation distance z (top to bottom) and at two distinct resolutions (left to right). Black lines: exact phase. Blue and red lines: phase retrieval referring to leading-order and when including next-to-leading-order. Image adopted with slight modifications from [Moo+10]

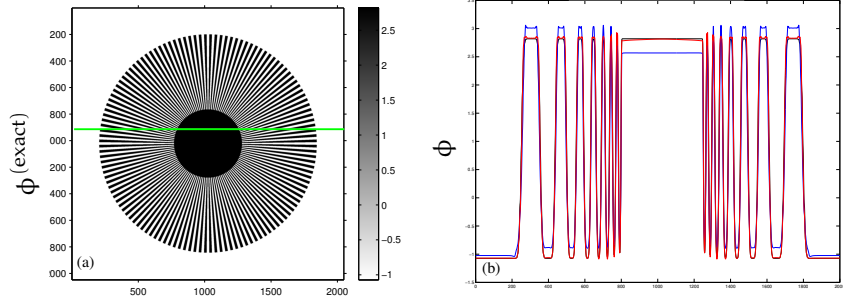


Figure 32: Phase maps of a Siemens star with 256 spokes in central projection at a resolution of 2048×2048 pixels. (a) Exact phase map at $z = 0$. (b) Line cut through exact phase map (black), leading-order result for phase retrieval (blue), and for phase retrieval including next-to-leading order (red) at $z = 0.3$ m. For the error measure we have $\langle \Psi^{(LO)} \rangle = 0.1535$ and $\langle \Psi^{(LO+NLO)} \rangle = 0.0347$, respectively. Image adopted with slight modifications from [Moo+10]

where $\phi^{(0)}$ either is the result to leading order (LO) or including the next-to-leading order (LO + NLO). A global error measure is given by $\langle \Psi \rangle$ defined as the mean of Ψ over all pixels as in Eq. (339).

Phase retrieval to leading and next-to-leading order is indicated in Fig. 30. Simulations were performed for a central projection of the Siemens star with $\delta_\omega = 10^{-7}$ at an X-ray energy of $E = 30$ keV on a $\delta_\omega = 0$ background, and for a thickness $d = 0.256$ mm. In order to avoid problems arising from unresolvable spokes segments, we introduced a central disk with constant phase shift at the centre of the Siemens star. The exact phase map, from which the intensity is computed by free-space propagation, is obtained from a Gaussian blurred version of the Siemens star. This is to avoid extreme phase jumps at object edges.

As Fig. 30(e) and (f) indicates, the difference map Ψ decreases when next-to-leading corrections are taken into account. To investigate the dependence on distance and resolution of the retrieved phase, we have considered line cuts through the phase map as indicated in Fig. 30(a) and shown in Fig. 31. When the standard deviation of the Gaussian blur is kept constant at 1.5 pixels, results do not change substantially for values of δ_ω smaller than 10^{-7} . (At a higher resolution the averaged-over length scale is thus shorter.) However, for $\delta_\omega > 10^{-6}$ strong deviations of retrieved from exact phase maps occur, both to leading order and next-to-leading order. This suggests that the assumption of weak phase variations to be violated. Strong phase variations yield large values of the coefficients in the power series of Eq. (333), impairing the convergence properties of the expansion.

Including next-to-leading order corrections closely retrieves the exact phase at a low pixel resolution (or large physical blurring scale),

see left column in Fig. 31. This holds for all distances z as indicated in Fig. 31. At high spatial resolution, phase retrieval is still observed to be improved, but edge-related artifacts induced by a stronger varying phase (smaller physical blurring scale) occur, see right column in Fig. 31. Increasing the spatial resolution at a fixed physical blurring scale we observe quantitatively stable results.

A more complex situation is investigated in Fig. 32, where the numbers of spokes in the Siemens star is increased and a large central disk is added. Thereby a hierarchy of scales is introduced to the object, given by the typical diameter of a spoke to the diameter of the disk. Comparing this case with the first line of Fig. 31, the leading-order result is observed to deviate much stronger from the exact phase in Fig. 32 than in Fig. 31. In particular, the leading-order retrieval in Fig. 32 overestimates phase shifts introduced by the spokes and underestimates phase shifts for the central region. When including corrections to next-to-leading order, we yield a significantly improved phase retrieval which makes up for a $\sim 10\%$ deviation of the leading-order result. In Fig. 32 the tendency of leading-order retrieval to over- or underestimate the phase shift is remedied, such that the mean value remains at zero at a slightly overestimated background to leading order and a well retrieved background when including next-to-leading order corrections. Phase retrieval beyond leading order being more accurate is due to the non-linearity of the corrections (maximal difference in phase shifts ~ 4). The inclusion of all powers of the Laplacian (CTF) but exclusion of non-linear corrections is expected to have improved on the edge-related artifacts only.

4.2 QUASIPARTICLE APPROACH

In the previous section we have discussed the relation between exit phase $\phi_0 \equiv \phi_{z=0}$ and propagated intensity contrast g_z in Fresnel theory, evading an exact inversion of the forward problem. This is due to couplings of transverse derivatives of ϕ_0 contributing non-linearly with up to infinite powers to g_z [Moo+10]. An expression up to quadratic order in ϕ_0 is given in Eq. (253). Large phase variations $\delta\phi_0$ thus represents strongly coupled classical fields, excluding a perturbative approach to the inverse problem as in Section 4.1. Upon identifying a scaling symmetry of the exit phase in the limit of vanishing phase variations $\phi_0 \rightarrow 0$ through the global $U(1)$ phase-shift invariance and analysing of how this symmetry is explicitly and dynamically broken by finite $\delta\phi_0$, the phase retrieval problem can be addressed in an efficient and non-perturbative fashion. Up to phase variations $|\delta\phi_0|$ in the order of unity, or more precisely up to the point where scaling symmetry is dynamically unbroken, the essentially non-linear relation between $\delta\phi_0$ and g_z can be rendered quasi-linear. This is reminiscent of the quasiparticle approach to systems of moderately

interacting point particles - a ubiquitous concept in condensed-matter and plasma physics and quantum field theory [Lan57; AK59; Hof11].

Fortuitously, essential characteristics of the linear contrast transfer persist in the quasiparticle sense. I.e. the dependence of contrast transfer on propagation distance z and shot noise favouring large values of z , the high spatial resolution of the retrieved phase ϕ_0 , and the feasibility of phase-attenuation duality for high X-ray energies and/or chemically homogeneous samples.

The analysis presented in the following is closely related to the work presented in [MHB11b; HMB11; Hof+14].

4.2.1 Linear models

Non-deterministic emission of photons by the X-ray source, light-matter interactions within the object, and the detection process entail random fluctuations of the noiseless intensity I_z . In the case of negligible camera dark currents or directly converting single-photon counting detectors, these fluctuations can effectively be modelled by Poisson statistics (shot noise). Invoked by short exposure times, shot noise then dominates. Predominantly impairing intensity contrast at small scales, shot noise in the intensity is a limiting factor reducing the maximum spatial resolution of $2\Delta x$ in the retrieved phase map. Given an X-ray beam of sufficiently high coherence, we now show on simulated phantom data that the average signal-to-noise ratio (SNR) of g_z enhances with increasing values of the propagation distance z . Phantom data is generated upon computing intensity maps from an exit wave front by forward propagation using full Fresnel theory (Eq. (93)). A pure-phase object is assumed with the Lena test pattern (512×512 pixels) used as phantom, see Figs. 18 and 33(a). The Lena test pattern is immersed in a background of zero phase shift with 1024×1024 pixels (symmetric zero padding).

Assuming perfect spatio-temporal coherence, parallel-beam incidence, and neglecting the effects of shot noise, a two-fold application of the Fresnel diffraction integral (see Section 2.3.2) yields

$$\hat{I}_z(\xi_{\perp}) = \int d^2x_{\perp} \exp(-i2\pi x_{\perp} \xi_{\perp}) \Psi_0(x_{\perp} - \frac{\lambda z}{2} \xi_{\perp}) \Psi_0^*(x_{\perp} + \frac{\lambda z}{2} \xi_{\perp}), \quad (349)$$

where $\hat{I}_z \equiv \mathcal{F} I_z$ demands Fourier transform of I_z as in Eq. (A.18). In the pure-phase case ($B = 0$) the exit wave fields reads $\Psi_0 = I^{(in)} \exp(i\phi_0)$. Expanding the exponential in Ψ_0 up to quadratic order

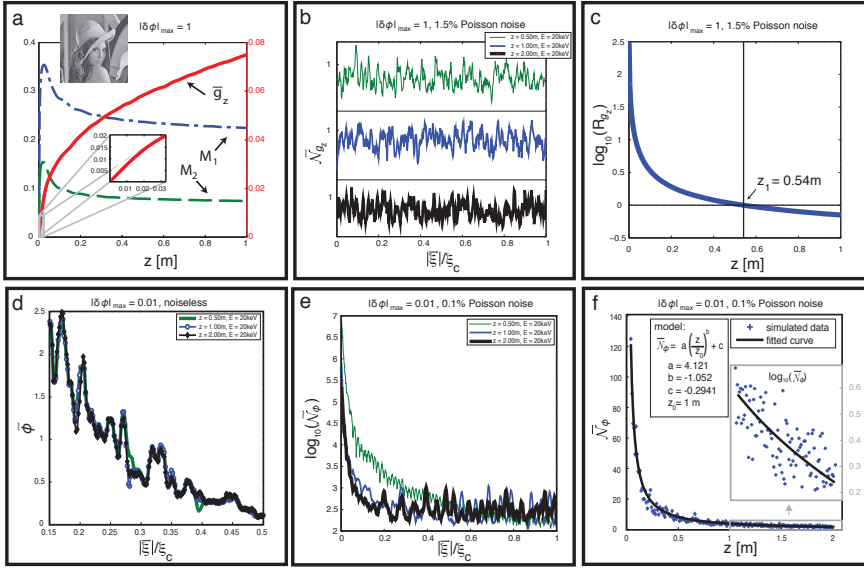


Figure 33: Analysis of image formation in full Fresnel theory and linear phase retrieval subject to statistical noise and in dependence of propagation distance z . A pure-phase object is assumed using the Lena test pattern as input phase map. At $E = 20$ keV, an exit phase with a maximum variation of $|\delta\phi_0|_{\max} = 1$ is the input for the simulated forward propagation used in (a) through (c) and of $|\delta\phi_0|_{\max} = 0.01$ (linear case) in (d) through (f). a, Transverse average of modulus of intensity contrast \bar{g}_z , and associated first and second moments, M_1 and M_2 , of function $|\hat{g}_z|$ in dependence of z . The peak positions of M_1 and M_2 indicate maximum edge enhancement. b, Radial spectra \tilde{N}_{g_z} , i.e. the angle averaged modulus of the Fourier transform of intensity noise N_{g_z} , for three distinct values of z and a shot-noise level of 1.5 % on I_z . Spectra exhibit white-noise nature and z independence. c, Semi-log plot of noise-to-signal ratio R_{g_z} (transverse average noise modulus \bar{N}_{g_z} to transverse average signal modulus of \bar{g}_z). d, Radial spectra \tilde{N}_{ϕ_0} of phase retrieved from noiseless g_z for three distinct values of z . Spectra are independent of z . e, Semi-log plot of radial noise spectra \tilde{N}_{ϕ_0} of phase maps retrieved from $I_z^{(\text{noise})}$ subject to 0.1 % shot noise and for three distinct values of z . f, Transverse average of modulus of noise \bar{N}_{ϕ_0} in phase map retrieved from $I_z^{(\text{noise})}$ subject to 0.1 % noise as a function of z . Image adopted from [Hof+14].

in ϕ_0 , yields upon substitution into Eq. (349) and use of the convolution theorem (Eq. (A.15))

$$\begin{aligned}\widehat{g}_z(\xi_{\perp}) &= 2 \sin(\pi \lambda z \xi^2) \widehat{\phi}_0(\xi) \\ &\quad - \cos(\pi \lambda z \xi^2) \int d^2 \xi' \widehat{\phi}_0(\xi') \widehat{\phi}_0(\xi - \xi') \\ &\quad + \exp(i \pi \lambda z \xi^2) \int d^2 \xi' \exp(-i 2 \pi \lambda z \xi \cdot \xi') \widehat{\phi}_0(\xi') \widehat{\phi}_0(\xi - \xi') \\ &\quad + O((\widehat{\phi}_0)^3).\end{aligned}\tag{350}$$

Given that ϕ_0 satisfies the CTF criterion of weakly varying phases,

$$|\delta\phi_0| \equiv |\phi_0(x_{\perp} - \frac{\lambda z}{2} \xi_{\perp}) - \phi_0(x_{\perp} + \frac{\lambda z}{2} \xi_{\perp})| \ll 1,\tag{351}$$

the right-hand side of Eq. (350) can be truncated at linear order in $\widehat{\phi}_0$, restoring linear transfer of contrast from $\widehat{\phi}_0$ to \widehat{g}_z as

$$\widehat{g}_z(\xi_{\perp}) = 2 \widehat{\phi}_0(\xi_{\perp}) \sin(\pi \lambda z \xi_{\perp}^2),\tag{352}$$

which is the known contrast transfer function (CTF). Provided that \widehat{g}_z exhibits zeros of the same order as those of the sine function in Eq. (352), which are given by

$$|\xi_{\perp}|_m \equiv \sqrt{\frac{m}{\lambda z}}, \quad m = \{0, 1, 2, \dots\},\tag{353}$$

CTF retrieval in Fourier space does not produce singularities.

In the limit $z \rightarrow 0$, the power-series expansion in Eq. (350) is dominated by the linear-in- z part of the linear-in- $\widehat{\phi}_0$ term, and linearised TIE (264) is recovered. In the following we will refer to the algebraic inversion of Eq. (264) as Paganin phase retrieval [Pago6]. Comparing the inverse transfer functions related to Paganin and CTF retrieval as depicted in Fig. 16, Paganin phase retrieval is observed to suppresses high-frequency information within the frequency band of

$$\xi_p \equiv \frac{1}{\sqrt{2 \lambda z}} < |\xi_{\perp}| < \xi_c.\tag{354}$$

The spatial cut-off frequency ξ_c is set by the effective linear pixel size Δx to $\xi_c = \frac{1}{2 \Delta x}$. Unless $\xi_c \propto \xi_p$ (Fig. 33(a)), Paganin phase retrieval depletes attainable compared to the maximum resolution set by the pixel size to $2 \Delta x$. For $E = 20$ keV and $\Delta x = 1 \mu\text{m}$, this already occurs at $z \approx 3.2$ cm. The short exposure times typically required for in vivo imaging result in count rates per pixel in the order of 4500. Imaging at such low values of z , intensity contrast g_z is unacceptably low compared to the high shot noise. The associated noise-to-signal ratio is denoted by R_{g_z} (see Fig. 33(c)). Conveniently, we define the maximum absolute phase variation $|\delta\phi_0|_{\max}$ as the maximum of the

left-hand-side of Eq. (351) over all admissible values of \mathbf{x}_\perp and ξ_\perp : $|\delta\phi_0|_{\max} = \max |\delta\phi_0|$. Furthermore, we introduce the average signal modulus \bar{g}_z and the associated spectral moments M_1 and M_2 . \bar{g}_z is defined as the average of the modulus of the intensity contrast

$$\bar{g}_z \equiv \langle |g_z| \rangle \equiv \frac{1}{A_{\text{FOV}}} \int_{\text{FOV}} d^2\mathbf{x}_\perp |g_z(\mathbf{x}_\perp)| , \quad (355)$$

where the normalisation factor A_{FOV} is the area related to the field of view (FOV) of detector

$$A_{\text{FOV}} \equiv \int_{\text{FOV}} d^2\mathbf{x}_\perp . \quad (356)$$

The i -th spectral moment is defined as

$$M_i \equiv \frac{1}{\int d^2\xi_\perp} \int d^2\xi_\perp \frac{|\xi_\perp|^i}{\xi_c} |\hat{g}_z(\xi_\perp)| , \quad (357)$$

where the region of integration is set by the cut-off frequency ξ_c . Thus the normalisation factor Eq. (357) reads $\frac{1}{\int d^2\xi_\perp} = (\Delta x)^2$. The behaviour of \bar{g}_z , and the spectral moments M_1 and M_2 as function of propagation distance z is depicted in Fig. 33(a) for phase variations of $|\delta\phi_0|_{\max} = 1$. As implied by linearised TIE, there is a linear rise of \bar{g}_z due to local contrast growth at edges of ϕ_0 up to the peak position z_p of M_1 and M_2 where maximum edge enhancement occurs. Though the amplitude of a given fringe saturates as z increases, the average signal modulus \bar{g}_z still increases beyond z_p . This is due to the tiling of the field of view through multiple, resolvable fringes per edge.

4.2.2 Influence of noise

In the following we investigate how this situation is influenced by shot noise. We define the noise of N_Q of a quantity Q as the difference between Q , evaluated for a given noise level of I_z , and Q , evaluated on the noiseless intensity I_z ,

$$N_Q(I_z) \equiv Q(I_z^{(\text{noise})}) - Q(I_z) . \quad (358)$$

Analogue to Eq. (355), we define the average noise modulus of g_z as

$$\bar{N}_{g_z} \equiv \frac{1}{A_{\text{FOV}}} \int_{\text{FOV}} d^2\mathbf{x}_\perp |N_{g_z}(\mathbf{x}_\perp)| , \quad (359)$$

with A_{FOV} as in Eq. (356). The noise-to-signal ratio then reads

$$R_{g_z} = \frac{\bar{N}_{g_z}}{\bar{g}_z} . \quad (360)$$

Figure 33(c) depicts R_{g_z} assuming a shot-noise level of 1.5 % on I_z . While R_{g_z} is large for $z < z_1$, it falls below unity beyond $z = z_1$, and

continuously approaches zero for $z \rightarrow \infty$ as implied by the behaviour of \bar{g}_z and \mathcal{N}_{g_z} in Fig. 33(a,b). Experimentally, the propagation distance cannot be raised indefinitely due to partial spatial coherence. According to the van-Cittert-Zernike theorem (Eq. (164)), the spatial extent of an incoherently emitting source introduces a blurring of sample points in the detected intensity maps. Using Eq. (196), the blur b relates to the propagation-induced transverse coherence length l_{\perp} (Eq. (184)) as

$$b \approx \frac{1}{2\xi_b} \approx \frac{\lambda z}{2l_{\perp}}, \quad (361)$$

where ξ_b denotes the blurring-induced cut-off frequency. Only if $b \lesssim \Delta x$ does contrast transfer (in Fourier space) reach the cut-off frequency ξ_c in compliance with Eq. (351). Otherwise, the source function suppresses frequencies in \hat{g}_z above $\xi_b \sim \frac{l_{\perp}}{\lambda z}$ [BW09; Wol07].

Let us now consider the influence of shot noise on the retrieved phase. Therefore, we define the radial phase spectra and the associated radial noise spectra as

$$\tilde{\phi}_0(\xi_{\perp}) \equiv \frac{1}{2\pi A_{\text{FOV}}} \int_0^{2\pi} d\theta |\hat{\phi}_0| \quad (362)$$

and

$$\tilde{\mathcal{N}}_{\phi_0}(\xi_{\perp}) \equiv \frac{1}{2\pi A_{\text{FOV}}} \int_0^{2\pi} d\theta |\hat{\mathcal{N}}_{\phi_0}|, \quad (363)$$

with A_{FOV} as in Eq. (356). Figure 33(d,e) depicts the radial spectra $\tilde{\phi}_0$ and the associated radial noise spectra $\tilde{\mathcal{N}}_{\phi_0}$ of the phase retrieved from CTF for three distinct values of z . While the radial spectra $\tilde{\phi}_0$ are approximately independent of z (Fig. 33(d)), the radial noise spectrum $\tilde{\mathcal{N}}_{\phi_0}$ as well as the average noise modulus $\bar{\mathcal{N}}_{\phi_0}$ fall off with increasing z as shown in Fig. 33(e) and (f), respectively.

We continue by analysing the z -dependence of the average noise modulus of the retrieved phase. We have

$$\begin{aligned} \bar{\mathcal{N}}_{\phi_0} &= \left\langle \left| \phi_0^{(\text{noise})} - \phi_0 \right| \right\rangle \\ &= \left\langle \left| \mathcal{F}^{-1} \frac{\mathcal{F} g_z^{(\text{noise})}}{f(|\xi_{\perp}|)} - \mathcal{F}^{-1} \frac{\mathcal{F} g_z}{f(|\xi_{\perp}|)} \right| \right\rangle \\ &= \left\langle \left| \mathcal{F}^{-1} \frac{\mathcal{F} \mathcal{N}_{g_z}}{f(|\xi_{\perp}|)} \right| \right\rangle, \end{aligned} \quad (364)$$

with ϕ_0 and g_z evaluated on the noiseless intensity I_z , and $f(|\xi_{\perp}|)$ denoting one of the transfer functions in Eqs. (263), (264), (273) and (275), respectively. The value of $\bar{\mathcal{N}}_{\phi_0}$ is dominated by the low-frequency

components on the right-hand side of Eq. (364), which we thus may approximate as

$$\begin{aligned}\bar{\mathcal{N}}_{\phi_0} &= \left\langle \left| \mathcal{F}^{-1} \frac{\mathcal{F} \mathcal{N}_{g_z}}{f(|\xi_\perp|)} \right| \right\rangle \propto \left\langle \left| \mathcal{F}^{-1} \frac{\mathcal{F} \mathcal{N}_{g_z}}{f(|\xi_\perp| \approx 0)} \right| \right\rangle \\ &\propto \frac{\langle |\mathcal{F}^{-1} \mathcal{F} \mathcal{N}_{g_z}| \rangle}{f(|\xi_\perp| \approx 0)} \\ &\propto \frac{\langle |\mathcal{N}_{g_z}| \rangle}{f(|\xi_\perp| \approx 0)}.\end{aligned}\quad (365)$$

Close to $|\xi_\perp| = 0$, the transfer function of Eqs. (263), (264), (273) and (275) are approximated by

$$\begin{aligned}f(|\xi_\perp| \approx 0) &\approx 2 (\pi \lambda z \xi_\perp^2 + \epsilon) \Big|_{|\xi_\perp| \approx 0} \\ &\approx 2 \left(\frac{\pi \lambda}{L^2} z + \epsilon \right),\end{aligned}\quad (366)$$

where have substituted the smallest finite value for $|\xi_\perp| = \frac{1}{L}$, L being the linear extend of a square detector. Here, ϵ is a small constant denoting either the duality parameter of Eq. (273) or an ad hoc regularisation as in Eqs. (287) and (294). For moderately varying phases, $|\delta\phi_0|_{\max} \lesssim 1$, variations of the intensity contrast are of the order $\mathcal{O}(1)$. Beyond edge enhancement, the (average) signal rises approximately with $g_z \propto \sqrt{z}$, see Fig. 33(a) and Fig. 17. Thus, since shot noise obeys Poisson statistics, \mathcal{N}_{g_z} increases as $\sqrt[4]{z}$ and can be considered constant. As a consequence, we infer from Eqs. (365) and (366) that phase noise decreases like z^{-1} as image detection moves towards the far-field regime:

$$\bar{\mathcal{N}}_{\phi_0} \propto \frac{1}{z}, \quad (367)$$

which is confirmed by the fit of Fig. 33(f).

4.2.3 Quasiparticle transfer of contrast

The weakly varying phase condition $|\delta\phi_0|_{\max} \ll 1$ does usually not comply with requirements imposed by in vivo X-ray phase-contrast microtomography (XPCμT) for developmental biology, see Chapter 6. E.g. an early-stage frog embryo of 1 mm diameter would produce an absolute phase shift of 152 at an X-ray energy of 30 keV, assuming a mean value of the real refractive index decrement of $\delta_\omega = 10^{-6}$. Thus assuming a phase variation of 1 %, we have $|\delta\phi_0|_{\max} \approx 1.5$, violating the validity of CTF phase retrieval. This would call for an exact inversion of Eq. (350), impossible to attain analytically.

In order to construct an approximation to the solution of Eq. (350) based on a single-distance intensity measurement, we appeal to symmetry considerations as a guiding principle. Equation (349) and every

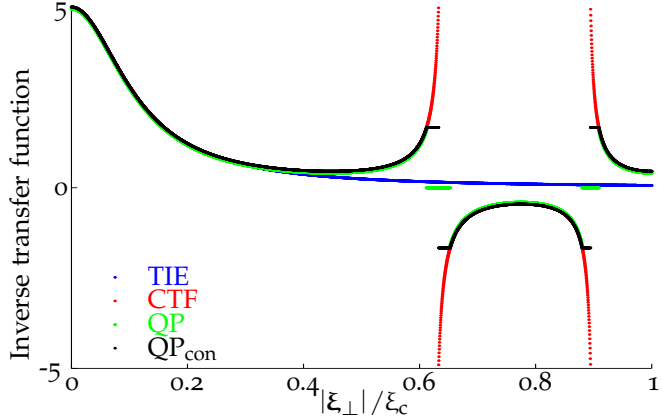


Figure 34: Radial dependence of inverse transfer functions related to linearised **TIE**, **CTF**, quasiparticle (**QP**), and modified quasiparticle (**QP_{con}**) approaches, see Eqs. (249), (265), (373) and (376), respectively. Regularisation as in Eq. (287) was used for **TIE**, and as in Eq. (294) for **CTF**, **QP**, and **QP_{con}**. Energy was set to $E = 12.4 \text{ keV}$ ($\lambda = 10^{-10} \text{ m}$), propagation distance to $z = 0.1 \text{ m}$, and pixel size to $\Delta x = 1 \mu\text{m}$, the regularisation parameter to $\alpha = 10^{-1}$, and the threshold for quasiparticle retrieval to $\delta = 0.2$. In the interest of clearer presentation, we have chosen values of α and δ considerably larger than the usually employed values for real data ranging between 10^{-2} and 10^{-3} , and 10^{-2} to 10^{-1} , respectively. The maximal cut-off frequency is $\xi_c = (2\Delta x)^{-1}$. The argument of depicted transfer function is $x = \frac{\pi\lambda z}{(2\Delta x)^2} \frac{|\xi_\perp|^2}{\xi_c^2} = 2.5\pi \frac{|\xi_\perp|^2}{\xi_c^2}$.

order in ϕ_0 in Eq. (350) are observed to be invariant under global phase shifts

$$\Psi_0 \rightarrow \exp(i\alpha) \Psi_0 = \sqrt{I_0} \exp \left[i \left(1 + \frac{\alpha}{\phi_0} \right) \right], \quad (368)$$

where α is a real parameter which determines how this global $U(1)$ symmetry acts on Ψ_0 . In the limit $|\delta\phi_0|_{\max} \rightarrow 0$ with ϕ_0 remaining finite the factor $1 + \frac{\alpha}{\phi_0}$ becomes a real constant S . Thus an invariance under global phase shifts transmutes into a symmetry under global phase scaling

$$\phi \rightarrow S\phi. \quad (369)$$

To elucidate the dynamics of forward propagation in Fresnel theory, we examine in what sense scaling symmetry persists at finite values of $|\delta\phi_0|_{\max}$. Therefore we investigate the behaviour of the radial intensity spectrum g_z under upscaling of the exit phase map as in Eq. (369), see Fig. 35(a,b) [MHB11b; HMB11]. The radial intensity contrast spectrum is defined analogue to Eq. (362) as

$$\tilde{g}_z \equiv \frac{1}{2\pi A_{\text{FOV}}} \int_0^{2\pi} d\theta |\hat{g}_z|. \quad (370)$$

By forward propagation simulated in full Fresnel theory, the zeros of \tilde{g}_z at $|\xi_\perp|_m \equiv \sqrt{\frac{m}{\lambda z}}$, as predicted by the linear-in- ϕ_0 CTF relation,

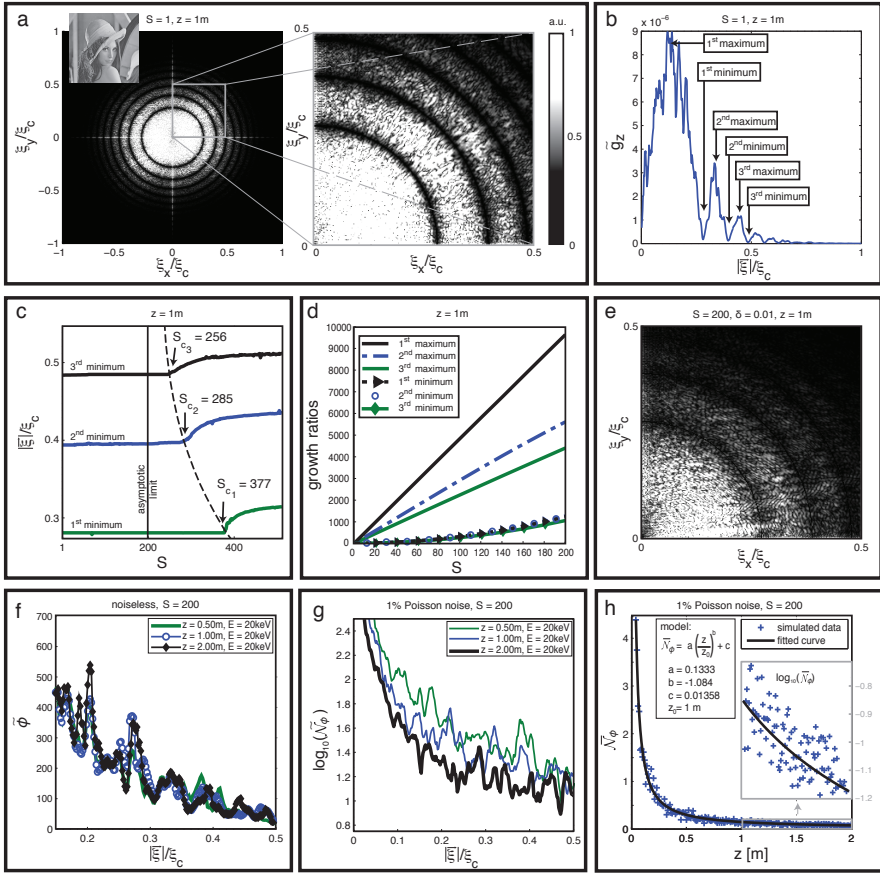


Figure 35: Quasiparticle behaviour of contrast transfer from phase to intensity up to criticality under simulated Fresnel forward propagation at $E = 20 \text{ keV}$. A maximum exit phase variation of $|\delta\phi_0|_{\max} = 0.01$, referring to the linear case with $S = 1$, is used as input for (a) and (b). In the non-linear case of (e) through (h) $S = 200$, corresponding to $|\delta\phi_0|_{\max} = 2$, is used. In (a) through (e), the propagation distance is fixed at $z = 1 \text{ m}$. a, Modulus of Fourier transform $|\tilde{g}_z|$ of intensity contrast g_z . b, Radial spectrum \tilde{g}_z . First three minima at positions $|\xi_{\perp}|_1$, $|\xi_{\perp}|_2$, and $|\xi_{\perp}|_3$ are clearly discernible. c, Minima positions $|\xi_{\perp}|_1$, $|\xi_{\perp}|_2$, and $|\xi_{\perp}|_3$ in dependence of S , upscaling the linear case. S_{c_m} appears to converge to a finite value of about 200 in the hypothetical (infinite-resolution) limit $m \rightarrow \infty$. d, Growth ratios: First three maxima and minima normalised to first minimum at $S = 1$ in dependence of S . e, Modulus of Fourier transformed modified intensity contrast, as defined in Eq. (376), for $\delta = 0.01$. f, Radial spectra $\tilde{\phi}_0$ of the phase retrieved from noiseless g_z , exhibiting independence of z . g, Semi-log plot of the radial noise spectra \tilde{N}_{ϕ_0} of phase retrieved from I_z subject to 1% shot noise for three distinct values of z . h, Transverse average of modulus of noise \bar{N}_{ϕ_0} in the phase retrieved from I_z subject to 1% Poisson noise as function of z . Image adopted from [Hof+14].

turn into minima at finite values of $|\delta\phi_0|_{\max}$. Under upscaling the phase ϕ_0 from the linear regime, where $|\delta\phi_0|_{\max} \ll 1$ at $S = 1$, the positions of these minima remain fixed at $|\xi_\perp|_m$ up to a critical value $S_c \gg 1$, where to phase variations $|\delta\phi_0|$ substantially above unity (Fig. 35(c)). The constancy of $|\xi_\perp|_m$ under phase upscaling necessitates the contribution of all orders on the right-hand-side of Eq. (350) [HMB11]. A truncation of Eq. (350) to finite, but beyond linear order in ϕ_0 would not exhibit such a behaviour.

Beyond critical upscaling $S > S_c$, the minima positions of \tilde{g}_z start to move like order parameters as in second-order phase transitions, see Fig. 35(c) for $m = \{1, 2, 3\}$. Moreover, the simulated data suggests the existence of a finite asymptote for $m \rightarrow \infty$ at $S_{c_m}, \forall m \geq 1$.

We continue by investigating of how the information of g_z is distributed in Fourier space. Let $|\xi_\perp|_{m,m-1}$ denote the positions of the maxima of \hat{g}_z in between adjacent minima at $|\xi_\perp|_m$ and $|\xi_\perp|_{m-1}$. Furthermore, we define growth ratios of the maxima and minima as

$$R_{m,m-1}(S) \equiv \frac{\tilde{g}_z(|\xi_\perp|_{m,m-1})(S)}{\tilde{g}_z(|\xi_\perp|_1)(S=1)} \quad (371)$$

and

$$R_m(S) \equiv \frac{\tilde{g}_z(|\xi_\perp|_m)(S)}{\tilde{g}_z(|\xi_\perp|_1)(S=1)}, \quad (372)$$

respectively. The dependencies of $R_{m,m-1}$ and R_m on S are depicted in Fig. 35(d) for $m = \{1, 2, 3\}$. Here, we observe a linear behaviour in S for $R_{m,m-1}$ and a non-linear one for R_m . Moreover, the curves R_m of minima growth ratios are degenerate. This indicates that non-linear terms in Eq. (350) conspire to add up to a correction periodic in $\pi\lambda z\xi_\perp^2$ and independent of S . Thus, the bulk of information in \hat{g}_z remains localised near the maximum positions $|\xi_\perp|_{m,m-1}$ as in the linear CTF case when $|\delta\phi_0|_{\max} \ll 1$ (Fig. 35(b)).

In the following, we will exploit these two properties, the inertness of the minima positions and the concentration of information near the maxima, by modifying the intensity contrast in Fourier space such that a quasi-linear contrast transfer is maintained as in Eq. (352). The modified intensity contrast $\hat{g}_z^{(QP)}$ neglects marginal, non-linear intensity contrast near minima positions $|\xi_\perp|_m$, assuring phase retrieval free of singularities. The modified intensity contrast is obtained from g_z by means of a binary filtering of \hat{g}_z for $\pi\lambda z\xi_\perp^2 > \frac{\pi}{2}$. Employing the binary filter to the singularity at zero frequencies would strongly modify the intensity contrast and distort phase retrieval. Thus, for vanishing frequencies a regularisation prescription as described in Section 2.3.4 is used. One may define the modified intensity $\hat{g}_z^{(QP)}$ as

$$\hat{g}_z(\xi_\perp) \rightarrow \hat{g}_z^{(QP)}(\xi_\perp) \equiv \Theta(|\sin(\pi\lambda z\xi_\perp^2)| - \delta) \hat{g}_z(\xi_\perp), \quad (373)$$

where Θ denotes the Heaviside step function, and $\delta \ll 1$ is a real positive constant. The domain of \hat{g}_z to be modified follows from Eq. (373) as

$$\begin{aligned}\delta &\geq |\sin(\pi\lambda z \xi_{\perp}^2)| = |\sin(\pi\lambda z (\xi_{\perp}^2 - |\xi_{\perp}|_m^2 + |\xi_{\perp}|_m^2))| \\ &= |\sin(\pi\lambda z (\xi_{\perp}^2 - |\xi_{\perp}|_m^2))| \\ &\approx |\pi\lambda z (\xi_{\perp}^2 - |\xi_{\perp}|_m^2)| \\ &= \pi\lambda z |(|\xi_{\perp}| + |\xi_{\perp}|_m)(|\xi_{\perp}| - |\xi_{\perp}|_m)| \\ &\approx \pi\lambda z 2|\xi_{\perp}|_m ||\xi_{\perp}| - |\xi_{\perp}|_m|.\end{aligned}\quad (374)$$

For $m \geq 1$, we define the set of frequencies within rings by

$$|\xi_{\perp}|_{\odot} \equiv \left\{ |\xi_{\perp}| - |\xi_{\perp}|_m \leq \frac{\delta}{2\pi\lambda z |\xi_{\perp}|_m} \right\}. \quad (375)$$

Demanding continuity, we may also employ the following modification of \hat{g}_z

$$\hat{g}_z^{(QP)}(\xi_{\perp}) \equiv \begin{cases} \frac{1}{\delta} |\sin(\pi\lambda z \xi_{\perp}^2)| \hat{g}_z(\xi_{\perp}) & \text{on rings } |\xi_{\perp}|_{\odot} \\ \hat{g}_z(\xi_{\perp}) & \text{otherwise.} \end{cases} \quad (376)$$

While phase retrieval using Eq. (373) neglects the information contained within $|\xi_{\perp}|_{\odot}$ completely, Eq. (376) takes into account a downsized version of the information within rings $|\xi_{\perp}|_{\odot}$, see Fig. 16. Practically, we do not observe a difference in using Eq. (373) or Eq. (376) for phase retrieval within a parameter range of $10^{-3} \leq \delta \leq 10^{-3}$. Thus, the neglect of information within rings $|\xi_{\perp}|_{\odot}$ is marginal. This is further justified by considering the support of the information filtered in \hat{g}_z . The cut-off frequency, set by the effective pixel size to $\xi_c = \frac{1}{2\Delta x}$, defines a disk of permissible frequencies with an area $A_c = \pi\xi_c^2$. Let A_{\odot} denote the summed area and N_{\odot} the number of rings within $|\xi| \leq \xi_c$. The latter is given by

$$N_{\odot} = \frac{\pi\lambda z \xi_c^2}{\pi} = \lambda z \xi_c^2, \quad (377)$$

and the area A_{\odot} calculates as

$$\begin{aligned}A_{\odot} &= \int_{|\xi_{\perp}|_{\odot}} d^2 \xi_{\perp} = 2\pi \int_{|\xi_{\perp}|_{\odot}} d|\xi_{\perp}| \\ &= \pi \sum_m^{N_{\odot}} |\xi_{\perp}|^2 \left[\frac{|\xi_{\perp}|_m + \frac{\delta}{2\pi\lambda z |\xi_{\perp}|_m}}{|\xi_{\perp}|_m - \frac{\delta}{2\pi\lambda z |\xi_{\perp}|_m}} \right] \\ &= \frac{2\delta}{\lambda z} \sum_m^{N_{\odot}} 1 = \frac{2\delta}{\lambda z} N_{\odot} \\ &= 2\delta \xi_c^2.\end{aligned}\quad (378)$$

Thus, the ratio of summed annular areas within disk $|\xi_{\perp}| \leq \xi_c$ to the area of the disk reads

$$R_{\odot} = \frac{A_{\odot}}{A_c} = \frac{2\delta}{\pi}, \quad (379)$$

which is small since δ is small. Thus, the support neglected in $\hat{g}_z^{(QP)}$ is not only marginal, but independent of experimental parameters E , z , and Δx .

The presented approach restores linearity between phase and intensity despite non-linear propagation effects. This is reminiscent of quasiparticle dispersion laws. In this sense, CTF represents a dispersion law between phase and intensity, when phase is associated with (complex) momentum and intensity with (complex) energy. Momentum and energy are parametrised by ξ_{\perp} labelling both effective 'particle' species away from $|\xi_{\perp}|_m$ and degenerate 'ground states' at $|\xi_{\perp}|_m$. For $S > 0$ scaling symmetry is explicitly broken by non-linear terms in Eq. (350) rendering the energies of the 'ground states', i.e. the values of the minima of \hat{g}_z at $|\xi_{\perp}|_m$, finite. However, for $S \leq S_c$, 'ground states' $|\xi_{\perp}|_m$ are invariant under phase upscaling and thus scaling symmetry remains dynamically unbroken.

Figure 35(f) depicts the angular averaged radial spectra of phase retrieved in the quasiparticle sense from noiseless g_z with parameters $S = 200$, $\delta = 10^{-2}$, and three distinct values of z . As in the linear case of Fig. 33(d), the spectra $\tilde{\phi}_0$ are independent of z . This indicates that, despite large phase variations of $|\delta\phi_0|_{\max} \approx 2$ and away from $|\xi_{\perp}|_m$, the dependence of non-linear terms on z effectively cancel in Eq. (350). At a shot-noise level of 1 %, the radial noise spectra \tilde{N}_{ϕ_0} (Fig. 35(g)) behave as in the linear case (Fig. 33(e)). This is also observed for the average noise modulus \bar{N}_{ϕ_0} of the retrieved phase as depicted in Fig. 35(h), observing the same z^{-1} decay as in Fig. 33(f).

4.2.4 Quasiparticle transfer under global phase-attenuation duality

As discussed in Section 2.3.3, absorptive effects can be accounted for assuming phase-attenuation duality, see Eq. (272). In the case of chemically homogeneous samples [Pag+02] or when quasi-free valence electron dominate the interaction of hard X-rays and matter [WLY05; WY09], we may write

$$B_0 = -\epsilon\phi_0, \quad (380)$$

where ϵ is a small positive constant, breaking the $U(1)$ phase-shift symmetry of Fresnel theory and shifting the zeros of CTF to the left (Eq. (273)) as

$$\hat{g}_z(\xi_{\perp}) = 2\sqrt{1 + \epsilon^2} \sin(\pi\lambda z \xi_{\perp}^2 + \arctan \epsilon) \hat{\phi}_0(\xi_{\perp}). \quad (381)$$

To a good approximation we may assume the refractive index of water for soft biological tissue. Thus, for energies $E = 20 \text{ keV}$ to 30 keV ,

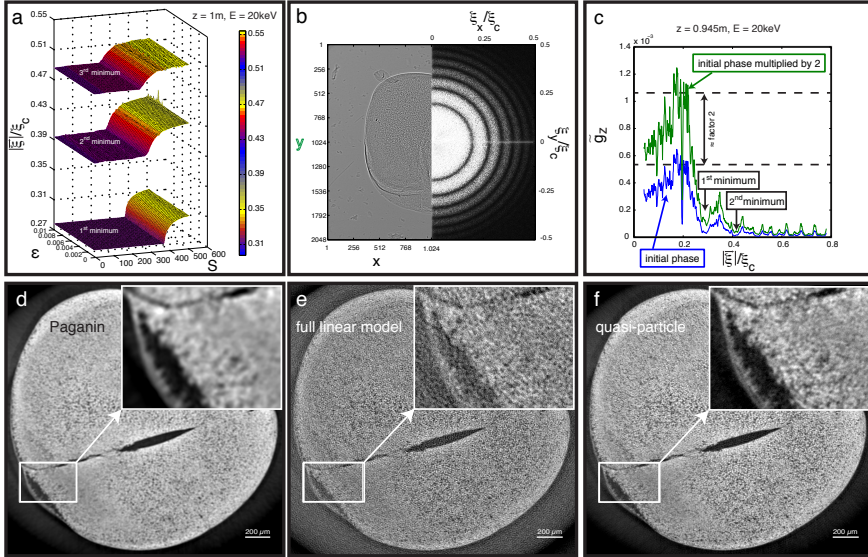


Figure 36: Global phase-attenuation duality versus upscaling and confrontation with experimental data on fixed frog embryo. (b) through (f) are based on tomographic data of a fixed, four-cell stage Xenopus frog embryo. a, Dependence of positions of first, second, and third minimum of the radial intensity spectrum \tilde{g}_z on upscaling parameter S and on duality parameter ϵ in simulated forward propagation. Lena image was used as input phase map with $|\delta\phi_0|_{\max}=0.01$ at $S=1$. The critical behaviour in S persists under variations of ϵ within $0 \leq \epsilon \leq 10^{-2}$. b, Intensity contrast g_z for a given projection angle (left) and associated modulus of its Fourier transform $|\hat{g}_z|$ (right). The visibility of several rings demonstrates the presence of information above the cut-off frequency ξ_P of Paganin phase retrieval (Eq. (354)). c, Radial spectrum \tilde{g}_z in blue is obtained from experimental data. The radial spectrum \tilde{g}_z in green results from forward propagation after upscaling the phase $\delta\phi_0$, retrieved using the quasiparticle approach with $\epsilon = 10^{-2.5}$ and $\delta = 0.1$, by a factor of two. d-f, Equal slice through tomographic reconstructions from phase maps using the phase-attenuation-duality versions of Paganin (Eq. (275)), CTF (Eq. (381)), and quasiparticle phase retrieval, respectively. Data was acquired with beamline ID19 at ESRF. Image adopted from [Hof+14].

one has $\epsilon = 6.0 \times 10^{-4}$ to 4.2×10^{-4} [HGD93]. Figure 36(a) depicts the dependence of minima positions $|\xi_{\perp}|_m$ on the upscaling parameter S and the proportionality constant ϵ within $10^{-2} \geq \epsilon \geq 10^{-3}$ in the forward simulation of g_z . The plots demonstrate that critical behaviour is maintained under phase-attenuation duality. Also, the growth ratios ($R_{m,m-1}, R_m$) of Fig. 35(d) are reproduced within this range of ϵ values.

In retrieving ϕ_0 from the experimental data related to Fig. 36(b), we have used $\delta = 10^{-1}$ and $\epsilon = 10^{-2.5}$. This value of ϵ is greater than that of water with $\epsilon_{\text{water}} \propto 0.5 \times 10^{-3}$, which is motivated by the fact that the reconstructed volumes exhibit unphysical large-scale

modulations when using ϵ_{water} for phase retrieval, see also Section 5.1. We interpret this as a violation of global phase-attenuation duality,

$$\epsilon = \text{constant} = \frac{\widehat{B}_0(\xi_{\perp})}{\widehat{\phi}_0(\xi_{\perp})}, \quad (382)$$

at small frequencies. Using Eq. (283) a value of $\langle \phi_0 \rangle$ is inferred from g_z , roughly matching the estimate obtained by projecting through water [HGD93]. Phase retrieval in Fig. 36(e) is based on Eq. (381) with the sine regularised as in Eq. (294) and a regularisation parameter $\alpha = \arctan \epsilon$. Such a prescription is superfluous when quasiparticle phase retrieval of Eqs. (373) and (376) is used.

4.2.5 *Ex vivo X-ray phase-contrast microtomography*

Here we apply XPCμT to image optically opaque embryos in developmental biology. Figure 36(b) depicts intensity contrast g_z and the associated Fourier transform $|\widehat{g}_z|$ obtained from a propagated intensity map of a fixed, four-cell stage Xenopus under parallel-beam incidence. Data was acquired with undulator beamline ID19 at ESRF at an energy $E = 20 \text{ keV}$, a monochromaticity $\frac{\Delta E}{E} = 10^{-4}$ due to a Si 111 double crystal monochromator (DCM), a sample-to-detector distance $z = 0.945 \text{ m}$, an effective detector pixel size $\Delta x = 0.75 \mu\text{m}$, a field of view of 2048×2048 pixels, an exposure time per tomographic projection $\Delta t = 2 \text{ s}$, and a number of tomographic projections over 360° of $N = 1599$. The experimental hutch is located 145 m from the source. The horizontal and vertical FWHM of the source are $s^{(h)} \approx 2.355 \times 51 \mu\text{m} \approx 120 \mu\text{m}$ and $s^{(v)} \approx 2.355 \times 9 \mu\text{m} \approx 21 \mu\text{m}$. Using the far field version of the van Cittert-Zernike theorem for an incoherent source of asymmetric Gaussian shape (Eq. (164)), the estimated horizontal and transversal transverse coherence length at the sample position are $l_c^{(h)} \approx 37 \mu\text{m}$ and $l_c^{(v)} = 212 \mu\text{m}$, respectively, see Eq. (184). Geometrical blurring, induced by the finite extend of the source according Eq. (185), amounts to $b^{(h)} = 0.78 \mu\text{m}$ and $b^{(v)} \approx 0.14 \mu\text{m}$, commensurate with spatial resolution. The scintillator material used was $13 \mu\text{m}$ thick $\text{Gd}_3\text{Ga}_5\text{O}_{12}$. With an approximate flux density of $1 \times 10^{12} \text{ photons/mm}^2/\text{s}$ and a conversion efficiency for X-rays to visible light of $\sim 5\%$, the exposure time amounts to 5.6×10^4 events per pixels. Thus shot noise occurs at a level of 0.4% which is negligible. In the Fourier transformed intensity map of Fig. 36(b) (right panel), this is manifested in the visibility of clearly discernible rings up to the spatial cut-off frequency $\xi_c = \frac{1}{2\Delta x}$.

To test the self-consistency of the quasiparticle approach, retrieved phase maps were upscaled as $\delta\phi_0 \rightarrow 2\delta\phi_0$ to be subsequently inserted into a simulated forward propagation. Here, the constancy of $|\xi_{\perp}|_m$ in $\tilde{g}_z^{(\text{fluct})}$ is observed in Fig. 36(c), evidencing self-consistency. See Eq. (280) for the definition of $g_z^{(\text{fluct})}$.

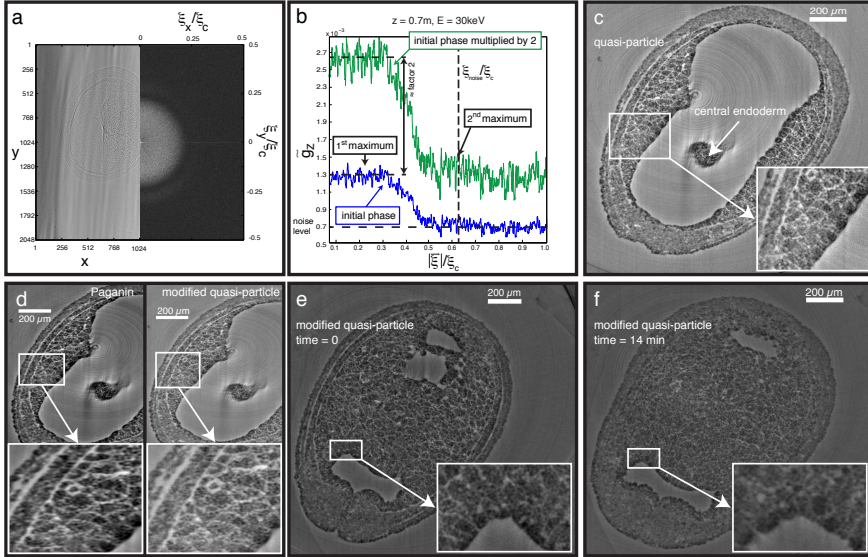


Figure 37: In vivo XPC μ T of the development in a Xenopus embryo at stage 17 during neurulation. a, Intensity contrast g_z at a given projection angle (left) and associated modulus of the Fourier transform $|\hat{g}_z|$ (right). While visibility of the second ring in the horizontal direction is restricted by insufficient beam coherence, visibility of higher-order rings is impaired by shot noise. b, Radial spectrum \tilde{g}_z in blue is obtained from experiment. The radial spectrum \tilde{g}_z in green results from simulated forward propagation after upscaling phase variations $\delta\phi_0$ by a factor of two, which were retrieved using the quasiparticle approach with $\epsilon = 0$ and $\delta = 0.1$. c, Dorsal-ventral slice through reconstruction using quasiparticle phase retrieval, see also Fig. 38(c). Artifacts in the region of the central endodermal ‘island’ arise from collective tissue motion during tomographic acquisition. d, Equal slice through reconstruction as in (c) using Paganin (left) and modified quasiparticle phase retrieval (Eq. (383)). The former suppresses frequencies higher than the first maximum of \tilde{g}_z , the latter cuts off shot-noise dominated frequencies beyond the second maximum, see (b). e, More posterior slice through reconstruction using modified quasiparticle phase retrieval. f, Same reconstruction of same slice as in (e) but after a time lapse of 14 min. Data was acquired with undulator beamline 32-ID at APS. Image adopted from [Hof+14].

Figure 36(d-f) depicts equal slices through volumes reconstructed from phase maps using Paganin (linearised TIE), CTF, and quasiparticle phase retrieval. Spatial resolution in Fig. 36(f) is clearly improved compared with Fig. 36(d). E.g. individual yolk platelets, discernible in Fig. 36(f), appear merged in Fig. 36(e). Also a double layered cell membrane can be distinguished in Fig. 36(d), not possible in Fig. 36(f). The impaired quality of the CTF reconstruction in Fig. 36(e) arises from poles at $|\xi_{\perp}|_m$ within the retrieved phase map in Fourier space, see Fig. 34.

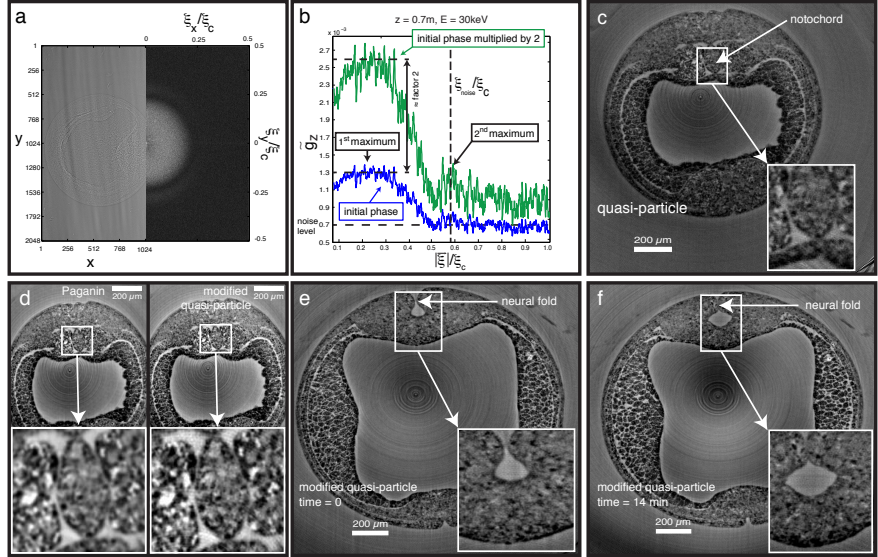


Figure 38: In vivo XPC μ T of the development in a Xenopus embryo at stage 19 (neural groove stage). a, Intensity contrast g_z of posterior part at given projection angle (left), and associated modulus of the Fourier transform $|\tilde{g}_z|$ (right). While visibility of the second ring in the horizontal direction is restricted by insufficient beam coherence, visibility of higher-order rings is impaired by shot noise. b, Radial spectrum \tilde{g}_z in blue is obtained from experiment. The radial spectrum \tilde{g}_z in green results from simulated forward propagation after upscaling the phase variation $\delta\phi_0$ by a factor of two, which were retrieved using the quasiparticle approach with $\epsilon = 0$ and $\delta = 0.1$. c, Dorsal-ventral slice through reconstruction using quasiparticle (right) phase retrieval, see also Fig. 37(c). d, Equal slice through reconstruction as in (c) using Paganin (left) and modified quasiparticle phase retrieval (Eq. (383)). The former suppresses frequencies higher than the first maximum position of \tilde{g}_z , the latter cuts off shot-noise dominated frequencies beyond the second maximum position, see (b). The enlarged region in right panel exhibits finely separated ring artifacts associated to detector inhomogeneities. These are washed out in left panel due to the suppression of high frequencies. e, More posterior slice through reconstruction using modified quasiparticle phase retrieval. f, Same reconstruction of the same slice as in (e) but after a time lapse of 14 min. Note the closing of the neural fold in-between tomograms (e) and (f). Data was acquired with undulator beamline 32-ID at APS. Image adopted from [Hof+14].

4.2.6 In vivo X-ray phase-contrast microtomography

In vivo XPC μ T data was acquired with undulator beamline 32-ID at APS, imaging Xenopus development throughout time and in 3D. The experimental station (B) of beamline 32-ID is located 70 m from the source. Figure 37(a,f) and Fig. 38(e,f) depict two slices of volumes acquired with a temporal separation of 14 min showing Xenopus embryos at stage 17 (late neural fold stage) and stage 19 (neural groove stage), respectively. At the given developmental stages, maximal endodermal cell speeds is about 1 $\mu\text{m}/\text{min}$. A time lapse of 14 min between consecutive tomograms ensures that endodermal cells with a typical diameter of $\sim 30 \mu\text{m}$ half overlap with itself after a single time lapse. For a given projection angle at time o , intensity contrast g_z and associated modulus of the Fourier transform $|\hat{g}_z|$ are shown in Fig. 37(a) and Fig. 38(a). Experimental parameters are $E = 30 \text{ keV}$, $\frac{\Delta E}{E} = 10^{-4}$ (Si 111 DCM), $z = 0.7 \text{ m}$, $\Delta x = 1.3 \mu\text{m}$, $\Delta t = 60 \text{ ms}$, and $N = 499$ over 180° . With an approximate flux density of $10 \times 10^{12} \text{ photons/mm}^2/\text{s}$ and a conversion efficiency for X-rays to visible light of $\sim 10\%$, an exposure time of 60 ms amounts to about 10^4 events per pixels and shot-noise level of $\sim 1\%$. This is considerably worse compared with ex vivo imaging conditions and impairs the visibility of higher-order rings in $|\hat{g}_z|$, letting noise dominates signal (Fig. 37(a), Fig. 38(a)).

In this experiment, a special operating mode of the storage ring was available, resulting in a reduced horizontal beam size (RHB) of $s^{(h)} \approx 120 \mu\text{m}$ instead of the nominal 280 μm . The vertical extend of the source was $s^{(v)} \approx 9 \mu\text{m}$. Asymmetric source dimensions entail a better visibility of rings in $|\hat{g}_z|$ along the vertical direction as compared to the horizontal direction due the larger vertical coherence length. Using the van Cittert-Zernike in the far field for an incoherent source of asymmetric Gaussian shape, the estimated horizontal and transversal transverse coherence length at the sample position are $l_c^{(h)} \approx 12 \mu\text{m}$ and $l_c^{(v)} = 160 \mu\text{m}$, respectively, see Eq. (184). The blur introduced by insufficient spatial coherence (Eq. (185)) is $b^{(h)} = 1.2 \mu\text{m}$ and $b^{(v)} = 0.09 \mu\text{m}$, commensurate with detector resolution.

Assuming a cut-off frequency of $\xi_c = \frac{1}{2\Delta x}$, transverse points of the wave front interfere over an extend of $\frac{\lambda_a}{2\Delta x} = 28.6 \mu\text{m}$ according to Eq. (349), which is smaller than the horizontal coherence length. The estimates on $l_c^{(h)}$ and $l_c^{(v)}$ represent lower bounds only, since in addition to propagation-induced there is intrinsic coherence in undulator radiation. As in Fig. 36(c) self-consistency is tested upon upscaling of retrieved phase maps as $\delta\phi_0 \rightarrow 2\delta\phi_0$ to be inserted into a simulated forward propagation. The vertical dashed line in Fig. 37(b) and (38)(b) indicates a frequency cut-off ξ_{noise} chosen at the second maximum of \tilde{g}_z . For frequencies above ξ_{noise} , the signal g_z is dom-

inated by noise and can be disregarded. Quasiparticle approaches of Eqs. (373) and (376) are thus modified as

$$\hat{g}_z^{(QP)}(\xi_{\perp}) \rightarrow (1 - \Theta(|\xi_{\perp}| - \xi_{\text{noise}})) \hat{g}_z^{(QP)}(\xi_{\perp}). \quad (383)$$

Figures (37)(c) and (38)(c) depict slices through reconstructed volumes at time 0 min employing quasiparticle phase retrieval according to Eq. (373), i.e. without cutting off high-frequency noise in \hat{g}_z . Artifacts of the endodermal 'island' in the central region of Fig. 37(b) arise from the collective movement of the endoderm during tomographic acquisition.

5

TOMOGRAPHY AND PHASE RETRIEVAL

Tomography is enabled by virtue of the projection approximation (Section 2.1.6) which associates phase shift and attenuation of the wave front at object exit to line integrals, i. e. Radon transformations, of the sample's refractive index, see Eq. (118) and Eq. (119), respectively. Real and imaginary of the refractive index (Eq. (115)) account for elastic scattering and absorption and are related to the electron density via Eq. (207) and Eq. (230), respectively. The acquisition of tomographic data thus facilitates the reconstruction of the three-dimensional electron density distribution of the object under investigation from its measured intensity and related phase maps.

The algorithm most widely applied for tomographic reconstruction is filtered backprojection (FBP) owing to its robustness and simplicity, the principles of which were described in Section 2.1.7. Recent technological developments in computer hardware (graphics processing units, parallel processing, etc.) facilitate the use of more advanced, but computationally intense reconstruction methods allowing to incorporate prior knowledge by means of algebraic techniques, neural networks, or others.

Algebraic techniques, based on Kaczmarz's method [Kac37], model the reconstruction problem as a large system of linear equations to be solved iteratively [KS01]. Examples amongst many are algebraic reconstruction technique (ART) [GBH70], simultaneous algebraic reconstruction technique (SART), simultaneous iterative reconstruction technique (SIRT) [AK84], discrete algebraic reconstruction technique (DART) [BS11], or conjugate gradient method for least squares (CGLS) [HS52].

Prior knowledge may also be incorporated via an artificial neural network to obtain a combination of FBP filters from a training data set. This approach has shown to produce high-quality reconstructions from a small number of noisy projections when an adequate training data set is available [PB13].

To maintain detector resolution after reconstruction, tomography calls for a considerably number of projections (Eq. (139)), unless for special cases such as objects owing a sparse representation or samples consisting of a few compositions only. In the former case the methods of compressed sensing are applicable [CTLo8; Dono6], and DART in the latter, both allowing to reduce the number of projections appreciably [BS11].

Regarding the large amount of data to be processed and the significantly increased complexity and computational cost in applying

algebraic techniques, we will here employ FBP-based reconstructions only. E. g. in a typical microtomography experiment with 2000×2000 pixels, $N = 1000$ projections, and single-precision data ($4\text{B} = 32\text{bit}$), a single scan already amounts to a data of 16 GB.

In this chapter we are concerned with two, mostly intertwined problems that is the reduction of the number of tomographic projections (to reduce dose or total scan time) and the improvement in quality of the reconstructed volume by a reduction of noise or artifacts such as streaks, rings, or large background variations.

In Section 5.1 we discuss large-scale (background) modulations superimposing tomographic reconstruction. Large-scale absorptive contributions to the propagated intensity distort the low-frequency part of the intensity spectrum which is further enhanced upon phase retrieval and local tomography. The former is due the contrast transfer functions approaching zero for vanishing frequencies (see Fig. 15), which upon inversion results in an increased sensitivity of phase retrieval to low frequencies. Local tomography is caused by the sample environment not being fully immersed into the field of view. The resulting large-scale modulations not only obscure small-scale structures within reconstructed volumes, but impair subsequent processing steps such as optical flow analysis, data segmentation, volume rendering, and visualisation in general. This calls for a proper treatment of which.

In Section 5.2 we exploit the fact that both FBP and (quasi)linear phase retrieval are operations acting linearly on projections and propagated intensity maps, respectively, and thus commute. Therefore, we may reverse the order of processing, i. e. to reconstruct an ‘intensity volume’ from the propagated intensity maps first, and subsequently retrieve the real refractive index decrement on the ‘intensity volume’. Backprojection of propagated intensity maps average over large-scale absorptive contributions which are further suppressed by the ramp filter of FBP. Therefore, retrieval of the real refractive index decrement from the ‘intensity volume’ is less prone to large-scale variations compared to the conventional processing order.

Section 5.3 is related to noise-induced ring artifacts which originate from the dark current of the camera becoming significant at low count rates.

In Section 5.4 we have performed an *in silico* experiment comparing different tomographic scanning modes, i. e. (discrete) stepwise or continuous rotation, and related reconstructions modalities. The simulation proposes to use continuous rotation in combination with an appropriately adopted reconstruction scheme. For a certain choice of projection numbers, we expect to find a trade-off between angular blur and the reduction of streak artifacts and noise.

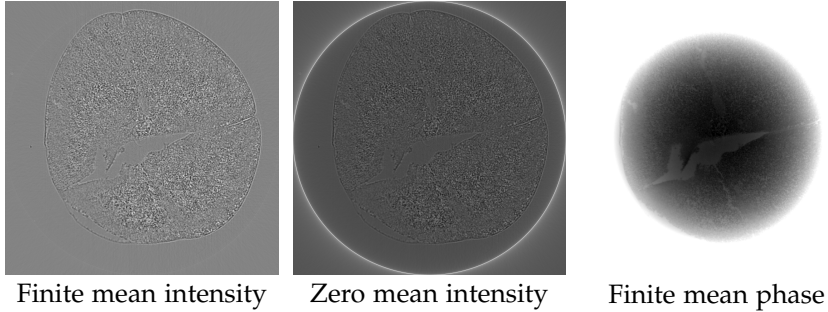


Figure 39: Slices of tomographic reconstructions from propagated intensity (left, middle) and retrieved phase maps (right). The implementation of FBP which was used for reconstruction employs a modified ramp filter which does not set the mean value (zero-frequency component) of the horizontal detector lines of the sinogram to zero. The global mean of the input sinogram remains finite and strongly influences the reconstruction due to local tomography. Left: Global mean value of intensity sinogram was set to zero manually. Middle, right: Global mean value of input sinograms were not set to zero. Compare right image with lower left image in Fig. 40, where the mean value of the input phase sinogram was set to zero before reconstruction. Intensity data of four-cell-stage Xenopus frog embryo was acquired with beamline ID19 at ESRF.

5.1 LARGE-SCALE MODULATIONS

Objects such as early developmental stages of Xenopus or zebrafish model organism are usually embedded in a sample container for fixation and to avoid drying up. For in vivo scans, the container is filled with nutrient solution to provide a life-sustaining environment for the developing embryo. While the object is typically fully immersed into the field of view (FOV), the sample container is only partly captured by the detector as illustrated in Fig. 45. This avoids discontinuities in the accumulated phase shift at the projected boundary of the sample container within the field of view. These discontinuities would otherwise compromise phase retrieval assuming weak (CTF) or moderately (quasiparticle) phase variations. Moreover, this effectively improves the usable dynamic range with which the sample can be imaged. Even if absorption is negligible as local contrast mechanism it reduces the overall (mean) intensity. E.g. flat-field corrected propagated intensity maps of a four-cell stage frog embryo exhibit a mean absorption of $\langle I_z/I_0 \rangle_{\text{FOV}} \approx 0.65$ at $E = 20 \text{ keV}$ (see Section 4.2.5 for details). Thus, when the sample container is smaller than the field of view, unattenuated parts of the beam require a larger dynamic range to capture the full intensity signal.

Regarding the sample container we are then concerned with the problem of local tomography [Far+01]. I.e. data is missing to reconstruct the sample container in its entity. Complete tomographic information is available only within a circle (cylinder) of the recon-

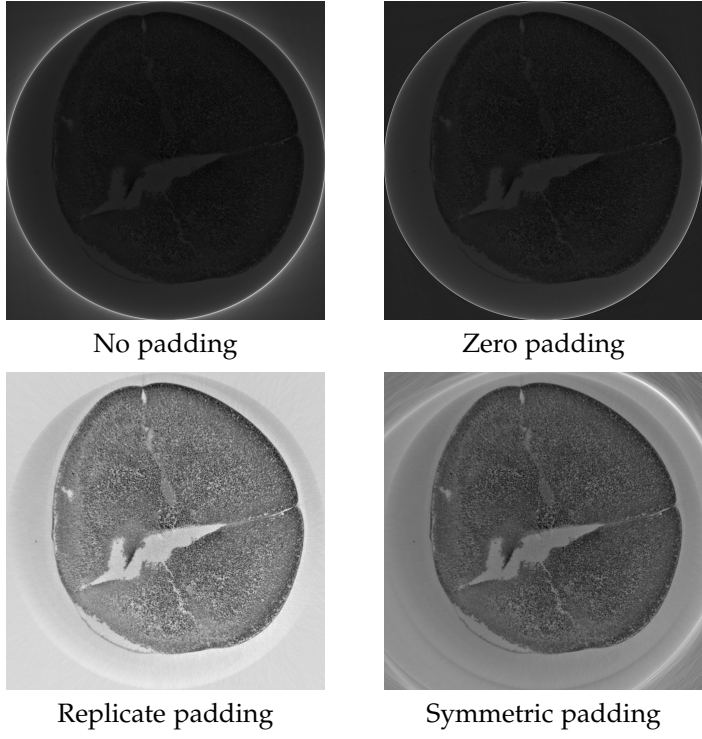


Figure 40: Effect of sinogram padding before tomographic reconstruction. Images depict slices of FBP reconstructions using input phase maps retrieved from propagated intensity maps which were acquired of a four-cell stage Xenopus as in Fig. 39. Quasiparticle phase retrieval was used with $\alpha = 10^{-2.5}$ and $\delta = 0.01$. Top left: No padding was applied to sinogram. Top right: Sinogram was zero padded before reconstruction. Bottom left: Sinogram was padded by replication of the values at the sinogram boundary (replicate padding). Bottom right: Sinogram was padded symmetrically by mirroring at the sinogram boundary (symmetric padding). The mean value was subtracted from all sinograms before reconstruction. The unpadded sinogram consists of $N = 1600$ projections and $N_x = 1962$ pixels. Sinograms were padded to $2 \times N_x$. Note the considerable reduction of large-scale modulations in the case of replicate and symmetric sinogram padding. However, a faint halo is introduced at the embryo boundary.

structed slice (volume), the diameter of which is determined by the horizontal extent of the detector (assuming a vertical rotation axis with the projected axis centred within the detector). Signals originating from the periphery of this circle contribute to the reconstruction volume but are not reconstructed themselves. Peripheral signals originating from localised features such as small inclusions of gas are clearly distinguishable in the sinogram as cropped sine curves, see Fig. 9. Computed tomography is non-local in the sense that the reconstruction of a function at a point P requires integrals over lines far from P [Far+01]. This results in artifacts within the reconstructed volume.

Employing absorption contrast, flat-field corrected intensity maps and corresponding sinograms take on values between zero and one.

Note that sinograms obtained by means of phase contrast are distinct from intensity sinograms. Low-frequency components in the projected object are strongly suppressed in the propagated intensity due to the transfer function approaching zero for vanishing frequencies, see Eq. (263) and Fig. 15. Absorption predominantly contributes to the low-frequency part of the propagated intensity spectrum, see Eq. (262). Thus, even if absorption is negligible as local contrast mechanism, low frequencies in the propagated intensity are distorted by large-scale absorptive contributions and enhanced upon phase retrieval. Large-scale absorption is almost always present in phase-contrast imaging. Consider e.g. the case of cylindrical sample container as in Fig. 45, which is wider than the field of view. The symmetry axis of the sample container does in general not coincide with rotation axis. Thus, homogeneous absorption of the X-ray beam within the sample container introduces large-scale absorptive modulations in the propagated intensity which are globally shifted during the tomographic scan. As a consequence, retrieved phase and corresponding sinograms are impaired by large-scale variations over the entire field of view. Even though FBP, or more precisely its the ramp filter, attenuates low-frequency components in the input maps, large-scale modulations are still present in the reconstructed volume.

Here, a remark concerning the discrete implementation of FBP is in order. As discussed in Section 2.3, the mean value of the exit phase is lost, unless phase-attenuation duality can be assumed (Section 2.3.3). In any case, large-scale absorptive effects influence the low-frequency part of the spectrum of retrieved phase maps. As a consequence, mean values along horizontal detector lines in the corresponding phase sinogram fluctuate in the direction of the projection angle, see top left image in Fig. 41. In general, the global two-dimensional mean of the phase sinogram then assumes a finite value. This should not affect FBP-based reconstructions employing a direct implementation of the ramp filter. Mean values along each horizontal detector line in the sinogram should then be set to zero by the ramp filter. Implementations of FBP as in MATLAB's `iradon` [MAT12] function or in the ASTRA toolbox [PBS11] account for the ramp filter being band limited. As a result, the implemented filter exhibits a small deviation at vanishing frequencies compared to the unadulterated ramp filter. In particular, the implemented filters remain finite at zero frequency. As a consequence, the global mean value of the input sinogram in combination with local tomography strongly influences the reconstruction: volumes reconstructed from intensity maps exhibit a halo, and volumes reconstructed from retrieved phase maps additionally exhibit tremendous large-scale modulations, see Fig. 39.

To address the problem of large-scale variations and local tomography (peripheral signals), numerous approaches are conceivable. (i) Using algebraic reconstruction techniques one can account for peri-

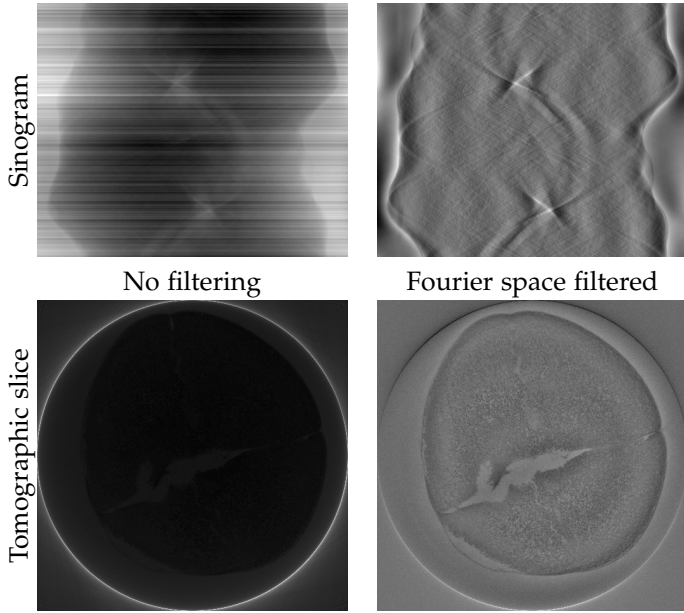


Figure 41: Fourier space filtering of phase sinogram. Top row: Unfiltered (left) and Fourier space filtered (right) sinogram of retrieved phase maps. Bottom row: Zoomed in slice through tomographic reconstruction from retrieved phase maps using the unfiltered (left) and filtered (right) sinogram of the top row. Phase maps were retrieved from propagated intensity maps of a four-cell-stage Xenopus frog embryo recorded with beamline ID19 at ESRF. Quasiparticle phase retrieval was used with regularisation parameter $\alpha = 10^{-2.5}$ and filter threshold $\delta = 0.1$.

peripheral signals by enlarging the volume to be reconstructed, thus increasing the system of linear equations. Thereby, information related to peripheral signals also contribute to regions outside of the disk where complete information is available. However, algebraic techniques such as SART, SIRT, or CGS are typically sensitive to large-scale variations. This may be dealt with via an appropriate choice of regularisation, e. g. Tikhonov regularisation [HO93], or by algebraically fitting background variations. (ii) The effects of local tomography on the reconstructed volume are mitigated by an adequate padding of the sinogram before backprojection. As shown Fig. 40, this can considerably reduce large-scale modulations in the reconstructed volume. See also chapter 3.3.3 of [KSo1] where such artifacts are called dishing. (iii) A brute force approach is to filter the sinogram using e. g. median, smoothing (mean, Gaussian, ball, etc.), or Fourier space filter. Large-scale variations can effectively removed upon filtering the low-frequency part of the spectrum in the projections or sinograms. Since phase retrieval is sensitive to these frequencies, it is likely to distort the retrieved phase upon modifying low frequencies, see Fig. 41. (iv) Reversing the order of phase retrieval and tomographic reconstruction as described in Section 5.2 offers another effective way to reduce large-scale modulations.

5.2 DIRECT RETRIEVAL OF THE REFRACTIVE INDEX DECREMENT

Both, the linear-in- ϕ_0 phase retrieval and FBP are operations acting linearly on the projection and thus commute. Therefore, we may interchange the order of these two operations. I.e. we reconstruct a volume from the intensity maps first, and subsequently retrieve the 'phase' on the 'intensity volume' employing a three-dimensional extension of the usual linear-in- ϕ_0 phase retrieval algorithms. Reversing the order of phase retrieval and FBP, we directly reconstruct the real refractive index decrement. Thus the term 'phase retrieval' is a misnomer and we therefore refer to it as direct retrieval of the refractive index decrement or short direct retrieval. As will be seen, the three-dimensional Fourier space filter for direct retrieval are directly obtained from the two-dimensional filter (inverse transfer functions) by replacing the horizontal frequency coordinate with the radial frequency coordinate expressed in the Cartesian frequency coordinates.

In the remainder of this section we will omit the subscripts of ϕ_0 and g_z indicating the dependence on the propagation distance. Furthermore, we explicitly indicate the dependence on the projection angle θ by an index θ . Hence $\phi_0 \rightarrow \phi_\theta$ and $g_0 \rightarrow g_\theta$. As in Fig. 8 of Section 2.1.7, (x, y) and (s, r) denote coordinates in a plane perpendicular to the rotation axis. While (x, y) relate to a stationary coordinate system which is fixed to the object, (s, r) are related to a coordinate system that is rotated about an angle $\theta - \frac{\pi}{2}$ with respect to the (x, y) system. Thus, s parametrises a point along the projection line, and r is the impact parameter denoting a point in the horizontal detector row. A detector row subtends an angle θ to the x -axis. Let the vertical direction be parametrised by the variable z and the rotation axis centred at $(x, y) = (s, y) = (0, 0)$.

Recall the definition of a one-dimensional projection of a function f as in Eq. (131)

$$\begin{aligned} p_\theta(r) &= \int_{-\infty}^{\infty} ds f(x(r, s), y(r, s)) \\ &= \int_{-\infty}^{\infty} ds f(s \cos \theta - r \sin \theta, s \sin \theta + r \cos \theta). \end{aligned} \quad (384)$$

By definition (Eq. (118)) the phase shift at object exit is the Radon transform of the real refractive index decrement δ_ω . Using the coordinates system (s, r) , it reads

$$\phi_\theta(r, z) = -k_0 \int_{-\infty}^{\infty} ds \delta_\omega(x(r, s), y(r, s), z), \quad (385)$$

where $k_0 = \frac{2\pi}{\lambda}$ is the wave number in vacuum. Accordingly, we will define the intensity contrast as a line integral by the introduction of an auxiliary function $G_\omega = G_\omega(x, y, z)$ as

$$g_\theta(r, z) = k_0 \int_{-\infty}^{\infty} ds G_\omega(x(r, s), y(r, s), z). \quad (386)$$

Thus G_ω is obtained by tomographic reconstruction from propagated intensity maps. For vanishing propagation distances, G_ω coincides with the imaginary part of the refractive index β_ω . Given a tomographic set of phase $\{\phi_\theta\}$ or intensity $\{g_\theta\}$ maps, δ_ω and G_ω can be reconstructed using the FBP formula of Eq. (135)

$$\delta_\omega(x, y, z) = -\frac{1}{k_0} \text{FBP}\{\phi_\theta(r, z)\}, \quad (387)$$

and

$$G_\omega(x, y, z) = \frac{1}{k_0} \text{FBP}\{g_\theta(r, z)\}. \quad (388)$$

To proceed we have to specify the notation of the Fourier transform in a plane in the rotating coordinate system and parallel to the rotation axis. As in Section 2.1.7, \mathcal{F}_{x_i} demands Fourier transformation with respect to the coordinate x_i , multiple indices indicating multiple Fourier transformations. The inverse Fourier transformation \mathcal{F}^{-1} is denoted in an analogous manner. Let (ξ_r, ξ_z) be the Fourier coordinates conjugate to (r, z) . The two-dimensional Fourier transform of ϕ_θ with respect to (r, z) then reads

$$(\mathcal{F}_{r,z} \phi_\theta)(\xi_r, \xi_z) \equiv \int_{-\infty}^{\infty} d\xi_r \int_{-\infty}^{\infty} d\xi_z e^{i2\pi(\xi_r r + \xi_z z)} \phi_\theta(r, z). \quad (389)$$

In the validity regime of linearised TIE and CTF, or in the quasi-particle sense, contrast transfer from phase to propagated intensity persists in an effectively linear way. Phase retrieval in Fourier space can then be understood as a multiplication of the Fourier transformed intensity contrast by a frequency-dependent filter α . The filter is given by the regularised inverse transfer functions of Eqs. (263), (264), (273), (275), (373) and (376), respectively. Phase retrieval in Fourier space then reads

$$(\mathcal{F}_{r,z} \phi_\theta)(\xi_r, \xi_z) = \alpha(\xi_r, \xi_z) (\mathcal{F}_{r,z} g_\theta)(\xi_r, \xi_z). \quad (390)$$

Using FBP the real refractive index decrement is restored from $\{\phi_\theta\}$ by

$$\delta_\omega(x, y, z) = \frac{-1}{k_0} \int_0^\pi d\theta \int_{-\infty}^{\infty} d\xi_r |\xi_r| e^{-i2\pi\xi_r(x \cos \theta + y \sin \theta)} (\mathcal{F}_r \phi_\theta)(\xi_r, z). \quad (391)$$

Inserting $1 = \mathcal{F}^{-1}_{\xi_z} \mathcal{F}_{z'}$ the phase-related term is written as

$$\mathcal{F}^{-1}_{\xi_z} \mathcal{F}_{z'} [(\mathcal{F}_r \phi_\theta)(\xi_r, z')] = \int_{-\infty}^{\infty} d\xi_z e^{-i2\pi\xi_z z} (\mathcal{F}_{r,z'} \phi_\theta)(\xi_r, \xi_z), \quad (392)$$

and Eq. (391) becomes

$$\begin{aligned}\delta_\omega(x, y, z) = & \frac{-1}{k_0} \int_0^\pi d\theta \int_{-\infty}^\infty d\xi_r |\xi_r| e^{-i2\pi\xi_r(x \cos \theta + y \sin \theta)} \\ & \times \int_{-\infty}^\infty d\xi_z e^{-i2\pi\xi_z z} (\mathcal{F}_{r,z'} g_\theta)(\xi_r, \xi_z).\end{aligned}\quad (393)$$

Upon substituting Eq. (390) into Eq. (393), we have

$$\begin{aligned}\delta_\omega(x, y, z) = & \frac{-1}{k_0} \int_0^\pi d\theta \int_{-\infty}^\infty d\xi_r \int_{-\infty}^\infty d\xi_z |\xi_r| \\ & e^{-i2\pi(x\xi_r \cos \theta + y\xi_r \sin \theta + z\xi_z)} \alpha(\xi_r, \xi_z) (\mathcal{F}_{r,z'} g_\theta)(\xi_r, \xi_z).\end{aligned}\quad (394)$$

Using the Fourier slice theorem (Eq. (134)), the intensity contrast can be expressed in terms of the auxiliary function G_ω as

$$(\mathcal{F}_r g_\theta)(\xi_r, z') = k_0 (\mathcal{F}_{x',y'} G_\omega)(\xi_r \cos \theta, \xi_r \sin \theta, z'). \quad (395)$$

Taking the Fourier transform of Eq. (395) with respect to z' we have

$$(\mathcal{F}_{r,z'} g_\theta)(\xi_r, \xi_z) = k_0 (\mathcal{F}_{x',y',z'} G_\omega)(\xi_r \cos \theta, \xi_r \sin \theta, \xi_z). \quad (396)$$

Substituting Eq. (396) into Eq. (394) yields

$$\begin{aligned}\delta_\omega(x, y, z) = & - \int_0^\pi d\theta \int_{-\infty}^\infty d\xi_r \int_{-\infty}^\infty d\xi_z |\xi_r| e^{-i2\pi(x\xi_r \cos \theta + y\xi_r \sin \theta + z\xi_z)} \\ & \times \alpha(\xi_r, \xi_z) (\mathcal{F}_{x',y',z'} G_\omega)(\xi_r \cos \theta, \xi_r \sin \theta, \xi_z).\end{aligned}\quad (397)$$

In the integration over the lower plane $\xi_r < 0$ we substitute $\theta = \theta' + \pi$ and $\xi_r = -\xi_r'$ and use $\cos(\theta + \pi) = -\cos \theta$ and $\sin(\theta + \pi) = -\sin \theta$ to change the integration from $\theta \in [0, \pi]$ and $\xi_r \in [-\infty, \infty]$ to $\theta \in [0, 2\pi]$ and $\xi_r \in [0, \infty]$,

$$\begin{aligned}\delta_\omega(x, y, z) = & - \int_0^{2\pi} d\theta \int_0^\infty d\xi_r \int_{-\infty}^\infty d\xi_z \xi_r e^{-i2\pi(x\xi_r \cos \theta + y\xi_r \sin \theta + z\xi_z)} \\ & \times \alpha(\xi_r, \xi_z) (\mathcal{F}_{x',y',z'} G_\omega)(\xi_r \cos \theta, \xi_r \sin \theta, \xi_z).\end{aligned}\quad (398)$$

Transforming from cylindrical to Cartesian Fourier coordinates,

$$\xi_x = \xi_r \cos \theta, \quad \xi_y = \xi_r \sin \theta, \quad (399)$$

we obtain the final result for direct retrieval as

$$\begin{aligned}\delta_\omega(x, y, z) = & - \mathcal{F}^{-1}_{\xi_x, \xi_y, \xi_z} \left[\alpha(\sqrt{\xi_x^2 + \xi_y^2}, \xi_z) (\mathcal{F}_{x',y',z'} G_\omega)(\xi_x, \xi_y, \xi_z) \right].\end{aligned}\quad (400)$$

In Eq. (400) we have reversed the order of phase retrieval and tomographic reconstruction. Thus retrieval of the real refractive index decrement is performed upon tomographic reconstruction of G_ω using propagated intensity maps as input and subsequently applying the three-dimensional version of the Fourier space filter α to the Fourier transformed volume of G_ω . Finally, the inverse three-dimensional Fourier transform is taken.

As a horizontal line of the two-dimensional filter becomes a plane upon reversing the processing order, a circle becomes a sphere as do the rings in the Fourier transformed intensity of Fig. 35(a).

The reconstruction scheme can be further modified by pulling the ramp filter $|\xi_r|$ out of FBP and combining it with the three-dimensional Fourier space filter. The real refractive index decrement is thus retrieved upon the backprojection (BP) of the unfiltered intensity contrast g_θ , yielding a volume $\text{BP}\{g_\theta\}$. The three-dimensional Fourier transform of $\text{BP}\{g_\theta\}$ is then taken and multiplied with the three-dimensional version of the phase filter $\alpha(\xi_r, \xi_z)$ and the Ram-Lak filter ξ_r with $\xi_r = \sqrt{\xi_x^2 + \xi_y^2}$. Inverse Fourier transformation yields the real refractive index decrement. The fact that the described combination of phase and ramp filter dispenses with two one-dimensional Fourier transformations is insignificant with regard to computational efficiency because the bottle neck is the interpolation between cylindrical and Cartesian coordinates.

To summarise, three principal reconstruction schemes are conceivable for phase-contrast tomography: (i) Phase retrieval based on Paganin, CTF, or quasiparticle approaches and subsequent tomographic reconstruction using FBP or ART. (ii) Tomographic reconstruction using FBP or ART and direct retrieval of the real refractive index decrement employing a three-dimensional version of Paganin, CTF, or quasiparticle approaches. (iii) Unfiltered backprojection (BP) and direct retrieval combined with ramp filtering. In Fig. 42 we compare schemes (i) and (ii) using FBP and quasiparticle (top) and Paganin (bottom) approaches. Compared with the conventional processing order, halo and background variations are less pronounced for direct retrieval and the object of interest is better to distinguish.

Besides the reduction of large-scale modulations facilitating subsequent data processing and analysis, one may further profit from the reversal of the processing order. As already discussed phase sinograms differs appreciably from sinograms which were obtained using conventional absorption contrast. However, sinograms obtained from propagated intensity maps resemble those of absorption-contrast data. Alternative reconstructions techniques, which work well for absorption-contrast data, can then be applied directly to the propagated intensities, circumventing the problems related to large-scale variations in the retrieved phase maps. Furthermore, when consid-

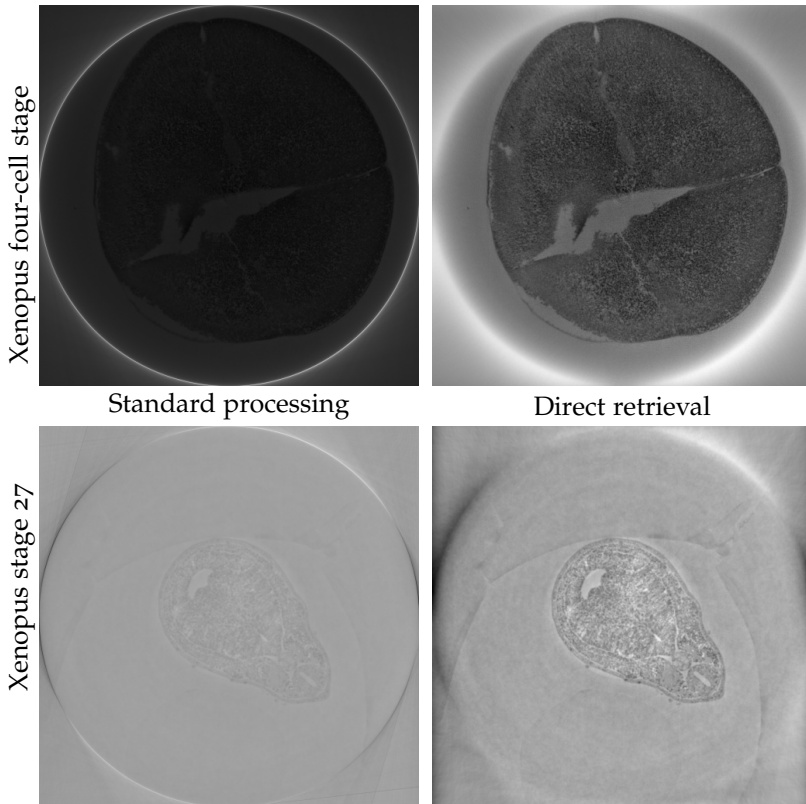


Figure 42: Standard processing order (left) versus direct retrieval (right) of the real refractive index decrement. Top row: Slices of reconstructions using intensity maps of a four-cell-stage Xenopus frog embryo recorded with beamline ID19 at ESRF as input, see Fig. 39 for the related ‘intensity volume’ reconstruction. Phase and direct retrieval employed the quasiparticle approach of Eq. (373) with a filter threshold of $\delta = 0.01$ and a regularisation parameter of $\alpha = 10^{-2.5}$. Bottom row: Reconstruction from intensity maps of a Xenopus frog embryo at stage 27 recorded with beamline 32-ID-B at APS. Phase and direct retrieval are based on Paganin (linearised TIE) with a regularisation parameter of $\alpha = 10^{-2.5}$.

ering different linear phase-retrieval approaches, tomographic reconstructions needs to be performed only once.

5.3 NOISE-INDUCED RING ARTIFACTS

Detector read-out noise owing to the camera dark current becomes significant at low count rates and then is discernible as quasi-periodic vertical stripes in the dark-field image. Being almost independent of the projection angle, such vertical stripes give rise to ring artifacts in horizontal planes of the reconstructed volumes. An efficient way to remove such ring artifacts is to perform the Fourier transform along the horizontal and angular coordinates of the sinogram, and then to replace the plane at value zero of the angle-conjugate coordinate with the median of a few adjacent, parallel lines. The filtered sinograms is

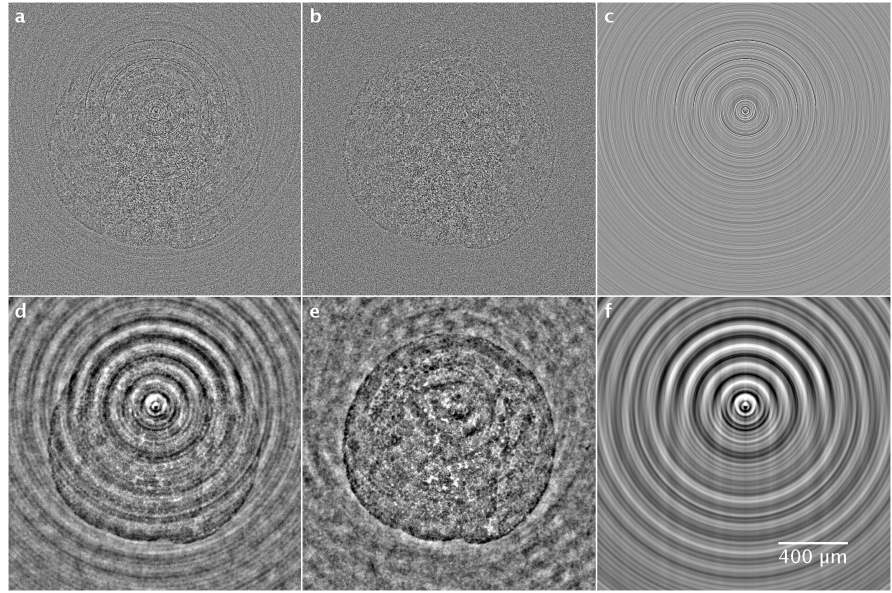


Figure 43: Horizontal slice through reconstructed volume at a position with low count rates due to monochromator modulations. a-c, Reconstruction based on propagated intensity maps. d-f, Reconstruction based on retrieved phase maps. A comparison of top (a-c) and bottom (d-f) row clearly indicates the need for phase retrieval. (a) and (d) refer to standard pre-processing, (b) and (e) are subject to additional sinogram filtering as described in Section 5.3. (c) and (f) show difference maps $(c) = (a) - (b)$ and $(f) = (d) - (e)$, respectively. Intensity maps were taken from an *in vivo* scan of a Xenopus frog embryo at stage 12 (mid-gastrulation). Data was acquired with bending-magnet beamline station 2-BM-B at APS using an X-ray energy of $E = 30 \text{ keV}$, a bandwidth of $\frac{\Delta E}{E} = 10^{-2}$ due to double-multilayer monochromator, an exposure time of $\Delta t = 15 \text{ ms}$, an effective pixel size of $\Delta x = 2.2 \mu\text{m}$, and a number of projections $N = 1200$ over 180° at continuous rotation. Image adopted from [Moo+14].

obtained upon computing the inverse Fourier transform, see Fig. 43. An additional advantage of this filtering is a homogenisation of mean gray values over all slices in the reconstructed volume thus facilitating subsequent data processing.

5.4 CONTINUOUS VERSUS DISCRETE ROTATION

In principle, two distinct scanning modes are available for tomographic experiments, i.e. (discrete) stepwise or continuous rotation. The latter is also referred to as on-the-fly or fly scan. Which one is used depends on the experimental constraints set by the synchrotron beamline and the envisaged spatio-temporal resolution. The stepper motor of the rotation stage and the communication between rotation stage, camera and (optional) fast shutter produce overhead in addition to the read-out time of the camera. E.g. data acquired of the four-cell-stage Xenopus frog (see Section 4.2.5) involved overhead times of

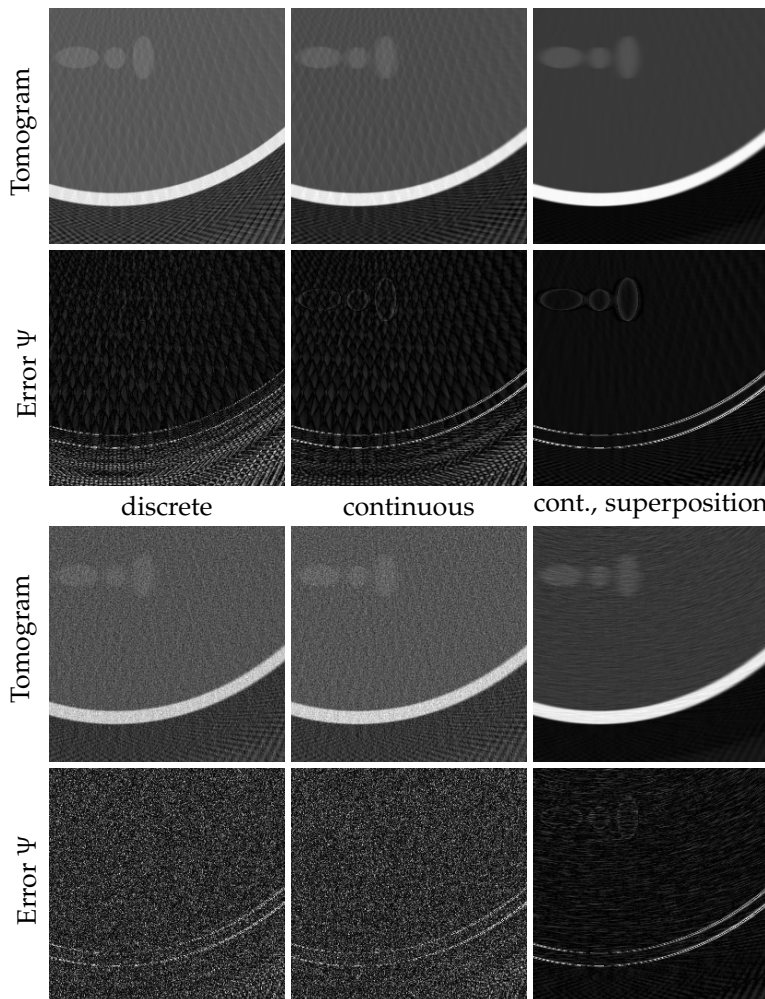


Figure 44: Comparison of different reconstructions involving a discrete or continuous scanning mode and a small number of projections, see text. Left column: Single reconstruction from discrete scan. Middle column: Single reconstruction from continuous scan. Right column: Superposition of ΔN angularly shifted reconstructions from continuous scan. Top row: Tomographic reconstructions $f^{(reco)}$. Second row: Error maps $\Psi \equiv |f^{(reco)} - f^{(exact)}|$ corresponding to the reconstructions in the top row. Third and fourth row: Same as first and second row, respectively, but subject to Poisson noise. Sinograms of unit mean value and varying from 0 to 2.18 are multiplied with an average count number per pixel of 10^5 before being subjecting to Poisson noise. Note the reduction of streak artifacts and noise. Reconstructions remain sharp in radial direction but are blurred in angular direction with respect to the rotation axis position. Images depict a region of interest with 256×256 pixels of the full image with 1024×1024 pixels. The full high-resolution sinogram, used to create the discrete and the continuous sinogram, contains $N = 2100$ projections with 1024 detector pixels. Reconstructions are performed using $N' = \frac{N}{\Delta N} = \frac{2100}{21} = 100$ projections. Reconstructions using $N' = 700$ are close to the exact image with only small errors at the object boundary. Within each row grayscales were linearly adjusted between 0 and 90 % of the minimum value of all pixels within the depicted regions of the underlying reconstructions.

about 0.6 s per image acquisition. If the total time required for a complete tomographic scan is not a limiting factor, stepwise rotation is the preferred choice, otherwise fly scans are used. In the latter case, blurring induced by sample rotation during image acquisition needs to be considered.

In the following we present an *in silico* experiment comparing continuous and stepwise rotation and possible modes of tomographic reconstruction. The test object is a standard Shepp-Logan phantom as depicted in Fig. 8. The phantom was created at a resolution of 4096×4096 pixels and subsequently binned by 2×2 pixels to yield a smoother image. The binned phantom image with a resolution of 2048×2048 pixels was used to compute a sinogram at a high number of projections N . The sinogram was subsequently binned by 1×2 pixels in the detector pixel direction and the phantom image binned by 2×2 pixels. The full resolution sinogram is now used to generate two distinct sinograms with a reduced number of projections $N' = \frac{N}{\Delta N}$. The first only contains each ΔN -th projection and is labelled 'discrete sinogram'. The second is obtained by averaging over ΔN adjacent projections of the full resolution sinogram and is labelled 'continuous sinogram'. It thus simulates the effect of angular blurring during data acquisition under continuous rotation. While the number of projections of the continuous and the discrete sinogram coincide, the continuous sinogram contains, in principle, more but angularly blurred information with respect to the discrete sinogram. The following three types of tomographic reconstructions based on sinograms with a reduced number of projections N' are conceivable:

- (i) Single reconstruction using N' projections of the discrete sinogram.
- (ii) Single reconstruction using N' projections of the continuous sinogram.
- (iii) Superposition of ΔN reconstructions using the continuous sinogram with N' projections and where each of the ΔN volumes is rotated by an angle increment $\frac{180^\circ}{N \Delta N}$ before superposition. Up to numerical uncertainties, this is identical to a single reconstruction using an upsampled sinogram with N projections where each horizontal detector lines of the continuous sinogram was duplicated ΔN times before reconstruction.

In Fig. 44 we compare reconstructions (i), (ii), and (iii) using a small number of projections $N' = 100$. For $N' = 700$ reconstructions are close the original phantom data with small errors at the object boundary only. The figure clearly indicates a reduction of noise and streak artifacts in the case of (iii), though at the expense of resolution in angular direction with respect to the rotation axis. In radial direction the reconstruction remains sharp as expected.

In previous experiments using continuous rotation, the angular blur at the object boundary was always kept at values in the order of the effective pixel size or below. E.g. in vivo scans of *Xenopus* frog embryos performed at 32-ID-B at APS, tomographic data was

acquired under continuous rotation with $N = 500$ projections over 180° within a total scan time of $T = 20\text{ s}$, an effective pixel size of $\Delta x = 1.1\text{ }\mu\text{m}$, and an exposure time of $\Delta t = 20\text{ ms}$. While the angular increment between subsequent projections amounts to a value of $\Delta\theta = 0.36^\circ$, the angular blur per exposure time is $\Delta\theta_b = \frac{\Delta t}{T}180^\circ = 0.18^\circ$ only. At the maximum extend of the embryo, which is a distance of $\sim 800\text{ }\mu\text{m}$ afar from the rotation axis, the angular blur corresponds to $\sim 2.5\text{ }\mu\text{m} \approx 2.3\Delta x$, commensurate with spatial resolution after phase retrieval. At such a low level of blur the superposition of angularly shifted tomograms only results in a faint reduction of noise away from the rotation axis.

Acquiring tomographic data under continuous rotation and using an appropriate reconstruction scheme to incorporate rotation-induced blurring, we expect to find a trade-off between resolution-compatible angular blur and the reduction of noise and streak artifacts.

6

X-RAY PHASE-CONTRAST IN VIVO MICROTOMOGRAPHY OF EMBRYONIC DEVELOPMENT

The work presented in this chapter is closely related to publications [Moo+13b; Moo+14].

6.1 MOTIVATION

The advent of microscopic imaging marks the origin of embryology, that is the scientific description of the earliest stages of animal development [WL95]. On documenting and comparing different embryonic stages of multiple (vertebrate) organisms, it was found that the development of the individual (ontogeny) resembles the evolution of its ancestors (phylogeny)¹, and that the same type of cells gives rise to the same type of structures in diverse organisms [Dar71; WL95; Hae66]. Trying to explain these observations in linking development to chromosomes and heredity resulted in the emergence of genetics and developmental biology, which further aim to describe how tissues form and what drives cells to develop into different kinds.

By studying the development on model organisms allows to understand particular biological phenomena and to carefully extrapolate the results to other organisms. This is due to the fact that all living organisms share a common descent and that metabolic and developmental pathways and genetic material are conserved over the course of evolution [Di 12]. More precisely, the study of model organisms permits to decipher how regulatory and interaction networks direct embryonic development, how they adapt during ageing or under environmental stress, and how they become dysregulated to cause disease, malformations, or birth defects [Xen]. Model organisms thus can serve to study human diseases.

There is an abundant number of model organism differing in the evolutionary distance to humans, experimental tractability, availability, and being differently apt for different fields of research. The *in vivo* experiments described in the following sections were performed on the *Xenopus* model organism.

6.1.1 *The Xenopus model organism*

Xenopus laevis, also known as the African clawed frog, is a widely used vertebrate model organism popular with developmental and cell

¹ To quote Ernst Haeckel, 1875: 'ontogeny recapitulates phylogeny'. [Hae66]

biologists. It is robust, fully aquatic and easy to maintain in captivity in the laboratory. It was the first vertebrate model organisms to be successfully cloned by Gurdon in 1962 [GEF58; Gur62c; Gur62c]. In the 1930s it was used as one of the first, simple methods for pregnancy testing for women [Hel+10]. By injection of chorionic gonadotropin - a hormone present in the urine of a pregnant woman - the production of eggs (ovulation) is stimulated and the frog induced to lay eggs [HG30]. In the laboratory, the same method is used to induce egg production on demand and year-round in a controlled manner, which is possible only for few species of frogs. The eggs of *Xenopus laevis* are large, ~ 1.0 mm to 1.5 mm in diameter, reliably produced in large quantities, and easily manipulated. *Xenopus* embryos develop externally, which allows experiments to be performed prior to or directly after fertilisation [Xen]. Embryo growth is fast such that within a couple of days, the tadpole has developed a fully functional set of organs which can be examined to determine if any experimental intervention has caused an effect [Xen]. The genome of *Xenopus laevis* species has been sequenced, displaying a high structural similarity with the human genome [Hel+10]. Findings from *Xenopus* can thus provide insights into human conditions and diseases [Xen; WLZ10].

Xenopus laevis serves as an invaluable tool for vertebrate experimental embryology because of the following features [Xen; WLZ10]:

- Frogs are easy to raise, and provide an abundant source of eggs and embryos for high-throughput experiments.
- Eggs are large, and develop externally into transparent tadpoles.
- Embryos are easily manipulated, and tolerate extensive manipulation such as tissue transplants or the dissection of single cells or germ layers.
- A range of materials such as nucleic acids, proteins, or whole nuclei can easily be injected into the whole embryo or specific cells.
- The fate of each early embryonic cell is known, which allows targeted gene knock-out, knockdown and overexpression studies.
- Cell-free extracts made from *Xenopus* oocytes are used as in vitro system to study fundamental aspects of cell and molecular biology [WLZ10].
- *Xenopus* oocytes are used as a system to study ion transport and channel physiology [WLZ10].
- *Xenopus* oocytes are widely used as an assay for environmental toxicology.

- The genes involved in diverse developmental and physiological processes have been identified in large-scale genetic screens.

This is why the *Xenopus* model organism turned into one of the most productive model systems to investigate the early period of embryonic development for studying vertebrate embryology and development, basic cell and molecular biology, genomics, neurobiology and toxicology, and to model human diseases.

6.2 X-RAY DOSE

The greatest limitation of XPC μ T is the dose of X-rays absorbed by the embryo. Per tomographic scan it amounts to approximately 2 kGy. Currently, this restricts the total length of time-lapse series to about two hours of development with later stages, say above 19, to sustain slightly longer. Although this is sufficient for tracing many important developmental events, further optimisation of a number of parameters bear the potential to extend this time scale. The precise impact of dose on the embryonic development is unknown and needs to be analysed in further studies. Up to now experiments indicate that after a certain amount of initial deposition of dose embryos decease after a certain lapse of time. This time span depends on the experimental conditions (energy, flux density, total exposure per tomographic scan, etc.) and on the developmental stage. Furthermore, analysis of time-lapse sequence shows that embryos develop normally until shortly before a sudden decay takes place. That is the cellular compound starts to disintegrate: the ectoderm ruptures and some cells ooze out the ectoderm while the bulk of cells collapses to the gravitational bottom of the embryo, see Fig. 49. Before the process of disintegration commences cells, in particular the large endodermal ones, are observed to become roundish. This probably indicates the onset of apoptosis. As a consequence, intensity contrast fades, especially at the embryo boundary, where contrast usually is most pronounced. This can be used as a criterion to abort the scan, see Fig. 49.

Radiation dose potentially induces heat load, direct breaking of hydrogen bonds, and radiolysis of water, which will be discussed in the following sections.

6.2.1 Heat load

To analyse radiation induced heat load on the sample, the rise of temperature was calculated numerically (Section 6.2.1.1) and compared with the estimate of a dedicated experiment (Section 6.2.1.2).

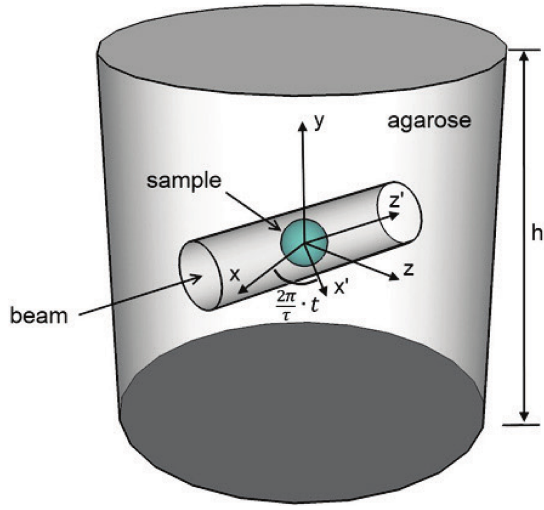


Figure 45: Schematic drawing of the sample, immersed into the X-ray beam, the environment it is embedded in (agarose and buffer solution are not distinguished), and the choice of coordinates. The rotation axis for tomography coincides with the y-axis. Image adopted from [Moo+13b].

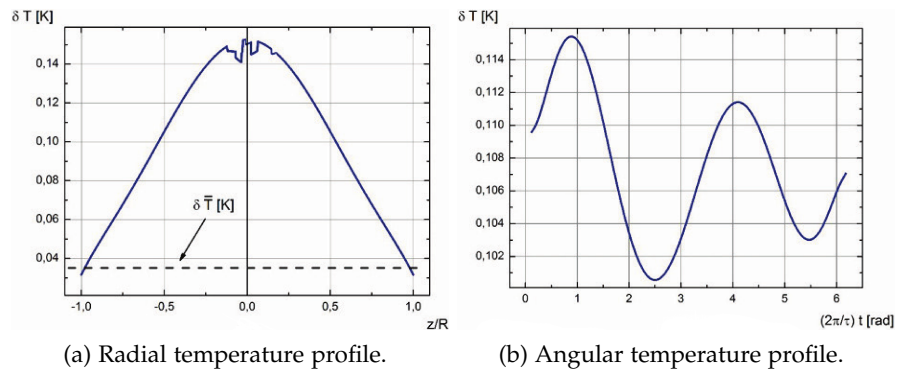


Figure 46: Numerical prediction of the radial ($y = x = 0$) temperature profile (a) and the angular temperature profile (b) for an X-ray energy of $E = 30$ keV, an incident photon flux density of $I_0 = 10^{12}$ photons/s/mm 2 , subject to a Gaussian beam profile with standard deviation $\sigma_x \times \sigma_y = 2 \times 1.5\text{mm}^2$, and a cylindrical sample container of radius $R = 0.6\text{ cm}$ and height $h = 3\text{ cm}$ as depicted in Fig. 45. Image adopted from [Moo+13b].

6.2.1.1 Numerical estimate

The heat flow in water is modelled with a thermal conductivity of $k = 0.6 \text{ J/s/cm/K}$, a specific heat capacity of $c_p = 4.18 \text{ J/g/K}$ at constant atmospheric pressure, and a mass density of $\rho = 1 \text{ g/cm}^3$. The attenuation length of water at an X-ray energy of $E = 30 \text{ keV}$ is $\mu^{-1} = 3.08 \text{ cm}$. The rise in temperature after one tomographic exposure of $\tau = 18 \text{ s}$ duration is estimated assuming that the entire energy of absorbed photons is converted into heat. A Gaussian beam profile is assumed with horizontal and vertical standard deviation of $\sigma_x \times \sigma_y = 2 \times 1.5 \text{ mm}^2$, and a central, monochromatic photon flux density of $I^{(\text{in})} = 10^{12} \text{ photons/s/mm}^2$. Radius and height of the cylindrical sample container (Eppendorf tube) are $R = 0.6 \text{ cm}$ and $h = 3 \text{ cm}$, respectively. For a schematic drawing see Fig. 45. By solving the heat equation

$$\partial_t \delta u = \alpha \nabla^2 \delta u + q, \quad (401)$$

we obtain a central rise in temperature of $\delta T_{r=0} = 0.15 \text{ K}$. Here δu denotes the change in heat density induced by the time-dependent heat source q , α the thermal diffusivity defined as $\alpha = \frac{k}{\rho c_p}$, and ∇^2 the three-dimensional Laplacian. The heat source is represented by a central intersection of the rotating beam with the polyethylene cylinder as

$$q(r) = \mu \exp \left(-\frac{x'^2}{2\sigma_x^2} - \frac{y'^2}{2\sigma_y^2} - \mu \sqrt{R^2 - x'^2} \right) \bar{I}^{(\text{in})}, \quad (402)$$

where $\bar{I}^{(\text{in})}$ denotes the central intensity (energy per time and area), and τ is the exposure time for a full tomographic scan. The coordinates of the rotating beam and the polyethylene cylinder are related by

$$\begin{aligned} x' &= x \cos \left(\frac{2\pi}{\tau} t \right) + z \sin \left(\frac{2\pi}{\tau} t \right), \\ z' &= z \cos \left(\frac{2\pi}{\tau} t \right) + x \sin \left(\frac{2\pi}{\tau} t \right). \end{aligned} \quad (403)$$

The free heat kernel

$$G(r - r', t - t') = \frac{1}{(4\pi\alpha(t - t'))^{3/2}} \exp \left(-\frac{(r - r')^2}{4\alpha(t - t')} \right) \quad (404)$$

was used to construct an approximate solution as

$$\delta u(r, \tau) = \int_0^\tau dt \int d^3 r' G(r - r', t - t') q(r(t)), \quad (405)$$

subject to the initial condition $\delta u = 0$. One has $\delta T = \frac{\delta u}{\rho c_p}$. The solution δT is a good approximation provided that $\delta T(|r| = R) < \bar{T}$, where

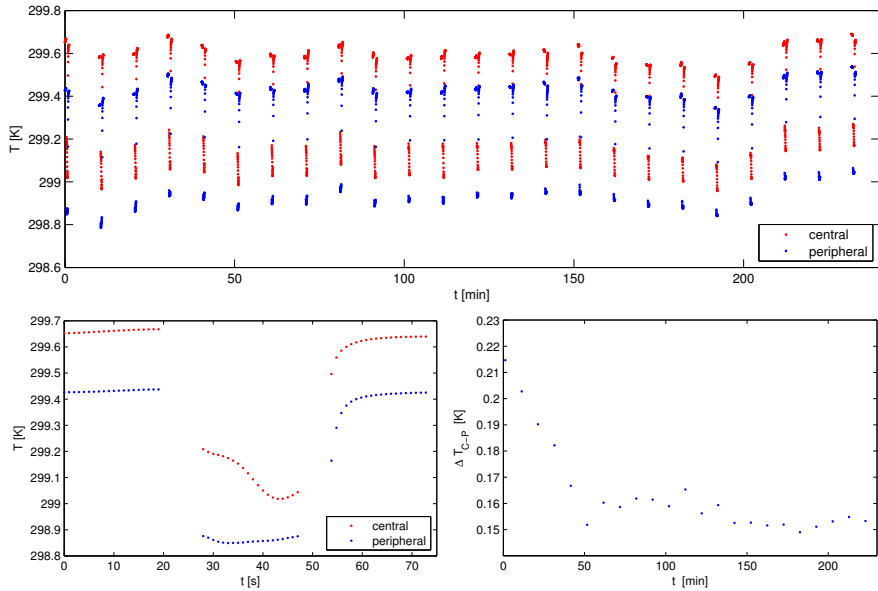


Figure 47: Measurement of temperature changes due to heat load on the sample container induced by X-ray absorption. The measurement procedure is described in Section 6.2.1.2. Top: Sequence of 24 cycles of temperature measurements T with a waiting time of about 10 min. The temperature was measured by two thermistors at a central and a peripheral position within an Eppendorf tube filled with water. Measurements at the centre are shown in red and at the peripheral position in blue. The two thermistors were identical and not calibrated. Bottom left: Temperature measurements resolved within one cycle (central: red, peripheral: blue). First series was taken before, second series during, and final series after exposure. Notice the equilibration towards the end of after-exposure measurements. Bottom right: The difference ΔT_{C-P} of central and peripheral temperatures at the end of the after-exposure measurements over all 24 cycles. Image adopted from [Moo+13b].

$\overline{\delta T}$ denotes the global rise in temperature for the limiting case of instantaneous propagation of heat: in the horizontal slice, where heat load is maximum, little heat flows out of the cylinder compared to instantaneous heat propagation that is confined to the cylinder. In turn, this implies heat conductivity to be sufficiently low with respect to the rate of heat entry for the self-consistency of assuming boundary conditions at spatial infinity only to hold. Figure 46 indicates that this condition is satisfied. With temperature rises of a small fraction of a Kelvin after the recording of a tomogram, heat load is excluded as a potential cause for abnormal development or even apoptosis during X-ray exposure.

6.2.1.2 Experimental measurement

In an experiment at beamline station 2-BM-B of APS at Argonne National Laboratory (ANL), performed under conditions which were identical to a typical in vivo scan (polyethylene tube filled with wa-

ter), the numerical estimate of Section 6.2.1.1 was verified. Comparing Fig. 46(a) and Fig. 47(c), the predicted value of the temperature difference ΔT_{C-P} between the central (C) and peripheral (P) position is observed to differ from the value measured in the X-ray experiment by $\sim 30\%$ only. Effects of mixing and self-capacitance cancel out in ΔT_{C-P} . In the experiment two identical thermistors (Thermometrics, RTD type sensor) were moved into and out of the beam region (4 mm vertical shift) to measure the temperature $T(r, \tau)$ at a central ($r = 0$) and at a peripheral ($r = R$) position over the course of time τ . A total of 24 measurement cycles were taken with a waiting time of ~ 10 min. Each cycle consists of three sequences of 100 temperature measurements with the first sequence performed within 20 s before X-ray exposure with the thermistors in the beam region (beam shut off), the second sequence within 20 s during X-ray exposure with the thermistors out of the beam region (beam on), and the last sequence within 20 s after X-ray exposure with the thermistors in the beam region (beam shut off). Each data point in the plots of Fig. 47 corresponds to an average within a group of five adjacent temperature values.

6.2.2 Direct impact

In [How+09], the maximum tolerable dose and the dose required for imaging to resolve three-dimensional structures were assessed in the context of X-ray diffraction microscopy on freeze-dried samples. The required dose was found to scale with the inverse fourth power of resolution, which was supported by experimental evidence. How much dose a sample can tolerate at a given resolution before an unacceptable degradation occurs is a matter of radiation chemistry and biology. The maximum tolerable dose cannot be estimated by a simple calculation and needs to be inferred from experimental results. It was determined from assembled data of various experimental measurements including data from X-ray and electron crystallography and conventional electron and X-ray microscopy. The maximum tolerable dose increases with decreasing resolution and only slightly depends on X-ray energy. As a rule of thumb the maximum tolerable dose estimates as 1.0×10^8 Gy per nanometre of resolution. At a resolution of ~ 10 nm, the required dose for imaging is in the order of the maximum tolerable dose being about 10^9 Gy. This is several orders of magnitude above the dose required for XPC μ T. A direct destruction of protein structures is thus of no concern for in vivo experiments using XPC μ T.

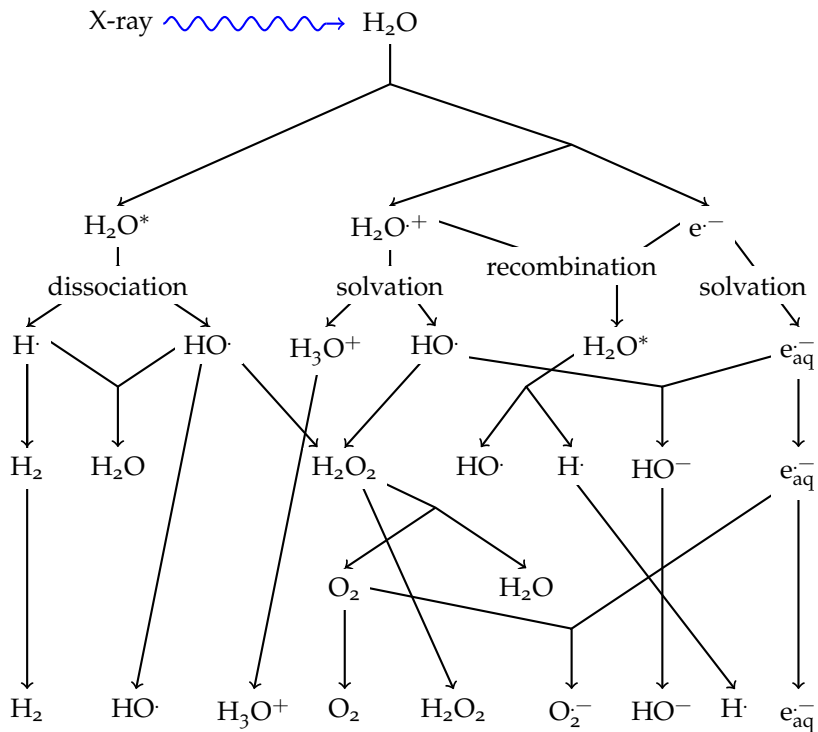


Figure 48: Radiolysis of (intracellular) water H_2O . Exposure of cells to high-energetic ionising radiation induces the radiolysis of water molecules into hydronium H_3O^+ , hydroxyl radicals HO^\cdot , solvated electrons e_{aq}^- , and elemental hydrogen H^\cdot . These radicals are themselves chemically reactive, and in turn recombine to produce a series of highly reactive oxygen species (ROS) such as superoxide HO_2 and peroxide H_2O_2 , inflicting oxidative damage to molecules within the cell [Are87].

6.2.3 Radiolysis of water

Of main concern in XPC μ T experiments involving biological samples is the radiation induced damage of DNA, mediated by reactive oxygen species (ROS) and overlapping with that caused by endogenous oxidative stress. ROS are produced by the radiolysis of cellular water. Radiolysis is the dissociation of molecules or atoms by highly energetic radiation into smaller particles such as atoms, ions, or radicals. When exposed to radiation, water molecules become ionised or excited and subsequently decompose in a series of energy transfer processes into both oxidising and reducing species as illustrated in Fig. 48 [Ger+54b; Ger+54a; Ham69; Are87; LaVoo; Wre10]. In the case an electron is expelled from a water molecule upon irradiation the primary ionic species produced are H_2O^+ and e^- . In aqueous solution the ionic species convert into their hydrated entities: hydronium (hydrated proton) H_3O^+ , the electrically neutral hydroxyl radical HO^\cdot , and the solvated electron e_{aq}^- . An excited state of water may be formed directly by radiation or by the recombination of H_2O^+ and e^- . The excited water molecule H_2O^* then dissociates into an ele-

mental hydrogen radical $\text{H}\cdot$ and a hydroxyl radical $\text{HO}\cdot$. The reactive radical species may further recombine to form stable products such as molecular H_2 , molecular O_2 , H_2O , or hydrogen peroxide H_2O_2 . The solvated electron e_{aq}^- may further react with oxygen to form superoxide (or hyperoxide) radicals O_2^- . The relative concentrations of H_3O^+ , $\text{HO}\cdot$, H_2O_2 , O_2 , H_2 , $\text{H}\cdot$, O_2^- , and e_{aq}^- change considerably within a short time scale following the initial interaction [Wre10].

The oxygen-oxygen bond in peroxides O_2^{2-} is unstable and easily splits into other reactive radicals via homolytic cleavage. Superoxides are potent oxidants implicating in cellular damage and deleterious effects to tissues [FSS99]. Hydrogen peroxide (H_2O_2), formed in human and animal organisms as a short-lived byproduct in biochemical processes, is toxic to cells due to the oxidation of proteins, membrane lipids, and DNA by the peroxide ion [Löf03]. The superoxide anion O_2^- and its protonated form, the hydroperoxyl (or perhydroxyl) radical $\text{HO}_2\cdot$, are in equilibrium in aqueous solution. Hydroperoxyl acts as an oxidant in biologically reactions and is an initiator of lipid peroxidation. Lipid peroxidation is the oxidative degradation of lipids in cell membranes (loss of electron by free radicals), resulting in cell damage. Superoxide potentially contributes to the pathogenesis of many diseases by means of oxidative damage it is inflicting on cells. In nearly all organisms living exposed to oxygen, the class of superoxide-scavenging enzymes, called superoxide dismutase (SOD), is developed as important antioxidant agents. SOD serves an extremely efficient enzyme, since it catalyses the neutralisation of superoxide almost as fast as the particles can meet by diffusion in a solution. SOD promotes the disproportionation of superoxide into oxygen and hydrogen peroxide which can be further degraded by the enzyme catalase into oxygen and water [Löf03].

To examine the pathogenic processes inflicted by radiation-induced oxidative stress, one may consider biomarkers as ROS itself (direct detection), products of lipid peroxidation, hydroxylated proteins, DNA base damage, or DNA strand breaks.

Radiolysis of water eventually results in the accumulation of lethal concentrations of radicals [Külo5]. These radicals damage both nucleic acids and native protein structures resulting in sudden disintegration of tissue structure as depicted in Fig. 49 (see also [Moo+13b]). As damage to genes is likely to result in altered or loss of protein function whenever and wherever those genes are expressed, we expect damage inflicted on DNA/ribonucleic acid (RNA) to affect embryo viability more severely than directly denatured proteins.

6.3 METHOD

A significant, universal understanding of cloning and crucial developmental processes such as gastrulation or neurulation has been gained

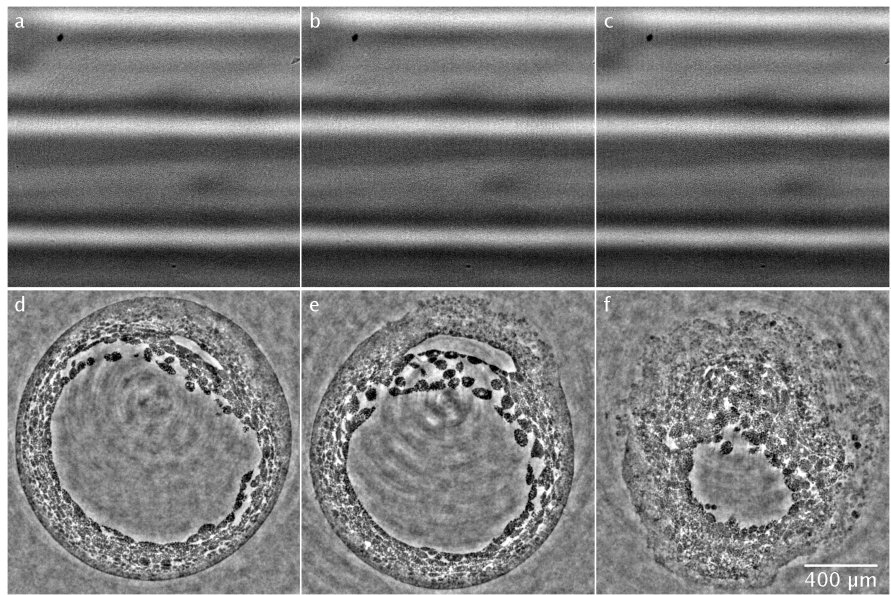


Figure 49: Correspondence between radiographs and central-horizontal slices of reconstructed tomograms showing disintegration of embryo. a-c, Radiographs of the same embryo at the same tomographic angle and for progressive points in time. Intensity contrast is increasingly diminished due to tissue dissolution. d-f, Central-horizontal slices through reconstructed volumes corresponding to (a-c), illustrating tissue damage. Image adopted from [Moo+14].

by analysing Xenopus embryos [Gur62b; Gur62a; KDS03]. However, because its embryos are optically opaque, the Xenopus model system has been lacking high-resolution imaging techniques for the observation of cell and tissue movements within the intact living embryo. In Xenopus embryos yolk is not limited to a yolk sac or a specified region of the egg/embryo, but evenly distributed in the form of small yolk platelets throughout the egg/embryo, rendering it opaque to visible light. To address this limitation, time-lapse *in vivo* XPC μ T was applied (Fig. 19) to developing Xenopus embryos, which enables imaging deep inside the embryos [Moo+13b].

In vivo imaging of Xenopus embryos employing XPC μ T involves the following stages. The preparation of the embryo [Kas+09], including *in vitro* fertilisation, embryo culturing, incubation, staging, and suspension apt for X-ray tomographic imaging. The adjustment of the beamline setup, including choice of energy and monochromaticity, adjustment of slits to reduce stray radiation, alignment of the rotation axis, synchronisation of camera and fast shutter (if used), focusing of microscope optics in the case of an indirect detector system, and so forth. The actual tomography in a synchrotron beam, involving sample mounting, tomographic acquisition with an appropriate choice of imaging parameters (see Section 6.3.3), and immediate phase retrieval and tomographic reconstruction to judge embryo vitality. Subsequent data analysis aims at time-resolved rendering and

4D in vivo imaging modality	time lapse	spatial resolution	time per tomo-gram	structural information	fluorescent labelling / contrast agents	penetration depth for opaque embryos
μ MRI	>24 h	\sim 25 μ m	\sim 1 h	dense	optional	whole embryo
confocal / light-sheet	>24 h	\sim 1 μ m	\sim 5 s	sparse	yes	surface, \sim 2-3 cell layers
XPC μ T	\sim 2 h	\sim 1 μ m	\sim 20 s	dense	no	whole embryo

Table 1: Comparison of four-dimensional (4D) in vivo imaging modalities in developmental biology.

segmentation of interesting structures and computation of velocity fields using optical flow methods. The derived velocity fields permit to visualise the overall cell and tissues dynamics, the tracking of cells and tissues via flow-field integration, and to distinguish active from passive migration via differential flow. The latter separates collective from individual cell motion and thus provides insight into the underlying propulsion mechanisms (convergent extension, epiboly, collective cell migration on bulk tissue, etc.).

6.3.1 Comparison with other methods

Using confocal light microscopy [RJF02] or digital scanned light-sheet microscopy [Hui+04; Kel+08] permits to image developmental processes in vivo at a spatio-temporal resolution comparable to XPC μ T, but for longer periods. However, their full four-dimensional potential is realised only with optically translucent embryos such as zebrafish and medaka and requires fluorescent labelling of selected subcellular structures. Moreover, only sparse structural information is provided in the sense that only isolated labelled parts contribute to the signal. In contrast, in vivo microscopic magnetic resonance imaging (μ MRI) yields dense structural information throughout the whole and optically opaque embryo (e.g. mice and Xenopus) while maintaining long time-lapse series [Pap+06; Pap+07b; Pap+07a]. However, this imaging modality is currently limited to a spatial resolution of about 25 μ m, and thus cannot resolve subcellular structures. Moreover, μ MRI may require the use of contrast agents in order to trace morphogenetic movements. Table 1 compares imaging parameters of four-dimensional in vivo imaging modalities in developmental biology.

6.3.2 Experimental setup

In the following we exemplarily discuss in vivo scans which were performed with bending-magnet beamline station 2-BM-B of APS at Argonne National Laboratory using a parallel X-ray beam of energy $E = 30$ keV at a bandwidth of $\frac{\Delta E}{E} = 10^{-2}$ due to a double-multilayer

monochromator. In vivo scans were also successfully conducted with undulator beamlines 32-ID at APS and ID19 at ESRF. Other X-ray microtomography beamlines of similar characteristics at third-generation synchrotron facilities can be used as well. The crucial parameters to be considered are a high flux density at $E \approx 30$ keV and a bandwidth of $\frac{\Delta E}{E} < 10^{-2}$, a fast detector system, which, in combination, permit to acquire tomograms within about 30 s; moreover, a sufficient coherence length at sample position, determined by the source size and source-sample distance (see Section 2.1.8), which allows to benefit from a strongly enhanced intensity signal at large propagation distance (1 m to 2 m) without loosing spatial resolution due to source blurring. The experimental setup is illustrated in Fig. 19. The choice of an X-ray energy of $E \approx 30$ keV is influenced by two factors.

First is the fact that the attenuation length of X-rays in water exhibits a strong power-law dependence on E . E.g. X-rays at 30 keV impinging centrally on the cylindrical sample container with a diameter of 1.2 cm are attenuated upon exit to about 68 % of their incident intensity. For lower energies and given the short exposure time of 15 ms to 20 ms, imposed by the requirements on embryo viability and the necessity to prevent motion blurring, the transmission decreases to values where the signal-to-noise ratio is unacceptable.

Secondly, the observation that embryo viability is unsatisfactory at lower energies. At $E = 20.33$ keV embryos started to disintegrate (Fig. 49) already after a few (1-3) tomograms. Again, this is induced by the strongly increasing absorption of X-rays with decreasing E and the thus increased deposition of X-ray dose.

The emission spectrum of the bending magnet at beamline 2-BM peaks at an energy of $E = 17$ keV. The spectral emission at $E = 30$ keV is reduced by 17 % with respect to the peak at 17 keV. With a transverse size of the X-ray beam of 2×1.5 mm 2 , the photon flux density on the sample is approximately 10^{12} photons/s/mm 2 .

A cylindrical polypropylene (Eppendorf) tube of radius $r = 6$ mm and height $h = 3$ cm serves as a sample container. The embryo is immersed in a buffer (nutrient) solution and suspended by the walls of a hollow agarose cone within that container. The tube is then mounted on a standard tomography stage.

Intensity contrast, generated upon free-space propagation of X-rays transmitted by the sample container, is recorded by a detector system positioned at sample-detector distance of $z = 62$ cm. Within a LuAg:Ce scintillator of 100 μm thickness, X-ray photons are converted into visible light. After being reflected by a mirror, the visible light is magnified by an optical microscope, placed at a 90° angular offset with respect to the optical axis of the X-ray beam (Fig. 19). The microscope optic consists of a Mitutoyo long working distance $\times 5$ lens. The magnified light is then detected within a pco.dimax CMOS camera with 2016×2016 pixels of size 11×11 μm^2 . This yields an effective

pixel size of $\Delta x = 2.2 \mu\text{m}$. The temperature in the experimental hutch was about 25°C , compatible with natural conditions of development. A significant rise of the sample temperature due to heat load by X-ray absorption was excluded in Section 6.2.1.

6.3.3 Optimisation of phase-contrast tomography setup

For propagation-based phase-contrast imaging, the detected intensity contrast enhances when the sample-to-detector distance z is increased, see Figs. 17 and 33(a). Owing to severe constraints on exposure times, imposed by the requirements on embryo viability, the near-field condition

$$z \ll 4 \frac{(\Delta x)^2}{\lambda}, \quad (406)$$

nominally required for phase retrieval within the edge-enhancement regime Eq. (249), is deliberately violated for the benefit of increased contrast. Edge-enhancing fringes of transverse extent λz , representing object information, are not resolved within this regime (Fig. 17), but become visible at sufficiently large z as they are resolved (Fig. 17) and intensity contrast dominates noise (Fig. 33(a)).

The propagation distance z can be increased only up to a point where the blurring of the detected image substantially affects the spatial resolution, i. e. where the blur b is comparable to the effective pixel size, see Eq. (185). This blurring is due to the finite extent of the X-ray source and a limited source-sample distance R , see Section 2.1.8.

At 2-BM-B, where $R \sim 50 \text{ m}$, a good compromise between enhanced intensity signal and image blurring is given at $z = 62 \text{ cm}$. The Van-Cittert-Zernike theorem for an incoherently emitting source of a horizontal size $s^{(v)} \approx 220 \mu\text{m}$ yields an estimate for the horizontal blur of $b^{(h)} = 3.4 \mu\text{m}$. This is well below the resolution limit of $\sim 2\Delta x = 2 \times 2.2 \mu\text{m} = 4.4 \mu\text{m}$ imposed by the Nyquist–Shannon sampling theorem [Nyq28; Sha49]. The vertical source size of a synchrotron beam is usually much smaller than its horizontal extend and thus not a limiting factor.

Tomographic projections were acquired under continuous rotation of the sample (on the fly). A number of $N = 1200$ projections over 180° were taken with a negligible read-out time of the camera. The value of N is determined from the requirement that the peripheral resolution at the object boundary is greater than the effective pixel size Δx of the detector. From Eq. (139) we have $N \geq \frac{\pi}{2} N_x$, where N_x denotes the horizontal number of effective pixels across the embryo's diameter of $\sim 1.2 \text{ mm}$.

Measurements were taken at an X-ray energy of $E = 30 \text{ keV}$, adjusted according to the two following considerations. First, at $E \sim 20, 25 \text{ keV}$ embryo viability was merely sufficient for a few tomograms, covering a small window of the embryonic development only.

Again, this is explained by the imaginary part β of the refractive index $n_\omega = 1 - \delta_\omega + i\beta$ falling off with increasing energy. Recall that, away from absorption edges, this fall-off is faster than that of the real decrement δ_ω , see Fig. 7.

Secondly, photon flux density, scintillator absorption efficiency, and δ_ω , which phase-contrast imaging is based upon, rapidly decay with increasing energies. In order to yield an acceptable signal-to-noise ratio well above 30 keV would require exposure times too long to capture the movement of cells and tissues. By moving from $E = 20 \text{ keV}$ to 30 keV , photon flux density [HGD93], scintillator efficiency [Mar+09], and the real refractive index decrement of water $\delta_\omega(\text{H}_2\text{O})$ (Fig. 7) drop by 15 %, 20 %, and 50 %, respectively. This trend continues more severely for X-ray energies $E > 30 \text{ keV}$. Typical cell velocities during *Xenopus* gastrulation are in the order of $\sim 2 \mu\text{m}/\text{min}$. At an effective pixel size of $2.2 \mu\text{m}$, this requires a full tomogram to be recorded within less than 1 min. For energies well above 30 keV, acceptable signal-to-noise ratios would require tomographic scan times of $> 1 \text{ min}$ because of the drops in photon flux density and scintillator efficiency. At 30 keV, an effective pixel size of $2.2 \mu\text{m}$, and an exposure per projection of 15 ms, shot noise in the incoming beam is about 0.4 %. Accounting for absorption in the sample suspension system and scintillator efficiency, shot noise remains acceptably low at about 1.8 %. However, read-out noise owing to the dark current of the camera becomes significant at low count rates.

Another means to reduce dose is to employ a fast shutter in order to avoid the sample to be exposed to X-rays in between image acquisition. However, this imposes additional constraints on available imaging parameters (spatial resolution, exposure time, total scan time, etc.). This is due to limitations caused by operating the shutter involving minimum and maximum length of an open-close cycle, minimum and maximum cycle rate, time needed to open and close the shutter (open and close flank of the shutter blade), size of the shutter aperture potentially obstructing the field of view, and so forth.

A waiting time of 10 min between consecutive tomograms is determined from the requirement that a typical endodermal cell of $\sim 40 \mu\text{m}$ diameter should not move more than approximately half its diameter in between the acquisition of consecutive tomograms. Such a displacement is acceptable for the computation of smooth velocity fields by means of optical flow methods.

6.4 GASTRULATION IN *XENOPUS LAEVIS* LIVE CELL IMAGING

The discussion in the following is adopted from [Moo+13b]. At an X-ray energy of about 30 keV, the experimental setup was configured to minimise dose while sufficient image contrast is maintained according to Section 6.3.3. In Section 6.2.1 heat load was found to be

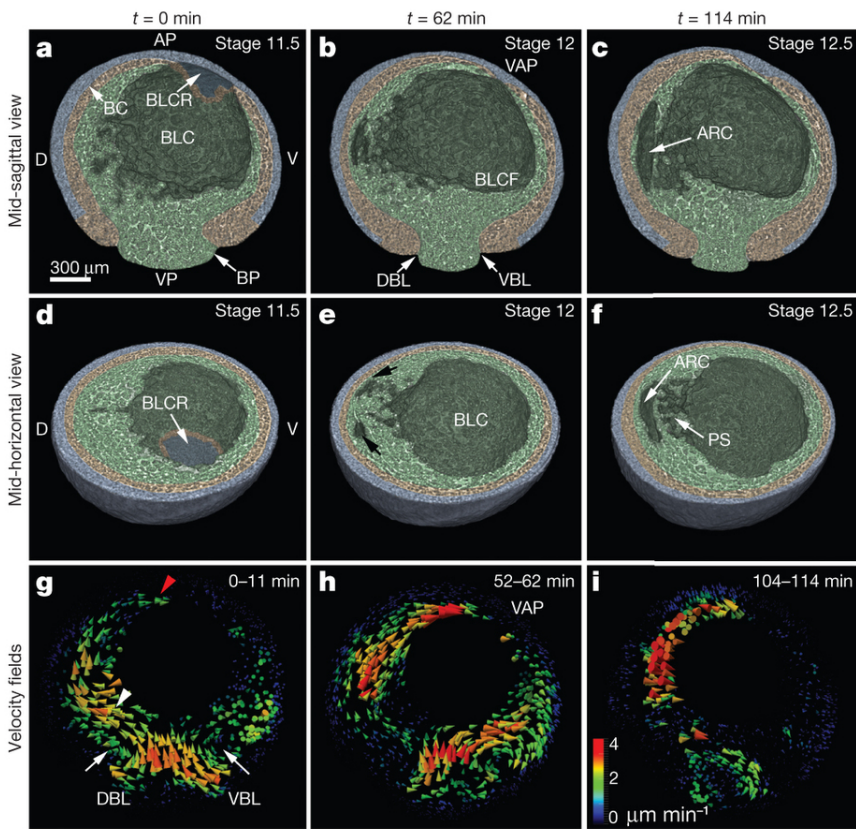


Figure 50: Three-dimensional time-lapse series visualising structure and dynamics of a *Xenopus laevis* embryo during mid-gastrulation. a-f, Renderings of mid-sagittally (a-c) and mid-horizontally (d-f) halved embryo at stages 11.5 (0 min), 12 (62 min) and 12.5 (114 min). Blue indicates ectoderm, orange mesoderm, and green endoderm. g-i, Velocity fields ν on a three-dimensional slab of 180 μm thickness and centred about the cutting planes of (a-c). For details on optical flow analysis see [Moo+13b; Moo+14]. Colour bar indicates velocity magnitude representation. Animal pole (AP), Archenteron (ARC), Brachet's cleft (BC), blastocoel (BLC), blastocoel floor (BLCF), blastocoel roof (BLCR), blastopore (BP), dorsal and ventral sides (D, V), dorsal and ventral blastopore lip (DBL, VBL), 'pipe' system within the interstitial tissue in-between archenteron and blastocoel (PS), ventral animal pole (VAP) and vegetal pole (VP). Migration of mesendodermal tissue on the blastocoel roof is indicated by the red arrowhead in (g). Image adopted from [Moo+13b].

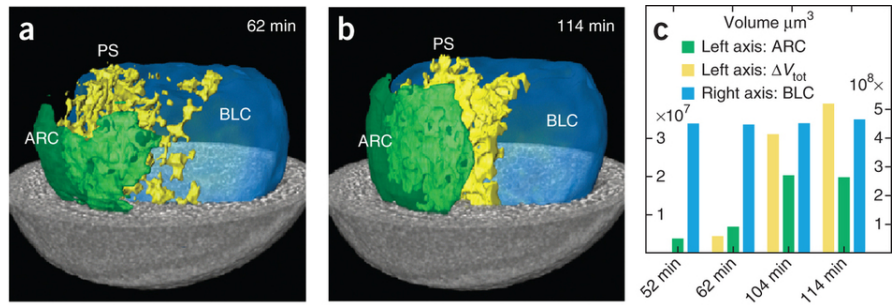


Figure 51: Cavity morphogenesis and quantitative assessment of morphological changes. a,b, Three-dimensional renderings of cavities of the archenteron (ARC), the blastocoel (BLC), and the ‘pipe’ system (PS) within the interstitial tissue in-between ARC and BLC for times 62 min and 114 min. c, Volume change of ARC, BLC, and gastrula (entire embryo) from 52 min to 114 min. Although the archenteron inflated, the blastocoel volume remained constant, whereas the volumes of the ‘pipe’ system and the entire embryo increased. This indicates that early archenteron expansion is driven by the uptake of external water [Tuf62]. Image adopted from [Moo+14].

negligible. Radiolysis of water eventually leads to the accumulation of lethal concentrations of radicals, resulting in a sudden disintegration of tissue structure, see Section 6.2.3 and Fig. 49. However, before the onset of apoptosis, embryonic viability and morphogenetic processes appear to be unimpaired. Being an easily disrupted developmental process, the closure of the blastopore was examined for a direct assay of embryo viability. Closure rates in X-rayed embryos were found to be comparable with that in control gastrulae which were viewed by light microscopy [Moo+13b]. Time-lapse *in vivo* sequences under various irradiation conditions, even harsher than those described in Section 6.3.3, were acquired [Moo+13a; Moo+13b], confirming normal development in X-rayed embryos.

Figure 50(a-c) depicts mid-sagittally halved renderings of an embryo during mid-gastrulation at developmental stages 11.5, 12.0 and 12.5. Specific embryonic structures can be identified, including the blastopore, Brachet’s cleft, archenteron, ventral and dorsal blastopore lips, blastocoel, blastocoel roof and floor, and the porous, interstitial tissue between archenteron and blastocoel (pipe system). Morphogenetic processes captured include the progression of epiboly (spread of ectodermal cells) by a thinning of the ectoderm, blastopore closure, and archenteron formation. Further processes captured are the crawling of cells on blastocoel floor, and in later stages, the closing of the blastocoel, the closing of the neural tube, and the migration of neural crest cells. Further structures identified in later stage are notochord, neural fold, prospective head endoderm, neural plate, somitogenic mesoderm, lateral plate mesoderm, endodermal yolk mass, eye anlage, brain anlage, remnants of the blastocoel, and others [Moo+13b; Moo+13a].

The time-lapse series of reconstructed volumes facilitate the analysis of morphological changes and cell/tissue movements by means of rendering, segmentation, and three-dimensional dense velocity fields obtained from optical flow methods [Bro+04]. Optical flow determines the displacement of a certain voxel in a given volume towards the associated voxel in the consecutive volume such that the difference in grey-values is minimised under certain constraints. Morphogenesis is the collective consequence of hierarchical, diverse, and coupled movements of cells and tissues. All of these movements can be captured by the velocity field \mathbf{v} . The velocity fields depicted in Fig. 50(g-i) reveal the collective movement of cells within the gastrula for several morphogenetic processes. This includes the rotation of the vegetal endoderm (white arrowhead in Fig. 50(g)) [WS99], the involution of the mesendoderm at the dorsal and ventral blastopore lip (white arrows in Fig. 50(g)), and the migration of the mesendoderm on the blastocoel roof towards the ventral animal pole (red arrowhead in Fig. 50(g-i)) [KDS03].

The Archenteron (or digestive tube) is the primordial gut that is formed during gastrulation in the developing embryo. The formation of which is among the least understood aspects of gastrulation. The mid-horizontal slice of Fig. 50(e) depicts two distinct, hollow regions (black arrows) which appear to be merged in Fig. 50(f). Renderings of the entire volume, shown in Fig. 51(a,b), reveal a heart-shaped and contiguous archenteron. This highlights the importance of three-dimensional imaging techniques. The increased porosity of the 'pipe' system within the interstitial tissue, as indicated by Fig. 51(a,b), may suggest that the inflation of the archenteron is driven by fluid transfer from the blastocoel via the 'pipe' system to the archenteron [Ewa+04]. This hypothesis could be addressed upon a segmentation of blastocoel, archenteron, cavities in the 'pipe' system, and the entire embryo (gastrula) at different times (Fig. 51(a-c)). Although the archenteron inflated, the blastocoel volume remained constant (Fig. 51(c)), whereas the volumes of the 'pipe' system and the entire embryo increased. Small cavities within the blastopore disappear well before the inflation of the archenteron and do not affect fluid balancing during the latter [Moo+13b]. This suggests early archenteron expansion not to be driven by fluid transfer from the blastocoel [Ewa+04], but instead by an uptake of external water [Tuf62]. The results concerning volume changes of the archenteron, the 'pipe' system, and the entire embryo (Fig. 51(a-c)), the conservation of cell-mass volume during gastrulation [Tuf62], and the absence of additional cavities in the embryonic fluid balance [Moo+13b] affirm archenteron inflation to be driven by the uptake of external water.

An interesting part of gastrulation is the active, non-invasive migration of mesendodermal cells on their ectodermal substrate. The acquired time-lapse sequences capture, in detail, the migration of the

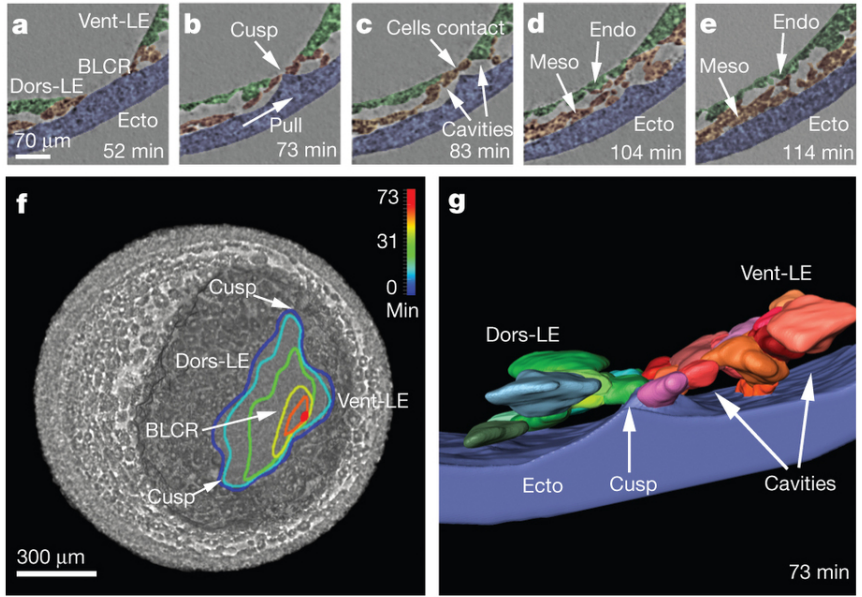


Figure 52: Formation of a transient ectodermal ridge during confrontation of head and ventral mesendoderm. a-e, Time-lapse sequence of sagittal slices through the confrontation zone at 52, 73, 83, 104 and 114 min showing the formation and relaxation of an ectodermal cusp on the blastocoel roof. Dorsal and ventral leading edges (Dors-LE, Vent-LE), ectoderm (blue), mesoderm (orange), endoderm (green). f, Time-lapse sequence of shrinking contours starting at 0 min (blue) and terminating at 73 min within a rendering of the halved embryo at 0 min. The contour indicates projections of the migrating leading edge along the posterior-anterior axis onto the horizontal plane. g, Three-dimensional rendering of individual cells, the ectodermal ridge, and cavities in-between in the confrontation zone at 73 min. Dors-LE cells (shades of green), Vent-LE cells (shades of red). Image adopted from [Moo+13b].

leading-edge head and ventral mesendoderm on the ectoderm of the blastocoel roof (Fig. 52(f)). The sagittal slices depicted in Fig. 52(a-e) show regions of contact and non-contact between the mesendoderm and the ectoderm, thereby creating cavities. This is consistent with the model in [Roh+11] which proposes that cell migration is driven by cycles of Eph/ephrin-dependent attachment and repulsion. Furthermore, a transient deformation of the ectoderm towards the centre of the blastocoel is observed during the migration of mesendodermal cells. Namely, a cusp is formed in the confrontation zone where the dorsal and ventral mesendoderm meet and make contact (Fig. 52(b,c)). The cusp shown in the sagittal slices in Fig. 52(b,c) corresponds to a ridge in three dimensions (Fig. 52(g)). This ridge may be induced by a local contraction of the ectoderm itself, or by a local, adhesive pull of the confronting dorsal and ventral mesendoderm. The spread of ectodermal cells (epiboly) over the surface of the gastrula runs opposite to the latter. When dorsal and ventral mesendoderm eventually

overlap, their contact with the ectodermal substrate is lost, the cusp relaxes (Fig. 52(c-e)), and new adhesive interactions between mesendodermal cells form (Fig. 52(c)). In explants, the formation of such a ridge is unlikely due to the disruption of tissue tension. To our knowledge this ridge has not been reported before.

7

SUMMARY AND OUTLOOK

In Chapter 1 historical steps in the discovery of X-rays and their immediate application for structure determination in material science and for two- and three-dimensional imaging in life sciences were recapitulated. Significantly enhanced coherence and brilliance of synchrotron radiation allow interference effects to arise upon beam propagation and thus to exploit the elastic scattering of X-rays by the sample via non-interferometric, propagation-based phase contrast. There, the object information is encoded in the phase of the transmitted and subsequently propagated wave field. The ensuing non-local and non-linear relation between propagated intensity and exit phase evades an exact analytic inversion of the forward problem. Thus, phase retrieval demands for an efficient approximation to approach an adequate solution. Owing to its simple instrumentation and dose efficiency propagation-based phase contrast is apt for high-resolution *in vivo* imaging.

In Chapters 2 and 3 theoretical and experimental principles of X-ray imaging were reviewed. Microscopic interactions of X-rays with matter were connected to an effective description in terms of the macroscopic refractive index. Using Fresnel theory, the interaction of quasi-parallel, monochromatic, hard X-rays with soft matter inducing phase variations in the ensuing wave field, the subsequent generation of intensity contrast upon forward propagation of the transmitted wave front, and the effects of partial beam coherence impairing emergent intensity contrast were described. Linear methods of phase retrieval based on the transport-of-intensity equation and the contrast transfer function, including a phase-attenuation duality which accounts for absorptive effects at large X-ray energies, were discussed in detail and tomographic reconstruction from retrieved phase maps, restoring the sample's electron density, was considered.

In Chapter 4 approaches to phase retrieval beyond linearity were presented.

In Section 4.1 a systematic extension of the linear phase retrieval for the propagation-based technique was developed in the case of pure-phase objects (soft tissue, polymers, etc.). Here, a model was proposed which expands intensity and phase of the propagated wave field in powers of the object-detector distance. Appealing to full Fresnel theory, the expansion coefficients were determined in terms of transverse derivatives acting on the phase at object exit. The ensuing partial differential equation exhibits non-linear behaviour at next-to-leading order and was approached in a perturbative fashion.

Apt to retrieve large phase variation over the entire field of view, this method demonstrated promising results for simulated phantom data of extended. Large variations in the refractive index are averaged in phase shifts accumulated along a ray path through a thick sample. The accumulate phase is thus less prone to small-scale variations within the projected object. This facilitates to fulfil the requirement of small values of transverse derivatives of the phase for the expansion of the intensity contrast to converge. The non-linear perturbative approach is therefore expected to be applicable to the tomography of samples introducing large phase shifts. Employing different basis sets than just powers in the propagation distance is presumed to yield better convergence properties of the expansion.

Section 4.2 discussed the case where considerable variations of the exit phase entail non-local and non-linear contrast transfer from exit phase to propagated intensity. Here, a phase-scaling symmetry, exact in the limit of vanishing phase variations, was identified and exploited in order to render contrast transfer quasi-linear, reminiscent to the concept of quasiparticles. Algebraic and linear phase retrieval then persists when using a mildly renormalised intensity.

Noise in the retrieved phase, induced by a given integrated, shot-noised intensity at a single propagation distance, was analysed in the case of ideal spatio-temporal coherence. Phase noise was found to decrease with the inverse propagation distance upon quasiparticle retrieval. For intensity contrast emerging upon free-space propagation of considerable phase variations at object exit, encountered e.g. in X-ray phase-contrast microtomography of early stage model organisms, quasiparticle phase retrieval serves as a powerful tool. For ex vivo imaging, superiority in resolution compared to conventional approaches to single-distance phase retrieval is demonstrated. For in vivo imaging, modified quasiparticle phase retrieval presently exhibits a more modest improvement of resolution, though significantly superior to the conventional modality. The drastically enhanced coherence and brilliance of X-ray beams, soon to be provided by various upgraded third generation synchrotron radiation facilities, render imaging at propagation distances in the tens of meters feasible, significantly improving the intensity signal. In vivo imaging under parallel-beam incidence and at a reasonable X-ray dose will then resolve with spatial resolution at the detector limit.

In Chapter 5 intricacies of tomography were discussed in the context of phase-contrast data. Of main concern are large-scale modulations superimposed on the tomographic reconstruction and thereby obscuring small-scale features of the object under investigation and impairing subsequent data processing and analysis. These large-scale modulations are caused by absorptive contributions to the intensity, distorting low-frequency components that are enhanced upon phase retrieval and local tomography. By reversing the order of phase

retrieval and tomographic reconstruction, the real refractive index decrement is directly retrieved from the 'intensity volume', which significantly reduces large-scale modulations compared to conventional processing order. Moreover, propagated intensity data can then be used as input for alternative (algebraic) tomographic reconstruction techniques which would otherwise be impaired by large-scale variations in the retrieved phase maps.

In Chapter 6, using highly coherent synchrotron radiation in the hard X-ray regime, high-resolution phase-contrast microtomography was conceived as a three-dimensional *in vivo* imaging modality to investigate early developmental processes in intact model-system embryos. Here, low-dose requirements demand short exposure times which calls for a single measurement at a large propagation distance.

Four-dimensional imaging of living early-stage vertebrate embryos presently requires a minimum X-ray dose which limits maximum time-lapse series to about two-hour duration and spatial resolution to about $2\text{ }\mu\text{m}$ at propagation distance in the order of 1 m [Moo+13b; Moo+14]. Introducing a moderate beam divergence to enable geometric magnification effectively increases spatial resolution (Fresnel scaling [Pago6]). X-ray phase-contrast microtomography will then resolve in the hundred-nanometre regime with commensurate or even longer periods of development due to a more localised dose deposition. On the instrumentation side, this will require focusing optics for hard X-rays such as Kirkpatrick-Baez mirrors [Req+09], long beamline hutches, and vacuum tubes downstream of the sample stage to prevent X-ray absorption by air before detection. Performing *in vivo* X-ray phase-contrast microtomography with such a setup will contribute to a profound understanding of e. g. developmental processes by the comparison of phenotypic effects of molecular perturbations at subcellular resolution and in four dimensions.

In particular, as demonstrated by the study in Section 6.4, *in vivo* propagation-based, single-distance X-ray phase-contrast microtomography combined with optical flow analysis serves as a powerful tool to investigate the embryonic development in *Xenopus laevis* in four dimensions. Differential flow analysis enabled to distinguish active from passive movement of cells and tissue, elucidating how collective motion (convergent extension, collective cell migration on bulk tissue, etc) is propelled by individual cell behaviour. At subcellular resolution, time-lapse series of up to two hours of development could be captured without adverse effects on embryo viability. Using this imaging modality in high-throughput perturbation experiments, can contribute to our understanding of the molecular mechanisms and biomechanical processes driving morphogenesis.

A

FOURIER ANALYSIS

A.1 DEFINITIONS USING ANGULAR FREQUENCIES

A.1.1 Fourier transformation

Consider a scalar function f of a real n -dimensional variable $x = (x_1, x_2, \dots, x_n)$. The n -dimensional Fourier transform of the function f is denoted $\hat{f} \equiv \mathcal{F}_x f$ where \mathcal{F}_x is the forward Fourier transform operator. The related inverse Fourier transform operator is denoted \mathcal{F}_k^{-1} . The Fourier variable conjugate to x is $k = (k_1, k_2, \dots, k_n)$. The operator \mathcal{F}_{x_i} demands Fourier transformation with respect to the argument x_i . A vector index in \mathcal{F}_x or multiple indices in $\mathcal{F}_{\{x_i\}}$ indicate multidimensional Fourier transformations with respect to the set of variables $\{x_i\}$. When no confusion can arise, we will omit the indices of the Fourier transform operators. The n -dimensional Fourier transform of the function f is defined as

$$\hat{f}(k) \equiv (\mathcal{F}_x f)(k) \equiv \frac{1}{(2\pi)^{n/2}} \int_{-\infty}^{\infty} d^n x f(x) \exp(i k \cdot x) \quad (A.1)$$

and the corresponding inverse Fourier transform as

$$f(x) \equiv (\mathcal{F}_k^{-1} \hat{f})(x) \equiv \frac{1}{(2\pi)^{n/2}} \int_{-\infty}^{\infty} d^n k \hat{f}(k) \exp(-i k \cdot x) . \quad (A.2)$$

With the above definitions an expression for the n -dimensional Dirac delta distribution follows as

$$\delta^n(x) = \frac{1}{(2\pi)^n} \int_{-\infty}^{\infty} d^n k \exp(i k \cdot x) . \quad (A.3)$$

For non-zero scalar α the Dirac delta distribution satisfies the scaling property

$$\delta^n(\alpha x) = \frac{\delta^n(x)}{|\alpha|^n} . \quad (A.4)$$

For referencing we will give explicit expressions for $n = \{1, 2, 3\}$. For $n = 1$ and setting $x = x_1$ and $k = k_1$, we have

$$\begin{aligned} \hat{f}(k) &\equiv (\mathcal{F}_x f)(k) \equiv \frac{1}{\sqrt{2\pi}} \int_{-\infty}^{\infty} dx f(x) \exp(ikx) , \\ f(x) &\equiv (\mathcal{F}_k^{-1} \hat{f})(x) \equiv \frac{1}{\sqrt{2\pi}} \int_{-\infty}^{\infty} dk \hat{f}(k) \exp(-ikx) . \end{aligned} \quad (A.5)$$

For $n = 2$ and setting $\mathbf{x}_\perp = (x_1, x_2)$ and $\mathbf{k}_\perp = (k_1, k_2)$, we have

$$\begin{aligned}\widehat{f}(\mathbf{k}_\perp) \equiv (\mathcal{F}_{\mathbf{x}_\perp} f)(\mathbf{k}_\perp) &\equiv \frac{1}{2\pi} \int_{-\infty}^{\infty} d^2 \mathbf{x}_\perp f(\mathbf{x}_\perp) \exp(i\mathbf{k}_\perp \cdot \mathbf{x}_\perp), \\ f(\mathbf{x}_\perp) \equiv (\mathcal{F}_{\mathbf{k}_\perp}^{-1} \widehat{f})(\mathbf{x}_\perp) &\equiv \frac{1}{2\pi} \int_{-\infty}^{\infty} d^2 \mathbf{k}_\perp \widehat{f}(\mathbf{k}_\perp) \exp(-i\mathbf{k}_\perp \cdot \mathbf{x}_\perp).\end{aligned}\quad (\text{A.6})$$

For $n = 3$ and setting $\mathbf{r} = (x_1, x_2, x_3)$ and $\mathbf{k} = (k_1, k_2, k_3)$, we have

$$\begin{aligned}\widehat{f}(\mathbf{k}) \equiv (\mathcal{F}_{\mathbf{r}} f)(\mathbf{k}) &\equiv \frac{1}{(2\pi)^{3/2}} \int_{-\infty}^{\infty} d^3 \mathbf{r} f(\mathbf{r}) \exp(i\mathbf{k} \cdot \mathbf{r}), \\ f(\mathbf{r}) \equiv (\mathcal{F}_{\mathbf{k}}^{-1} \widehat{f})(\mathbf{r}) &\equiv \frac{1}{(2\pi)^{3/2}} \int_{-\infty}^{\infty} d^3 \mathbf{k} \widehat{f}(\mathbf{k}) \exp(-i\mathbf{k} \cdot \mathbf{r}).\end{aligned}\quad (\text{A.7})$$

A.1.2 Convolution theorem

Let $*$ indicate (one-dimensional) convolution with respect to coordinate x_i . The n -dimensional convolution of scalar functions f and g is defined as

$$f(\mathbf{x}) * * \cdots * g(\mathbf{x}) = \int_{-\infty}^{\infty} d^n \mathbf{x}' f(\mathbf{x}') g(\mathbf{x} - \mathbf{x}'). \quad (\text{A.8})$$

The convolution theorem in n -dimensional space using the Fourier transform as defined in Eq. (A.1) and Eq. (A.2) reads

$$\mathcal{F}_{\mathbf{x}}[f(\mathbf{x}) * * \cdots * g(\mathbf{x})] = (2\pi)^n (\mathcal{F}_{\mathbf{x}} f) \times (\mathcal{F}_{\mathbf{x}} g). \quad (\text{A.9})$$

A.1.3 Fourier derivative theorem

Appealing to the Fourier representation of function f , the Fourier derivative theorem reads

$$\frac{\partial^m}{\partial x_i^m} f(\mathbf{x}) = \mathcal{F}_{\mathbf{k}_i}^{-1} [(-ik_i)^m \mathcal{F}_{\mathbf{x}_i} f(\mathbf{x})], \quad (\text{A.10})$$

with $m \in \mathbb{N}_0$.

A.2 DEFINITIONS USING ORDINARY FREQUENCIES

Here we will give expressions for the formulae of Appendix A.1 when using ordinary frequencies, $\xi = (\xi_1, \xi_2, \dots, \xi_n)$, instead of angular frequencies \mathbf{k} with $\mathbf{k} = 2\pi\xi$. The advantage of defining the Fourier transform using ordinary instead of angular frequencies is that factors $\frac{1}{(2\pi)^{n/2}}$ vanish in Eq. (A.11) and Eq. (A.12) compared to the definitions in Eq. (A.1) and Eq. (A.2). Moreover, the factor $(2\pi)^{n/2}$ vanishes in the definition of the convolution theorem. Furthermore, numerical implementations usually employ discretised version of the Fourier transforms as defined below.

A.2.1 Fourier transformation

The n -dimensional Fourier transform of the function f using ordinary frequencies ξ is defined as

$$\widehat{f}(\xi) \equiv (\mathcal{F}_x f)(\xi) \equiv \int_{-\infty}^{\infty} d^n x f(x) \exp(i2\pi\xi \cdot x) \quad (\text{A.11})$$

and the corresponding inverse Fourier transform as

$$f(x) \equiv (\mathcal{F}_{\xi}^{-1} \widehat{f})(x) \equiv \int_{-\infty}^{\infty} d^n \xi \widehat{f}(\xi) \exp(-i2\pi\xi \cdot x). \quad (\text{A.12})$$

With the above definitions the n -dimensional Dirac delta distribution reads

$$\delta^n(x) = \int_{-\infty}^{\infty} d^n \xi \exp(i\xi \cdot x). \quad (\text{A.13})$$

A.2.2 Convolution theorem

The convolution theorem in n -dimensional space using the Fourier transform as defined in Eq. (A.11) and Eq. (A.12) reads

$$\mathcal{F}_x [f(x) * \dots * g(x)] = (\mathcal{F}_x f) \times (\mathcal{F}_x g). \quad (\text{A.14})$$

For $n = 2$ and setting $x_{\perp} = (x_1, x_2)$ we have

$$\mathcal{F}_{x_{\perp}} [f * g] = (\mathcal{F}_{x_{\perp}} f) \times (\mathcal{F}_{x_{\perp}} g). \quad (\text{A.15})$$

A.2.3 Fourier derivative theorem

Appealing to Eq. (A.12) and Eq. (A.11), the Fourier derivative theorem reads

$$\frac{\partial^m}{\partial x_i^m} f(x) = \mathcal{F}_{\xi_i}^{-1} [(-i2\pi\xi_i)^m \mathcal{F}_{x_i} f(x)], \quad (\text{A.16})$$

with $m \in \mathbb{N}_0$.

For referencing we will give explicit expressions for $n = \{1, 2, 3\}$. For $n = 1$ and setting $x = x_1$ and $\xi = \xi_1$, we have

$$\begin{aligned} \widehat{f}(\xi) &\equiv (\mathcal{F}_x f)(\xi) \equiv \int_{-\infty}^{\infty} dx f(x) \exp(i2\pi\xi x), \\ f(x) &\equiv (\mathcal{F}_{\xi}^{-1} \widehat{f})(x) \equiv \int_{-\infty}^{\infty} d\xi \widehat{f}(\xi) \exp(-i2\pi\xi x). \end{aligned} \quad (\text{A.17})$$

For $n = 2$ and setting $x_{\perp} = (x_1, x_2)$ and $\xi = (\xi_1, \xi_2)$, we have

$$\begin{aligned} \widehat{f}(\xi_{\perp}) &\equiv (\mathcal{F}_{x_{\perp}} f)(\xi_{\perp}) \equiv \int_{-\infty}^{\infty} d^2 x_{\perp} f(x_{\perp}) \exp(i2\pi\xi_{\perp} \cdot x_{\perp}), \\ f(x_{\perp}) &\equiv (\mathcal{F}_{\xi_{\perp}}^{-1} \widehat{f})(x_{\perp}) \equiv \int_{-\infty}^{\infty} d^2 \xi_{\perp} \widehat{f}(\xi_{\perp}) \exp(-i2\pi\xi_{\perp} \cdot x_{\perp}). \end{aligned} \quad (\text{A.18})$$

For $n = 3$ and setting $\mathbf{r} = (x_1, x_2, x_3)$ and $\boldsymbol{\xi} = (\xi_1, \xi_2, \xi_3)$, we have

$$\begin{aligned}\widehat{f}(\boldsymbol{\xi}) &\equiv (\mathcal{F}_{\mathbf{r}} f)(\boldsymbol{\xi}) \equiv \int_{-\infty}^{\infty} d^3 \mathbf{r} f(\mathbf{r}) \exp(i2\pi \boldsymbol{\xi} \cdot \mathbf{r}) , \\ f(\mathbf{r}) &\equiv (\mathcal{F}_{\boldsymbol{\xi}}^{-1} \widehat{f})(\mathbf{r}) \equiv \int_{-\infty}^{\infty} d^3 \boldsymbol{\xi} \widehat{f}(\boldsymbol{\xi}) \exp(-i2\pi \boldsymbol{\xi} \cdot \mathbf{r}) .\end{aligned}\tag{A.19}$$

LIST OF FIGURES

Figure 1	Finite-range scattering potential.	24
Figure 2	Situation related to the Helmholtz-Kirchhoff diffraction integral.	25
Figure 3	Situation related to a special case of the Helmholtz-Kirchhoff diffraction integral.	26
Figure 4	Small-angle approximation.	28
Figure 5	Fraunhofer diffraction at a circular aperture (Airy pattern).	34
Figure 6	Projection approximation and forward propagating in Fresnel theory.	36
Figure 7	The refractive index in dependence of energy.	37
Figure 8	The Fourier slice theorem and filtered backprojection.	39
Figure 9	Sinograms of Shepp-Logan phantom and Xenopus frog.	41
Figure 10	Fourier space sampling under tomographic backprojection.	43
Figure 11	Emergence of a transverse coherence limit from a quasimonochromatic source.	45
Figure 12	Van Cittert-Zernike theorem in the far field.	46
Figure 13	Geometrical blurring of image points induced by the finite extent of the illuminating source.	52
Figure 14	Intensity contrast in dependence of propagation distance.	54
Figure 15	Linear Transfer functions between phase and intensity.	66
Figure 16	Fourier space filter (regularised inverse transfer function) for standard phase retrieval.	67
Figure 17	Evolution of fringes in the propagated intensity from an edge-like phase object in simulated forward propagation.	71
Figure 18	Lena test pattern and its Fourier transform.	74
Figure 19	Experimental setup for propagation-based X-ray phase-contrast microtomography.	82
Figure 20	Spectrum of a Tungsten X-ray tube.	84

Figure 21	Layout of the ANKA synchrotron radiation facility.	86
Figure 22	Radiation emitted in a long magnet.	87
Figure 23	Radiation emitted in a short magnet.	88
Figure 24	Comparison of monochromatic and quasi-monochromatic propagated intensities.	91
Figure 25	Flat field from a multilayer monochromator.	92
Figure 26	Heat load induced flat-field modulations.	93
Figure 27	Asymmetric one-dimensional Bragg diffraction in a Bragg magnifier.	94
Figure 28	Magnification by cone-beam geometry.	94
Figure 29	Indirect detector system involving a scintillator, microscope optics, and digital camera.	97
Figure 30	Leading-order phase retrieval and next-to-leading-order correction from propagated intensity of a Siemens-star phase object.	106
Figure 31	Line cuts in leading-order phase retrieval and next-to-leading-order correction from propagated intensity of a Siemens-star phase object.	107
Figure 32	Leading-order phase retrieval and next-to-leading-order correction from propagated intensity of a modified Siemens-star phase object.	108
Figure 33	Image formation in full Fresnel theory and linear phase retrieval for the pure-phase case subject to statistical noise in dependence of propagation distance.	111
Figure 34	Fourier space filter (regularised inverse transfer functions) for linear and quasilinear phase retrieval.	116
Figure 35	Quasiparticle behaviour of relation between intensity contrast and phase up to criticality under simulated Fresnel forward propagation.	117
Figure 36	Global phase-attenuation duality versus upscaling and confrontation with experimental data on fixed frog embryo.	121
Figure 37	In vivo XPC μ T of Xenopus development during neurulation in a stage-17 embryo.	123
Figure 38	In vivo XPC μ T of Xenopus development within stage-19 embryo.	124

Figure 39	Tomographic reconstruction from propagated intensity and retrieved phase maps. 129
Figure 40	Effect of sinogram padding before tomographic reconstruction. 130
Figure 41	Fourier space filtering of phase sinogram. 132
Figure 42	Phase retrieval and subsequent tomographic reconstruction vs. tomographic reconstruction of propagated intensity and retrieval of real-refractive index increment. 137
Figure 43	Filtering of noise-induced ring artifacts. 138
Figure 44	Comparison of tomographic reconstructions involving a discrete or continuous scanning mode. 139
Figure 45	Schematic drawing of a sample immersed into X-ray beam for numerical heat load computation. 146
Figure 46	Numerical prediction of the temperature profile within the sample environment due to X-ray-induced heat load. 146
Figure 47	Measurement of temperature changes due to heat load on the sample container induced by X-ray absorption. 148
Figure 48	Radiolysis of intracellular water. 150
Figure 49	Correspondence between radiographs and central-horizontal slices of reconstructed tomograms, and disintegration of embryonic compound. 152
Figure 50	3D time-lapse series visualising structure and dynamics of <i>Xenopus laevis</i> embryo during mid-gastrulation. 157
Figure 51	Cavity morphogenesis and quantitative assessment of morphological changes. 158

Figure 52

Formation of a transient ectodermal ridge during confrontation of head and ventral mesendoderm. [160](#)

LIST OF TABLES

Table 1

Comparison of four-dimensional *in vivo* imaging modalities in developmental biology. [153](#)

ACRONYMS

- ANKA** Angströmquelle Karlsruhe
APS Advanced Photon Source
ANL Argonne National Laboratory
ART algebraic reconstruction technique
BP backprojection
BM bending magnet
CCD charge-coupled device
CGLS conjugate gradient method for least squares
CMOS complementary metal-oxide-semiconductor
CT computed tomography
CTF contrast transfer function
DART discrete algebraic reconstruction technique
DCM double crystal monochromator
DESY Deutsches Elektron-Synchrotron
DNA deoxyribonucleic acid
ESRF European Synchrotron Radiation Facility
EXAFS extended X-ray absorption fine structure
FBP filtered backprojection
FEL free-electron laser
FFT fast Fourier transform
FOV field of view
FWHM full width at half maximum
GPU graphics processing unit
ID insertion device
IPS Institute for Photon Science and Synchrotron Radiation
μMRI microscopic magnetic resonance imaging
RNA ribonucleic acid
ROS reactive oxygen species
SART simultaneous algebraic reconstruction technique
SASE self-amplified spontaneous emission
SIRT simultaneous iterative reconstruction technique
SNR signal-to-noise ratio
SOD superoxide dismutase
TIE transport-of-intensity equation
TFT thin-film transistor
XASF X-ray absorption fine structure
XANES X-ray absorption near-edge structure
XFEL X-ray free-electron laser
XPCμT X-ray phase-contrast microtomography

BIBLIOGRAPHY

- [Air35] G. B. Airy. ‘On the Diffraction of an Object-glass with Circular Aperture’. In: *Transactions of the Cambridge Philosophical Society* 5 (1835), pp. 283–291.
- [AK59] A. A. Abrikosov and I. M. Khalatnikov. ‘The theory of a Fermi liquid (the properties of liquid ${}^3\text{He}$ at low temperatures)’. In: *Reports on Progress in Physics* 22.1 (1959), p. 329. URL: <http://stacks.iop.org/0034-4885/22/i=1/a=310>.
- [AK84] A. H. Andersen and A. C. Kak. ‘Simultaneous algebraic reconstruction technique (SART): a superior implementation of the art algorithm’. In: *Ultrason Imaging* 6.1 (Jan. 1984). [PubMed:6548059], pp. 81–94.
- [Ama+12] J. Amann et al. ‘Demonstration of self-seeding in a hard-X-ray free-electron laser’. In: *Nat Photon* 6.10 (Oct. 2012), pp. 693–698. ISSN: 1749-4885. DOI: [10.1038/nphoton.2012.180](https://doi.org/10.1038/nphoton.2012.180). URL: <http://dx.doi.org/10.1038/nphoton.2012.180>.
- [And+00] J. Andruszkow et al. ‘First Observation of Self-Amplified Spontaneous Emission in a Free-Electron Laser at 109 nm Wavelength’. In: *Phys. Rev. Lett.* 85 (18 Oct. 2000), pp. 3825–3829. DOI: [10.1103/PhysRevLett.85.3825](https://doi.org/10.1103/PhysRevLett.85.3825). URL: <http://link.aps.org/doi/10.1103/PhysRevLett.85.3825>.
- [ANK13] ANKA. ANKA *Instrumentation Book 2012*. Sept. 2013.
- [Are87] Victor Arena. *Ionizing radiation and life: an introduction to radiation biology and biological radiotracer methods*. Saint Louis: Mosby, 1987, pages.
- [Baro4] Charles G. Barkla. ‘Polarisation in Röntgen Rays’. In: *Nature* 69 (Mar. 1904), p. 463. DOI: [10.1038/069463a0](https://doi.org/10.1038/069463a0).
- [Baro5] Charles G. Barkla. ‘Polarized Röntgen radiation’. In: *Phil. Trans. Roy. Soc. Lond. A* 204 (1905), p. 467.
- [BDC96] M. Op de Beeck, D. Van Dyck and W. Coene. ‘Wave function reconstruction in HRTEM: the parabola method’. In: *Ultramicroscopy* 64.1–4 (1996), pp. 167–183. ISSN: 0304-3991. DOI: [10.1016/0304-3991\(96\)00058-7](https://doi.org/10.1016/0304-3991(96)00058-7). URL: <http://www.sciencedirect.com/science/article/pii/0304399196000587>.

- [Bec93] J. M. Beckers. ‘Adaptive Optics For Astronomy: Principles, Performance, And Applications’. In: *Annu. Rev. Astron. Astrophys* 31 (1993), pp. 11–62. DOI: [10.1146/annurev.aa.31.090193.000305](https://doi.org/10.1146/annurev.aa.31.090193.000305). URL: <http://www.annualreviews.org/doi/abs/10.1146/annurev.aa.31.090193.000305>.
- [BH65] U. Bonse and M. Hart. ‘An X-ray Interferometer’. In: *Applied Physics Letters* 6.8 (1965), pp. 155–156. DOI: [10.1063/1.1754212](https://doi.org/10.1063/1.1754212). URL: <http://scitation.aip.org/content/aip/journal/apl/6/8/10.1063/1.1754212>.
- [BIB96] V. A. Bushuev, V. N. Ingal and E. A. Belyaevskaya. ‘Dynamical theory of images generated by noncrystalline objects for the method of phase-dispersive introscopy’. In: *Crystallography Reports* 41.5 (1996), pp. 766–774. ISSN: 1562-689X; 1063-7745.
- [Bol98] Ludwig Eduard Boltzmann. *Vorlesungen über Gastheorie. II. Theil. Theorie van der Waals'; Gase mit zusammengesetzten Molekülen; Gasdissociation; Schlussbemerkungen*. Vorlesungen über Gastheorie. J. A. Barth, 1898. URL: http://www.deutschestextarchiv.de/book/show/boltzmann_gastheorie02_1898.
- [Boo+07] M. J. Booth et al. ‘Adaptive optics in microscopy’. In: *Phil. Trans. R. Soc. A* 365 (2007), pp. 2829–2843. DOI: [10.1098/rsta.2007.0013](https://doi.org/10.1098/rsta.2007.0013). URL: <http://rsta.royalsocietypublishing.org/content/365/1861/2829.abstract>.
- [Bor26a] Max Born. ‘Quantenmechanik der Stoßvorgänge’. German. In: *Zeitschrift für Physik* 38.11–12 (1926), pp. 803–827. ISSN: 0044-3328. DOI: [10.1007/BF01397184](https://doi.org/10.1007/BF01397184). URL: <http://dx.doi.org/10.1007/BF01397184>.
- [Bor26b] Max Born. ‘Zur Quantenmechanik der Stoßvorgänge’. German. In: *Zeitschrift für Physik* 37.12 (1926), pp. 863–867. ISSN: 0044-3328. DOI: [10.1007/BF01397477](https://doi.org/10.1007/BF01397477). URL: <http://dx.doi.org/10.1007/BF01397477>.
- [Bra13] William Lawrence Bragg. ‘The diffraction of short electromagnetic waves by a crystal’. In: *Proceedings of the Cambridge Philosophical Society*. Vol. 17. 1913, pp. 43–57.
- [Bre52] H. Bremmer. ‘On the asymptotic evaluation of diffraction integrals with a special view to the theory of defocusing and optical contrast’. In: *Physica* 18.6–7 (1952), pp. 469–485. ISSN: 0031-8914. DOI: [10.1016/S0031-8914\(52\)80079-5](https://doi.org/10.1016/S0031-8914(52)80079-5). URL: <http://www.sciencedirect.com/science/article/pii/S0031891452800795>.

- [Bri60] Léon Brillouin. *Wave propagation and group velocity*. New York: Academic Press, 1960, p. 154.
- [Bro+04] Thomas Brox, Andrés Bruhn, Nils Papenberg and Joachim Weickert. ‘High Accuracy Optical Flow Estimation Based on a Theory for Warping’. English. In: *Computer Vision - ECCV 2004*. Ed. by Tomás Pajdla and Jiří Matas. Vol. 3024. Lecture Notes in Computer Science. Springer Berlin Heidelberg, 2004, pp. 25–36. ISBN: 978-3-540-21981-1. DOI: [10.1007/978-3-540-24673-2_3](https://doi.org/10.1007/978-3-540-24673-2_3). URL: http://dx.doi.org/10.1007/978-3-540-24673-2_3.
- [Broo2] Andrei V. Bronnikov. ‘Theory of quantitative phase-contrast computed tomography’. In: *J. Opt. Soc. Am. A* 19.3 (Mar. 2002), pp. 472–480. DOI: [10.1364/JOSAA.19.000472](https://doi.org/10.1364/JOSAA.19.000472). URL: <http://josaa.osa.org/abstract.cfm?URI=josaa-19-3-472>.
- [BS11] K. J. Batenburg and J. Sijbers. ‘DART: A Practical Reconstruction Algorithm for Discrete Tomography’. In: *Image Processing, IEEE Transactions on* 20.9 (Sept. 2011), pp. 2542–2553. ISSN: 1057-7149. DOI: [10.1109/TIP.2011.2131661](https://doi.org/10.1109/TIP.2011.2131661).
- [BW09] Max Born and Emil Wolf. *Principles of Optics: electromagnetic theory of propagation, interference and diffraction of light*. 7. (expanded) ed. Cambridge [u.a.]: Cambridge University Press, 2009. ISBN: 978-0-521-64222-4. URL: <http://digitool.hbz-nrw.de:1801/webclient/DeliveryManager?pid=3270821>.
- [Cec+11] A. Cecilia et al. ‘Characterisation of LSO:Tb scintillator films for high resolution X-ray imaging applications’. In: *Nuclear Instruments and Methods in Physics Research Section A: Accelerators, Spectrometers, Detectors and Associated Equipment* 633, Supplement 1 (2011). 11th International Workshop on Radiation Imaging Detectors (IWORLD), S292–S293. ISSN: 0168-9002. DOI: [10.1016/j.nima.2010.06.192](https://doi.org/10.1016/j.nima.2010.06.192). URL: <http://www.sciencedirect.com/science/article/pii/S0168900210013823>.
- [Cha+11] Henry N. Chapman et al. ‘Femtosecond X-ray protein nanocrystallography’. In: *Nature* 470.7332 (2011), pp. 73–77. ISSN: 0028-0836. DOI: [femto](https://doi.org/10.1038/nature09750). URL: <http://dx.doi.org/10.1038/nature09750>.
- [Cha+97] D. Chapman et al. ‘Diffraction enhanced X-ray imaging’. In: *Physics in Medicine and Biology* 42.11 (1997), p. 2015. DOI: [10.1088/0031-9155/42/11/001](https://doi.org/10.1088/0031-9155/42/11/001). URL: <http://stacks.iop.org/0031-9155/42/i=11/a=001>.

- [Che+11] R. C. Chen et al. ‘Phase retrieval in quantitative x-ray microtomography with a single sample-to-detector distance’. In: *Opt. Lett.* 36.9 (May 2011), pp. 1719–1721. DOI: [10.1364/OL.36.001719](https://doi.org/10.1364/OL.36.001719). URL: <http://ol.osa.org/abstract.cfm?URI=ol-36-9-1719>.
- [Clo99] Peter Cloetens. ‘Contribution to Phase Contrast Imaging, Reconstruction and Tomography with Hard Synchrotron Radiation’. PhD Dissertation. Vrije Universiteit Brussel, 1999.
- [Com23] Arthur H. Compton. ‘A Quantum Theory of the Scattering of X-rays by Light Elements’. In: *Phys. Rev.* 21 (5 May 1923), pp. 483–502. DOI: [10.1103/PhysRev.21.483](https://doi.org/10.1103/PhysRev.21.483). URL: <http://link.aps.org/doi/10.1103/PhysRev.21.483>.
- [Coo17] W. D. Coolidge. *X-ray tube*. US Patent 1,211,092. Jan. 1917. URL: <http://www.google.com/patents/US1211092>.
- [Cor63] Allan MacLeod Cormack. ‘Representation of a Function by Its Line Integrals, with Some Radiological Applications’. In: *Journal of Applied Physics* 34.9 (1963), pp. 2722–2727. DOI: [10.1063/1.1729798](https://doi.org/10.1063/1.1729798). URL: <http://scitation.aip.org/content/aip/journal/jap/34/9/10.1063/1.1729798>.
- [Cor64] Allan MacLeod Cormack. ‘Representation of a Function by Its Line Integrals, with Some Radiological Applications. II’. In: *Journal of Applied Physics* 35.10 (1964), pp. 2908–2913. DOI: [10.1063/1.1713127](https://doi.org/10.1063/1.1713127). URL: <http://scitation.aip.org/content/aip/journal/jap/35/10/10.1063/1.1713127>.
- [CTLo8] Guang-Hong Chen, Jie Tang and Shuai Leng. ‘Prior image constrained compressed sensing (PICCS): A method to accurately reconstruct dynamic CT images from highly undersampled projection data sets’. In: *Medical Physics* 35.2 (2008), pp. 660–663. DOI: [10.1118/1.2836423](https://doi.org/10.1118/1.2836423). URL: <http://scitation.aip.org/content/aapm/journal/medphys/35/2/10.1118/1.2836423>.
- [Dar71] Charles Darwin. *On the origin of species*. Fifth. On The Origin of Species By Means of Natural Selection, or the Preservation of favored Races in the Struggle for Life. New York: D. Appleton and Co., 1871, p. 470. DOI: [dx.doi.org/10.5962/bhl.title.28875](https://doi.org/10.5962/bhl.title.28875). URL: <http://www.biodiversitylibrary.org/item/71804>.

- [Dav+02] C. David, B. Nöhammer, H. H. Solak and E. Ziegler. ‘Differential x-ray phase contrast imaging using a shearing interferometer’. In: *Applied Physics Letters* 81.17 (2002), pp. 3287–3289. DOI: [10.1063/1.1516611](https://doi.org/10.1063/1.1516611). URL: <http://scitation.aip.org/content/aip/journal/apl/81/17/10.1063/1.1516611>.
- [Dav+95] T. J. Davis et al. ‘Phase-contrast imaging of weakly absorbing materials using hard X-rays’. In: *Nature* 373.6515 (Feb. 1995), pp. 595–598. URL: <http://dx.doi.org/10.1038/373595a0>.
- [Di 12] M. Di Carlo. ‘Simple model systems: a challenge for Alzheimer’s disease’. In: *Immunity & Ageing* 9.1 (2012), p. 3.
- [Die+11] R. Dietsch et al. ‘Performance of Multilayer Monochromators for Hard X-Ray Imaging with Coherent Synchrotron Radiation’. In: *AIP Conference Proceedings* 1365.1 (2011), pp. 77–80. DOI: [10.1063/1.3625308](https://doi.org/10.1063/1.3625308). URL: <http://scitation.aip.org/content/aip/proceeding/aipcp/10.1063/1.3625308>.
- [Dono6] D.L. Donoho. ‘Compressed sensing’. In: *Information Theory, IEEE Transactions on* 52.4 (Apr. 2006), pp. 1289–1306. ISSN: 0018-9448. DOI: [10.1109/TIT.2006.871582](https://doi.org/10.1109/TIT.2006.871582).
- [DS16] Peter Joseph William Debye and Paul Scherrer. ‘Interferenzen an regellos orientierten Teilchen im Röntgenlicht. I.’ In: *Nachrichten von der Gesellschaft der Wissenschaften zu Göttingen, Mathematisch-Physikalische Klasse* 1916 (1916), pp. 1–15. URL: <http://eudml.org/doc/58947>.
- [Dys49] Freeman John Dyson. ‘The Radiation Theories of Tomonaga, Schwinger, and Feynman’. In: *Phys. Rev.* 75 (3 Feb. 1949), pp. 486–502. DOI: [10.1103/PhysRev.75.486](https://doi.org/10.1103/PhysRev.75.486). URL: <http://link.aps.org/doi/10.1103/PhysRev.75.486>.
- [EB54] Arthur Erdélyi and Harry Bateman. *Tables of integral transforms*. New York: McGraw-Hill, 1954, p. 410.
- [Eino5] Albert Einstein. ‘Über einen die Erzeugung und Verwandlung des Lichtes betreffenden heuristischen Gesichtspunkt’. In: *Annalen der Physik* 322.6 (1905), pp. 132–148. ISSN: 1521-3889. DOI: [10.1002/andp.19053220607](https://doi.org/10.1002/andp.19053220607). URL: <http://dx.doi.org/10.1002/andp.19053220607>.

- [Ewa+04] Andrew J. Ewald et al. ‘Regional requirements for Dishevelled signaling during *Xenopus* gastrulation: separable effects on blastopore closure, mesendoderm internalization and archenteron formation’. In: *Development* 131.24 (2004), pp. 6195–6209. DOI: [10.1242/dev.01542](https://doi.org/10.1242/dev.01542). URL: <http://dev.biologists.org/content/131/24/6195.abstract>.
- [Far+01] A. Faridani et al. ‘Introduction to Local Tomography’. In: *Radon Transforms and Tomography*. Ed. by E. T. Quinto et al. Vol. 278. Contemporary Mathematics. American Mathematical Society, Providence, Rhode Island. American Mathematical Society, Providence, Rhode Island, 2001, pp. 29–47.
- [Fey49a] Richard Phillips Feynman. ‘Space-Time Approach to Quantum Electrodynamics’. In: *Phys. Rev.* 76 (6 Sept. 1949), pp. 769–789. DOI: [10.1103/PhysRev.76.769](https://doi.org/10.1103/PhysRev.76.769). URL: <http://link.aps.org/doi/10.1103/PhysRev.76.769>.
- [Fey49b] Richard Phillips Feynman. ‘The Theory of Positrons’. In: *Phys. Rev.* 76 (6 Sept. 1949), pp. 749–759. DOI: [10.1103/PhysRev.76.749](https://doi.org/10.1103/PhysRev.76.749). URL: <http://link.aps.org/doi/10.1103/PhysRev.76.749>.
- [Fey50] Richard Phillips Feynman. ‘Mathematical Formulation of the Quantum Theory of Electromagnetic Interaction’. In: *Phys. Rev.* 80 (3 Nov. 1950), pp. 440–457. DOI: [10.1103/PhysRev.80.440](https://doi.org/10.1103/PhysRev.80.440). URL: <http://link.aps.org/doi/10.1103/PhysRev.80.440>.
- [FG53] Rosalind Elsie Franklin and Raymond G. Gosling. ‘Molecular Configuration in Sodium Thymonucleate’. In: *Nature* 171.4356 (Apr. 1953), pp. 740–741. URL: <http://dx.doi.org/10.1038/171740a0>.
- [FGZ80] E. Förster, K. Goetz and P. Zaumseil. ‘Double crystal diffractometry for the characterization of targets for laser fusion experiments’. In: *Kristall und Technik* 15.8 (1980), pp. 937–945. ISSN: 1521-4079. DOI: [10.1002/crat.19800150812](https://doi.org/10.1002/crat.19800150812). URL: <http://dx.doi.org/10.1002/crat.19800150812>.
- [FKL13] Walter Friedrich, Paul Knipping and Max Theodor Felix von Laue. ‘Interferenzerscheinungen bei Röntgenstrahlen’. In: *Annalen der Physik* 346.10 (1913), pp. 971–988. ISSN: 1521-3889. DOI: [10.1002/andp.19133461004](https://doi.org/10.1002/andp.19133461004). URL: <http://dx.doi.org/10.1002/andp.19133461004>.

- [FSS99] Susan E. Forest, Michael J. Stimson and John D. Simon. 'Mechanism for the Photochemical Production of Superoxide by Quinacrine'. In: *The Journal of Physical Chemistry B* 103.19 (1999), pp. 3963–3964. DOI: [10.1021/jp9902809](https://doi.org/10.1021/jp9902809). URL: <http://dx.doi.org/10.1021/jp9902809>.
- [GBH70] Richard Gordon, Robert Bender and Gabor T. Herman. 'Algebraic Reconstruction Techniques (ART) for three-dimensional electron microscopy and X-ray photography'. In: *Journal of Theoretical Biology* 29.3 (1970), pp. 471–481. ISSN: 0022-5193. DOI: [10.1016/0022-5193\(70\)90109-8](https://doi.org/10.1016/0022-5193(70)90109-8). URL: <http://www.sciencedirect.com/science/article/pii/0022519370901098>.
- [GEF58] John Bertrand Gurdon., T. R. Elsdale and M. Fischberg. 'Sexually Mature Individuals of *Xenopus laevis* from the Transplantation of Single Somatic Nuclei'. In: *Nature* 182.4627 (July 1958), pp. 64–65. URL: [http://dx.doi.org/10.1038/182064a0](https://doi.org/10.1038/182064a0).
- [Ger+54a] Rebeca Gerschman, Daniel L. Gilbert, Sylvanus W. Nye and Wallace O. Fenn. 'Influence of X-Irradiation on Oxygen Poisoning in Mice.' In: *Experimental Biology and Medicine* 86.1 (1954), pp. 27–29. DOI: [10.3181/00379727-86-21002](https://doi.org/10.3181/00379727-86-21002). URL: <http://ebm.sagepub.com/content/86/1/27.abstract>.
- [Ger+54b] Rebeca Gerschman et al. 'Oxygen Poisoning and X-irradiation: A Mechanism in Common'. In: *Science* 119.3097 (1954), pp. 623–626. DOI: [10.1126/science.119.3097.623](https://doi.org/10.1126/science.119.3097.623). URL: <http://www.sciencemag.org/content/119/3097/623.short>.
- [Gib02] Josiah Willard Gibbs. *Elementary Principles in Statistical Mechanics: Developed with Especial Reference to the Rational Foundations of Thermodynamics*. C. Scribner's sons, 1902. URL: <http://books.google.de/books?id=2oc-AAAAIAAJ>.
- [Gla34] Otto Glasser. *Wilhelm Conrad Röntgen and the early history of the Röntgen rays*. Springfield, Ill.: C. C. Thomas, 1934, pages.
- [GN96] T. E. Gureyev and K. A. Nugent. 'Phase retrieval with the transport-of-intensity equation. II. Orthogonal series solution for nonuniform illumination'. In: *J. Opt. Soc. Am. A* 13.8 (Aug. 1996), pp. 1670–1682. doi: [10.1364/JOSAA.13.001670](https://doi.org/10.1364/JOSAA.13.001670). URL: <http://josaa.osa.org/abstract.cfm?URI=josaa-13-8-1670>.

- [GRN95] T. E. Gureyev, A. Roberts and K. A. Nugent. ‘Phase retrieval with the transport-of-intensity equation: matrix solution with use of Zernike polynomials’. In: *J. Opt. Soc. Am. A* 12.9 (Sept. 1995), pp. 1932–1941. DOI: [10.1364/JOSAA.12.001932](https://doi.org/10.1364/JOSAA.12.001932). URL: <http://josaa.osa.org/abstract.cfm?URI=josaa-12-9-1932>.
- [GS72] R. W. Gerchberg and W. O. Saxton. ‘A practical algorithm for the determination of the phase from image and diffraction plane pictures’. In: *Optik* 35 (1972), pp. 237–246.
- [GTE02] Sol M. Gruner, Mark W. Tate and Eric F. Eikenberry. ‘Charge-coupled device area x-ray detectors’. In: *Review of Scientific Instruments* 73.8 (2002), pp. 2815–2842. DOI: [10.1063/1.1488674](https://doi.org/10.1063/1.1488674). URL: <http://scitation.aip.org/content/aip/journal/rsi/73/8/10.1063/1.1488674>.
- [Gui77] Jean-Pierre Guigay. ‘Fourier transform analysis of Fresnel diffraction patterns and in-line holograms’. In: *Optik* 49 (1977), p. 121.
- [Gui78] Jean-Pierre Guigay. ‘The ambiguity function in diffraction and isoplanatic imaging by partially coherent beams’. In: *Opt. Commun.* 26 (1978), p. 136. DOI: [10.1016/0030-4018\(78\)90037-8](https://doi.org/10.1016/0030-4018(78)90037-8). URL: <http://www.sciencedirect.com/science/article/pii/0030401878900378>.
- [Gur+04] T. E. Gureyev, A. Pogany, D. M. Paganin and S. W. Wilkins. ‘Linear algorithms for phase retrieval in the Fresnel region’. In: *Optics Communications* 231.1–6 (2004), pp. 53–70. ISSN: 0030-4018. DOI: [10.1016/j.optcom.2003.12.020](https://doi.org/10.1016/j.optcom.2003.12.020). URL: <http://www.sciencedirect.com/science/article/pii/S0030401803023320>.
- [Gur+06a] T. E. Gureyev et al. ‘Linear algorithms for phase retrieval in the Fresnel region. 2. Partially coherent illumination’. In: *Opt. Commun* 259 (2006), pp. 569–580. DOI: [10.1016/j.optcom.2005.09.072](https://doi.org/10.1016/j.optcom.2005.09.072). URL: <http://www.sciencedirect.com/science/article/pii/S0030401805010357>.
- [Gur+06b] T. E. Gureyev et al. ‘Phase-and-amplitude computer tomography’. In: *Appl. Phys. Lett.* 89 (2006), p. 034102. DOI: [10.1063/1.2226794](https://doi.org/10.1063/1.2226794). URL: http://apl.aip.org/resource/1/applab/v89/i3/p034102_s1.
- [Gur62a] J. B. Gurdon. ‘Multiple genetically identical frogs’. In: *J. Hered.* 53 (1962). [PubMed:[13951336](https://pubmed.ncbi.nlm.nih.gov/13951336/)], pp. 5–9.

- [Gur62b] J.B. Gurdon. 'Adult frogs derived from the nuclei of single somatic cells'. In: *Developmental Biology* 4.2 (1962), pp. 256–273. ISSN: 0012-1606. DOI: [10.1016/0012-1606\(62\)90043-X](https://doi.org/10.1016/0012-1606(62)90043-X). URL: <http://www.sciencedirect.com/science/article/pii/001216066290043X>.
- [Gur62c] John Bertrand Gurdon. 'The Developmental Capacity of Nuclei taken from Intestinal Epithelium Cells of Feeding Tadpoles'. In: *Journal of Embryology and Experimental Morphology* 10.4 (1962), pp. 622–640. URL: <http://dev.biologists.org/content/10/4/622.abstract>.
- [Hae66] Ernst Haeckel. *The Evolution of Man: A Popular Exposition of the Principal Points of Human Ontogeny and Phylogeny*. 1898th ed. New York: D. Appleton and Co., 1866, p. 540. DOI: [10.5962/bhl.title.25748](https://doi.org/10.5962/bhl.title.25748). URL: <http://www.biodiversitylibrary.org/bibliography/25748>.
- [Ham69] William H. Hamill. 'Model for the radiolysis of water'. In: *The Journal of Physical Chemistry* 73.5 (1969), pp. 1341–1347. DOI: [10.1021/j100725a027](https://doi.org/10.1021/j100725a027). URL: <http://dx.doi.org/10.1021/j100725a027>.
- [Har+01] Joerg Harms et al. 'High Resolution Structure of the Large Ribosomal Subunit from a Mesophilic Eubacterium'. In: *Cell* 107.5 (2001), pp. 679–688. URL: [http://www.cell.com/cell/abstract/S0092-8674\(01\)00546-3](http://www.cell.com/cell/abstract/S0092-8674(01)00546-3).
- [Hel+10] Uffe Hellsten et al. 'The Genome of the Western Clawed Frog *Xenopus tropicalis*'. In: *Science* 328.5978 (2010), pp. 633–636. DOI: [10.1126/science.1183670](https://doi.org/10.1126/science.1183670). URL: <http://www.sciencemag.org/content/328/5978/633.abstract>.
- [Her88] Heinrich Hertz. 'Ueber die Ausbreitungsgeschwindigkeit der electrodynamischen Wirkungen'. In: *Annalen der Physik* 270.7 (1888), pp. 551–569. ISSN: 1521-3889. DOI: [10.1002/andp.18882700708](https://doi.org/10.1002/andp.18882700708). URL: <http://dx.doi.org/10.1002/andp.18882700708>.
- [HG30] Lancelot Hogben and Cecil Gordon. 'Studies on the Pituitary: VII. The Separate Identity of the Pressor and Melanophore Principles'. In: *Journal of Experimental Biology* 7.3 (1930), pp. 286–292. URL: <http://jeb.biologists.org/content/7/3/286.short>.

- [HGD93] B.L. Henke, E.M. Gullikson and J.C. Davis. 'X-ray interactions: photoabsorption, scattering, transmission, and reflection at E=50-30000 eV, Z=1-92'. In: *At. Data Nucl. Data Tables* 54.2 (1993), pp. 181–342. DOI: [10.1006/adnd.1993.1013](https://doi.org/10.1006/adnd.1993.1013). URL: <http://www.sciencedirect.com/science/article/pii/S00092640X83710132>.
- [Hig+05] O. Hignette et al. 'Efficient sub 100nm focusing of hard x rays'. In: *Review of Scientific Instruments* 76.6, 063709 (2005), pages. DOI: [10.1063/1.1928191](https://doi.org/10.1063/1.1928191). URL: <http://scitation.aip.org/content/aip/journal/rsi/76/6/10.1063/1.1928191>.
- [HMB11] Ralf Hofmann, Julian Moosmann and Tilo Baumbach. 'Criticality in single-distance phase retrieval'. In: *Opt. Express* 19.27 (Dec. 2011), p. 25881. DOI: [10.1364/OE.19.025881](https://doi.org/10.1364/OE.19.025881). URL: <http://dx.doi.org/10.1364/OE.19.025881>.
- [HO93] P. Hansen and D. O'Leary. 'The Use of the L-Curve in the Regularization of Discrete Ill-Posed Problems'. In: *SIAM Journal on Scientific Computing* 14.6 (1993), pp. 1487–1503. DOI: [10.1137/0914086](https://doi.org/10.1137/0914086). URL: <http://dx.doi.org/10.1137/0914086>.
- [Hof+14] Ralf Hofmann et al. 'Single-distance, high-resolution in vivo imaging with propagation-based X-ray phase contrast'. To be submitted. 2014.
- [Hof04] Albert Hofmann. *The Physics of Synchrotron Radiation*. Cambridge Monographs on Particle Physics, Nuclear Physics and Cosmology. Cambridge University Press, May 2004. ISBN: 9781139451109. DOI: [10.2277/0521308267](https://doi.org/10.2277/0521308267).
- [Hof11] Ralf Hofmann. *The Thermodynamics of Quantum Yang-Mills Theory: Theory and Applications*. World Scientific, Dec. 2011, p. 480. ISBN: 9789814329040. URL: <http://www.worldscientific.com/worldscibooks/10.1142/8015>.
- [Hop55] H. H. Hopkins. 'The Frequency Response of a Defocused Optical System'. In: *Royal Society of London Proceedings Series A* 231 (July 1955), pp. 91–103. DOI: [10.1098/rspa.1955.0158](https://doi.org/10.1098/rspa.1955.0158).
- [Hou73] Godfrey Newbold Hounsfield. 'Computerized transverse axial scanning (tomography): Part 1. Description of system'. In: *The British Journal of Radiology* 46.552 (1973). PMID: 4757352, pp. 1016–1022.

- DOI: [10.1259/0007-1285-46-552-1016](https://doi.org/10.1259/0007-1285-46-552-1016). URL: <http://dx.doi.org/10.1259/0007-1285-46-552-1016>.
- [How+09] M.R. Howells et al. ‘An assessment of the resolution limitation due to radiation-damage in X-ray diffraction microscopy’. In: *Journal of Electron Spectroscopy and Related Phenomena* 170.1–3 (2009). Radiation Damage, pp. 4–12. ISSN: 0368-2048. DOI: [10.1016/j.elspec.2008.10.008](https://doi.org/10.1016/j.elspec.2008.10.008). URL: <http://www.sciencedirect.com/science/article/pii/S0368204808001424>.
- [HS52] Magnus R. Hestenes and Eduard Stiefel. ‘Methods of Conjugate Gradients for Solving Linear Systems’. In: *Journal of Research of the National Bureau of Standards* 49.6 (1952), pp. 409–436.
- [Hui+04] Jan Huisken et al. ‘Optical Sectioning Deep Inside Live Embryos by Selective Plane Illumination Microscopy’. In: *Science* 305.5686 (2004), pp. 1007–1009. DOI: [10.1126/science.1100035](https://doi.org/10.1126/science.1100035). URL: <http://www.sciencemag.org/content/305/5686/1007.abstract>.
- [Hul17] A. W. Hull. ‘A New Method of X-Ray Crystal Analysis’. In: *Phys. Rev.* 10 (6 Dec. 1917), pp. 661–696. DOI: [10.1103/PhysRev.10.661](https://doi.org/10.1103/PhysRev.10.661). URL: <http://link.aps.org/doi/10.1103/PhysRev.10.661>.
- [HYFoo] Christiaan Huygens, Thomas Young and Augustin Fresnel. *The wave theory of light; memoirs of Huygens, Young and Fresnel*, American Book Company, New York, Cincinnati, 1900, pages.
- [Jac99] John David Jackson. *Classical electrodynamics*. 3. ed. New York: Wiley, 1999. ISBN: 978-0-471-30932-1; 0-471-30932-X. URL: <http://swbplus.bsz-bw.de/bsz072816562cov.htm>.
- [Kac37] Stefan Kaczmarz. ‘Angenäherte Auflösung von Systemen linearer Gleichungen’. In: *Bulletin International de l’Académie Polonaise des Sciences et des Lettres. Classe des Sciences Mathématiques et Naturelles. Série A, Sciences Mathématiques* 35 (1937), pp. 355–357.
- [Kas+09] Jubin Kashef et al. ‘Cadherin-11 regulates protrusive activity in Xenopus cranial neural crest cells upstream of Trio and the small GTPases’. In: *Genes & Development* 23.12 (2009), pp. 1393–1398. DOI: [10.1101/gad.519409](https://doi.org/10.1101/gad.519409). URL: <http://genesdev.cshlp.org/content/23/12/1393.abstract>.

- [KDS03] Ray Keller, Lance A. Davidson and David R. Shook. 'How we are shaped: The biomechanics of gastrulation'. In: *Differentiation* 71.3 (2003), pp. 171–205. ISSN: 1432-0436. DOI: [10.1046/j.1432-0436.2003.710301.x](https://doi.org/10.1046/j.1432-0436.2003.710301.x). URL: <http://dx.doi.org/10.1046/j.1432-0436.2003.710301.x>.
- [Kei05] K. Keith A. Nugent. 'X-ray Image Reconstruction using the Transport of Intensity Equation'. In: *Proc. 8th Int. Conf. X-ray Microscopy*. Vol. 7. IPAP Conf. Series. 2005, pp. 399–402.
- [Kel+08] Philipp J. Keller, Annette D. Schmidt, Joachim Wittbrodt and Ernst H. K. Stelzer. 'Reconstruction of Zebrafish Early Embryonic Development by Scanned Light Sheet Microscopy'. In: *Science* 322.5904 (2008), pp. 1065–1069. DOI: [10.1126/science.1162493](https://doi.org/10.1126/science.1162493). URL: <http://www.sciencemag.org/content/322/5904/1065.abstract>.
- [KG82] Otto Kratky and Otto Glatter. *Small angle X-ray scattering / edited by O. Glatter and O. Kratky*. English. Academic Press London; New York, 1982, p. 515. ISBN: 0122862805.
- [Kim86] Kwang-Je Kim. 'Brightness, coherence and propagation characteristics of synchrotron radiation'. In: *Nuclear Instruments and Methods in Physics Research Section A: Accelerators, Spectrometers, Detectors and Associated Equipment* 246.1–3 (1986), pp. 71–76. ISSN: 0168-9002. DOI: [10.1016/0168-9002\(86\)90048-3](https://doi.org/10.1016/0168-9002(86)90048-3). URL: [http://dx.doi.org/10.1016/0168-9002\(86\)90048-3](http://dx.doi.org/10.1016/0168-9002(86)90048-3).
- [Kim89] Kwang-Je Kim. 'Characteristics of synchrotron radiation'. In: *AIP Conference Proceedings* 184.1 (1989), pp. 565–632. DOI: [10.1063/1.38046](https://doi.org/10.1063/1.38046). URL: <http://scitation.aip.org/content/aip/proceeding/aipcp/10.1063/1.38046>.
- [Kir98] Earl J. Kirkland. *Advanced Computing in Electron Microscopy*. Plenum Press, 1998. ISBN: 9780306459368.
- [KN29] Oskar Klein and Yoshio Nishina. 'Über die Streuung von Strahlung durch freie Elektronen nach der neuen relativistischen Quantendynamik von Dirac'. German. In: *Zeitschrift für Physik* 52.11–12 (1929), pp. 853–868. ISSN: 0044-3328. DOI: [10.1007/BF01366453](https://doi.org/10.1007/BF01366453). URL: <http://dx.doi.org/10.1007/BF01366453>.
- [Koc+98] Andreas Koch, Carsten Raven, Per Spanne and Anatoly Snigirev. 'X-ray imaging with submicrometer resolution employing transparent luminescent screens'.

- In: *J. Opt. Soc. Am. A* 15.7 (July 1998), pp. 1940–1951.
 DOI: [10.1364/JOSAA.15.001940](https://doi.org/10.1364/JOSAA.15.001940). URL:
<http://josaa.osa.org/abstract.cfm?URI=josaa-15-7-1940>.
- [Koh+03] Yoshiki Kohmura, Tetsuya Ishikawa, Hidekazu Takano and Yoshio Suzuki. ‘Shearing X-ray interferometer with an X-ray prism’. In: *Journal of Applied Physics* 93.4 (2003), pp. 2283–2285. DOI: [10.1063/1.1536718](https://doi.org/10.1063/1.1536718). URL:
<http://scitation.aip.org/content/aip/journal/jap/93/4/10.1063/1.1536718>.
- [KP87] D. C. Koningsberger and R. Prins, eds. *X-Ray Absorption: Principles, Applications, Techniques of EXAFS, SEXAFS and XANES*. John Wiley and Sons, New York, 1987, p. 688. DOI: [10.1002/xrs.1300180112](https://doi.org/10.1002/xrs.1300180112). URL:
<http://dx.doi.org/10.1002/xrs.1300180112>.
- [Kra79] Vladimir B. Krapchev. ‘Kinetic Theory of the Ponderomotive Effects in a Plasma’. In: *Phys. Rev. Lett.* 42 (8 Feb. 1979), pp. 497–500. DOI:
[10.1103/PhysRevLett.42.497](https://doi.org/10.1103/PhysRevLett.42.497). URL: <http://link.aps.org/doi/10.1103/PhysRevLett.42.497>.
- [KS01] Avinash C. Kak and Malcolm Slaney. *Principles of Computerized Tomographic Imaging*. Society for Industrial and Applied Mathematics, 2001. DOI:
[10.1137/1.9780898719277](https://doi.org/10.1137/1.9780898719277). URL: <http://epubs.siam.org/doi/abs/10.1137/1.9780898719277>.
- [Külo5] Dietmar Kültz. ‘Molecular And Evolutionary Basis Of The Cellular Stress Response’. In: *Annual Review of Physiology* 67.1 (2005). PMID: 15709958, pp. 225–257. DOI: [10.1146/annurev.physiol.67.040403.103635](https://doi.org/10.1146/annurev.physiol.67.040403.103635). URL: <http://dx.doi.org/10.1146/annurev.physiol.67.040403.103635>.
- [KW57] Rudolf H. A. Kohlrausch and Wilhelm Eduard Weber. ‘Elektrodynamische Maßbestimmungen: insbesondere Zurückführung der Stromintensitäts-Messungen auf mechanisches Maass’. In: *Abhandlungen der Mathematisch-physischen Klasse der Königl. Sächsischen Gesellschaft der Wissenschaften* 28 (1857), p. 219.
- [Lan+08] Max Langer, Peter Cloetens, Jean-Pierre Guigay and Françoise Peyrin. ‘Quantitative comparison of direct phase retrieval algorithms in in-line phase tomography’. In: *Medical Physics* 35.10 (2008), pp. 4556–4566. DOI: [10.1118/1.2975224](https://doi.org/10.1118/1.2975224). URL:
<http://scitation.aip.org/content/aapm/journal/medphys/35/10/10.1118/1.2975224>.

- [Lan+12] M. Langer, P. Cloetens, A. Pacureanu and F. Peyrin. 'X-ray in-line phase tomography of multimaterial objects'. In: *Opt. Lett.* 37.11 (2012), p. 2151. DOI: [10.1364/OL.37.002151](https://doi.org/10.1364/OL.37.002151). URL: <http://www.opticsinfobase.org/ol/abstract.cfm?uri=ol-37-11-2151>.
- [Lan+14] Max Langer et al. 'Priors for X-ray in-line phase tomography of heterogeneous objects'. In: *Philosophical Transactions of the Royal Society A: Mathematical, Physical and Engineering Sciences* 372.2010 (2014), pp. 1–9. DOI: [10.1098/rsta.2013.0129](https://doi.org/10.1098/rsta.2013.0129). URL: <http://rsta.royalsocietypublishing.org/content/372/2010/20130129.abstract>.
- [Lan57] Lev Davidovich Landau. 'The Theory of a Fermi liquid'. In: *Sov. Phys. JETP* 3 (1957), pp. 920–925.
- [LaVoo] Jay A. LaVerne. 'OH Radicals and Oxidizing Products in the Gamma Radiolysis of Water'. In: *Radiation Research* 153.2 (Feb. 2000), pp. 196–200. ISSN: 0033-7587. DOI: [10.1667/0033-7587\(2000\)153\[0196:ORA0PI\]2.0.CO;2](https://doi.org/10.1667/0033-7587(2000)153[0196:ORA0PI]2.0.CO;2). URL: [http://www.rrjournal.org/doi/abs/10.1667/0033-7587\(2000\)153\[0196:ORA0PI\]2.0.CO;2](http://www.rrjournal.org/doi/abs/10.1667/0033-7587(2000)153[0196:ORA0PI]2.0.CO;2).
- [Lin95] Peter F. Lindley. 'The use of synchrotron radiation in protein crystallography'. In: *Radiation Physics and Chemistry* 45.3 (1995). Applications of synchrotron X-radiation, pp. 367–383. ISSN: 0969-806X. DOI: [10.1016/0969-806X\(93\)E0005-P](https://doi.org/10.1016/0969-806X(93)E0005-P). URL: <http://www.sciencedirect.com/science/article/pii/0969806X93E0005P>.
- [Löf03] Georg [Hrsg.] Löffler, ed. *Biochemie und Pathobiochemie*. 7., völlig neu bearb. Aufl. Springer-Lehrbuch. Berlin: Springer, 2003. ISBN: 3-540-42295-1.
- [Lüb+00] D. Lübbert et al. 'μm-resolved high resolution X-ray diffraction imaging for semiconductor quality control'. In: *Nuclear Instruments and Methods in Physics Research Section B: Beam Interactions with Materials and Atoms* 160.4 (2000), pp. 521–527. ISSN: 0168-583X. DOI: [10.1016/S0168-583X\(99\)00619-9](https://doi.org/10.1016/S0168-583X(99)00619-9). URL: <http://www.sciencedirect.com/science/article/pii/S0168583X99006199>.
- [Mar+09] T. Martin et al. 'LSO-Based Single Crystal Film Scintillator for Synchrotron-Based Hard X-Ray Micro-Imaging'. In: *Nuclear Science, IEEE Transactions on*

- 56.3 (June 2009), pp. 1412–1418. ISSN: 0018-9499. DOI: [10.1109/TNS.2009.2015878](https://doi.org/10.1109/TNS.2009.2015878).
- [MAT12] MATLAB. (*R2010a*). Natick, Massachusetts: The MathWorks Inc., 2012.
- [Max64] James Clerk Maxwell. ‘A Dynamical Theory of the Electromagnetic Field’. In: *Philosophical Transactions of the Royal Society of London* 155 (1864), pp. 459–512. DOI: [10.1098/rstl.1865.0008](https://doi.org/10.1098/rstl.1865.0008). URL: <http://rstl.royalsocietypublishing.org/content/155/459.short>.
- [Mei22] Lise Meitner. ‘Über die Entstehung der β -Strahl-Spektren radioaktiver Substanzen’. German. In: *Zeitschrift für Physik* 9.1 (1922), pp. 131–144. ISSN: 0044-3328. DOI: [10.1007/BF01326962](https://doi.org/10.1007/BF01326962). URL: <http://dx.doi.org/10.1007/BF01326962>.
- [MHB11a] Julian Moosmann, Ralf Hofmann and Tilo Baumbach. ‘Nonlinear, single-distance phase retrieval and Schwinger regularization’. In: *physica status solidi (a)* 208.11 (2011), pp. 2511–2515. ISSN: 1862-6319. DOI: [10.1002/pssa.201184267](https://doi.org/10.1002/pssa.201184267). URL: <http://dx.doi.org/10.1002/pssa.201184267>.
- [MHB11b] Julian Moosmann, Ralf Hofmann and Tilo Baumbach. ‘Single-distance phase retrieval at large phase shifts’. In: *Opt. Express* 19 (2011), p. 12066. DOI: [10.1364/OE.19.012066](https://doi.org/10.1364/OE.19.012066). URL: <http://dx.doi.org/10.1364/OE.19.012066>.
- [MKo6] Thierry Martin and Andreas Koch. ‘Recent developments in X-ray imaging with micrometer spatial resolution’. In: *Journal of Synchrotron Radiation* 13.2 (Mar. 2006), pp. 180–194. DOI: [10.1107/S0909049506000550](https://doi.org/10.1107/S0909049506000550). URL: <http://dx.doi.org/10.1107/S0909049506000550>.
- [Mom+03] Atsushi Momose et al. ‘Demonstration of X-Ray Talbot Interferometry’. In: *Japanese Journal of Applied Physics* 42.7B (2003), p. L866. URL: <http://stacks.iop.org/1347-4065/42/i=7B/a=L866>.
- [Momo3] Atsushi Momose. ‘Phase-sensitive imaging and phase tomography using X-ray interferometers’. In: *Opt. Express* 11.19 (Sept. 2003), pp. 2303–2314. DOI: [10.1364/OE.11.002303](https://doi.org/10.1364/OE.11.002303). URL: <http://www.opticsexpress.org/abstract.cfm?URI=oe-11-19-2303>.

- [Mom95] Atsushi Momose. ‘Demonstration of phase-contrast X-ray computed tomography using an X-ray interferometer’. In: *Nucl. Inst. Meth. A* 352 (1995), p. 622. DOI: [10.1016/0168-9002\(95\)90017-9](https://doi.org/10.1016/0168-9002(95)90017-9). URL: <http://www.sciencedirect.com/science/article/pii/0168900295900179>.
- [Moo+10] Julian Moosmann, Ralf Hofmann, Andrei V. Bronnikov and Tilo Baumbach. ‘Nonlinear phase retrieval from single-distance radiograph’. In: *Optics Express* 18 (2010), p. 25771. DOI: [10.1364/OE.18.025771](https://doi.org/10.1364/OE.18.025771). URL: <http://dx.doi.org/10.1364/OE.18.025771>.
- [Moo+13a] Julian Moosmann et al. *In vivo Microtomography of Xenopus Gastrulation: Time-lapse volumes (4D)*. 2013. URL: <http://www.xenbase.org/entry/doNewsRead.do?id=120>.
- [Moo+13b] Julian Moosmann et al. ‘X-ray phase-contrast *in vivo* microtomography probes new aspects of *Xenopus gastrulation*’. In: *Nature* 497.7449 (16th May 2013). Letter, pp. 374–377. ISSN: 0028-0836. URL: <http://dx.doi.org/10.1038/nature12116>.
- [Moo+14] Julian Moosmann et al. ‘Time-lapse X-ray phase-contrast microtomography for *in vivo* imaging and analysis of morphogenesis’. In: *Nat. Protocols* 9.2 (Feb. 2014), pp. 294–304. ISSN: 1754-2189. URL: <http://dx.doi.org/10.1038/nprot.2014.033>.
- [Neu+00] Richard Neutze et al. ‘Potential for biomolecular imaging with femtosecond X-ray pulses’. In: *Nature* 406.6797 (Aug. 2000), pp. 752–757. ISSN: 0028-0836. URL: <http://dx.doi.org/10.1038/35021099>.
- [Nug+96] K. A. Nugent et al. ‘Quantitative Phase Imaging Using Hard X Rays’. In: *Phys. Rev. Lett.* 77.14 (Sept. 1996), pp. 2961–2964. DOI: [10.1103/PhysRevLett.77.2961](https://doi.org/10.1103/PhysRevLett.77.2961). URL: <http://link.aps.org/doi/10.1103/PhysRevLett.77.2961>.
- [NWo8] Ya. I. Nesterets and S. W. Wilkins. ‘Phase-contrast imaging using a scanning-doublegrating configuration’. In: *Opt. Express* 16.8 (Apr. 2008), pp. 5849–5867. DOI: [10.1364/OE.16.005849](https://doi.org/10.1364/OE.16.005849). URL: <http://www.opticsexpress.org/abstract.cfm?URI=oe-16-8-5849>.
- [Nyg28] Harry Nyquist. ‘Certain Topics in Telegraph Transmission Theory’. In: *American Institute of Electrical Engineers, Transactions of the* 47.2 (Apr. 1928),

- pp. 617–644. ISSN: 0096-3860. DOI: [10.1109/T-AIEE.1928.5055024](https://doi.org/10.1109/T-AIEE.1928.5055024).
- [Old61] William H. Oldendorf. ‘Isolated Flying Spot Detection of Radiodensity Discontinuities Displaying the Internal Structural Pattern of a Complex Object’. In: *Bio-Medical Electronics, IRE Transactions on* 8.1 (Jan. 1961), pp. 68–72. ISSN: 0096-1884. DOI: [10.1109/TBME.1961.4322854](https://doi.org/10.1109/TBME.1961.4322854).
- [OSo8] A. Olivo and R. D. Speller. ‘A novel x-ray imaging technique based on coded apertures making phase contrast imaging feasible with conventional sources’. In: *Nuclear Science Symposium Conference Record, 2008. NSS '08. IEEE.* Oct. 2008, pp. 1447–1450. DOI: [10.1109/NSSMIC.2008.4774687](https://doi.org/10.1109/NSSMIC.2008.4774687).
- [Pag+02] D. Paganin et al. ‘Simultaneous phase and amplitude extraction from a single defocused image of a homogeneous object’. In: *Journal of Microscopy* 206.1 (2002), pp. 33–40. ISSN: 1365-2818. DOI: [10.1046/j.1365-2818.2002.01010.x](https://doi.org/10.1046/j.1365-2818.2002.01010.x). URL: <http://dx.doi.org/10.1046/j.1365-2818.2002.01010.x>.
- [Pago6] David M. Paganin. *Coherent X-Ray Optics*. Oxford University Press, 2006.
- [Pap+06] Cyrus Papan et al. ‘Time-lapse tracing of mitotic cell divisions in the early Xenopus embryo using microscopic MRI’. In: *Developmental Dynamics* 235.11 (2006), pp. 3059–3062. ISSN: 1097-0177. DOI: [10.1002/dvdy.20947](https://doi.org/10.1002/dvdy.20947). URL: <http://dx.doi.org/10.1002/dvdy.20947>.
- [Pap+07a] Cyrus Papan et al. ‘Formation of the dorsal marginal zone in Xenopus laevis analyzed by time-lapse microscopic magnetic resonance imaging’. In: *Developmental Biology* 305.1 (2007), pp. 161–171. ISSN: 0012-1606. DOI: [10.1016/j.ydbio.2007.02.005](https://doi.org/10.1016/j.ydbio.2007.02.005). URL: <http://www.sciencedirect.com/science/article/pii/S0012160607001029>.
- [Pap+07b] Cyrus Papan et al. ‘Two-dimensional and three-dimensional time-lapse microscopic magnetic resonance imaging of Xenopus gastrulation movements using intrinsic tissue-specific contrast’. In: *Developmental Dynamics* 236.2 (2007), pp. 494–501. ISSN: 1097-0177. DOI: [10.1002/dvdy.21045](https://doi.org/10.1002/dvdy.21045). URL: <http://dx.doi.org/10.1002/dvdy.21045>.
- [Pap74] Athanasios Papoulis. ‘Ambiguity function in Fourier optics’. In: *J. Opt. Soc. Am.* 64.6 (June 1974), pp. 779–788. DOI: [10.1364/JOSA.64.000779](https://doi.org/10.1364/JOSA.64.000779). URL: <http://dx.doi.org/10.1364/JOSA.64.000779>.

- //www.opticsinfobase.org/abstract.cfm?URI=josa-64-6-779.
- [PB13] D.M. Pelt and K.J. Batenburg. ‘Fast Tomographic Reconstruction From Limited Data Using Artificial Neural Networks’. In: *Image Processing, IEEE Transactions on* 22.12 (Dec. 2013), pp. 5238–5251. ISSN: 1057-7149. DOI: [10.1109/TIP.2013.2283142](https://doi.org/10.1109/TIP.2013.2283142).
- [PBS11] W.J. Palenstijn, K.J. Batenburg and J. Sijbers. ‘Performance improvements for iterative electron tomography reconstruction using graphics processing units (GPUs)’. In: *Journal of Structural Biology* 176.2 (2011), pp. 250–253. ISSN: 1047-8477. DOI: [10.1016/j.jsb.2011.07.017](https://doi.org/10.1016/j.jsb.2011.07.017). URL: <http://www.sciencedirect.com/science/article/pii/S1047847711002267>.
- [Pfe+06] Franz Pfeiffer, Timm Weitkamp, Oliver Bunk and Christian David. ‘Phase retrieval and differential phase-contrast imaging with low-brilliance X-ray sources’. In: *Nat Phys* 2.4 (Apr. 2006), pp. 258–261. ISSN: 1745-2473. URL: [http://dx.doi.org/10.1038/nphys265](https://doi.org/10.1038/nphys265).
- [Plao1] Max Planck. ‘Ueber das Gesetz der Energieverteilung im Normalspectrum’. In: *Annalen der Physik* 309.3 (1901), pp. 553–563. ISSN: 1521-3889. DOI: [10.1002/andp.19013090310](https://doi.org/10.1002/andp.19013090310). URL: <http://dx.doi.org/10.1002/andp.19013090310>.
- [PN98] David M. Paganin and Keith A. Nugent. ‘Noninterferometric Phase Imaging with Partially Coherent Light’. In: *Phys. Rev. Lett.* 80 (12 Mar. 1998), pp. 2586–2589. DOI: [10.1103/PhysRevLett.80.2586](https://doi.org/10.1103/PhysRevLett.80.2586). URL: <http://link.aps.org/doi/10.1103/PhysRevLett.80.2586>.
- [Pol21] M. Polanyi. ‘Das Röntgen-Faserdiagramm’. German. In: *Zeitschrift für Physik* 7.1 (1921), pp. 149–180. ISSN: 0044-3328. DOI: [10.1007/BF01332786](https://doi.org/10.1007/BF01332786). URL: <http://dx.doi.org/10.1007/BF01332786>.
- [PP13] Daniele Pelliccia and David M. Paganin. ‘X-ray phase imaging with a laboratory source using selective reflection from a mirror’. In: *Opt. Express* 21.8 (Apr. 2013), pp. 9308–9314. DOI: [10.1364/OE.21.009308](https://doi.org/10.1364/OE.21.009308). URL: <http://www.opticsexpress.org/abstract.cfm?URI=oe-21-8-9308>.

- [PS01] B. C. Platt and R. Shack. ‘History and principles of Shack-Hartmann wavefront sensing’. In: *Journal of Refractive Surgery* 17.5 (Oct. 2001), pp. 573–577. ISSN: 1081-597X. URL: <http://view.ncbi.nlm.nih.gov/pubmed/11583233>.
- [Rac+10] A. Rack et al. ‘Comparative study of multilayers used in monochromators for synchrotron-based coherent hard X-ray imaging’. In: *Journal of Synchrotron Radiation* 17.4 (July 2010), pp. 496–510. DOI: 10.1107/S0909049510011623. URL: <http://dx.doi.org/10.1107/S0909049510011623>.
- [Rad86] Johann Radon. ‘On the determination of functions from their integral values along certain manifolds’. In: *Medical Imaging, IEEE Transactions on* 5.4 (Dec. 1986), pp. 170–176. ISSN: 0278-0062. DOI: 10.1109/TMI.1986.4307775.
- [Rei13] Eugenie Samuel Reich. ‘Ultimate upgrade for US synchrotron’. In: *Nature* 501 (2013). Nature News Physics, pp. 148–149.
- [Req+09] G. Requena et al. ‘Sub-micrometer synchrotron tomography of multiphase metals using Kirkpatrick-Baez optics’. In: *Scripta Materialia* 61.7 (2009), p. 760. ISSN: 1359-6462. DOI: 10.1016/j.scriptamat.2009.06.025. URL: <http://www.sciencedirect.com/science/article/pii/S1359646209004333>.
- [RHW71] G. Rosenbaum, K. C. Holmes and J. Witz. ‘Synchrotron Radiation as a Source for X-ray Diffraction’. In: *Nature* 230.5294 (Apr. 1971), pp. 434–437. URL: <http://dx.doi.org/10.1038/230434a0>.
- [RJF02] Seth W. Ruffins, Russell E. Jacobs and Scott E. Fraser. ‘Towards a Tralfamadorian view of the embryo: multidimensional imaging of development’. In: *Current Opinion in Neurobiology* 12.5 (2002), pp. 580–586. ISSN: 0959-4388. DOI: 10.1016/S0959-4388(02)00366-5. URL: <http://www.sciencedirect.com/science/article/pii/S0959438802003665>.
- [RKT89] S. M. Rytov, Y. A. Kravtsov and V. I. Tatarskii. *Principles of statistical radiophysics. 4. Wave propagation through random media*. Springer, Berlin (Germany, F.R.), 1989, p. 198.

- [Roh+11] N. Rohani et al. ‘EphrinB/EphB signaling controls embryonic germ layer separation by contact-induced cell detachment’. In: *PLoS Biol.* 9.3 (Mar. 2011), e1000597. DOI: [10.1371/journal.pbio.1000597](https://doi.org/10.1371/journal.pbio.1000597).
- [Rön96] Wilhelm Conrad Röntgen. ‘On a new kind of rays’. In: *Nature* 53 (1896), pp. 274–276. DOI: [10.1038/053274b0](https://doi.org/10.1038/053274b0). URL: <http://www.nature.com/nature/journal/v53/n1369/pdf/053274b0.pdf>.
- [Ruh+14] A. Ruhlandt, M. Krenkel, M. Bartels and T. Salditt. ‘Three-dimensional phase retrieval in propagation-based phase-contrast imaging’. In: *Phys. Rev. A* 89 (3 Mar. 2014), p. 033847. DOI: [10.1103/PhysRevA.89.033847](https://doi.org/10.1103/PhysRevA.89.033847). URL: <http://link.aps.org/doi/10.1103/PhysRevA.89.033847>.
- [Ryd96] Lewis H. Ryder. *Quantum Field Theory*. 2nd ed. Cambridge University Press, 13th June 1996. ISBN: 0521478146. URL: <http://www.worldcat.org/isbn/0521478146>.
- [Sak93] Jun John Sakurai. *Modern Quantum Mechanics (Revised Edition)*. Ed. by San Fu Tuan. 1st ed. Addison Wesley, 10th Sept. 1993. ISBN: 0201539292. URL: <http://www.worldcat.org/isbn/0201539292>.
- [Sax78] W. O. Saxton. *Computer Techniques for Image Processing in Electron Microscopy*. Advances in electronics and electron physics / Supplement 10. New York, NY, USA: Academic Press Inc., 1978.
- [Sch+oo] Frank Schluenzen et al. ‘Structure of Functionally Activated Small Ribosomal Subunit at 3.3 Å Resolution’. In: *Cell* 102.5 (2000), pp. 615–623. ISSN: 0092-8674. DOI: [10.1016/S0092-8674\(00\)00084-2](https://doi.org/10.1016/S0092-8674(00)00084-2). URL: <http://www.sciencedirect.com/science/article/pii/S0092867400000842>.
- [Sch+94] G. Schmahl et al. ‘Phase-contrast X-ray Microscopy Studies’. In: *Optik* 97.4 (Oct. 1994), pp. 181–182. ISSN: 0030-4026.
- [Sch26] Erwin Schrödinger. ‘An Undulatory Theory of the Mechanics of Atoms and Molecules’. In: *Phys. Rev.* 28 (6 Dec. 1926), pp. 1049–1070. DOI: [10.1103/PhysRev.28.1049](https://doi.org/10.1103/PhysRev.28.1049). URL: <http://link.aps.org/doi/10.1103/PhysRev.28.1049>.
- [Sch48a] Julian Schwinger. ‘On Quantum-Electrodynamics and the Magnetic Moment of the Electron’. In: *Phys. Rev.* 73 (4 Feb. 1948), pp. 416–417. DOI:

- [10.1103/PhysRev.73.416](https://doi.org/10.1103/PhysRev.73.416). URL:
<http://link.aps.org/doi/10.1103/PhysRev.73.416>.
- [Sch48b] Julian Schwinger. ‘Quantum Electrodynamics. I. A Covariant Formulation’. In: *Phys. Rev.* 74 (10 Nov. 1948), pp. 1439–1461. DOI: [10.1103/PhysRev.74.1439](https://doi.org/10.1103/PhysRev.74.1439). URL:
<http://link.aps.org/doi/10.1103/PhysRev.74.1439>.
- [Sch92] Julian Schwinger. ‘Casimir effect in source theory II’. English. In: *Letters in Mathematical Physics* 24.1 (1992), pp. 59–61. ISSN: 0377-9017. DOI: [10.1007/BF00430003](https://doi.org/10.1007/BF00430003). URL: <http://dx.doi.org/10.1007/BF00430003>.
- [SD11] Manuel Sánchez del Río and Roger J. Dejes. ‘XOP v2.4: recent developments of the x-ray optics software toolkit’. In: *Proc. SPIE* 8141 (2011), pages. DOI:
[10.1117/12.893911](https://doi.org/10.1117/12.893911). URL:
<http://dx.doi.org/10.1117/12.893911>.
- [Sha49] Claude Elwood Shannon. ‘Communication in the Presence of Noise’. In: *Proceedings of the IRE* 37.1 (Jan. 1949), pp. 10–21. ISSN: 0096-8390. DOI:
[10.1109/JRPROC.1949.232969](https://doi.org/10.1109/JRPROC.1949.232969). URL:
<http://ieeexplore.ieee.org/xpl/articleDetails.jsp?arnumber=1697831>.
- [SKo3] P. Schäfer and R. Köhler. ‘Asymmetric Bragg reflection as X-ray magnifier’. In: *Journal of Physics D: Applied Physics* 36.10A (2003), A113. URL:
<http://stacks.iop.org/0022-3727/36/i=10A/a=323>.
- [Sni+95] A. Snigirev et al. ‘On the possibilities of x-ray phase contrast microimaging by coherent high-energy synchrotron radiation’. In: *Rev. Sci. Instrum.* 66.12 (1995), pp. 5486–5492. DOI: [10.1063/1.1146073](https://doi.org/10.1063/1.1146073). URL:
<http://link.aip.org/link/?RSI/66/5486/1>.
- [Som12] Arnold Sommerfeld. ‘Über die Beugung der Röntgenstrahlen’. In: *Annalen der Physik* 343.8 (1912), pp. 473–506. ISSN: 1521-3889. DOI:
[10.1002/andp.19123430802](https://doi.org/10.1002/andp.19123430802). URL:
<http://dx.doi.org/10.1002/andp.19123430802>.
- [Spi95] P. K. Spiegel. ‘The first clinical X-ray made in America – 100 years.’ In: *American Journal of Roentgenology* 164.1 (Jan. 1995), pp. 241–243. ISSN: 0361-803X. URL:
[http://dx.doi.org/10.2214/ajr.164.1.7998549](https://doi.org/10.2214/ajr.164.1.7998549).
- [Sta+02] Marco Stampanoni, Gunther Borchert, Rafael Abela and Peter Ruegsegger. ‘Bragg magnifier: A detector for submicrometer x-ray computer tomography’. In: *Journal of Applied Physics* 92.12 (2002), pp. 7630–7635. DOI:

- [10.1063/1.1520722](https://doi.org/10.1063/1.1520722). URL:
<http://link.aip.org/link/?JAP/92/7630/1>.
- [Sti57] Ulrich Stille. ‘Die Konstante c in der Elektrodynamik: Kohlrausch und Weber: “Elektrodynamische Maassbestimmungen”, 1856–1956’. In: *Physik Journal* 13.1 (1957), pp. 14–22. ISSN: 1521-3722. DOI: [10.1002/phbl.19570130103](https://doi.org/10.1002/phbl.19570130103). URL:
<http://dx.doi.org/10.1002/phbl.19570130103>.
- [Str85] N. Streibl. ‘Three-dimensional imaging by a microscope’. In: *J. Opt. Soc. Am. A* 2.2 (Feb. 1985), pp. 121–127. DOI: [10.1364/JOSAA.2.000121](https://doi.org/10.1364/JOSAA.2.000121). URL: <http://josaa.osa.org/abstract.cfm?URI=josaa-2-2-121>.
- [Tea82] Michael Reed Teague. ‘Irradiance moments: their propagation and use for unique retrieval of phase’. In: *J. Opt. Soc. Am.* 72.9 (Sept. 1982), pp. 1199–1209. DOI: [10.1364/JOSA.72.001199](https://doi.org/10.1364/JOSA.72.001199). URL: <http://www.opticsinfobase.org/abstract.cfm?URI=josa-72-9-1199>.
- [Tea83] Michael Reed Teague. ‘Deterministic phase retrieval: a Green’s function solution’. In: *J. Opt. Soc. Am.* 73.11 (Nov. 1983), pp. 1434–1441. DOI: [10.1364/JOSA.73.001434](https://doi.org/10.1364/JOSA.73.001434). URL: <http://www.opticsinfobase.org/abstract.cfm?URI=josa-73-11-1434>.
- [TGE97] Mark W. Tate, Sol M. Gruner and Eric F. Eikenberry. ‘Coupling format variations in x-ray detectors based on charge coupled devices’. In: *Review of Scientific Instruments* 68.1 (1997), pp. 47–54. DOI: [10.1063/1.1147611](https://doi.org/10.1063/1.1147611). URL: <http://scitation.aip.org/content/aip/journal/rsi/68/1/10.1063/1.1147611>.
- [Tom46] Sin-Itiro Tomonaga. ‘On a Relativistically Invariant Formulation of the Quantum Theory of Wave Fields’. In: *Progress of Theoretical Physics* 1.2 (1946), pp. 27–42. DOI: [10.1143/PTP.1.27](https://doi.org/10.1143/PTP.1.27). URL: <http://ptp.oxfordjournals.org/content/1/2/27.short>.
- [TT08] Barry N. Taylor and Ambler Thompson. *The International System of Units (SI). National Institute of Standards and Technology Special Publication 330 (2008 Edition)*. National Institute of Standards and Technology / U.S. Department of Commerce, 2008.
- [Tuf62] P. H. Tuft. ‘The uptake and distribution of water in the embryo of Xenopus laevis (Daudin)’. In: *J. Exp. Biol.* 39 (Mar. 1962), pp. 1–19.

- [Tur+04] L. Turner et al. ‘X-ray phase imaging: Demonstration of extended conditions for homogeneous objects’. In: *Opt. Express* 12.13 (June 2004), pp. 2960–2965. DOI: [10.1364/OPEX.12.002960](https://doi.org/10.1364/OPEX.12.002960). URL: <http://www.opticsexpress.org/abstract.cfm?URI=oe-12-13-2960>.
- [TVo1] A. C. Thompson and D. Vaughan, eds. *X-ray Data Booklet*. Third, September 2009. Authors: A. C. Thompson and D. Attwood and E. Gullikson and M. Howells and K.-J. Kim and J. Kirz and J. Kortright and I. Lindau and Y. Liu and P. Pianetta and A. Robinson and J. Scofield and J. Underwood and G. Williams and H. Winick. Lawrence Berkeley National Laboratory, University of California, Jan. 2001. URL: <http://xdb.lbl.gov/>.
- [WC53] James Dewey Watson and Francis Harry Compton Crick. ‘Molecular Structure of Nucleic Acids: A Structure for Deoxyribose Nucleic Acid’. In: *Nature* 171.4356 (Apr. 1953), pp. 737–738. URL: <http://dx.doi.org/10.1038/171737a0>.
- [Wig32] Eugene Wigner. ‘On the Quantum Correction For Thermodynamic Equilibrium’. In: *Phys. Rev.* 40 (5 June 1932), pp. 749–759. DOI: [10.1103/PhysRev.40.749](https://doi.org/10.1103/PhysRev.40.749). URL: <http://link.aps.org/doi/10.1103/PhysRev.40.749>.
- [Wil+96] S. W. Wilkins et al. ‘Phase-contrast imaging using polychromatic hard X-rays’. In: *Nature* 384.6607 (Nov. 1996), pp. 335–338. DOI: [10.1038/384335a0](https://doi.org/10.1038/384335a0). URL: <http://dx.doi.org/10.1038/384335a0>.
- [Wil96] E. J. N. Wilson. ‘Fifty years of synchrotrons’. In: *Particle accelerator. Proceedings, 5th European Conference, EPAC 96, Sitges, Spain, June 10-14, 1996. Vol. 1-3*. Ed. by S. Myers et al. Vol. C960610. Bristol, Inst. Phys., 1996, 1996, pp. 135–139. URL: <http://accelconf.web.cern.ch/AccelConf/e96/PAPERS/0RALS/FRX04A.PDF>.
- [WLo4] Xizeng Wu and Hong Liu. ‘A new theory of phase-contrast x-ray imaging based on Wigner distributions’. In: *Medical Physics* 31.9 (2004), pp. 2378–2384. DOI: [10.1118/1.1776672](https://doi.org/10.1118/1.1776672). URL: <http://scitation.aip.org/content/aapm/journal/medphys/31/9/10.1118/1.1776672>.
- [WL95] Edmund B. Wilson and Edward Leaming. *An atlas of the fertilization and karyokinesis of the ovum*. Columbia biological series. by Edmund B. Wilson ... with the co-operation of Edward Leaming ... New York, Pub. for the Columbia university press by Macmillan and co.,

- 1895, p. 76. DOI: [10.5962/bhl.title.6244](https://doi.org/10.5962/bhl.title.6244). URL: <http://www.biodiversitylibrary.org/item/28167>.
- [WLY05] Xizeng Wu, Hong Liu and Aimin Yan. 'X-ray phase-attenuation duality and phase retrieval'. In: *Opt. Lett.* 30.4 (Feb. 2005), pp. 379–381. DOI: [10.1364/OL.30.000379](https://doi.org/10.1364/OL.30.000379). URL: <http://ol.osa.org/abstract.cfm?URI=ol-30-4-379>.
- [WLZ10] John B. Wallingford, Karen J. Liu and Yixian Zheng. 'Xenopus'. In: *Current Biology* 20.6 (2010), R263–R264. DOI: [10.1016/j.cub.2010.01.012](https://doi.org/10.1016/j.cub.2010.01.012). URL: [http://www.cell.com/current-biology/abstract/S0960-9822\(10\)00015-1](http://www.cell.com/current-biology/abstract/S0960-9822(10)00015-1).
- [Wolo7] Emil Wolf. *Introduction to the theory of coherence and polarization of light*. 1. publ. Cambridge [u.a.]: Cambridge Univ. Press, c2007. ISBN: 978-0-521-82211-4.
- [Wre10] J. C. Wren. 'Steady-State Radiolysis: Effects of Dissolved Additives'. In: *Nuclear Energy and the Environment*. Ed. by Chien M. Wai and Bruce J. Mincher. American Chemical Society, 2010. Chap. 24, pp. 271–295. DOI: [10.1021/bk-2010-1046.ch022](https://doi.org/10.1021/bk-2010-1046.ch022). URL: <http://pubs.acs.org/doi/abs/10.1021/bk-2010-1046.ch022>.
- [WS99] R. Winklbauer and M. Schurfeld. 'Vegetal rotation, a new gastrulation movement involved in the internalization of the mesoderm and endoderm in Xenopus'. In: *Development* 126.16 (1999), pp. 3703–3713. URL: <http://dev.biologists.org/content/126/16/3703.abstract>.
- [WY09] Xizeng Wu and Aimin Yan. 'Phase retrieval from one single phase contrast x-ray image'. In: *Opt. Express* 17.13 (June 2009), pp. 11187–11196. DOI: [10.1364/OE.17.011187](https://doi.org/10.1364/OE.17.011187). URL: <http://www.opticsexpress.org/abstract.cfm?URI=oe-17-13-11187>.
- [Xen] Xenbase. *The Xenopus model organism database*. URL: <http://www.xenbase.org/>.
- [Youo2] Thomas Young. 'The Bakerian Lecture: On the Theory of Light and Colours'. English. In: *Philosophical Transactions of the Royal Society of London* 92 (1802), pages. ISSN: 02610523. URL: <http://www.jstor.org/stable/107113>.

- [Zer42a] Frits Zernike. 'Phase contrast, a new method for the microscopic observation of transparent objects'. In: *Physica* 9.7 (1942), pp. 686–698. ISSN: 0031-8914. DOI: [10.1016/S0031-8914\(42\)80035-X](https://doi.org/10.1016/S0031-8914(42)80035-X). URL: <http://www.sciencedirect.com/science/article/pii/S003189144280035X>.
- [Zer42b] Frits Zernike. 'Phase contrast, a new method for the microscopic observation of transparent objects part II'. In: *Physica* 9.10 (1942), pp. 974–986. ISSN: 0031-8914. DOI: [10.1016/S0031-8914\(42\)80079-8](https://doi.org/10.1016/S0031-8914(42)80079-8). URL: <http://www.sciencedirect.com/science/article/pii/S0031891442800798>.
- [Zer55] Frits Zernike. 'How I Discovered Phase Contrast'. In: *Science* 121.3141 (1955), pp. 345–349. DOI: [10.1126/science.121.3141.345](https://doi.org/10.1126/science.121.3141.345). URL: <http://www.sciencemag.org/content/121/3141/345.short>.

ACKNOWLEDGEMENTS

First of all, I am very much indebted to my doctoral advisor PD Dr. Ralf Hofmann. His enduring support and encouragement were essential on the way to my doctorate. I am very grateful for his guidance, the many enlightening discussions, and his invaluable theoretical input. And also his support in a number of experiments at APS and ESRF.

I am also indebted to Professor Dr. Tilo Baumbach for the opportunity to do my doctorate at the Institute for Photon Science and Synchrotron Radiation (IPS) / ANKA. I am very grateful for his support and his scientific input.

Special thanks to Daniel Hänschke for his support in a number of experiments at ANKA and ESRF, and the many discussions on theoretical and experimental aspects in imaging experiments and on computational issues concerning data processing and handling.

Special thanks to Venera Weinhardt for her support during a number of experiments, her help on data processing and discussions on imaging matters.

Special thanks to Jubin Kashef for providing first biological test samples, his help during a number of experiments at APS and ESRF, and his valuable input and insights regarding biological matters.

Special thanks also to Lukas Helfen for his great support and commitment in numerous experiments at beamlines ID15, ID19, and BM05 at ESRF. I also would like to thank Alexander Rack for the great support and commitment in experiments at beamline ID19.

Special thanks also to Xianghui Xiao for his great support and commitment in various experiment at 2-BM and 32-ID at APS. I also would like to thank Kamel Fezzaa, Alex Dery, and Francesco de Carlo for assistance using beamlines 2-BM and 32-ID.

Many thanks to Tomas Farago for his support in experiments at ID19 and discussions on computational issues, Alexey Ershov for his support during experiment at ID19 and his work on optical flow, Steffen Hahn for his support during experiment at ID19 and on data processing, Angelica Cecilia for her help during beam times at TopoTomo, Thomas Vandekamp for his support during experiment at ID19 and his help on graphics illustration and sample holders, Martin Köhl for setting up computational infrastructure at IPS, Suren A. Chilingaryan for providing PyHST support, Madeleine Hertel for support during experiment at 32-ID, and not to forget Alexander Schober for his support during experiments at 32-ID and ID19 and his work on numerical simulations and graphics illustrations.

I would like to thank Margit Helma for her administrative help. Moreover, I would like to thank my colleagues and former colleagues Jochen Butzer, Markus Riotte, Tomy dos Santos Rolo, Marthe Kaufholz, Patrick Vagovic, Elias Hamann, Thomas König, Marcus Zuber, Feng Xu, Yin Cheng, Yang Yang, Nicole Hiller, Steffen Hillenbrand, Markus Schwarz, and all the members and former members of ANKA, IPS, former ISS, and LAS.

I would like to thank Carole LaBonne's group at Northwestern University (NU) for providing frogs and laboratory equipment during experiments at APS, and in particular Maneeshi Prasad for his great help us during beam times at APS.

I would like to thank Professor K. Joost Batenburg for his hospitality at the Center of Mathematics and Informatics (CWI) in Amsterdam and discussions on tomography. Many thanks also to Daniel Pelt, Paul M. de Zeeuw, Folkert Bleichrodt, Willem Jan Palenstijn, and Tristan van Leeuwen for discussing algebraic and neural-network-based reconstruction techniques.

Last, but not least I would like to thank my parents Hans and Sylvia Moosmann and my spouse Sara Tavernar for their great support during all the time.

I acknowledge the Synchrotron Light Source ANKA for provision of instruments at their beamlines, and the European Synchrotron Radiation Facility for provision of synchrotron radiation facilities. Use of the Advanced Photon Source was supported by the U.S. DOE under Contract No. DE-AC02-06CH11357. This research partially was funded by the German Federal Ministry of Education and Research under grant numbers 05K12CK2, 05K12VH1 and by EXTREMA COST Action MP1207 supported by the European Commission.